

AD-A084 338

GENERAL ELECTRIC CO SANTA BARBARA CA TEMPO
LORAN-C SIGNAL ANALYSIS PROPAGATION MODEL EVALUATION.(U)
JUL 79 B GAMBILL, K SCHWARTZ

F/G 20/14

UNCLASSIFIED

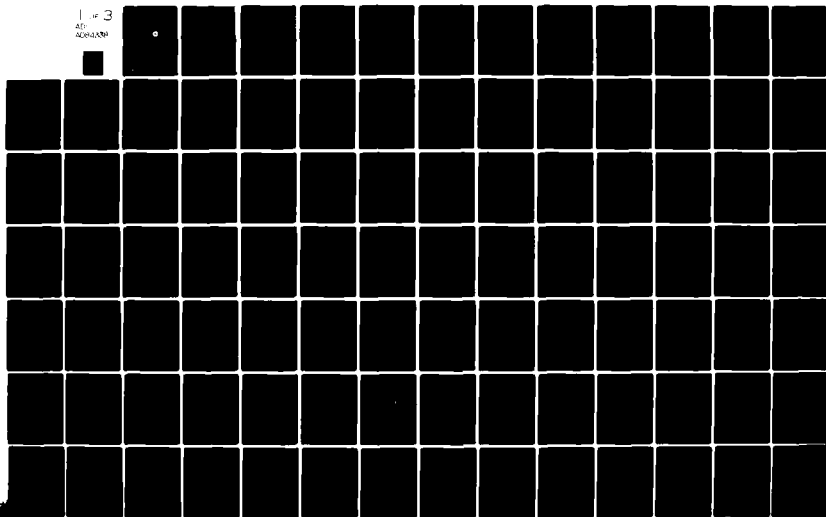
6E78TMP-51

USCG -D-20-80

DOT-C6-64810-A

NL

1 of 3
AD-A084 338



REPORT NO. CG-D-20-80

(12)

LEVEL

LORAN-C SIGNAL ANALYSIS PROPAGATION MODEL EVALUATION

ADA 084338

Burt Gambill
Kenneth Schwartz

General Electric—TEMPO
816 State Street
Santa Barbara, CA. 93110



July 1979

FINAL REPORT

DTIC
ELECTE
MAY 19 1980
A

DDC FILE COPY.

PREPARED FOR
US. DEPARTMENT OF TRANSPORTATION
UNITED STATES COAST GUARD
OFFICE OF RESEARCH AND DEVELOPMENT
WASHINGTON, D.C. 20590

DISTRIBUTION STATEMENT A
Approved for public release
Distribution Unlimited

80 5 15 001

NOTICE

This document is disseminated under the sponsorship of the Department of Transportation in the interest of information exchange. The United States Government assumes no liability for its contents or use thereof.

The contents of this report do not necessarily reflect the official view or policy of the Coast Guard; and they do not constitute a standard, specification, or regulation.

This report, or portions thereof may not be used for advertising or sales promotion purposes. Citation of trade names and manufacturers does not constitute endorsement or approval of such products.

Technical Report Documentation Page

1. Report No. (18) USCGAD-29-89		2. Government Accession No. AD-A084 338		3. Recipient's Catalog No.	
4. Title and Subtitle (6) Loran-C Signal Analysis Propagation Model Evaluation		5. Report Date (11) July 1979		6. Performing Organization Code (12)	
7. Author(s) (10) Burt Gambill, Kenneth Schwartz		8. Performing Organization Report No. (14) GE78TMP-51		9. Performing Organization Name and Address General Electric (TEMPO) 816 State Street Santa Barbara, CA 93102	
10. Sponsoring Agency Name and Address U.S. Coast Guard G-FPC-2/71 Washington, DC 20590		11. Work Unit No. (TRAIS)		12. Contractor Grant No. (15) DOT-CG-64810 A	
13. Type of Report and Period Covered (9) Final Report, June 1977 to May 1978		14. Sponsoring Agency Code		15. Supplementary Notes	
16. Abstract <p>This report compares predictions of groundwave propagation time with experimental values. The prediction methods included an integral equation technique that accounts for both terrain and impedance variations, a method developed by J.R. Wait that accounts for impedance variations, and Millington's or Pressey's technique that accounts for inhomogeneous impedance. Experimental incremental time-of-arrival data were acquired between eight sites along a propagation path from Searchlight, NV. to Ft. Cronkhite (near San Francisco Bay). The major conclusions reached from the analysis and comparison of results are:</p> <ul style="list-style-type: none"> a. Terrain variations produce significant local and cumulative phase variations, in this case, a cumulative large increase in total secondary phase. b. Impedance values need to be known to within less than a factor of two to be sufficient for preparing charts for navigation in restricted waterways. c. A priori definition of terrain variation can be performed with required accuracy - a priori definition of surface impedance values with sufficient accuracy is unlikely without supporting measurements, and d. A combination of predictions and measurements is required for accurate chart preparation. Predictions can be used to define appropriate measurement locations and to interpolate between measurement values. 					
17. Key Words Groundwave Propagation Terrain Variations Inhomogeneous Impedance Integral Equation Time-of-arrival Measurements			18. Distribution Statement Document is available to the public through the National Technical Information Service, Springfield, VA 22161.		
19. Security Classif. (of this report) Unclassified		20. Security Classif. (of this page) Unclassified		21. No. of Pages 22. Price	

17. Time Difference Measurement
 Propagation Predictions
 Experimental and Predicted Comparisons

Accession For	
NHIS Class	<input checked="" type="checkbox"/>
D. C. 112	<input checked="" type="checkbox"/>
Unpublished	<input type="checkbox"/>
Justification	
By	
Date	
Approved by	
Dist.	A. 112/107 or special
A	

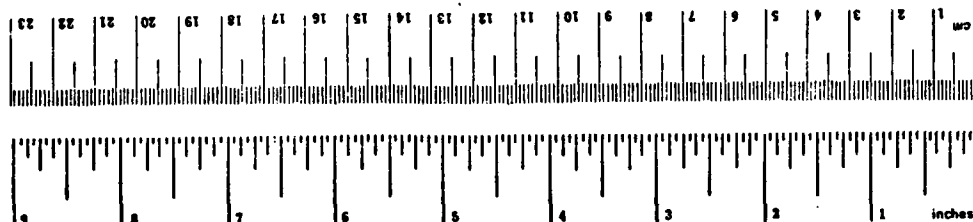
METRIC CONVERSION FACTORS

Approximate Conversions to Metric Measures

Symbol	When You Know	Multiply by	To Find	Symbol
LENGTH				
in	inches	2.5	centimeters	cm
ft	feet	30	centimeters	cm
yd	yards	0.9	meters	m
mi	miles	1.6	kilometers	km
AREA				
in ²	square inches	6.5	square centimeters	cm ²
ft ²	square feet	0.09	square meters	m ²
yd ²	square yards	0.8	square meters	m ²
mi ²	square miles	2.6	square kilometers	km ²
	acres	0.4	hectares	ha
MASS (weight)				
oz	ounces	28	grams	g
lb	pounds	0.45	kilograms	kg
	short tons (2000 lb)	0.9	tonnes	t
VOLUME				
tblsp	tablespoons	5	milliliters	ml
fl oz	fluid ounces	15	milliliters	ml
c	cups	30	milliliters	ml
pt	pints	0.24	liters	l
qt	quarts	0.47	liters	l
gal	gallons	0.95	liters	l
yd ³	cubic feet	3.8	liters	l
	cubic feet	0.03	cubic meters	m ³
	cubic yards	0.76	cubic meters	m ³
TEMPERATURE (exact)				
°F	Fahrenheit temperature	5/9 (after subtracting 32)	Celsius temperature	°C

Approximate Conversions from Metric Measures

Symbol	When You Know	Multiply by	To Find	Symbol
LENGTH				
mm	millimeters	0.04	inches	in
cm	centimeters	0.4	inches	in
m	meters	3.2	feet	ft
km	kilometers	1.1	yards	yd
		0.6	miles	mi
AREA				
cm ²	square centimeters	0.16	square inches	in ²
m ²	square meters	1.2	square yards	yd ²
km ²	square kilometers	0.4	square miles	mi ²
ha	hectares (10,000 m ²)	2.5	acres	
MASS (weight)				
g	grams	0.035	ounces	oz
kg	kilograms	2.2	pounds	lb
t	tonnes (1000 kg)	1.1	short tons	
VOLUME				
ml	milliliters	0.03	fluid ounces	fl oz
l	liters	2.1	pints	pt
l	liters	1.06	quarts	qt
l	liters	0.26	gallons	gal
m ³	cubic meters	35	cubic feet	ft ³
m ³	cubic meters	1.3	cubic yards	yd ³
TEMPERATURE (exact)				
°C	Celsius temperature	9/5 (then add 32)	Fahrenheit temperature	°F



1 in = 2.54 (exact). For other exact conversions and more detailed tables, see NBS Misc. Publ. 286, Units of Lengths and Measures, Price \$2.25. SD Catalog No. C13.10.286.

PREFACE AND ACKNOWLEDGMENTS

This work was supported by the United States Coast Guard Office of Research and Development. Coast Guard Project Officers have included Commander R. Cassis, Commander James Walker, Captain William Flanders, and Dr. Surendra Nath Samaddar. Contributions were provided by several individuals and organizations. These are listed below in alphabetical order.

1. Dr. Donald Chandler (General Electric—TEMPO) provided useful technical suggestions and performed the technical review of this report.
2. Mr. Walter Dean (Magnavox) and Mr. Robert Goddard (Internav) provided useful assistance in TOA and TD data interpretation.
3. Mr. Samuel Horowitz (formerly with U.S. Air Force ESD) provided card images, user documentation and useful inputs for the GFE Integral Equation Prediction program.
4. Mr. John Illgen (General Electric—TEMPO) provided assistance in planning Loran data collection, in interpreting Loran TOA and TD data, and in collecting supplementary system and geophysical data.
5. Mr. Ted Kostigen (consultant General Electric—TEMPO) developed the terrain data base from topographic maps.
6. Messrs. Ralph Johler and Robert Doherty (Colorado Radio Prediction Laboratory) provided detailed information on algorithms in the Integral Equation Prediction program.
7. Dr. Lawrence Nelson (General Electric—TEMPO) developed models and software to reduce the Loran TOA data.
8. Dr. Surendra Nath Samaddar (USCG G-D) provided useful discussions and specific inputs relative to weather-induced Loran phase fluctuations.
9. Lt Cmdr Andrew Sedlock (USCG G-D) assisted in selecting measurement sites and supervised the accurate survey of site locations.
10. Dr. James Thompson (General Electric—TEMPO) developed the data base for the surface impedance values.
11. Useful discussions were held with Captain William Flanders, Dr. Don Feldman and Commanders Bill Jones and Dave Clements, all of USGG.

TABLE OF CONTENTS

DOCUMENTATION PAGE

PREFACE

METRIC CONVERSION FACTORS

SECTION		Page
1	INTRODUCTION	1
2	PREDICTION TECHNIQUES	4
	Smooth Homogeneous Earth Theory	4
	Millington's Technique	5
	Wait's Multiple Segment Technique	9
	Integral Equation Solution	12
	The Integral Equation Formulae	14
	Comparison Between Multisegment Smooth Earth Theory and the Integral Equation Method	17
	Comparison Between Wait's Multisegment Theory and Millington's Technique	25
	Comparison Between Millington's Technique and the Integral Equation Method	29
	Program Operation	29
	Applications	31
3	WEATHER EFFECTS	35
	Refractive Index of Air and Equivalent Earth Radius	36
	Inclusion of Weather Effects in Propagation Codes	40
	Model Limitations - Need for Further Research	43
	An Example of Predicted Weather Effects	45
	Phase Fluctuation Produced An Apparent Surface Impedance Change	55
4	EXPERIMENTAL RESULTS	60
	Experiment Sites	61
	Measurements	61
5	WORST CASE PATH PREDICTIONS AND COMPARISON WITH EXPERIMENTAL RESULTS	68
	Terrain Data	68
	Surface Impedance	71
	Predictions	77
	Comparison Between Predicted and Measured Values	93
	Comparison Between Millington's Technique and the Integral Equation Method	97
	Comparison with USCG Conductivity Map	103

SECTION		Page
6	PREPARATION OF HARBOR GRID	106
	Initial Procedures - Simplified Predictions	
	Using Local Disturbances	106
	Harbor Experiment	119
	Harbor Experiment Conclusions	124
7	CONCLUSIONS AND RECOMMENDATIONS	127
	Conclusions	127
	Recommendations	132
APPENDIX		
A	DETAILS OF THE SMOOTH HOMOGENEOUS EARTH THEORY	A-1
	Short Distance Approximations	A-1
	Series Solution	A-4
B	NUMERICAL EVALUATION AND ADDITIONAL INVESTIGATIONS OF WAIT'S MULTIPLE SEGMENT TECHNIQUE	B-1
	Computer Solution	B-1
	Investigation of Approximations	B-4
C	DETAILS OF INTEGRAL EQUATION FORMULATION	C-1
D	MULTILAYER IMPEDANCE	D-1
E	TERRAIN DATA FOR WORST CASE PATH	E-1
F	MATERIALS AND CONDUCTIVITIES ALONG THE WORST CASE PATH	F-1

ILLUSTRATIONS

Figure		
2-1(a)	Illustrating Millington's technique.	7
2-1(b)	Illustrating Millington's technique.	7
2-2	Multisegment smooth earth propagation path.	9
2-3	Illustrating multisegment integration scheme.	11
2-4	Geometry for propagation over irregular terrain.	15
2-5	Secondary phase vs distance as predicted by HUFLOC (ϕ_H) and MULSEG (ϕ_M).	18
2-6	Additive phase changes produced by a Gaussian hill.	24
2-7	Comparison of MULSEG and Millington for a 2 segment path.	26
2-8(a)	Comparison of MULSEG and Millington for a 5 segment path (sea to land).	27

Figure		Page
2-8(b)	Comparison of Millington and MULSEG results for a 5 segment path (land to sea).	28
2-9	Execution time versus number of integration points for HUFLOC.	32
3-1	N units versus temperature and α for various values of relative humidity and a pressure of 1000 mb.	38
3-2	N units versus temperature and α for various values of relative humidity and a pressure of 870 mb.	39
3-3	Atmospheric pressure (reduced to sea level) at Reno, NV over the time period 13 December to 22 December 1977.	46
3-4	Surface temperature at Reno, NV over the time period 13 December to 22 December 1977.	47
3-5	Dew point temperature at Reno, NV over the time period 13 December to 22 December 1977.	48
3-6	N units computed at Reno, NV over the time period 13 December to 22 December 1977.	49
3-7	Ratio of earth radius to effective earth radius at Reno, NV compiled over the time period 13 December to 22 December 1977.	50
3-8	Phase variation over a 100 km path using the values of N and effective earth radius from Figures 3-6 and 3-7. ($\sigma = 0.01$).	51
3-9	Phase variation over a 300 km path using the values of N and effective earth radius from Figures 3-6 and 3-7. ($\sigma = 0.01$).	52
3-10	Phase variation over a 500 km path using the values of N and effective earth radius from Figures 3-6 and 3-7. ($\sigma = 0.01$).	53
3-11	Phase variation over a 700 km path using the values of N and effective earth radius from Figures 3-6 and 3-7. ($\sigma = 0.01$).	54
3-12	Measurement sites during stability experiment.	56
3-13	Time difference at Silver Springs and Arbuckle.	57
4-1	WCP data collection sites relative to the GEODESIC.	62
5-1	Original worst case path terrain data.	70
5-2	Areas of high, moderate and low near-surface resistivity in the United States, as indicated by resistivity measurements near radio stations.	73

Figure		Page
5-3	Amplitude of the surface impedance as a function of distance along the worst case path.	78
5-4	Smooth terrain data for the worst case path.	80
5-5a	Comparison between smoothed and raw data in the vicinity of site Tecopa.	81
5-5b	Comparison between smoothed and raw data in the vicinity of site Death Valley.	82
5-5c	Comparison between smoothed and raw data in the vicinity of site Darwin.	83
5-5d	Comparison between smoothed and raw data in the vicinity of site Delilah.	84
5-5e	Comparison between smoothed and raw data in the vicinity of site Friant.	85
5-5f	Comparison between smoothed and raw data in the vicinity of site Merced.	86
5-5g	Comparison between smoothed and raw data in the vicinity of site Crows Landing.	87
5-5h	Comparison between smoothed and raw data in the vicinity of site Livermore.	88
5-6	Secondary phase along the worst case path S-3, $\Delta X = 0.9$ km.	91
5-7	Computed secondary phase on worst case path, $S = 6$ km, $\Delta X = 0.9$ km comparing effect of original impedance to that for which each conductivity value was reduced in a factor of 2.	94
5-8	Approximation of the surface impedance for a Millington calculation.	98
5-9	Comparison between the integral equation and Millington's Technique results.	99
5-10	Comparison of HUFLOC and Millington amplitude calculation results for worst case path.	100
5-11	Comparison of Millington's technique with the integral equation technique (with terrain variations suppressed).	101
5-12	Results of Millington's impedance optimization.	102
5-13	Comparison of Millington with impedance optimized and experimental results.	104
6-1	Effect of a land sea interface on the secondary phase.	107

Figure		Page
6-2	Phase change vs distance from the land sea transition.	108
6-3	Sample of initial grid for San Francisco Harbor.	111
6-4	First order TDX variations (ns) produced by land sea boundary effect.	113
6-5	First order TDY variation (ns) produced by land sea boundary effect.	114
6-6	Phase error produced by reflection from Golden Gate Bridge.	118
6-7	San Francisco Harbor test area.	120
B-1	Coordinates for describing wave propagation on a spherical surface.	B-5
B-2	Plane view of the inhomogeneous surface showing the coordinates α and y and the boundary for the inhomogeneous region.	B-9
B-3	Geometry near singular point.	B-10
C-1	Geometry for propagation over an inhomogeneous, irregular terrain.	C-3
C-2	Geometry used for defining variations in $\frac{\partial r_2}{\partial n}$.	C-16
C-3	Amplitude and phase errors of term T as a function of elevation error for ($\sigma = 10^{-3}$, $\epsilon/\epsilon_0 = 15$, $r_2 = 300$ km and nominal slope $z'_k = 0$).	C-19
C-4	Amplitude and phase errors of term T as a function of elevation error for $\sigma = 10^{-3}$, $\epsilon/\epsilon_0 = 15$, $r_2 = 300$ km and nominal slope $z'_k = 0.1$).	C-20
D-1	Impedance amplitude (Case 1).	D-3
D-2	Impedance phase (Case 1).	D-4
D-3	Impedance amplitude (Case 2).	D-5
D-4	Impedance phase (Case 2).	D-6
D-5	Impedance amplitude (Case 3).	D-7
D-6	Impedance phase (Case 3).	D-8
D-7	Impedance amplitude (Case 4).	D-9
D-8	Impedance phase (Case 4).	D-10
D-9	Impedance amplitude (Case 5).	D-11
D-10	Impedance phase (Case 5).	D-12
D-11	Impedance amplitude (Case 6).	D-13
D-12	Impedance phase (Case 6).	D-14

TABLES

Table		Page
2-1	MULSEG predictions of the secondary phase (ns) correction as a function of the integration step size.	20
2-2	HUFLOC predictions of the secondary phase (ns) Correction as a function of the integration step size.	21
2-3	Secondary phase (ns) correction vs distance.	21
2-4	Two segment path parameters.	25
2-5	Five segment path parameters.	25
3-1	Propagation parameter variations with the refractive index.	41
3-2	Constants for linear equation defining ϕ_s as a function of α .	42
3-3	Conductivity and time difference changes.	59
4-1	Worst case path calibration and measurement sites.	61
4-2	Mean value of TD at WCP measurement sites.	63
4-3	Calibrator and time of arrival data for WCP Measurement sites.	66
5-1	Worst case path data collection points.	69
5-2	Generalized resistivity ranges for rocks of different lithology and age.	72
5-3	Summary of resistivities measured about radio stations.	74
5-4	Parameters for different HUFLOC (INEQ2E) computer runs for worst case path.	89
5-5	Computed secondary phase in nanoseconds at the original worst case path data sites for the different calculational conditions given in Table 5-4.	90
5-6	Comparison of predicted (case 3) and measured results from the worst case path.	96

Table		Page
5-7	Secondary phase (ns) relative to Tecopa.	105
6-1	Summary of harbor fixed site data reduction and grid preparation.	122
A-1	Minimum distance in kilometers to obtain N digit accuracy with S terms in the series expansion for the groundwave attenuation functions.	A-7
A-2	Comparison of procedures for computing the attenuation function.	A-8
B-1	Amplitude and phase as a function kd.	B-7
C-1	Variation of $\partial r_2 / \partial n$ due to variation in local terrain slope at various distances from the receiver.	C-17
F-1	Age and geologic material symbols.	F-2
F-2	R-index vs index.	F-4
F-3	Conductivity and dielectric constant values for materials used on worst case path.	F-5
F-4	Assumed geologic structure along the worst case path.	F-6

SECTION 1

INTRODUCTION

Loran-C is a pulsed hyperbolic or range-range radionavigation system operating in the 90-110 kHz band. At ranges less than 1000 to 2000 kilometers from the transmitters, depending on surface impedance values, Loran-C receivers track signals propagated via the groundwave. The achievable position accuracy depends on a number of factors and conditions including:

- a. Equipment induced fluctuations
- b. Mode of operation - absolute position, repeatable position or differential mode
- c. Calibration - number of calibration points and procedures for extrapolating between measurement points over the coverage area
- d. Monitor location(s) - location of monitor site relative to the coverage area
- e. Control policy - procedures for maintaining the control standard time difference
- f. Environmental effects - uncertainties in mean values and variations in surface impedance or refractive index of the air
- g. Prediction error - failure of prediction technique to properly account for known or estimated environmental variations.

One objective of the Loran-C Signal Analysis project is to perceive potential improvements in the accuracy and control of Loran-C through a better understanding of Loran-C signal characteristics. In this report we are primarily concerned with prediction errors that result from approximations or omissions in prediction techniques or uncertainties

in environmental parameters, their relationship to the choice of mode of operation, calibration procedures, monitor location and control policy, and their magnitude relative to equipment fluctuations.

Prediction techniques refer to computer programs that perform numerical solutions of the wave equation, subject to an impedance boundary condition at the earth's surface. Different approximations to represent the earth boundary include a smooth, homogeneous (constant surface impedance) boundary, smooth inhomogeneous boundary, and an irregular (including terrain variations), inhomogeneous boundary. In all cases, the earth is considered to be spherical* with equivalent radius a_e , where a_e is different (usually larger) than the actual earth radius a , to account for the refractive effects of the atmosphere. The ratio $\alpha = a/a_e$ is referred to as the vertical lapse rate.

In this report we present the results of reviewing four groundwave propagation prediction techniques and testing them against each other and against a carefully controlled experimental data base. The four techniques are

1. Classical, Homogeneous Spherical Earth - a well researched technique documented by comprehensive published literature.
2. Pressey's or Millington's - a semiempirical technique that accounts for inhomogeneous impedance, and is currently used for Loran-C chart preparation.
3. Wait's Multisegment Spherical Earth (MULSEG) - an extension of the classical theory to account for inhomogeneous impedance.
4. Integral Equation Solution - a GFE computer program (HUFLOC) provided by the U.S. Coast Guard to calculate signals over irregular, inhomogeneous terrain.

The methods are evaluated in terms of their ability to reproduce experimental measurements and practical application. Desirable improvements in the prediction techniques are suggested.

Section 2 describes these techniques and outlines the important steps in the calculation procedures. Details of the calculation proce-

*Terrain variations (when included) are referenced to a smooth sphere.

dures are presented in Appendices A, B, and C. In addition, parametric testing and comparison between two methods (3 and 4 above) have been carried out for cases where their regions of applicability overlap. The integral equation solution is tested against the reciprocity property for several cases. The computer program operation for each method is discussed and data preparation requirements and computer running time are described.

In Section 3 the effect of atmospheric variations on propagation is discussed. The relations between standard atmospheric parameters (pressure, temperature, dew point temperature or humidity) and the refractive index and effective earth radius are given. Methods for including the refractive index and effective earth radius in the predictions are described. Limitations of the current theory with recommendations for further research are also discussed. An example of predicted weather induced fluctuations, using sample surface weather parameters from a site in the West Coast coverage area, is provided.

Section 4 describes an experiment that was designed to provide a data base to evaluate the prediction techniques. The experiment provided incremental (site-to-site) changes in signal time of arrival (TOA) at sites approximately on the geodesic from Searchlight, Nevada (Yankee Secondary) to Ft. Cronkhite, CA. This path is referred to as the Worst Case Path (WCP). The experimental procedures and results, with an estimate of accuracy of the results, are also reproduced.

Section 5 describes the results from various prediction techniques and compares the predictions with the data collected in the experiment discussed in Section 4. Sensitivity to computational procedures and to input parameters is discussed.

Section 6 describes some procedures and initial results for preparing a map of spatial anomalies of time differences (TD's) in the San Francisco Harbor. These initial results were used in planning the experiment in the San Francisco Harbor. The results of measurements in San Francisco Harbor defining measured spatial anomalies are also summarized in this section.

Section 7 provides a summary and recommendations for further analyses.

SECTION 2

PREDICTION TECHNIQUES

The theory of the propagation of radio waves over the earth's surface was developed first for a smooth homogeneous earth model, then for an inhomogeneous earth, and finally for an irregular and inhomogeneous earth. The salient features of the propagation theories are presented in this section. The technical details are reproduced in three appendices, A, B and C.

SMOOTH HOMOGENEOUS EARTH THEORY

Extensive research has been carried out on the theory of ground wave propagation over a smooth homogeneous earth. The research has been comprehensively reported in the open published literature. Computational procedures are available that produce a higher degree of precision than the input data, ie, the measurements of the electrical properties of the earth. The idealized theory has little direct application to the Loran-C prediction problem, since most propagation paths between Loran-C transmitters and user locations include irregular, nonspherical, inhomogeneous segments. However, the calculational techniques form a part of more complete models and for this reason computational procedures and associated accuracies are important.

The discussion presented here and in Appendix A is a summary of various presentations in the literature. They are collected here for easy reference when referring to computer programs and applications defined later. Details of three forms of the smooth spherical earth theories are presented in Appendix A: two short distance approximations and a series expansion. The series expansion is more accurate but requires many terms for the shorter distances. Thus, switch points from one calculation to another are defined.

In all cases, the received field E is defined as

$$E = E_0 W \quad (2-1)$$

where W , the attenuation function, is a function of the earth curvature and the surface impedance, and E_0 is the unbounded region reference field defined in air by

$$E_0 = \frac{0.3 \sqrt{p}}{d} \left[1 - \frac{1}{(k_1 d)^2} - \frac{i}{k_1 d} \right] e^{-ik_1 d} \quad \text{v/m} \quad (2-2)$$

and

- E = peak value of the electric field (v/m)
- p = average transmitter power (kW)
- d = path length (km)
- $k_1 = 2\pi\eta f/c$ = wave number in air (km^{-1})
- f = wave frequency (hz)
- c = speed of light in vacuum (2.997925×10^5 km/s)
- η = refractive index of air .

From Equation 2-1 and 2-2 it can be seen that $k_1 d$ is the primary phase factor and the phase of W is the secondary phase factor.

For the smooth earth theory weather and atmospheric conditions enter through the wave number, k_1 , and the effective earth radius, a_e , a factor used to calculate W . A method of computing the effective earth radius is given in Section 3 where it is shown that the effective earth radius is a function of $\frac{dn}{dh}$ where h is the altitude. The phase of W is only slightly affected by change in η ($\eta - 1 \approx .003$) but does reflect changes in $\frac{dn}{dh}$. The phase of E_0 will change directly with changes in η . In general the phase change in E_0 from a change in k_1 is opposite to the phase change in W for the corresponding change in $\frac{dn}{dh}$ and hence a_e .

MILLINGTON'S TECHNIQUE

Millington's Technique is a semi-empirical method originally developed to compute the attenuation function amplitude over an inhomogeneous propagation path. The method is described in detail in Reference 2-1. It was extended by Pressey to compute phase of the attenuation function (Reference 2-2). Briefly a path is divided into segments with

- 2-1. Millington, G., "Groundwave Propagation Over an Inhomogeneous Smooth Earth," Proceedings IEE, Parts I and II (1949, Vol 96, p 53) and Part III (1950, Vol 97, p 200).
- 2-2. Pressey, B.G., "The Measurement of the Phase Velocity of Ground-wave Propagation at Low Frequencies over a Land Path," Paper 1438, Radio Section, Proceedings IEE, 20 October, 1952.

length d_1, d_2, d_3, \dots with each segment characterized by a surface impedance $\Delta_1, \Delta_2, \Delta_3, \dots$. The method assumes that the slope of the phase function or logarithm of the composite attenuation function is determined by the slope of the corresponding homogeneous attenuation function. Figure 2-1 illustrates the calculation method. Shown on the figure are idealized plots of the logarithm of the magnitude of the attenuation function for three values of the normalized surface impedance $\Delta_1, \Delta_2, \Delta_3$. As illustrated, Δ_1 is the surface impedance from the transmitter to a distance d_1 , Δ_2 is the surface impedance of the second segment of length d_2 from $d = d_1$ to $d = d_1 + d_2$, etc. The complete attenuation function does not have to be calculated, just the values labeled W_1, W_2, \dots, W_{10} using the methods of Appendix A for a smooth homogeneous earth.

The composite attenuation functions are computed for the transmitter to receiver path (W_A) and the receiver to transmitter path (W_B). Letting $w_i = \ln|W_i|$ these functions are computed for the example from

$$w_A = w_1 - (w_2 - w_3) - (w_4 - w_5) \quad (2-3a)$$

$$w_B = w_6 - (w_7 - w_8) - (w_9 - w_{10}) \quad (2-3b)$$

and the final estimate of the composite is

$$w_T = \frac{w_A + w_B}{2} \quad (2-3c)$$

This averaging procedure is used to force the empirical prediction to be reciprocal. To compute the secondary phase, the same procedure is followed except that the phase is used instead of the logarithm of the amplitude of the attenuation function.

A computer program adapted from Reference 2-3 has been programmed at TEMPO to use Millington's technique for chart generation, utilizing calibration measurements. This program, except for TEMPO modifications, is well documented in Reference 2-3. The functions performed by the user and the program are summarized briefly below. Modifications added at TEMPO are also indicated.

- 2-3. Coast Guard furnished documentation of Program EEE-11, "Computation of LORAN-C System Standard Deviation and Conductivities."

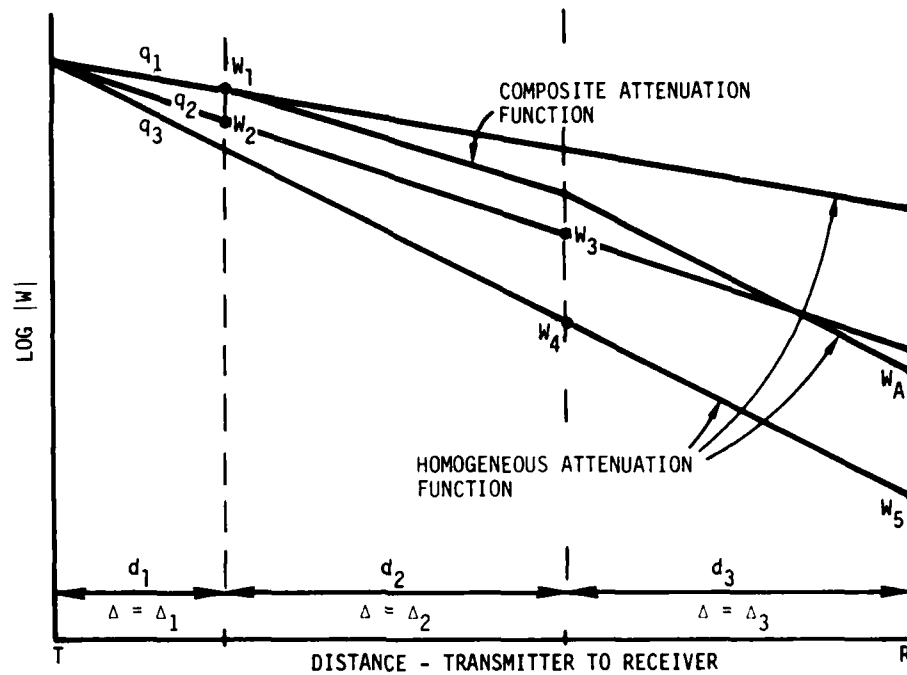


Figure 2-1(a). Illustrating Millington's technique.

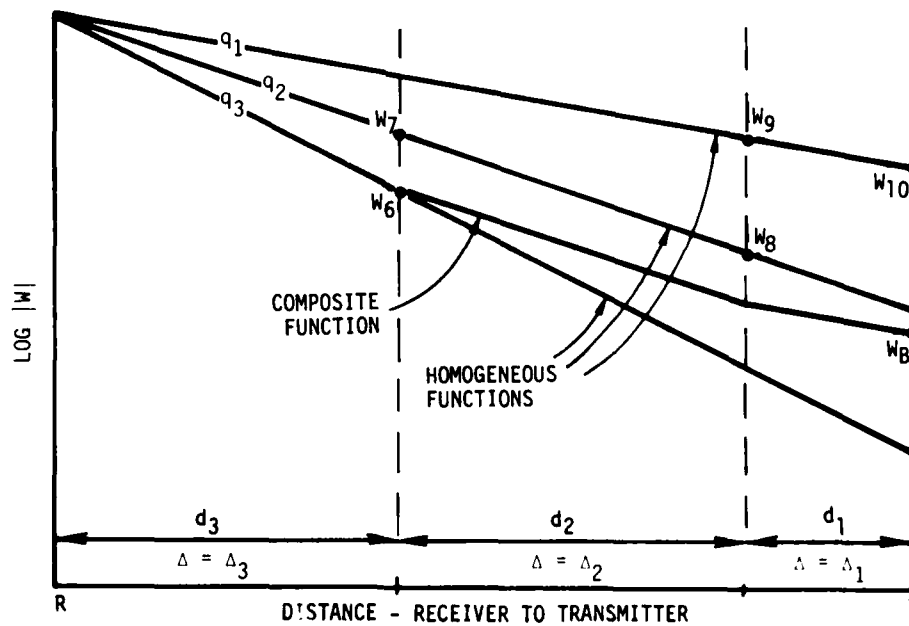


Figure 2-1(b). Illustrating Millington's technique.

- Time difference measurements for one or more transmitter-secondary pairs and one or more monitor locations are obtained.
- The area over which the signals propagate is divided into sub-areas and a best estimate of the conductivity and a range of conductivities is defined for each sub-area.
- Each path from Master and Secondary to each monitor site is divided into segments defined by the path intersections with conductivity area boundaries.
- The secondary phase factor is calculated for each path using Millington's technique. This calculation is iterated, varying the conductivity of each area over the permissible range of conductivities for that area.
- The best conductivity values for the areas are defined as those that minimize the standard deviation of the difference between measured and computed time difference at all monitor sites.

The principal modification provided at TEMPO was to change the method of computing the TSF*. In the program given in Reference 2-3, The ASF[†] was computed using a parabolic fit to precomputed ASFs. This analytic procedure was replaced by the three smooth homogeneous earth procedures for calculating the attenuation function as given in Appendix A, with a control subroutine to select the appropriate calculation methods. The modification provides:

- a. Complete freedom in choice of surface impedance values for each path segment.
- b. The capability to vary the equivalent earth's radius on the path if desired.

This computer program is operational and has been used for impedance map generation for a path from Searchlight, Nevada to Ft. Cronkhite, California.

*Total Secondary Phase Factor - Phase of W (see Equation 2-1).

†Additional Secondary Phase Factor - Phase of W [land] - Phase of W [sea water].

WAIT'S MULTIPLE SEGMENT TECHNIQUE

For an inhomogeneous spherical earth, Wait (Reference 2-4) has extended the homogeneous theory described above and in Appendix A to include propagation paths with multiple segments, each segment with a different surface impedance. The path is illustrated in Figure 2-2, with the nomenclature modified slightly from Reference 2-4.

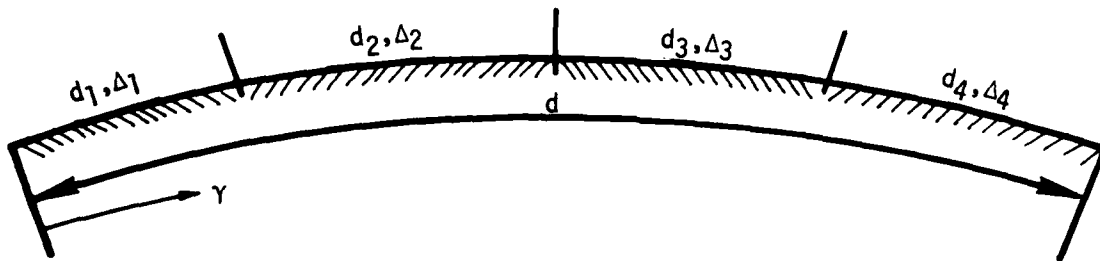


Figure 2-2. Multisegment smooth earth propagation path.

The path of total length d has four segments of length d_1 , d_2 , d_3 , and d_4 and effective normalized surface impedance of Δ_1 , Δ_2 , Δ_3 , Δ_4 . Formulae for a single or multilayer earth are discussed in Appendix D.

Wait presents formulae for 2 and 3 segment paths in Reference 2-2. For the 2 segment path, the composite attenuation function $W'(d, \Delta_1, \Delta_2)$ is defined by

$$W'(d, \Delta_1, \Delta_2) = W(d, \Delta_2) - \left(\frac{ik_1 d}{2\pi} \right)^{1/2} (\Delta_1 - \Delta_2) \cdot \int_0^d \frac{W(d-\gamma, \Delta_2) W(\gamma, \Delta_1) d\gamma}{[\gamma(d-\gamma)]^{1/2}} \quad (2-4)$$

where the attenuation functions $W(d, \Delta_2)$, $W(d - \gamma, \Delta_2)$, $W(\gamma, \Delta_1)$ are calculated using smooth homogeneous earth theory. The variable, γ , is defined in Figure 2-2 and k_1 is the wave number in air.

2-4. Wait, J.R., "Electromagnetic Surface Waves," Advances in Radio Research (ed. by J.A. Saxton), Vol. 1, pp. 157-217, Academic Press, London, 1964.

For the three segment path, the composite attenuation function is defined as

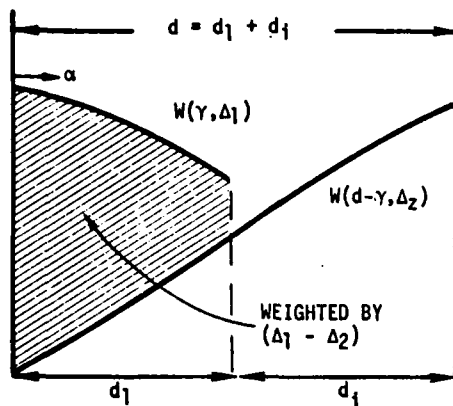
$$\begin{aligned}
 W'(d, \Delta_1, \Delta_2, \Delta_3) &= W(d, \Delta_3) - \left(\frac{ik_1 d}{2\pi}\right)^{1/2} (\Delta_1 - \Delta_3) \cdot \\
 &\int_0^{d_1} \frac{W(d-\gamma, \Delta_3) W(\gamma, \Delta_1)}{[\gamma(d-\gamma)]^{1/2}} d\gamma \\
 &- \left[\frac{ik_1 d}{2\pi}\right]^{1/2} (\Delta_2 - \Delta_3) \int_{d_1}^{d_1+d_2} \frac{W(d-\gamma, \Delta_3) W'(\gamma, \Delta_1, \Delta_2) d\gamma}{[\gamma(d-\gamma)]^{1/2}} \quad (2-5)
 \end{aligned}$$

where $W'(\gamma, \Delta_1, \Delta_2)$ is the composite attenuation function for the two part segment evaluated using Equation 2-4.

For an n segment path Equation 2-5 can be generalized to read

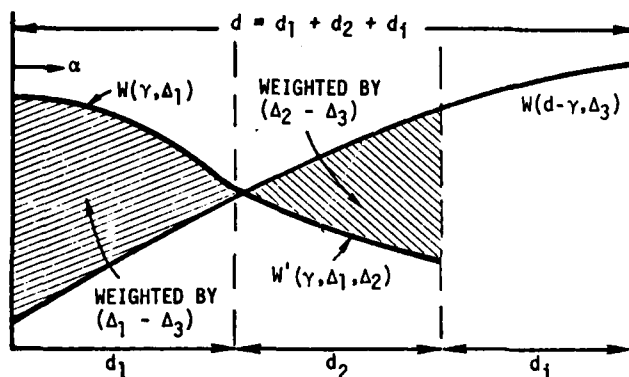
$$\begin{aligned}
 W'(d, \Delta_1, \Delta_2, \dots, \Delta_n) &= W(d, \Delta_n) - \left(\frac{ik_1 d}{2\pi}\right)^{1/2} (\Delta_1 - \Delta_n) \cdot \\
 &\int_0^{d_1} \frac{W(d-\gamma, \Delta_n) W(\gamma, \Delta_1) d\gamma}{[\gamma(d-\gamma)]^{1/2}} \dots \\
 &- \left[\frac{ik_1 d}{2\pi}\right]^{1/2} (\Delta_{n-1} - \Delta_n) \int_{d_1+d_2+\dots+d_{n-2}}^{d_1+d_2+\dots+d_{n-1}} \frac{W(d-\gamma, \Delta_n) W'(\gamma, \Delta_1, \Delta_2, \dots, \Delta_{n-1}) d\gamma}{[\gamma(d-\gamma)]^{1/2}} \quad (2-6)
 \end{aligned}$$

The calculations are illustrated graphically in Figure 2-3 where idealized attenuation functions (they are really complex quantities) are shown and the integration interval and impedance weighting function are shown. The continuation to four segments is shown and extension to additional segments is obvious.



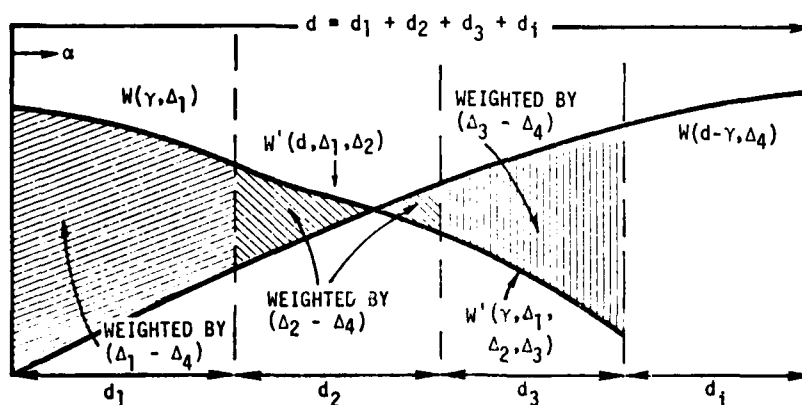
NOTE:

By varying d_i from 0 to d_2 , $W'(d, \Delta_1, \Delta_2)$ can be defined over the total interval.



NOTE:

By varying d_i from 0 to d_3 , $W'(d, \Delta_1, \Delta_2, \Delta_3)$ can be defined over the interval.



NOTE:

By varying d_i from 0 to d_4 , $W'(d, \Delta_1, \Delta_2, \Delta_3, \Delta_4)$ can be defined over the interval.

Figure 2-3. Illustrating multisegment integration scheme.

For all but the first interval it is necessary to define the W' functions by a prior integration with sufficient resolution as a function of distance to allow subsequent integrations. This is done, as indicated on the figure by varying d in the definition of $W(d-\gamma, \Delta_n)$ between the limits

$$\sum_{i=1}^{n-1} d_i \geq d > \sum_{i=1}^n d_i \quad (2-7)$$

where n is the total number of segments.

INTEGRAL EQUATION SOLUTION

Millington's and Wait's multisegment theories can be applied to the calculation of the phase and amplitude of a propagating ground wave when the propagation path is electromagnetically inhomogeneous but only for smooth spherical geometry. In general, propagation paths encountered on Loran C chains are also irregular, experiencing large variations in height along the path as well as the changes in the surface electrical impedance. Hufford (Reference 2-5) initially proposed an integral equation solution to the problem of predicting the phase and amplitude of a ground wave signal propagated over irregular, inhomogeneous terrain. This work was further amplified by Johler and Berry (Reference 2-6) who developed a computer code for numerically solving the integral equation.

The Coast Guard has provided to TEMPO a GFE computer code (HUFLOC) which was developed by the Air Force Loran Special Project Office to predict the ground wave signal propagation over inhomogeneous and irregular terrain. This code incorporates the program INEQ2E which was developed by Johler and Berry to solve the integral equation model. The code was originally developed for a CDC computer and was adapted at TEMPO for operation of the GE-Honeywell computer.

-
- 2-5. Hufford, G.A., "An Integral Equation Approach to the Problem of Wave Propagation over an Irregular Surface," *Quart. Appl. Math.*, 9, p.391, 1952.
 - 2-6. Johler, J.R., and L.A. Berry, "LORAN-C Phase Corrections over Inhomogeneous, Irregular Terrain," ESSA Tech. Report IER59-ITSA-56, 1967.

The computer program was supplied with two test cases but no up-to-date documentation. There was no information on integration step size requirements, terrain data requirements or the numerical accuracy of the computed results. Only very cursory checks can be made against other existing theories, ie, smooth earth theories. These shed little light on the effect of terrain irregularity or the high degree of electromagnetic inhomogeneity which supposedly can be handled by HUFLOC (INEQ2E). While attempting to acquire a sufficient data base for using HUFLOC, the following interim steps were taken:

1. Verification of formulae that provide the basis for the prediction.
2. Definition, from the program listing, of the actual computations performed by the computer model and comparison with the results of (1) above.
3. Initiation of those verification tests that could be accomplished including
 - a. Comparison of the model output with Wait's multisegment program for smooth, inhomogeneous earth. Because of the nature of the multisegment code, this includes a comparison with the classical smooth earth theory.
 - b. Testing for reciprocity in predictions, by interchanging transmitter and receiver location for an inhomogeneous path.
 - c. Examination of the sensitivity of program output to input geophysical quantities.

The detailed description of the work performed on points 1 and 2 as well as part of point 3 of the above list is contained in Appendix C. The comparison of the integral equation results with those from Wait's multisegment program for a smooth, inhomogeneous earth comparison with the reciprocity property are contained in this section.

Reciprocity requires obtaining the same answer for the additive phase calculation on a given path independent of the direction of integration. The problem bears heavily on the accuracy of the numerical algorithms used in the integration along the path. To simplify data input for the reciprocity calculations, a Gaussian shaped hill was used for the terrain elevation profile. The examination of the code results with detailed terrain and impedance data representative of a real path is deferred to the discussion of the worst case path propagation predictions.

THE INTEGRAL EQUATION FORMULAE

Initially, the only available documentation for the INEQ2E subroutine in the HUFLOC program was found in Johler and Berry (Reference 2-6). A master equation in the report (Equation 2.21) was used as a starting point to check the equations programmed in INEQ2E. Since there were significant inconsistencies between this equation and the GFE program, the development of the equation was reconstructed. After some algebraic manipulation an equation was obtained for $(W(O)-1)$ where $W(O)$ is the complex attenuation factor for propagation from the transmitter to the point of observation (O). The details are provided in Appendix C. The equation obtained is

$$W(O) - 1 = - \frac{r_0}{x} \sqrt{\frac{ik_1}{2\pi}} \int_0^x W(s) \exp \left\{ - ik_1(r_1 + r_2 - r_0) \right\} \\ \cdot \left[\Delta + \left(1 + \frac{1}{ik_1 r_2} \right) \frac{\partial r_2}{\partial n} \right] \sqrt{\frac{x}{s(x-s)}} ds \left\{ \frac{r'_1 r'_2}{r_1 r_2} \right\} \left\{ \frac{\left(1 + \frac{z}{a_e} \right)^2}{\hat{e}_r \cdot \hat{n}} \right\} .$$

(2-8)

The geometric quantities r_0 , r_1 and r_2 are defined by Figure 2-4.
The other quantities are defined as

k_1 = wave number in air at the earth's surface

Δ = relative surface impedance (Z/Z_0), $Z_0 = 377$ ohms

x = projection of r_0 onto the spherical surface

s or r_1' = projection of r_1 onto the spherical surface

z = elevation above the reference sphere at Q

\hat{e}_r = unit vector in the radial direction

\hat{n} = unit vector normal to the surface at Q

a_e = effective earth's radius

r_2' = projection of r_2 onto the spherical surface.

The last two terms in curly brackets do not appear in the original documentation. The term $(1 + z/a_e)^2$ can be at most of magnitude 1.003 and in general can be replaced by unity. The term $(\hat{e}_r \cdot \hat{n})$ can be written as

$$(\hat{e}_r \cdot \hat{n})^{-1} = \sqrt{1 + (z')^2}$$

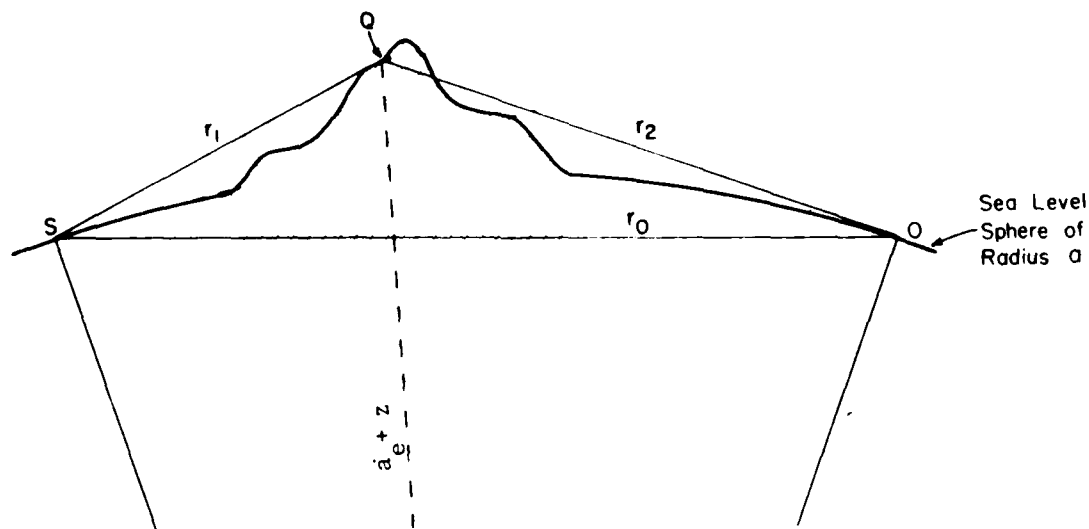


Figure 2-4. Geometry for propagation over irregular terrain.

where z' is the rate of change of z in the direction of propagation, defined at Q. The term

$$\frac{r_1' r_2'}{r_1 r_2} \cdot \sqrt{1 + (z')^2}$$

appears in the INEQ2E coding.

The integral formulation given by Equation 2-8 is derived using an approximate boundary condition, the Leontovich condition given by

$$\frac{\partial E}{\partial n} \doteq i k_1 \Delta E \left\{ 1 + (z')^2 \right\}^{-1/2} \quad (2-9)$$

where $i = \sqrt{-1}$. As pointed out by Johler (Reference 2-7) the condition was further approximated as

$$\frac{\partial E}{\partial n} \approx i k_1 \Delta E \quad (2-9a)$$

even though $(z')^2$ may become relatively large for an irregular terrain and $\sqrt{1 + (z')^2}$ can approach 1.4. This factor should be dividing Δ in Equation 2-8. It is not in the INEQ2E coding. Further, in the evaluation of $\frac{\partial r}{\partial n}$ our analysis showed that there was a factor missing of the form

$$\left\{ 1 + \left(\frac{a_e z'}{a_e + z} \right)^2 \right\}^{-1/2} \approx \left\{ 1 + (z')^2 \right\}^{-1/2} \quad (2-9b)$$

The inclusion of this factor would have approximately canceled the same factor in the numerator of the integrand which arises from $(\hat{e}_2 \cdot \hat{n})^{-1}$. The dismissal of this factor puts a strong requirement on the surface altitude fluctuations. In effect, it requires that $(z')^2 \ll 1$ at all points along the integration path. On the worst case path, it was necessary to smooth the terrain data over a six kilometer (\sim two wavelength) interval to insure that $|z'|$ was always of the order of 0.1 or less.

2-7. J.R. Johler, CRPLi Report 77-9, December 1, 1977.

COMPARISON BETWEEN MULTISEGMENT SMOOTH EARTH THEORY AND THE INTEGRAL EQUATION METHOD

The initial tests of the integral equation technique (HUFLOC code) were carried out using a smooth, electrically inhomogeneous earth. This test was chosen since direct comparison could be made against the smooth earth multisegment theory (MULSEG code). For the first test a three segment path was used with each segment 100 kilometers in length. The conductivity and relative dielectric constant, ϵ/ϵ_0 , for the path are given by

$$\sigma = \begin{cases} .0001 \text{ mhos/m} & 0 \leq r \leq 100 \text{ km} \\ .003 & 100 < r \leq 200 \text{ km} \\ 5.0 & 200 < r \leq 300 \text{ km} \end{cases} \quad (2-10)$$

$$\epsilon/\epsilon_0 = \begin{cases} 10. & 0 \leq r \leq 100 \text{ km} \\ 15. & 100 < r \leq 200 \text{ km} \\ 80. & 200 < r < 300 \text{ km} \end{cases} \quad (2-11)$$

This gives a relative impedance Δ of

$$\Delta = \begin{cases} .1902+.1064i = .2179 \mid \underline{.50992} & 0 \leq r \leq 100\text{km} \\ .03088+.02998i = .04304 \mid \underline{.7706} & 100 < r \leq 200\text{km} \\ .0007460(1+i) = .001055 \mid \underline{.7854} & 200 < r \leq 300 \text{ km} \end{cases} \quad (2-12)$$

The integration step used in MULSEG was 10 km and in HUFLOC, 1 km. The results of the calculation of the phase of W, the attenuation function, using HUFLOC and MULSEG for the path with the transmitter at $r = 0$ and the receiver at $0 < r \leq 300$ is shown in Figure 2-5, labeled

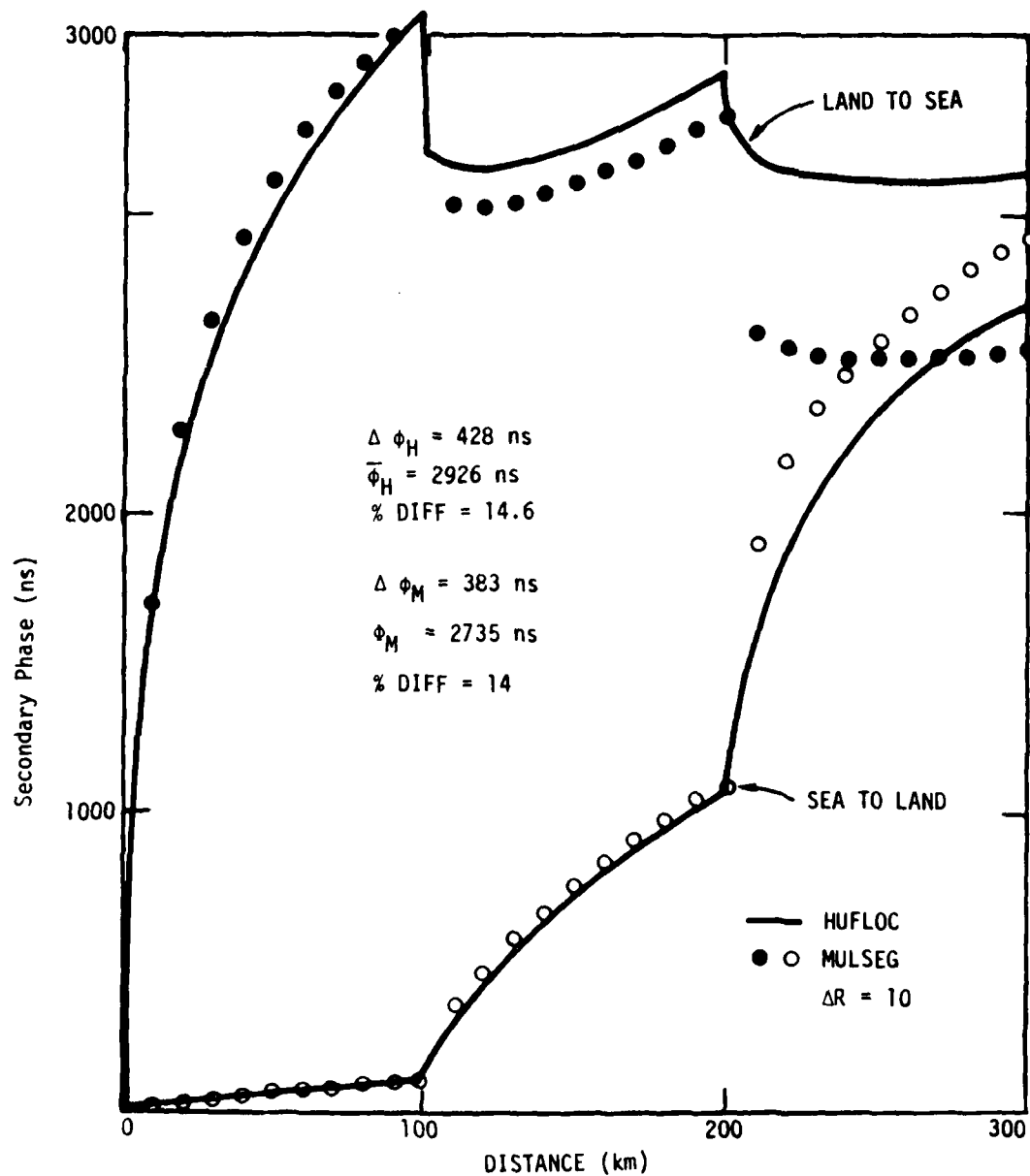


Figure 2-5. Secondary phase vs distance as predicted by HUFLOC (ϕ_H) and MULSEG (ϕ_M).

"Land to Sea." The solid line is the HUFLOC calculation and the filled circles are for MULSEG. The comparison appears relatively good over the first 100 kilometers but becomes progressively worse after each impedance transition. At the end point of the 300 km path, the difference between the HUFLOC and MULSEG prediction is ~ 600 ns.

To further investigate this discrepancy in the secondary phase delay calculations, the positions of the transmitter and receiver were interchanged. The result of the second set of calculations, also shown in Figure 2-5 are labeled "Sea to Land." At 300 km the difference between the MULSEG and HUFLOC predictions is ~ 200 ns, somewhat less but not satisfactory. What is worse, neither HUFLOC nor MULSEG predicted the same phase over both paths, apparently violating the reciprocity conditions. The net phase difference for HUFLOC was ~ 430 ns and for MULSEG 380 ns.

If neither HUFLOC nor MULSEG calculates the same secondary phase correction over reciprocal propagation paths, which if either code is correct? To answer this question we went to a much shorter, two segment propagation path of total length 60 km. The conductivity and relative dielectric constant along the path are given by

$$\sigma = \begin{cases} .003 & 0 \leq r \leq 30 \text{ km} \\ 5.0 & 30 \leq r \leq 60 \text{ km} \end{cases} \quad (2-13)$$

$$\epsilon/\epsilon_0 = \begin{cases} 15. & 0 \leq r \leq 30 \text{ km} \\ 80. & 30 \leq r \leq 60 \text{ km} \end{cases} \quad (2-14)$$

The multisegment code was run with a variety of different integration steps (Δr) for this path and its reciprocal. The path with the transmitter at $r = 0$ was termed the land to sea path and with the transmitter at $r = 60$ km, the sea to land path. The calculated results

for the secondary phase in nanoseconds are shown in Table 2-1 for the total 60 km path. Several points are immediately obvious. First, the phase difference $\Delta\phi$ between a path and its reciprocal increases with increasing Δr . Second, on the sea to land path, the net change in the calculated phase is ~ 0.6 ns for $2 \leq \Delta r \leq 15$ km, a rather remarkable result at first glance. Almost the entire variation occurs in the land to sea path. This has been traced to an increasing violation of the approximation used in the present MULSEG code where it is assumed that the major portion of the integrand (see Appendix B) varies very slowly from one integration point to the next. The quantity $\bar{\phi}$ is the mean for the path and its reciprocal and the column designated by % is $100(\Delta\phi/\bar{\phi})$. From the results it is apparent that the correct value for the phase over the total 60 km path is approximately 523 ns.

Table 2-1. MULSEG predictions of the secondary phase (ns) correction as a function of the integration step size.

$\Delta r(\text{km})$	Land to Sea	Sea to Land	$\Delta\phi$	$\bar{\phi}$	%
2	522.4	523.0	0.6	522.7	.1
3	520.0	523.1	1.1	522.6	.2
5	521.4	523.1	1.7	522.3	.3
10	519.9	523.3	3.4	521.6	.7
15	518.4	523.6	5.2	520.9	1.0

The same type of calculation was carried out using HUFLOC. In this case three values of Δr were compared, 1.0, 0.5, and 0.25 km. The predictions are shown in Table 2-2. The phase difference $\Delta\phi$ decreases from 94 ns to 44 ns as Δr is decreased from 1 km to 0.25 km. However, the change in the phase appears to occur uniformly with the change in Δr , independent of the path direction. Note that the mean value of the path and its reciprocal is approaching 521 ns as Δr decreases. Considering the differences in the theories, this is good agreement.

Table 2-2. HUFLOC predictions of the secondary phase (ns) correction as a function of the integration step size.

$\Delta r(\text{km})$	Land to Sea	Sea to Land	$\Delta\phi$	$\bar{\phi}$	%
1	565.5	471.6	93.9	518.5	18.1
0.5	551.6	488.0	63.3	519.8	12.2
0.25	542.5	499.0	43.5	520.7	8.4

The computations show that reciprocity violations result from numerical differences, not theoretical ones. They indicate the requirement for a short integration step and subsequent long calculation time for accurate results using the current formulations of HUFLOC.

Additional data on the secondary phase correction are shown in Table 2-3 where the phase predictions are listed as a function of distance for the two paths. For MULSEG $\Delta r = 2$ km and for HUFLOC, $\Delta r = 0.25$ km. For the first 30 kilometers of each path HUFLOC is actually being compared against the homogeneous earth theory. For the high conductivity portion in the sea to land path the two results are almost identical. For the other path there is a slight offset (~ 6 ns) which is generated near the beginning of the HUFLOC integration. In light of the apparently

Table 2-3. Secondary phase (ns) correction vs distance.

$d(\text{km})$	Land to Sea Path		Sea to Land Path	
	MULSEG	HUFLOC	MULSEG	HUFLOC
10	394.6	388.3	11.8	11.6
20	560.5	554.3	19.7	19.7
30	689.7	683.6	27.9	28.0
40	544.8	564.8	291.6	266.3
50	526.6	546.5	418.2	393.6
60	522.4	542.5	523.0	499.0

greater problem for long ranges and inhomogeneous paths, this seems insignificant at the present time. Of great importance is the change in computer running time (and hence cost) for a given run as a function of the step size. The decrease by a factor of four in the step size increased the running time by a factor of ten. The number of points for the integration increased by 4 and the running time for most of the computations increases as the square of the number of points. However, there is an initial setup which just varies as the number of points and which weights the total running time.

The results in Table 2-3 indicated that for each segment, the MULSEG and HUFLOC results were different only by a constant but that the constant changed abruptly at the transition of the surface impedance. It is possible that the basic formulation of the integral equation technique cannot properly handle the discontinuity in the impedance. However, it is more likely that this is in the integration algorithm rather than the basic theory. There is an alternative formulation of the integral theory developed by Ott and Berry (Reference 2-8) and Ott (Reference 2-9). A computer program based on this theory was run for the 60 kilometer segments. The results for the land to sea and sea to land runs were 526.7 ns and 522.3 ns, essentially in agreement with the MULSEG runs. The cost was approximately 4.4 times as great as for a HUFLOC run using $\Delta x = 1$ km and 60% of the HUFLOC run using $\Delta x = 0.25$ km. At the present time, this code is not integrated in a package to handle complex terrain data.

In addition to the smooth earth calculations we made a second set of test calculations based on a Gaussian shaped hill. This is a test case that has been used for both types of integral equation techniques in the published literature. The altitude variation for the hill was taken as

- 2-8. Ott, R.H. and L.A. Berry, "An Alternative Integral Equation for Propagation Over Irregular Terrain," Radio Science, Vol 5, #5 767-771 (1970).
- 2-9. Ott, R.H. "An Alternative Integral Equation for Propagation Over Irregular Terrain," Radio Science, Vol 6, #4, p. 429-436 (1971).

$$z(s) = 2500 \exp\left\{-9\left(\frac{s-50}{8}\right)^2\right\} \text{ meters} \quad (2-15)$$

where s is the distance from the transmitter in kilometers. The peak of the hill is at $s = 50$ km and was placed in the center of the propagation path. The ground conductivity was taken as 0.003 mhos/m with $\epsilon_g/\epsilon_0 = 10$. The computed results with and without the hill are shown in Figure 2-6. The hill shape and extent are indicated at the bottom of the figure. The circles are the computed phase for the reciprocal paths where the path was shortened by 10 km increments and the center of the Gaussian hill was correspondingly closer to the beginning of the reciprocal path. For example the point marked $s = 60$ indicates that the reciprocal path was 60 km long and that the hill was centered at $r = 10$ km from the start of the integration. This is reciprocal to the value of $r = 60$ for the forward calculation with the hill centered 50 km from the start of the integration. An increasing departure from reciprocity is indicated as the reciprocal paths become less symmetric. At $s = 60$ km, the difference is 87 ns. The fact that there is no departure from reciprocity at $s = 90$ or 100 kilometers is not an indication that the result is exact, only that the symmetry of the integration path has made up for the different error accumulations which were in evidence in the nonsymmetric 2 and 3 segment paths.

The results shown indicate that for a 1 km integration slip the integral equation technique is numerically nonreciprocal for both irregular terrain and a nonhomogeneous path. The source of the nonreciprocity is a built-in inadequacy in the numerical analysis used to solve the integral equation. The indications are that the error buildup from impedance variations decreases as the surface impedance decreases. The Gaussian hill may also be a very stressing case for the integral equation. The major variation in the terrain altitude takes place within a two wave length (6 kilometers) region. Such rapid variations possibly violate the approximation of a vertically polarized groundwave used in the theory.

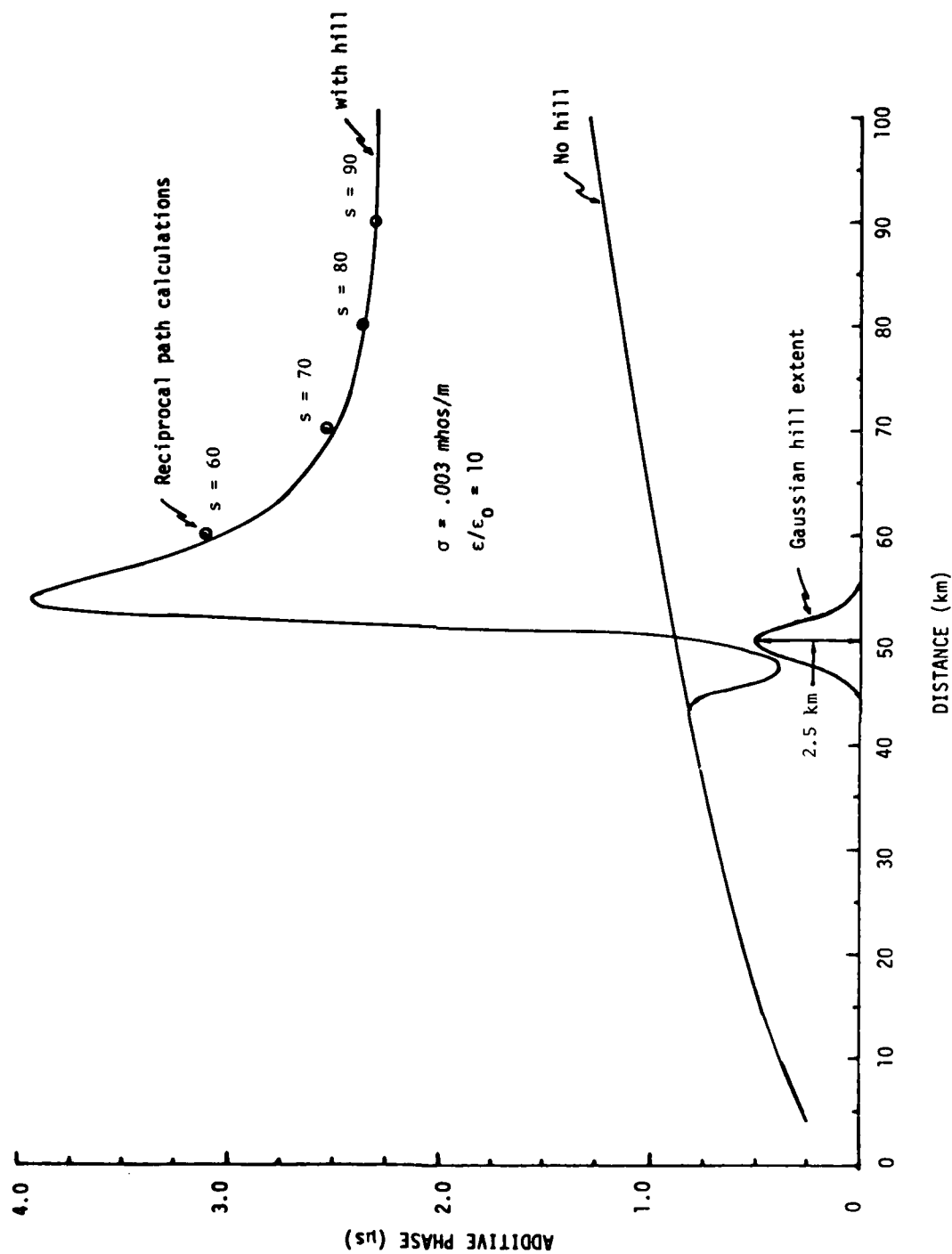


Figure 2-6. Additive phase changes produced by a Gaussian hill.

COMPARISON BETWEEN WAIT'S MULTISEGMENT THEORY AND MILLINGTON'S TECHNIQUE

Several cases were run to compare the results of the empirical technique of Pressey with the theoretically rigorous multisegment theory of Wait (MULSEG). The first case shown in Figure 2-7 is for a two segment path with the segment details given in Table 2-4.

Table 2-4. Two segment path parameters.

Segment No.	Length (km)	$\sigma(\text{mhos/m})$	ϵ/ϵ_0
1	150	.0025	10.
2	150	5.0	80.

For the first segment the two methods are identical. The Millington's method does not predict as great a phase recovery at the surface impedance transition as MULSEG. The largest difference is approximately 40 ns and the difference decreases with distance past the transition.

The second test to be illustrated was carried out for a five segment path. The path parameters are listed in Table 2-5.

Table 2-5. Five segment path parameters.

Segment No.	Length (km)	$\sigma(\text{mhos/m})$	ϵ/ϵ_0
1	60	.0025	10.
2	60	.0008	10.
3	60	.01	10.
4	60	.02	10.
5	60	5.0	80.

The calculated result is shown in Figure 2-8. As in the two segment path, the two techniques differ slightly at the transition between two very different surface impedances. The calculation for the reciprocal path is shown in Figure 2-8b. Of particular importance is the fact that both MULSEG and Millington, beside giving almost identical results, are also reciprocal, ie for a given path the answer is independent of the direction of integration.

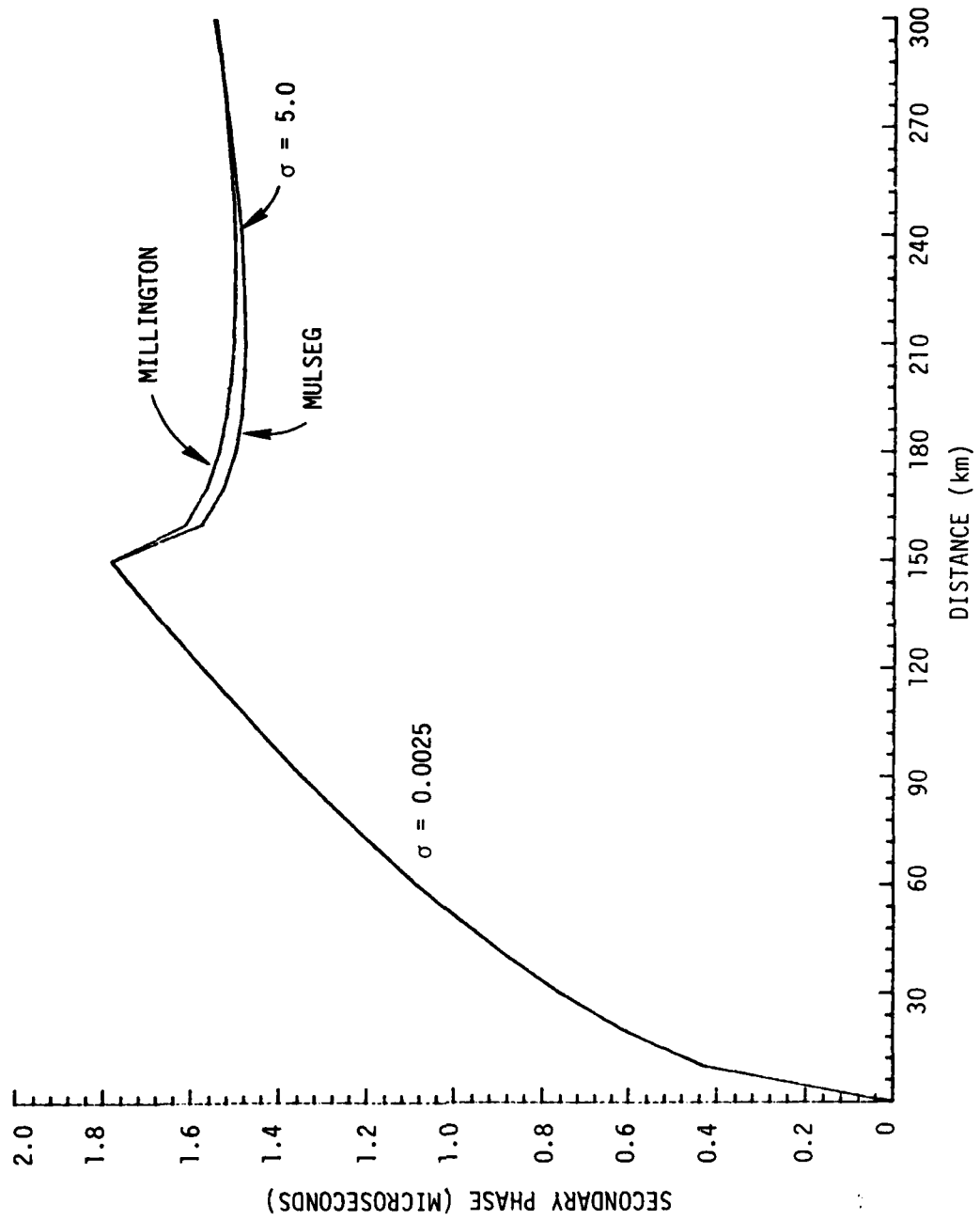


Figure 2-7. Comparison of MULSEG and Millington for a 2 segment path.

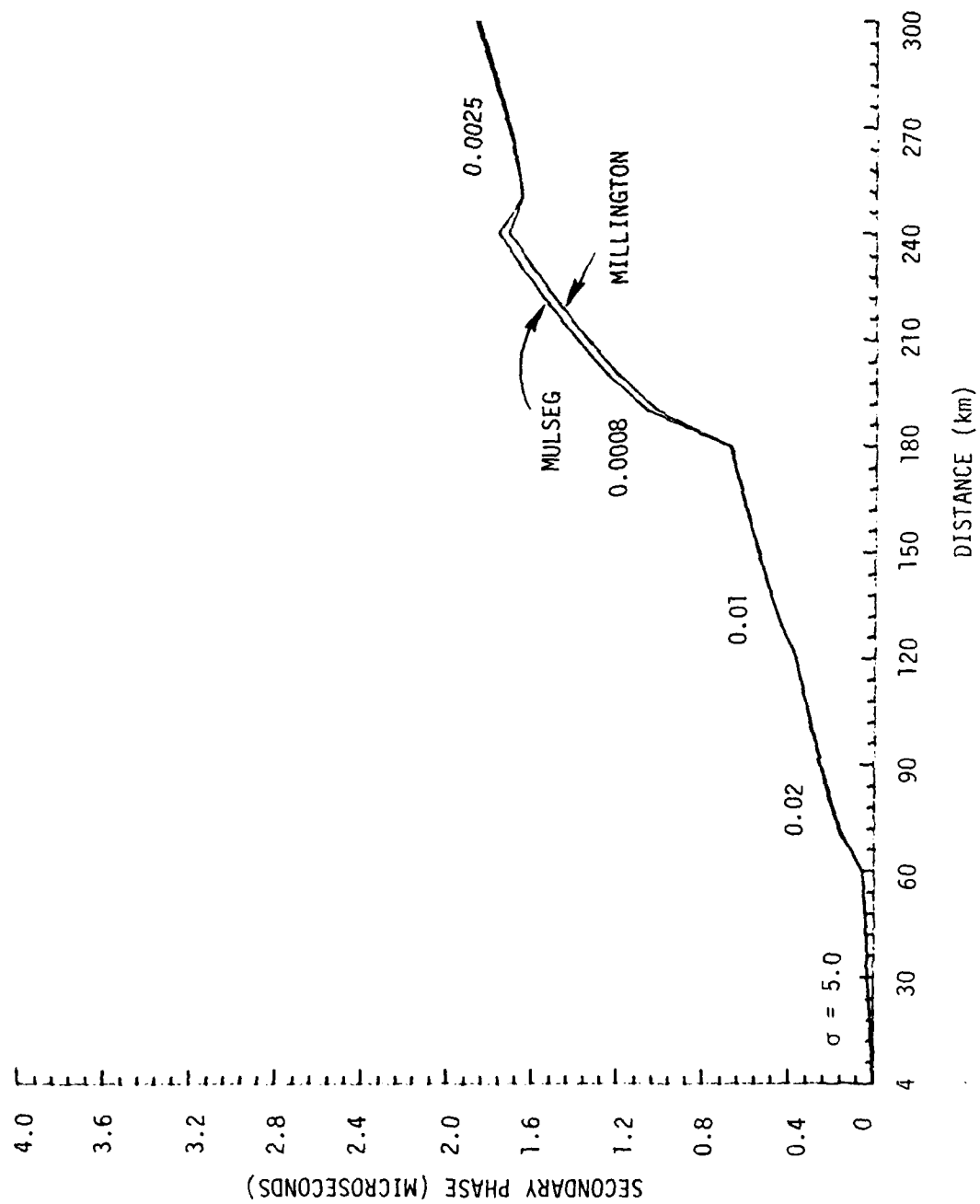


Figure 2-8a. Comparison of MULSEG and MILLINGTON for a 5 segment path (sea to land).

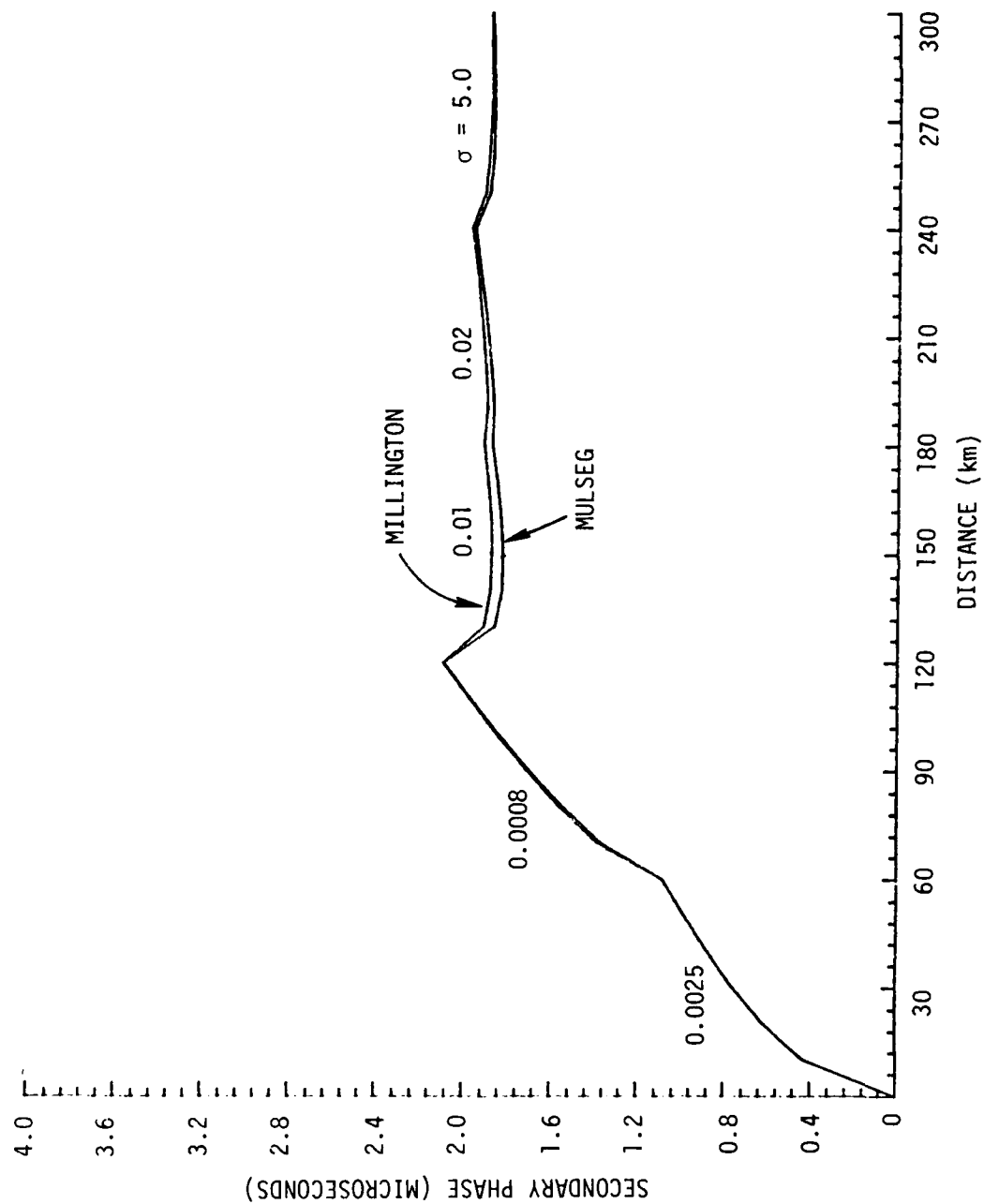


Figure 2-8b. Comparison of Millington and MULSEG results for a 5 segment path (land to sea).

COMPARISON BETWEEN MILLINGTON'S TECHNIQUE AND THE INTEGRAL EQUATION METHOD

Comparative calculations were made using Millington's technique and the integral equation for the Worst Case Path. The discussion of this comparison is deferred until Section 5.

PROGRAM OPERATION

Data Preparation

Data preparation for both Wait's multisegment code (MULSEG) and the Millington Technique code are relatively simple and similar. For both codes, the propagation paths must be divided into segments which correspond to regions with similar surface impedances. For data output at points other than impedance boundaries, the path may be further subdivided for Millington's method. For each segment the conductivity, dielectric constant and layer thickness must be provided. An added constraint for the current version of MULSEG is the requirement that each segment must be an integral multiple of the integration step size. This is of no great importance for a test program.

Data preparation for HUFLOC (INEQ2E) requires much greater effort and detail than for either MULSEG or Millington. Both topographic (height vs range) and geological (material or earth electrical structure vs range) are required at as small an interval as is appropriate for the level of accuracy inherent in the groundwave propagation solution and the numerical techniques used to evaluate the integral equation. Unfortunately, this problem had not been previously addressed. Therefore the topographic data base for the worst case propagation path was determined to the highest accuracy available from topographic maps with many data points only 100 meters apart. This level of data produced difficulties in the solution of the integral equation when the integration step was much larger than the level of detail. Initially, an integration step of ~ 1 kilometer was used ($\sim \lambda/3$). However, the integration routine sets the exact size

of the integration step to make the distance between the transmitter and receiver be an integral multiple of the integration step size. For different values of the total distance, the change in step size was sufficient to produce minor modifications in the topography interpolated from the initial raw data. These differences in the topography produced variations upward to several hundred nanoseconds in the computed secondary phase at a particular point. It was decided to filter (or smooth) the input topographical data in the subroutine which obtains it from the data tape (GETELV). Approximately 2350 initial altitude points are smoothed and reduced in number so that there is one smoothed data point for a distance of one-half of the smoothing interval. Therefore, if the smoothing interval is 6 km, data is produced every 3 km.

The geological data base was also determined to as fine a detail as possible from existing maps. For this data there were approximately 230 intervals along the worst case propagation path. Many of these intervals were as small as 0.25 km. However, in general, no attempt was made to smooth either the conductivity or dielectric constant or depth of the layers. On two test runs, the computed surface impedance was smoothed but this produced only small changes in the computed phase. In most cases, when the geology was a strong function of distance, the topography dominated the calculated results.

For the use of HUFLOC (INEQ2E) on arbitrary propagation paths in a large area, both the topographical and geological data must be provided on a fine grid covering the entire area. In Reference 2-10, Horowitz indicates that an input data grid 30 seconds of arc on a side was used for the data base for calculations in Germany. This corresponds to data points every ~ 925 meters. The data for an integration point was obtained by using two dimensional interpolation. It is not noted in the report whether or not sensitivity checks were made.

2-10. Horowitz, S., "Users Guide for ESC Loran Grid Prediction Program," RADC-TR-77407, December 1977.

Running Time

The running time for both MULSEG and Millington's Method calculations are relatively short when compared to runs for the integral equation technique (HUFLOC-INEQ2E). For both, the running time is approximately proportional to the product of the total number of calculational points and the number of segments. Since MULSEG computes an integral there are more points for a MULSEG run than for a Millington run. Further, there is an alternate mode available for Millington calculations using a file of precomputed runs for single segment paths. The Millington comparison data was obtained using this alternate method.

The HUFLOC runs tend to take more computer time. Figure 2-9 shows the execution time on a Honeywell 6080 as a function of the number of integration points, n . The execution time varies as $n^{2.7}$. This reflects both the data setup time before the integral calculations start as well as the actual integration. Further, the execution cost is only about 50% of the cost of a run. For the Honeywell 6080, the memory residence cost makes up most of the rest of the total cost.

APPLICATIONS

Rigorously both MULSEG and Millington are applicable only for a smooth spherical earth. However, both have been applied to paths for which the terrain variations should provide an important part in the calculation of the secondary phase. As shown later in Section 5, for a given path the terrain fluctuations tend to increase the total calculated secondary phase. Therefore, to compensate for ignoring the effect of terrain, the smooth earth theories require high surface impedance (ie, lower electrical conductivity) along the propagation path. With a sufficiently large number of possible input data combinations, it is possible that the proper manipulation of the input for Millington could closely match experimental data over an arbitrary path. The input impedance segmentation might only bear a faint resemblance to the actual geological structure along the over land path where the topography is an important parameter, but

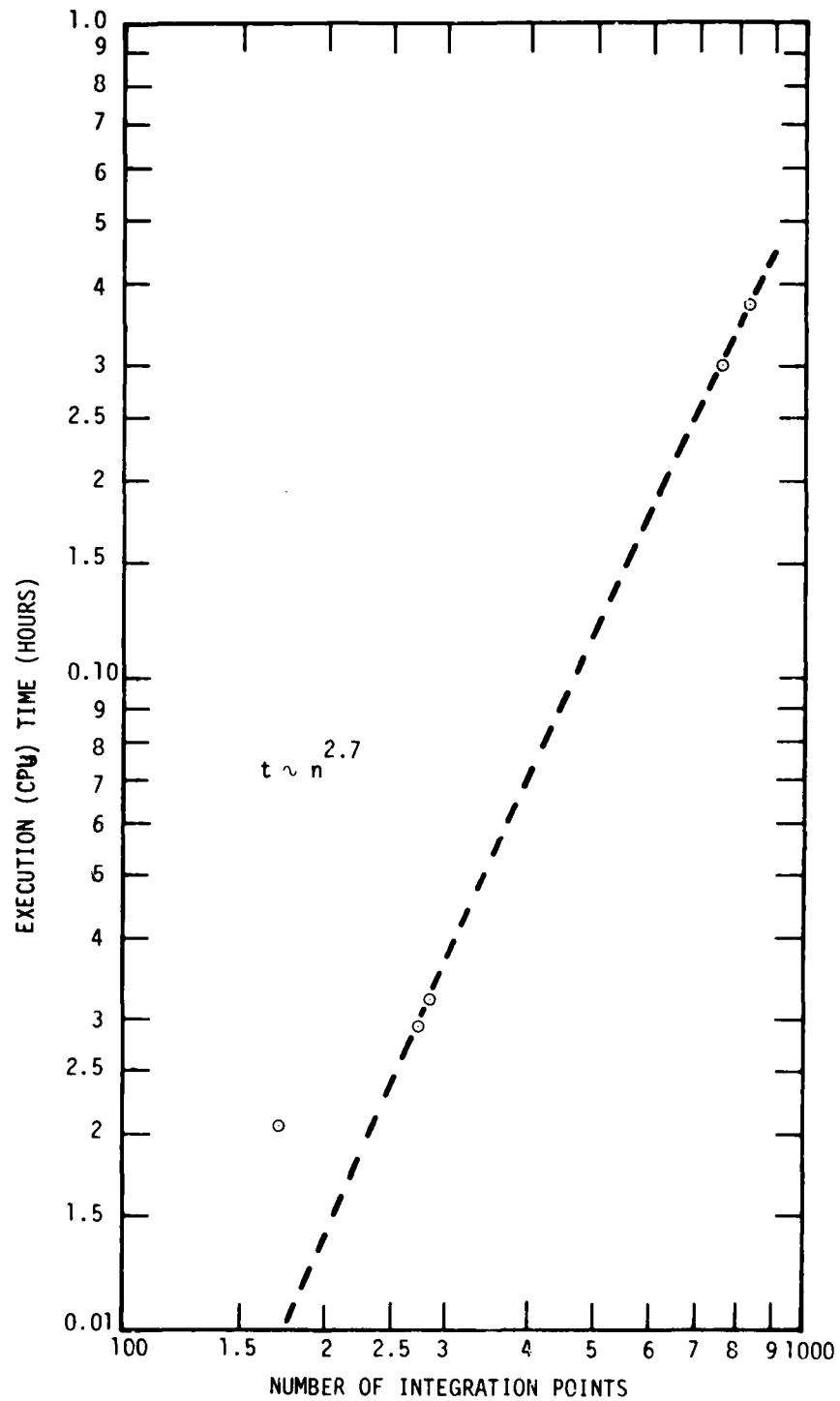


Figure 2-9. Execution time versus number of integration points for HUFLOC.

would be very accurate over the sea water path segments and other regions which are relatively smooth. If the parameters of the over land portion of the propagation path were so chosen that they matched the experimental data up to the land sea boundary, then the calculations for the over water portions would be as accurate as any other means of calculation.

To properly match a set of experimentally derived data with the integral equation technique, geological data grid development would be required in much the same manner as has been proposed by Burch, et al (Reference 2-11) and by Horowitz (Reference 2-10). It is very likely that the measurement program required to insure that a numerical predictive technique is accurate over an entire region might be more difficult than experimental calibration of the specific region. Further a particular representation of the geological structure determined by fine tuning the conductivity and segment sizes to match the data will depend on the data base, on the particular program used and on the integration step size, degree of smoothing and method of data interpolation. The latter are applicable to the integral equation technique. Thus, the fine tuning is likely not to give a unique result for the data base, no matter which technique is used. In this context, however, the integral equation technique does offer the capability of a more reasonable and very likely a more accurate calculation for regions that are not adequately covered by an experimental data base. This provides an automatic fine scale calculation effect produced by the terrain variations which is unattainable using smooth earth theories such as Millington's and Wait's methods. Further, the terrain altitude grid can be determined with greater accuracy than the electrical impedance data. Therefore, once the questions of smoothing and integration step size (discussed in Section 5) have been resolved, only the accuracy of the impedance data need be questioned. For the integral technique, the impedance values and the regions of changing impedance, though requiring more detail do not have to bear the entire burden for the accuracy of the secondary phase calculation.

- 2-11. Burch, L.B., R.H. Doherty and J.R. Johler, Loran Calibration by Prediction, Navigation; J. Inst. Navigation, Vol 23, No. 3, Fall, 1976, pp 195-200.

Improvements

MULSEG (Wait's multisegment theory) and Millington's technique are well tested programs that are strictly applicable to smooth, inhomogeneous spherical earth propagation paths. Within this restriction both are efficient and easy to use. Because of the close comparison between Millington and MULSEG results and the simplicity of Millington calculations, Millington's method is recommended.

The major improvements required are automated procedures for impedance data generation and definition of error bounds resulting from neglecting terrain variations.

Improvements required in the integral equation program have been discussed earlier. In summary, the requirements are

1. A comprehensive sensitivity analysis to define dependence on computation step size, on the granularity of the input terrain and impedance data, and on uncertainty in the impedance specification.
2. A revision of the numerical techniques to improve the accuracy of prediction without requiring very small calculation step size and consequently long computing times.
3. Automation of the data base preparation.

SECTION 3 WEATHER EFFECTS

The properties of the earth's atmosphere enter into the theory of radio wave propagation in two distinct ways. From Equation 2-2 the primary phase delay is

$$\phi_p = -k_1 d = -\frac{2\pi f d}{c/\eta} = -\frac{2\pi \eta d}{\lambda} \quad (3-1)$$

where k_1 is the wave number in air for frequency f , λ is the wavelength in free space, c is the free space velocity of light (2.997925×10^5 km/s), η is the index of refraction of air and d is the distance between the transmitter and receiver. Since η is greater than unity ($\eta - 1 \sim 3 \times 10^{-4}$) the primary phase delay through the earth's atmosphere is greater than that through free space for a given distance, d .

The slight difference from unity in η has negligible effect in the calculation of W , the attenuation function. However, the vertical gradient of the index of refraction has an important effect on the secondary phase factor. The wave propagation problem has not been solved for an arbitrary variation of η with altitude. However, Wait (Reference 3-1), Bremmer (Reference 3-2) and others have shown that the propagation calculations can be made using an equivalent earth radius a_e if, as a first approximation, the vertical gradient of η is constant, ie, the variation of the refractive index is linear with altitude. The effective earth radius is given by

$$a_e = \frac{a}{1 + a \frac{d\eta}{dz}} \quad (3-2)$$

-
- 3-1. Wait, J.R., "Electromagnetic Waves in Stratified Media," Pergamon Press, The MacMilland Co., New York, Second Ed., 1970.
 - 3-2. Bremmer, H., "Terrestrial Radio Waves," Elsevier Publishing Co., 1949.

where a is the real earth radius and $\frac{d\eta}{dz}$ is the vertical gradient. Though developed for skywave propagation, the concept of the equivalent earth radius has also been applied to the groundwave propagation.

We will first examine the behavior of the index of refraction with respect to the atmospheric pressure, temperature and relative humidity. We will then investigate ways in which the weather variations can be included in the propagation calculations.

REFRACTIVE INDEX OF AIR AND EQUIVALENT EARTH RADIUS

Weather variations (changes in temperature, pressure and humidity) produce variations in the refractive index of the air. Using conventional notations (Reference 3-3)

$$(\eta - 1) 10^6 = N = \frac{77.6}{T} (P + 4810 \frac{e}{T}) \quad (3-3)$$

where

η = refractive index of air

N = variation of the refractive index from unity (parts/million)

T = absolute temperature $^{\circ}K$

P = atmospheric pressure (mb)

e = partial water vapor pressure (mb).

Meteorological measurements normally include pressure, temperature and humidity data. The partial water vapor pressure is related to specific humidity by (Reference 3-3)

$$e = \frac{SP}{622} \quad (3-4)$$

where S is the specific humidity in grams of water per kilogram of air. When the relative humidity is specified, the specific humidity is

$$S = \frac{R_H S_o}{100} \quad (3-5)$$

3-3. Boithias, L., "Structure of the tropospheric refractive index and propagation," Telecommunication Journal, Vol 43, June 1976, pp. 419-416.

where

R_H = relative humidity (percent of saturated value), and
 S_o = the saturated mixture ratio, defined by the approximate relation

$$S_o = \frac{1.69 \times 10^{12}}{p} \exp - \frac{5434}{T} \quad (3-6)$$

Using Equations 3-3 through 3-6, the quantity $N = (\eta-1) 10^6$ has been evaluated as a function of temperature for $p = 1000$ mb and 870 mb and for parametric values of the relative humidity. The results are shown in Figure 3-1 and 3-2 and agree with those presented in Reference 3-4. For the temperature range 235 to 303°K (-4°F to 86°F) N can range from a low of 250 to greater than 400, depending on the humidity.

The gradient of η is obtained on the assumption that N varies exponentially with altitude,

$$N = N_s e^{-bz} \quad (3-7)$$

where N_s is the value of N at the earth's surface, and z is in kilometers. Then

$$\frac{d\eta}{dz} = -bN_s * 10^{-6} \quad (3-8)$$

When only surface values of the weather variables are available,

b is estimated (Reference 3-4 and 3-5) from the quantity

$$\Delta N = -7.32 \exp (0.005577N_s) \quad (3-9)$$

where

$$\Delta N = N(z=1) - N(z=0) = N_1 - N_s \quad (3-10)$$

3-4. Bean, B.R., and E.J. Dutton, "Radio Meteorology," NBS Monograph 92, March, 1966.

3-5. Bean, B.R., and E.J. Dutton, "Radiometeorological Parameters and Climatology," Telecommunication Journal, Vol 43, June 1976, pp. 427-435.

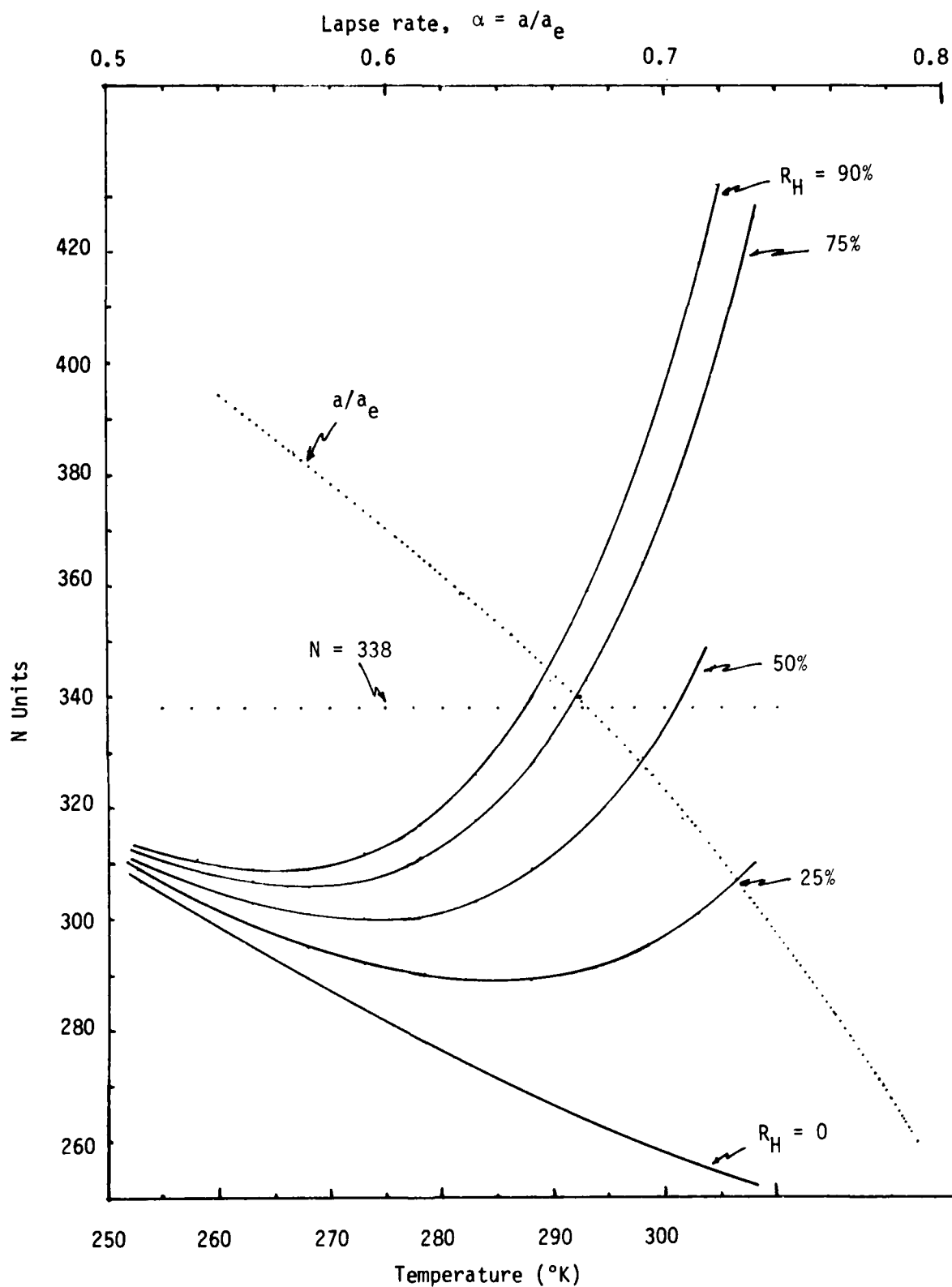


Figure 3-1. N units versus temperature and α for various values of relative humidity and a pressure of 1000 mb.

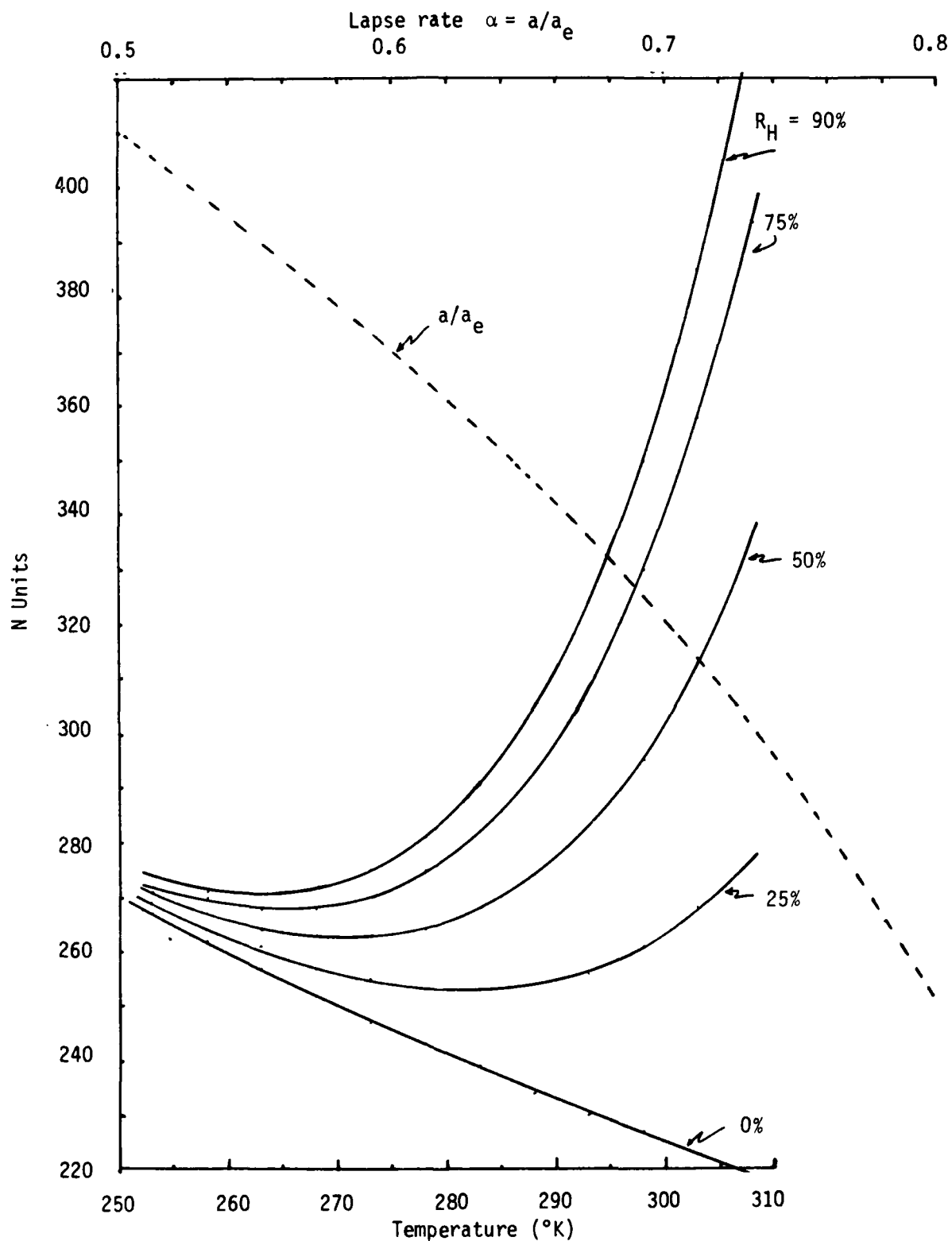


Figure 3-2. N units versus temperature and α for various values of relative humidity and a pressure of 870 mb.

Using Equation 3-7, b is given by

$$b = \ln \left(1 + \frac{\Delta N}{N_s} \right)^{-1} \quad (3-11)$$

Using Equation 3-8, 3-9, and 3-11, a_e has been calculated as a function of N_s using $a = 6367$ km. The ratio a/a_e is also plotted in Figure 3-1 and 3-2. It can be seen that a/a_e decreases as N increases with $a/a_e \approx 2/3$ for $N = 340$ and $3/4$ for $N = 285$.

INCLUSION OF WEATHER EFFECTS IN PROPAGATION CODES

To investigate the weather-produced variations on the propagation predictions, it is first desirable to write the total or composite phase Φ_c in terms of the free space phase Φ_o , the direct effect of the air on the free space phase $\Delta\Phi_o$ and the distance dependent secondary phase term $\Phi_s(d)$:

$$\Phi_c = \Phi_o + \Delta\Phi_o + \Phi_s(d) \quad (3-12)$$

where

$$\Phi_o = -k_o d$$

$$\Delta\Phi_o = -(k_1 - k_o)d$$

$$\Phi_s(d) = \text{computed secondary phase.}$$

The sum of $\Phi_o + \Delta\Phi_o$ is the primary phase, i.e.

$$\Phi_o + \Delta\Phi_o = -k_1 d \quad (3-13)$$

and this is the simplest term into which changing weather properties along the propagation path can be included. If k_1 is varying along the propagation path, the first order modification would be to calculate an average wave number \bar{k} over the path defined by

$$\bar{k} = \frac{1}{d} \int_0^d k_1(x) dx. \quad (3-14)$$

This definition of an average wave number can then be used as a first order modification for k_1 (and hence $\frac{dn}{dz}$ and a_e) that is used in calculating W , the ground wave attenuation function. To see the possible effect of such a substitution, consider the smooth homogeneous earth propagation theory for which details are given in Appendix A. For large distances, beyond the short distances approximation switch, the term $\phi_s(d)$ is given approximately by (see Equation A-7)

$$\phi_s(d) = -XR_e(t_1) \quad (3-15)$$

where X is the normalized distance, R_e means real part of and t_1 is the complex eigenvalue for the leading (least attenuated) term in the series expansion. Variations in the refractive index n also change the value of t_s which enter into the total value for $\phi_s(d)$ but we are interested here in the change produced directly in the leading term of the series. The most important phase variation occurs because of the dependence of X (Equation A-3) on the effective earth radius.

Table 3-1 shows the variations in N (using Equation 3-3), effective earth radius (using Equation 3-2), X , $\Delta\phi_0$, and $\phi_s(d)$ for two values of ground conductivity. In defining $\phi_s(d)$, only the leading term in Equation A-7 is used, so the results are strictly applicable for a distance greater than 200-300 km. The variations are shown for a range of N that may be encountered in the West Coast coverage area.

Table 3-1. Propagation parameter variations with the refractive index.

N	ΔN	a_e (km)	X/d (km^{-1})	$\Delta\phi_0/d$ ns/km	$\sigma = 10^{-3}$ $\epsilon/\epsilon_0 = 15$	$\sigma = 5$ $\epsilon/\epsilon_0 = 80$
					ϕ_s/d ns/km	ϕ_s/d ns/km
200	-22.3	7497	2.668^{-3}	-0.667	-6.21	-2.24
250	-29.5	7960	2.572^{-3}	-0.834	-5.96	-2.15
300	-39.0	8680	2.443^{-3}	-1.0	-5.62	-2.02
350	-51.5	9870	2.266^{-3}	-1.167	-5.18	-1.87

The tabular entries show that it is necessary to consider variations in η and its gradient for long paths. They also show that changes produced by variations in N in the primary and secondary phase factors are in opposite directions. For example, if N changes from 200 to 350, $\Delta\phi_0/d$ decreases 1 ns/km, ϕ_s/d for $\sigma = 10^{-3}$ mho/m increases 1 ns/km, and ϕ_s/d for $\sigma = 5$ mhos/m increases 0.35 ns/km. Thus, when N and the gradient of N are related as in Equation 3-8, the primary and secondary phase changes partially compensate.

For more detailed data on the effect of earth curvature on the predicted phase, parametric calculations of the secondary phase were carried out for values of α of 0.67, 0.75, 0.85, and 1.0. The results show that for fixed distance and surface impedance, the phase is essentially linearly proportional to α , ie, the phase can be represented by

$$\phi_s \approx a + b\alpha$$

Table 3-2 gives values of a and b for various distances and for ground conductivity values of 0.001, 0.01, and 5 mhos/m. Since b increases significantly with distance, weather produced variations will be greater over long propagation paths.

Table 3-2. Constants for linear equation defining ϕ_s as a function of α .

Conductivity (mhos/m)	Distance (km)	a	b
0.001	100	2080	97
	200	2835	293
	300	3365	560
	400	3775	885
	500	4105	1255
	600	4390	1665
	700	4640	2095
	800	4875	2545
	900	5095	3005
	1000	5320	3455
0.01	100	685	75
	200	960	240
	300	1180	435
	400	1375	655
	500	1555	890
	600	1730	1140
	700	1905	1390
	800	2080	1645
	900	2255	1900
	1000	2430	2155
5.0	100	30	80
	200	45	220
	300	65	385
	400	90	570
	500	120	765
	600	160	960
	700	210	1150
	800	265	1340
	900	325	1530
	1000	390	1710

MODEL LIMITATIONS - NEED FOR FURTHER RESEARCH

In each of the three theoretical techniques for calculating the wave propagation discussed in Section 2 the assumption is made explicitly that the index of refraction at the earth's surface is a constant independent of position. As shown by Fock (Reference 3-6), the index of refraction need not be independent of height but may have a constant gradient. The constant gradient gives rise to the concept of an equivalent earth radius. For the cases of immediate interest to Fock, the constant gradient approximation is reasonable since he considers initially those cases where the change in the index of refraction is small over a wavelength of the radiated wave. For Loran-C the wavelength is 3 km which is approximately four tenths of an atmospheric scale height and the assumption of a linear gradient is somewhat in error. Fock also attempts to solve the differential equation governing the propagation for an arbitrary variation of η with altitude by making an expansion in a small parameter β given by

$$\beta = \frac{1}{h_0} \left(\frac{a_e}{2k^2} \right)^{1/3}$$

where $h_0 \approx 7$ km is the atmospheric scale height. For $f = 100$ kHz, $\beta = 1.3$ and is not small. An obvious extension of the theory of surface wave propagation would be to provide a method for the solution of the propagation problem with an exponentially varying index of refraction where the wavelength is a sizeable fraction of the atmospheric scale height.

3-6. Fock, V.A., "Electromagnetic Diffraction and Propagation Problems, Chapter 13, "Propagation of Direct Wave Around the Earth," Pergamon Press, 1965.

The present theoretical techniques all assume that the index of refraction varies linearly, ie, the derivative of the index of refraction with altitude is constant. As pointed out earlier, this leads to the use of an equivalent earth radius in the propagation calculations. To a first approximation, this effective earth's radius can be derived using the average index of refraction along the entire path. Using surface weather data, the linear gradient theory has been used to calculate the change in phase caused by the predicted change in the index of refraction and the equivalent earth radius. The data is described below. On the basis of this data, however, the net fluctuation in the secondary phase for a given path is on the order of ± 10 ns. It is possible that the inclusion of temperature inversion data and the resultant more complex variation in the index of refraction might produce a greater phase fluctuation. This cannot be tested with present theoretical techniques. In addition, large amounts of precipitation over portions of an overland propagation path may produce variations in the surface conductivity and hence the surface impedance. It would be expected that significant rainfall in a normally dry region would increase the conductivity and decrease the surface impedance, thus reducing the secondary phase for a path crossing the affected region. Consideration of changes in the surface conditions is also required in the analysis of weather related phase variations for Loran-C propagation.

It is possible that empirical modifications can be made for the groundwave programs which cannot be easily justified on theoretical grounds but might be capable of reflecting the propagation change produced by weather variations along a path. In MULSEG and Millington's technique the programs could be modified to use either the locally determined effective earth radius or one averaged from the transmitter to the point of observation. Such a scheme could also be incorporated into the integral equation formulation but extreme care is required in the application of this type of modification. Significant testing would be required plus comparison with experimental data to insure that any results be consistent with observation and were physically acceptable.

AN EXAMPLE OF PREDICTED WEATHER EFFECTS

An example of predicted weather produced fluctuations was produced using surface weather data from a station (Reno, NV) near the master transmitter. Figure 3-3 shows the atmospheric pressure in millibars, reduced to sea level. In the example, these values were multiplied by 0.9 to account for the elevation of the station. Figures 3-4 and 3-5 show the temperature and dew point temperature taken at Reno. Figure 3-6 shows the value of N , computed using Equation 3-3, and Figure 3-7 shows the value of $\alpha = a/a_e$ computed using Equation 3-2. Figures 3-8 through 3-11 show the phase fluctuations which are the sum of the primary and secondary phase fluctuation for path lengths of 100, 300, 500 and 700 kilometers. The phase fluctuations are small, showing a maximum value of ~15 nanoseconds. These values agree in order of magnitude with the experimental observations during the current Loran-C Signal Analysis West Coast Experiment, with one exception, where it is postulated that a larger change was produced as a result of precipitation-induced surface impedance change. A discussion of this exceptional case follows.

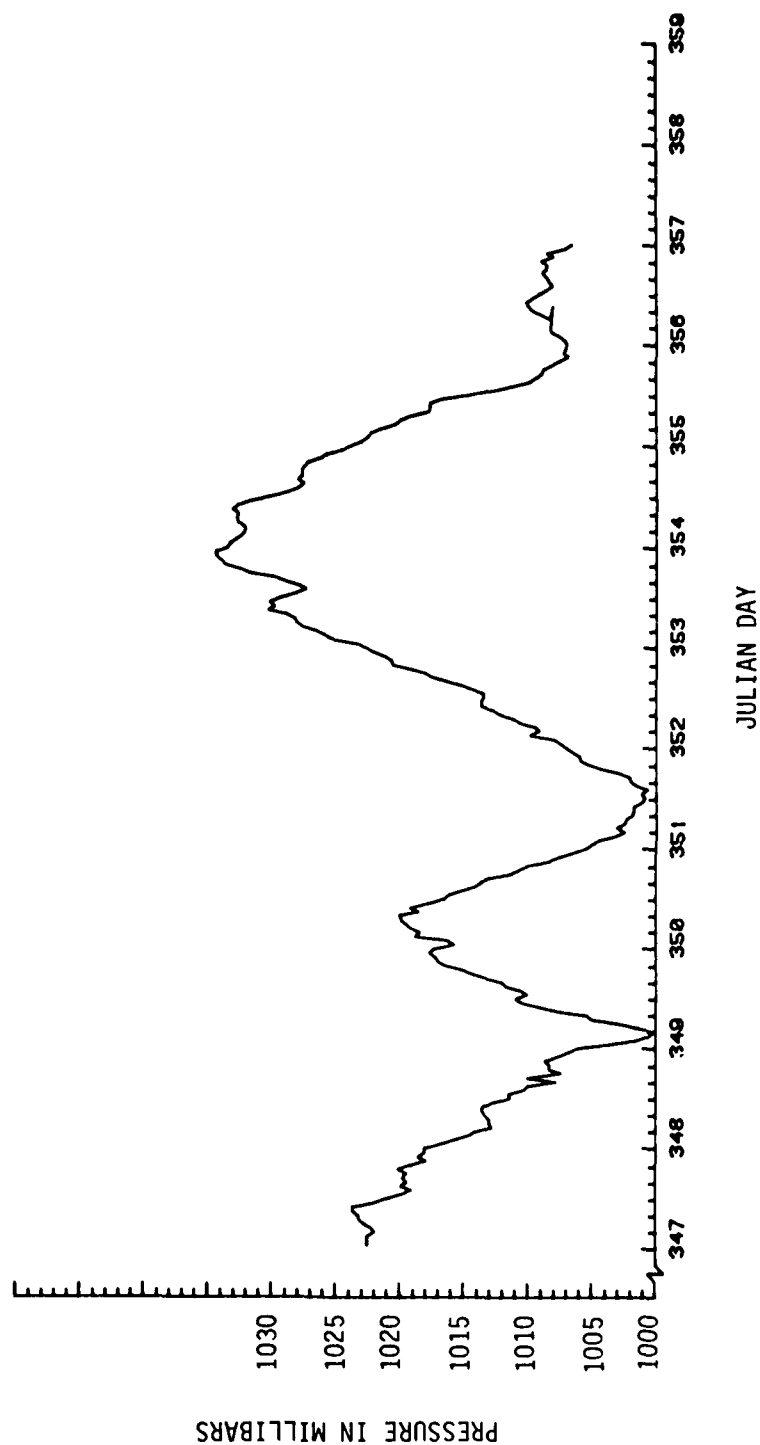


Figure 3-3. Atmospheric pressure (reduced to sea level) at Reno, NV over the time period 13 December to 22 December 1977.

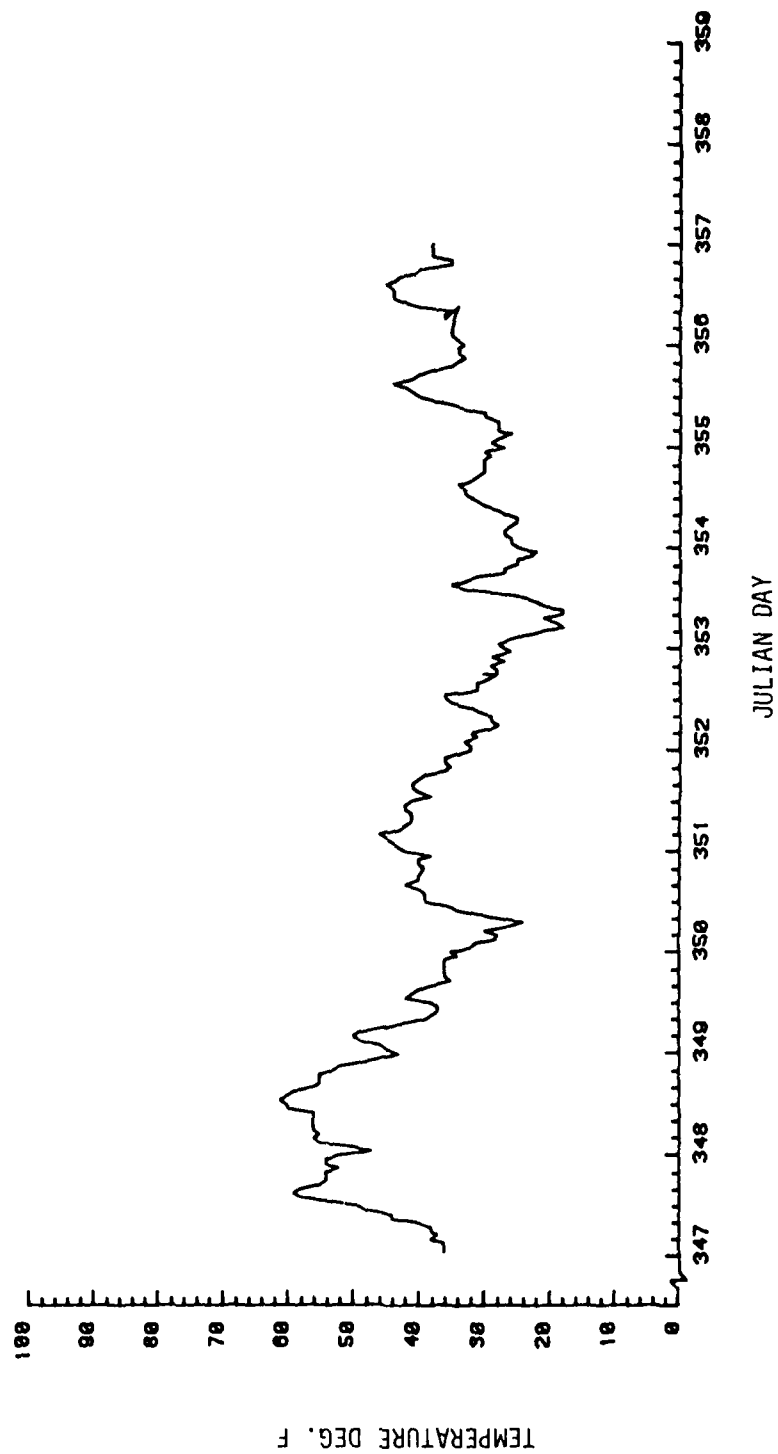


Figure 3-4. Surface temperature at Reno, NV over the time period 13 December to 22 December 1977.

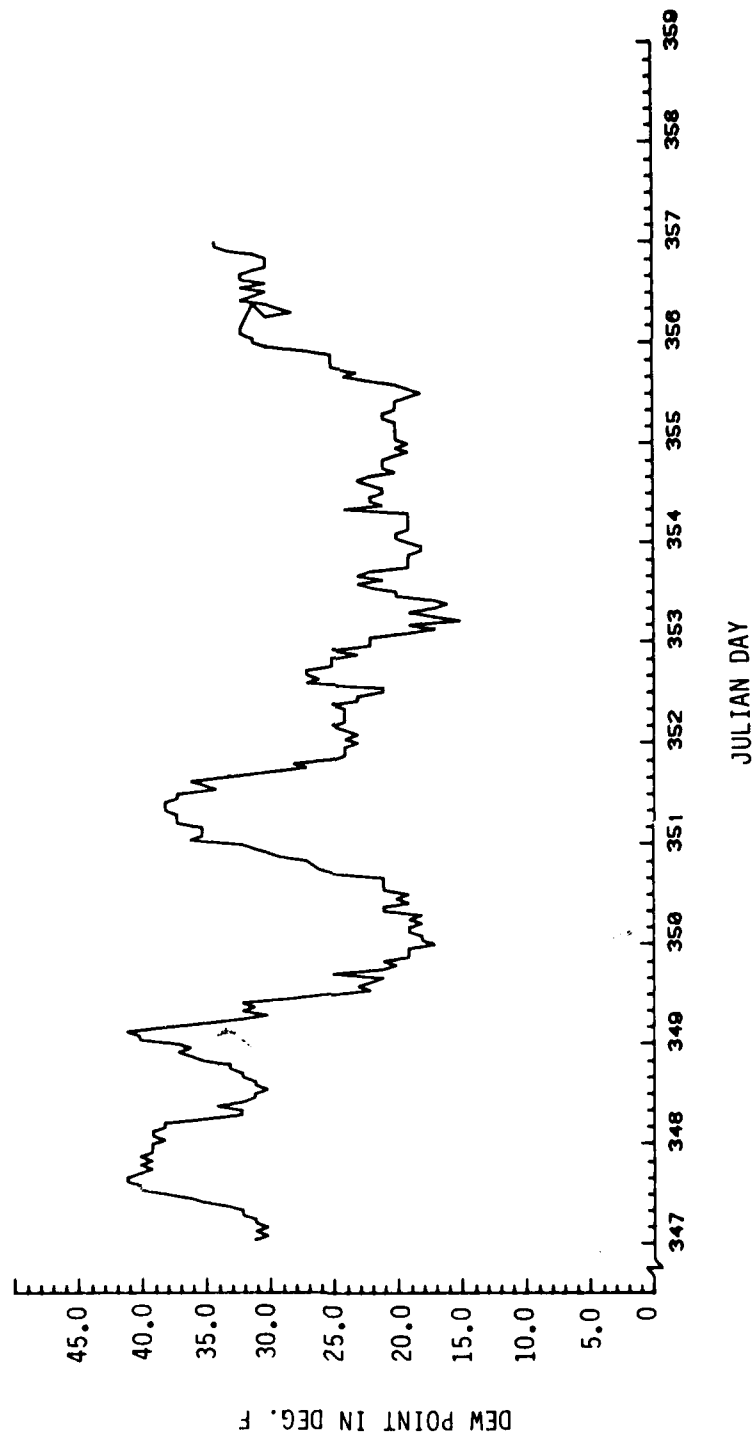


Figure 3-5. Dew point temperature at Reno, NV over the time period 13 December to 22 December 1977.

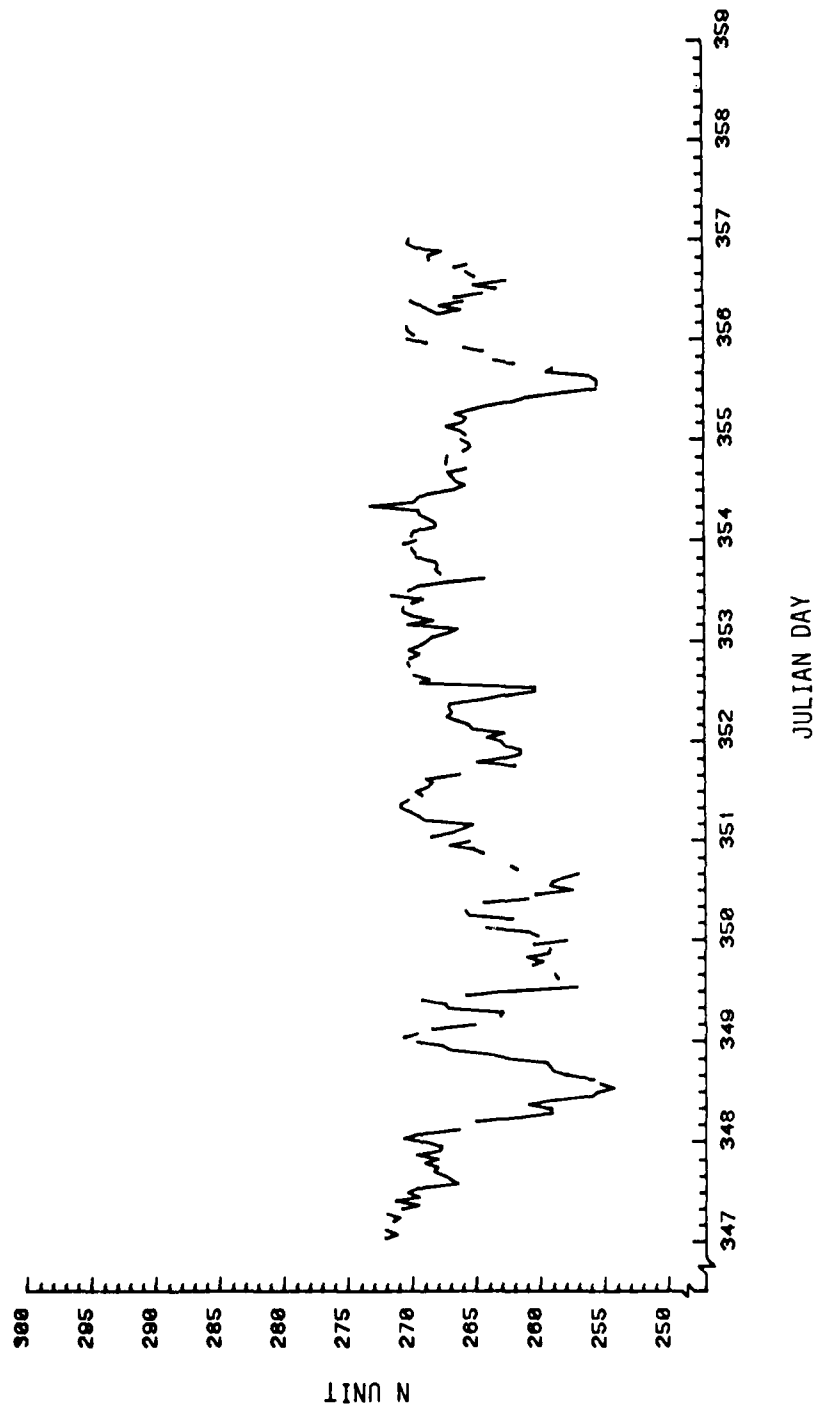


Figure 3-6. N units computed at Reno, NV over the time period
13 December to 22 December 1977.

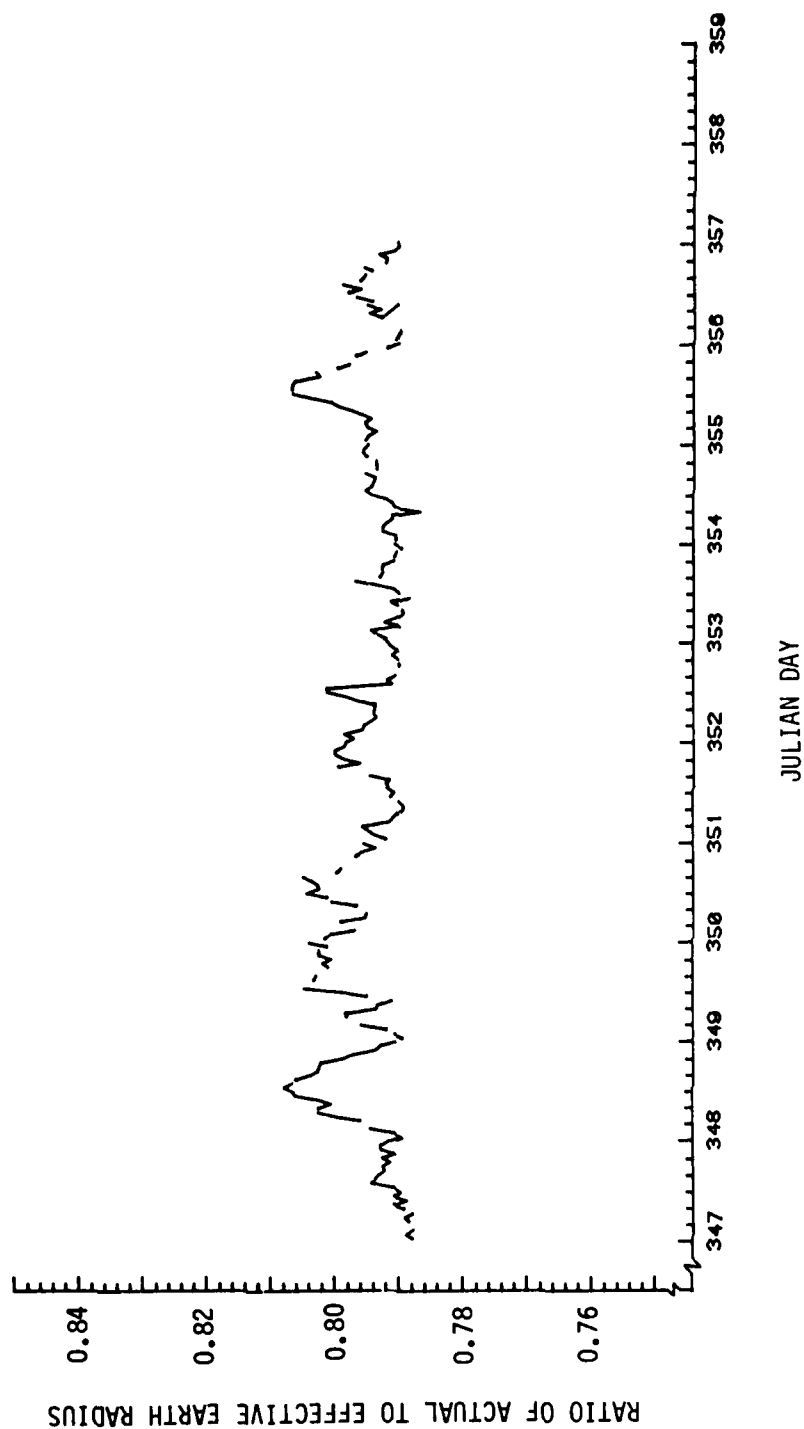


Figure 3-7. Ratio of earth radius to effective earth radius at Reno, NV compiled over the time period 13 December to 22 December 1977.

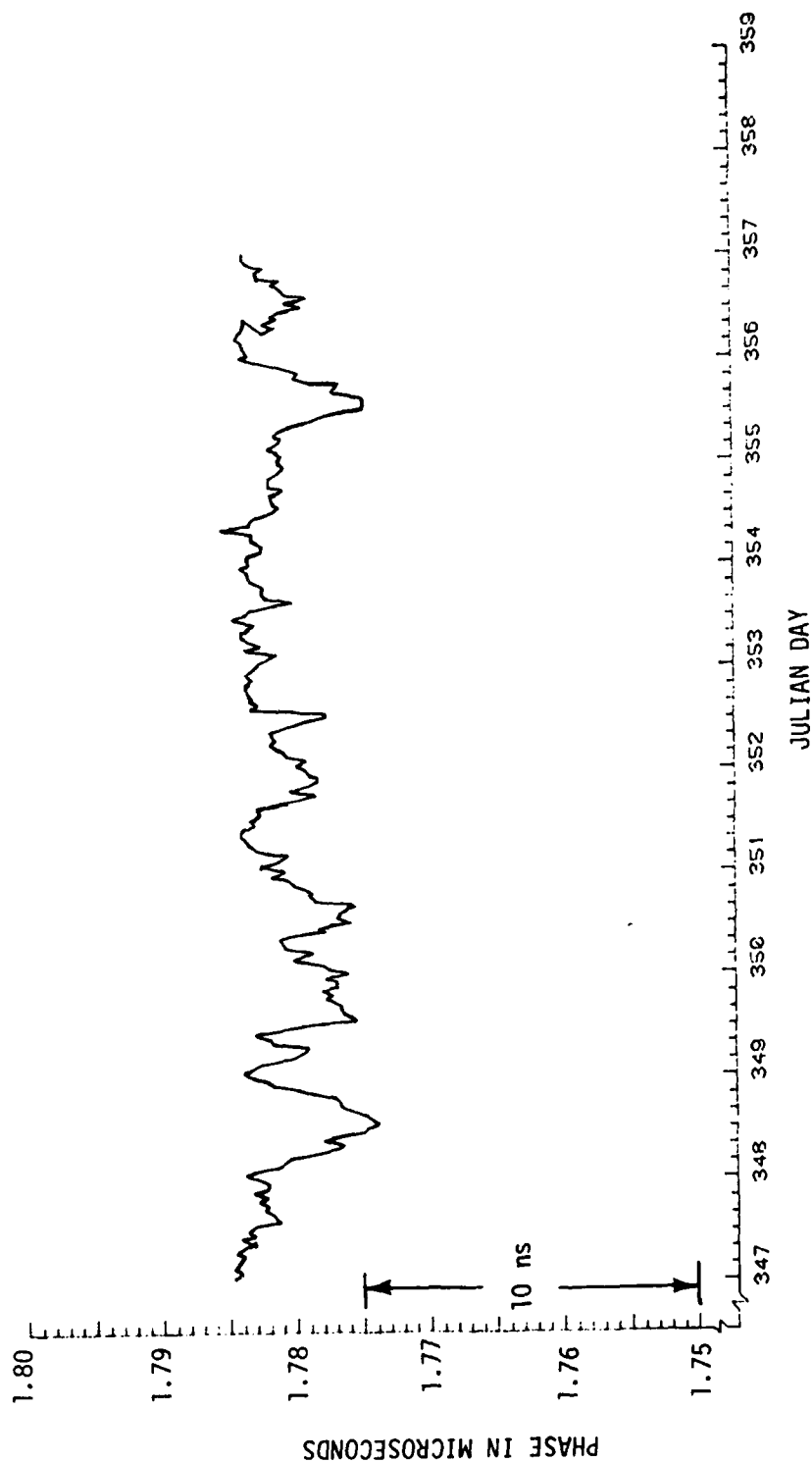


Figure 3-8. Phase variation over a 100 km path using the values of N and effective earth radius from Figures 3-6 and 3-7. ($\sigma = 0.01$)

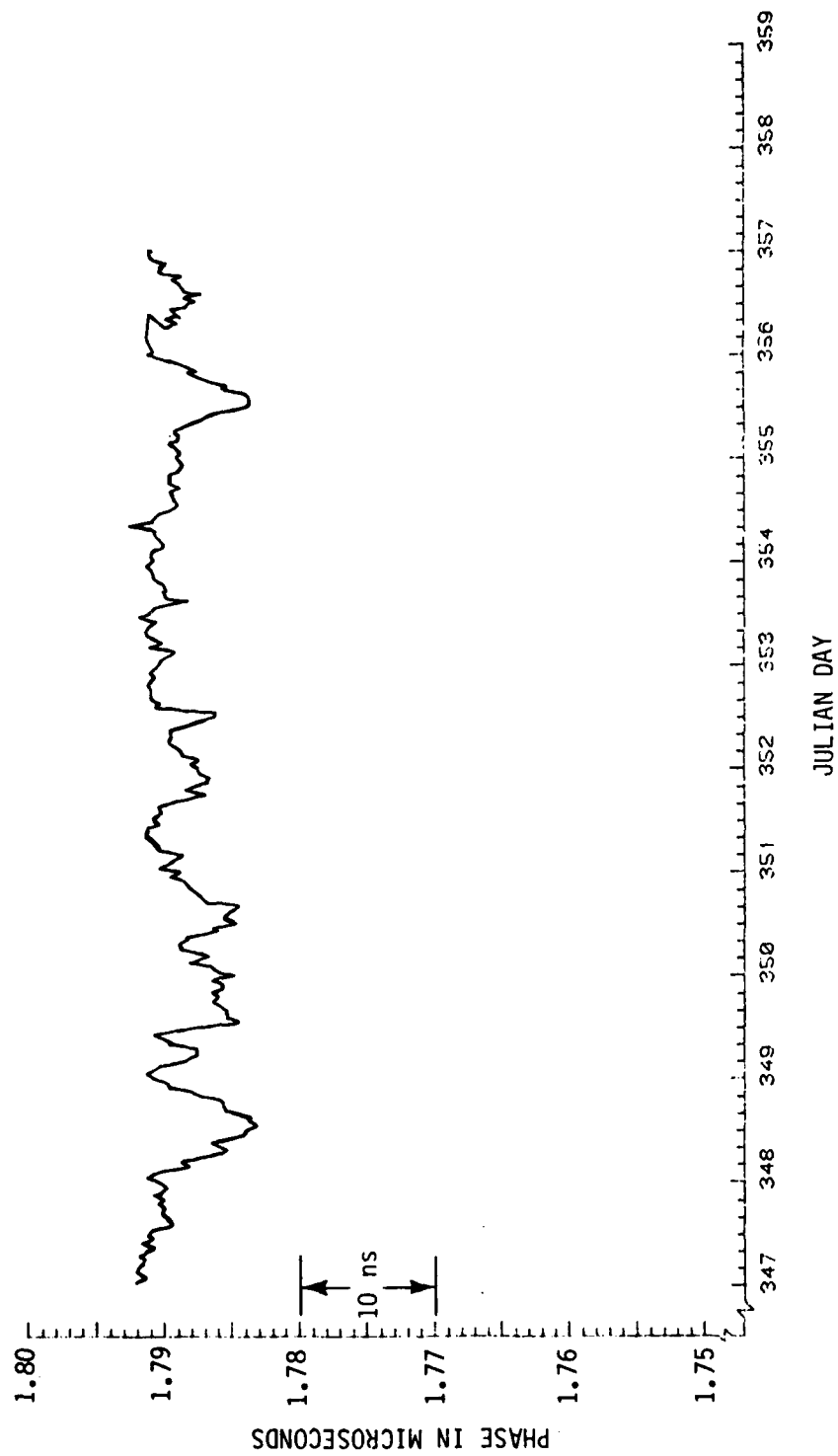


Figure 3-9. Phase variation over a 300 km path using the values of N and effective earth radius from Figures 3-6 and 3-7. ($\sigma = 0.01$)

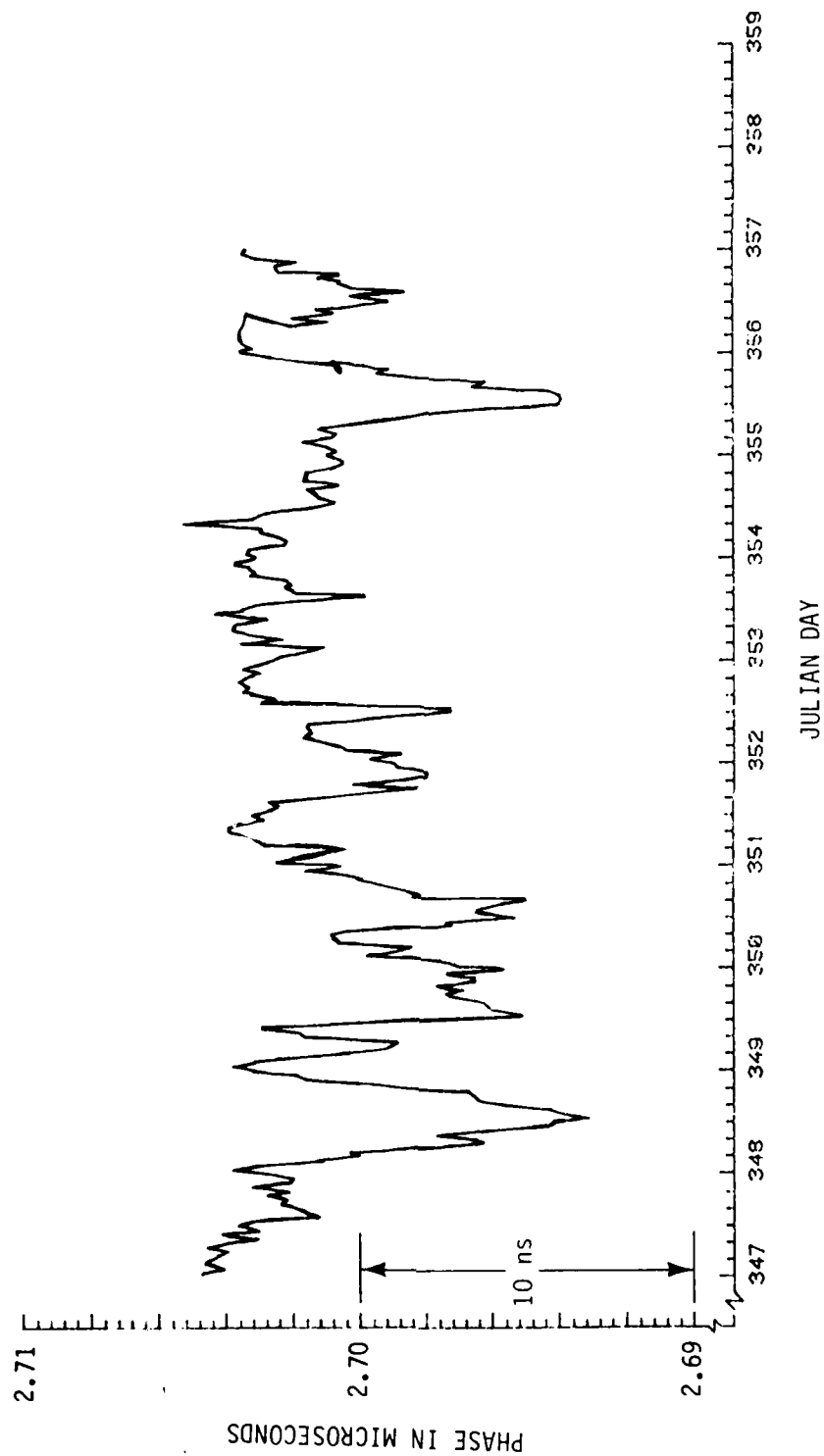


Figure 3-10. Phase variation over a 500 km path using the values of N and effective earth radius from Figures 3-6 and 3-7. ($\sigma = 0.01$)

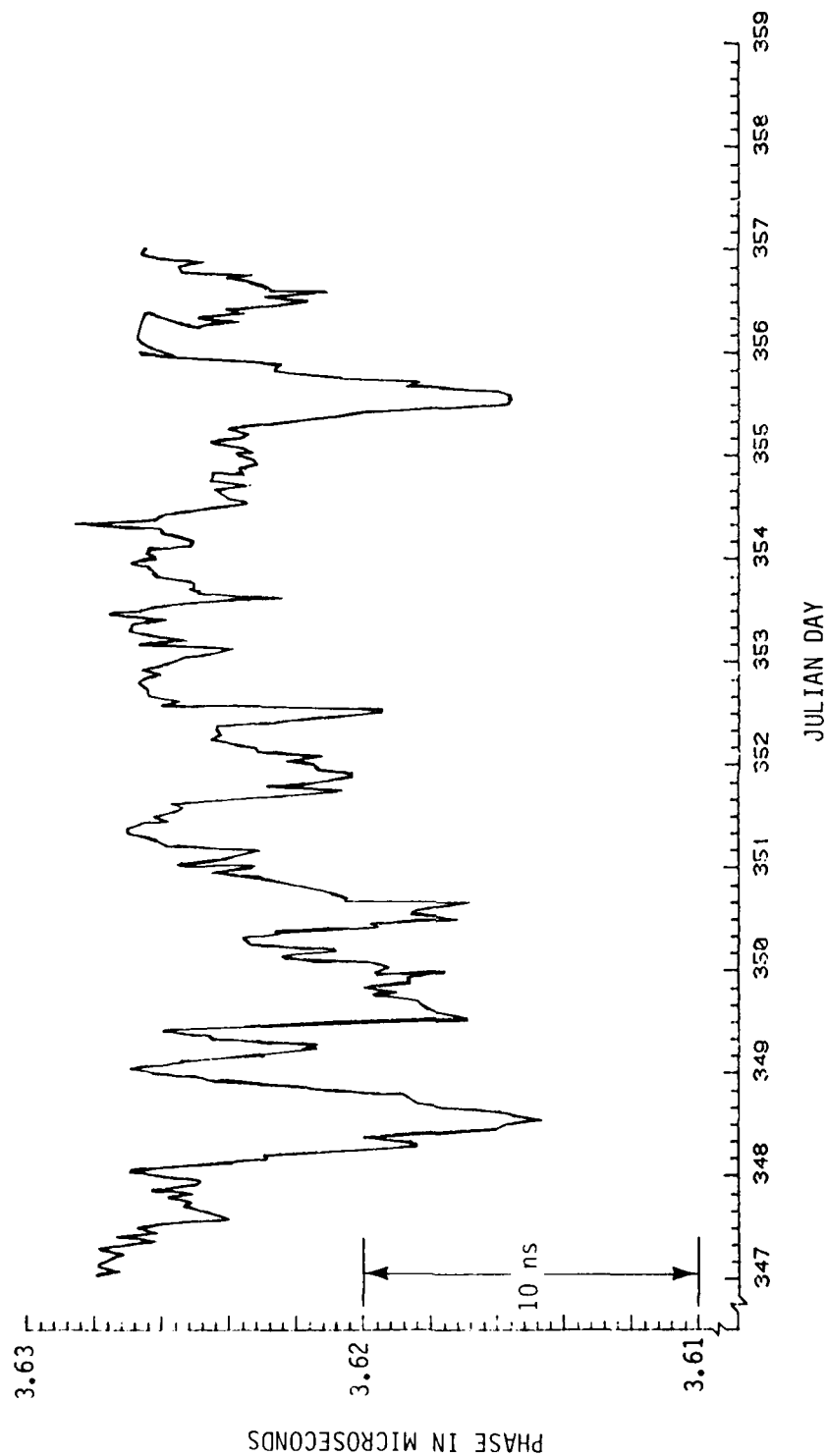


Figure 3-11. Phase variation over a 700 km path using the values of N and effective earth radius from Figures 3-6 and 3-7. ($\sigma = 0.01$)

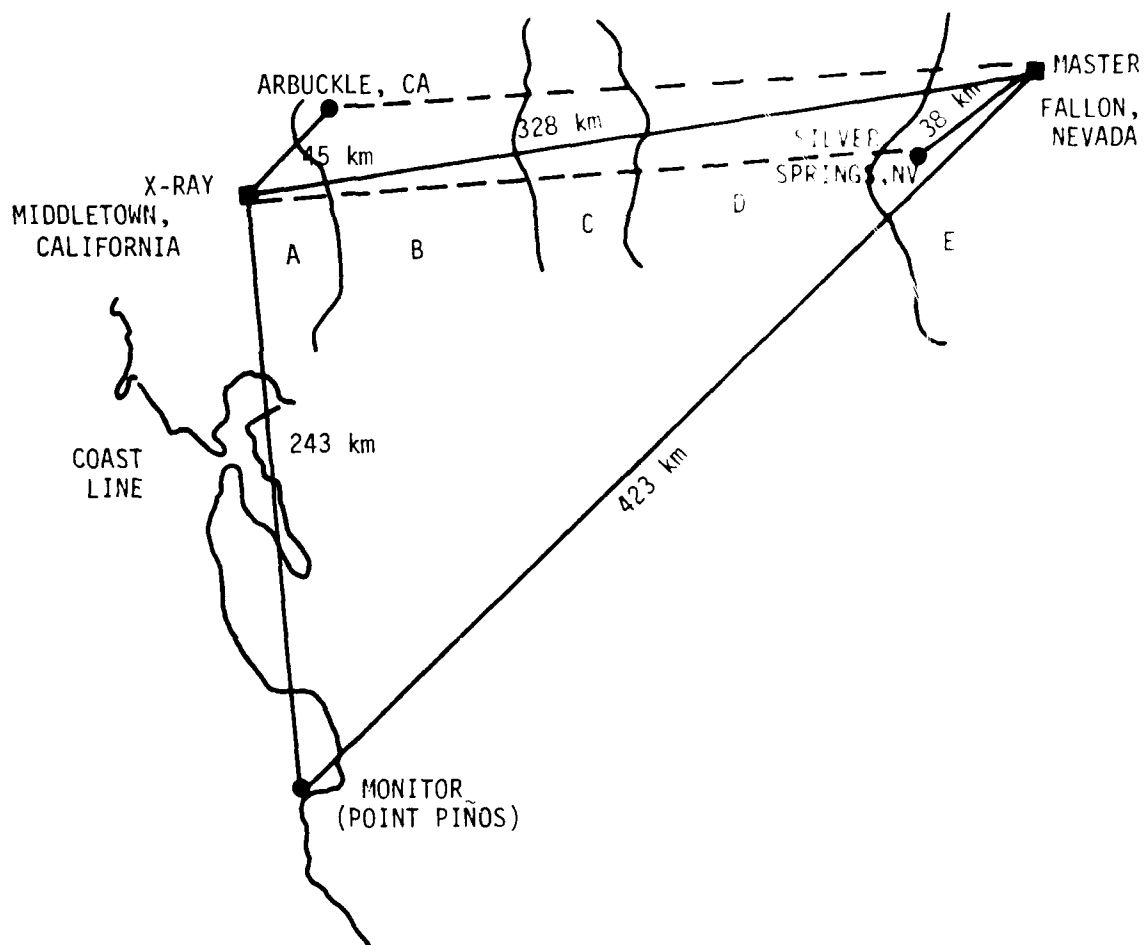
TIME DIFFERENCE VARIATIONS PRODUCED BY AN APPARENT SURFACE IMPEDANCE CHANGE

During the Stability Experiment, one of a series of experiments performed using the West Coast U.S. Loran-C chain, time difference measurements were made near the Master, X-ray and Yankee transmitters. Figure 3-12 shows the relative locations of the X-ray and Master transmitters, the adjacent measurement sites, and the system area monitor (SAM) at Point Piños, CA, which controls the X-ray and Yankee secondaries. The experiment was designed to provide separate measures of chain (timing) and propagation induced components of time difference fluctuations.

The data manipulations required to separate the chain and propagation induced fluctuations assume that propagation variations on short paths (X-ray to Arbuckle and Master to Silver Springs) are negligible and that propagation variations on the long paths (X-ray to Silver Springs and Master to Arbuckle) are identical. These assumptions may be satisfied for variations induced by atmospheric refractive index changes* but are not satisfied for variations induced by surface impedance changes. This conclusion will be important in the following discussion.

During the period from December 14 to December 19, 1977 (Julian Days 346 to 353) the X-ray time difference decreased at Silver Springs and increased at Arbuckle, but by a smaller amount. (See Figure 3-13). During this period there were a number of weather fronts and a large amount of precipitation in the experiment area. The data at both sites fluctuate with approximately a 24-hour period, believed to be caused by an interfering signal during the nighttime. The fluctuations preclude precise interpretation of the data. The trends in the data over the period are evident and very approximate estimates are that the mean X-ray time difference decreased 120 to 160 ns at Silver Springs and increased 40 to 60 ns at Arbuckle. Data processing that neglected propagation induced variations over the short paths, resulted in an

*Not verified or refuted by the experimental data.



Other distances:
 Arbuckle to Master - 384 km
 Silver Springs to Middletown - 290 km

Figure 3-12. Measurement sites and conductivity area boundaries for the stability experiment.

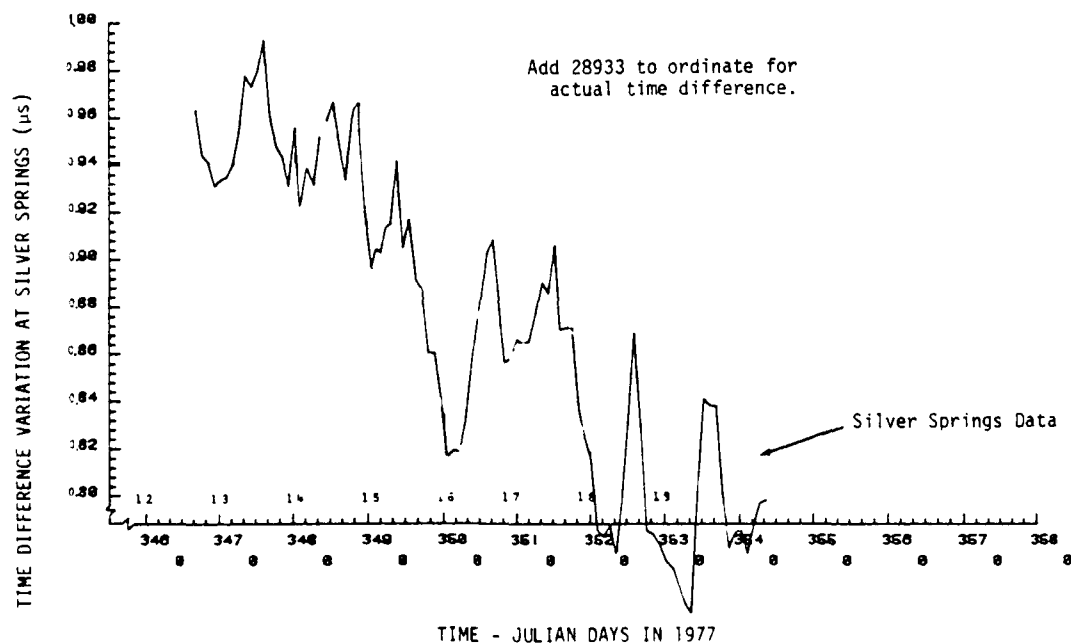
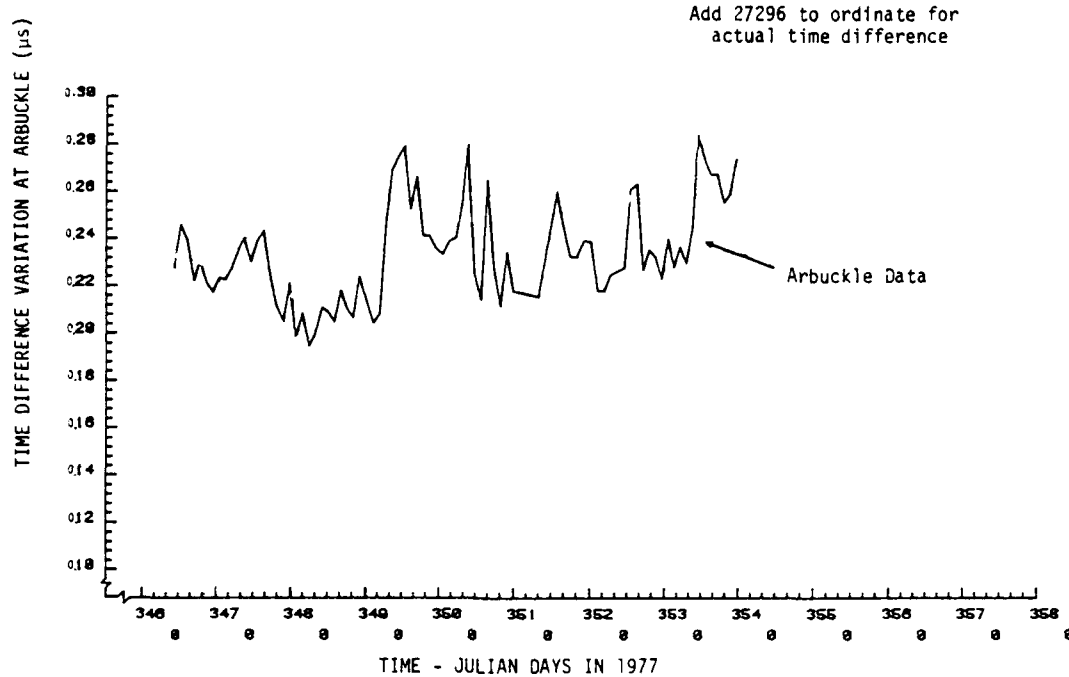


Figure 3-13. Time differences at Silver Springs and Arbuckle.

estimate of about 80 ns decrease in the propagation phase delay on the long paths. The magnitude and long duration of the propagation induced variations indicate that the cause was change in surface impedance, not refractive index. Thus, the assumptions required to manipulate the data are violated and further analysis is required.

In a separate analysis of these data, Samaddar (Reference 3-6), used supporting TINO (time interval number or pseudo time difference) data taken at the transmitter sites to further explain the observations. His analysis of the TINO data for the December 14 to 19 time period indicates:

1. The effective emission delay at X-ray remained essentially constant, ie, the propagation induced variations of time difference at the SAM were essentially balanced on the X-ray to SAM and Master to SAM paths and control action corrected only relative clock drift.
2. The net decrease in propagation delay along the baseline path from X-ray to Master was about 100 ns.

Based on (1) above, the total time difference variations at Silver Springs and Arbuckle are propagation induced. The apparent chain variations that we deduced from the experimental data should be attributed primarily to the neglect of variations on the short paths.

In this report, it is not our intent to reassess the stability experiment but to illustrate that observed propagation variations can be reproduced with reasonable assumptions of impedance variation. The following example shows that the observations may be explained by relatively small surface impedance changes. Approximate boundaries for areas with differing conductivity, labeled A through E, are shown on Figure 3-12. By performing secondary phase calculations using Millington's technique, first using nominal conductivity values for these segments and then values slightly above the nominal values, and by

3-6. "Weather Effects on Loran-C Propagation," Dr. S.N. Samaddar, U.S. Coast Guard (G-DOE-4/TP54) Washington, DC 20590 (to be published).

assuming that phase versus conductivity variations are linear over a small range in conductivity, we can obtain the following equations:

$$\Delta TD_{SS} = -86\Delta\sigma_A - 5\Delta\sigma_B - 31\Delta\sigma_C - 977\Delta\sigma_D + 176\Delta\sigma_E \approx -120 \text{ to } -160 \text{ ns}$$

$$\Delta TD_A = -116\Delta\sigma_A + 11\Delta\sigma_B + 36\Delta\sigma_C + 307\Delta\sigma_D + 103\Delta\sigma_E \approx 40 \text{ to } 60 \text{ ns}$$

$$\Delta T_{XM} = -85\Delta\sigma_A - 8\Delta\sigma_B - 29\Delta\sigma_C - 420\Delta\sigma_D - 101\Delta\sigma_E \approx -116 \text{ ns}$$

where

$\Delta\sigma_i$ = change in conductivity for the i th segment (mhos/m)

ΔTD_{SS} = change in X-ray TD at Silver Springs (ns)

ΔTD_A = change in X-ray TD at Arbuckle (ns)

ΔT_{XM} = change in phase delay along the Master X-ray path (ns)

Note, as expected, the large sensitivity to variation of the low conductivity segment (segment D).

A trial and error solution produced the results in Table 3-3. Since there are more unknowns than equations, other solutions may be obtained. Other interpretations of the data,* so long as the variations are in the 100's of ns range, may also be explained by reasonable variations in σ_i .

Table 3-3. Conductivity and time difference changes.

Segment	Nominal mmhos/m	Change mmhos/m	Time Difference	Computed Change
A	2	+0.3	ΔTD_{SS}	-136.9 ns
B	8	0.0	ΔTD_A	+ 41.9 ns
C	2	+1.0	ΔT_{XM}	-106.6 ns
D	0.5	+0.1		
E	2	+0.1		

*An alternate interpretation can be obtained by estimating that the time difference decrease at Silver Springs is slightly less than the time difference decrease on the X-ray-Master baseline. This would result in time difference changes approximately proportional to path length and could be explained by a general but small increase in conductivity all along the baseline.

SECTION 4

EXPERIMENTAL RESULTS

This section summarizes the Worst Case Path (WCP) Experiment results. Comparison between the experimental data and predicted results is deferred to the next section.

Measurements of phase time difference (TD), and signal arrival times (TOA) were taken at eight sites over a period of 60 days, as nearly as possible along the Yankee to San Francisco Harbor path, between Searchlight, Nevada, and Ft. Cronkhite, California. The main reason for taking these measurements was to compile a comprehensive experimental data base for comparison with predicted results from several known prediction techniques. Analysis and interpretation of the differences between measured and predicted data were to lead to a better understanding of Loran-C signal characteristics and an evaluation of available prediction techniques (computer codes) so that their application can be put into perspective with calibration as accurate tools for user data preparation and system analysis.

The Searchlight/Ft. Cronkhite path was selected for the experiment as a worst-case-path example, because of its extremely variable terrain and demonstrable history of short-term weather variations. The assumption was that irregular terrain and variable surface impedance along the path would produce experimental results that differed significantly from simple model predictions and therefore would provide a data base for thoroughly testing models that account for irregular terrain and impedance.

It was also expected that weather variations typical of the time of year might occur during data collection periods along the path. If large variations in measured data concurred with significant weather

phenomena then the data would provide additional guidance to improve models of weather produced variations in the prediction codes.

EXPERIMENT SITES

Figure 4-1 identifies the nearest towns where WCP data collection sites were established to take phase TOA measurements. The figure is not drawn to scale, but is intended to show the approximate, relative off-set distance of these locations from the geodesic. The precise (receiver) antenna position locations were used to compute predictions. The latitude and longitude in WGS-72 coordinates and the distance from each site to the Searchlight transmitter are shown in Table 4-1.

Table 4-1. Worst case path calibration and measurement sites.

Site	Latitude** (deg, min, sec)	Longitude** (deg, min, sec)	Distance From** Searchlight (Yankee) Transmitter (km)
Jean*	35 46 24.89	115 19 38.25	68.976
Tecopa**	35 49 05.58	116 11 05.02	136.678
Death Valley	36 03 32.45	116 50 19.47	201.449
Darwin	36 19 28.15	117 40 09.80	281.737
Delilah***	36 48 14.23	119 07 09.62	422.010
Friant**	36 59 38.84	119 42 16.20	478.270
Merced**	37 11 19.51	120 21 08.31	539.778
Crows Landing**	37 25 30.67	121 06 18.81	611.493
Livermore**	37 37 26.00	121 46 03.10	674.053
Ft. Cronkhite	37 50 29.47	122 32 41.17	746.697
* Calibration site ** Corrected for antenna offset from DMA markers - WGS 72 coordinates *** Inaccessible - no measurements			

MEASUREMENTS

Time difference data for X-ray (TDX) and Yankee (TDY), and time of arrival data for Master (TOAM), X-ray (TOAX) and Yankee (TOAY) were

THIS IS NOT A SCALED FIGURE
The data collection sites are shown at
approximate, relative distances from
the geodesic.

--- 300 meters for offsets

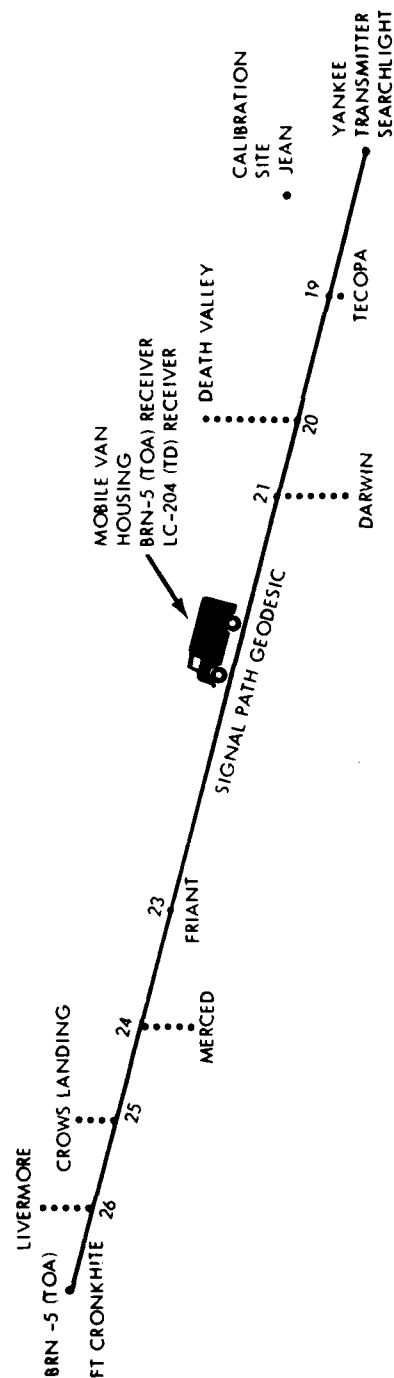


Figure 4-1. Data collection sites relative to the GEODESIC.

recorded for approximately three days at each of the worst case path measurement sites using an AN/BRN-5 receiver. Mean values of the TD are shown in Table 4-2. In the following, TOAY data is emphasized since it represents the signal along the WCP.

Table 4-2. Mean Value of TD at WCP measurement sites.

Site	TDX	TDY
Tecopa	28674.491	40835.183
Death Valley	28627.787	41218.738
Darwin	28540.667	41663.932
Delilah	No Data	
Friant	28164.779	42582.931
Merced	27973.838	42788.470
Crows Landing	27710.952	42980.373
Livermore	27459.547	43105.918
Ft. Cronkhite	27192.460	43210.931

Since it was not practical to keep the receiver and cesium time standard powered at all times, a portable TOA calibrator was used to reference the cesium standard in the AN/BRN-5 to the cesium standard at the Searchlight transmitter. The TOA calibrator consisted of a cesium standard controlling a Loran Signal Generator. Measurements were made using the TOA calibrator signal at a site Jean near the Searchlight transmitter and at the WCP measurement sites. The calibrator signal was substituted for the X-ray signal into a time difference receiver at Jean, providing simultaneous measurements of TDC (Calibrator to master time difference) and TDY. At the measurement sites, the calibrator signal replaced the Master signal into the BRN-5, resulting in simultaneous measurements of TOAC (calibrator time of arrival, referenced to the BRN-5 time standard) and TOAY. Assuming any propagation induced fluctuations

over the short path from Searchlight to Jean are negligible, the calibrator and Yankee data can be processed to give the change in TOA from site to site.

The algebraic manipulation used to calculate actual site to site changes in TOA,*taking into account the phase change of the mobile receiver cesium standard relative to the Yankee standard is:

$$\Delta\text{TOAY}_j = \text{TOAY}_j - \text{TOAY}_{j-1} + \delta_{jy} \quad (4-1)$$

where

TOAY_j = measured TOAY at site j

δ_{jy} = Phase change of mobile receiver cesium standard relative to the Yankee cesium standard during the time interval between measurements at site j and site $j - 1$.

The phase change, δ_{jy} , was estimated using measurements taken with the portable TOA calibrator. Calibrator data were taken alternately at site Jean near the Yankee transmitter (TD data) and the mobile site (TOA data). The drift was estimated from

$$\hat{\delta}_{jy} = \hat{\delta}_{jc} + \hat{\delta}_{cy} \quad (4-2)$$

where

$\hat{\delta}_{jc}$ is an estimate of the phase change of the mobile receiver cesium standard relative to the calibrator cesium standard

$\hat{\delta}_{cy}$ is an estimate of the phase change of the calibrator cesium standard relative to the Yankee cesium standard.

$\hat{\delta}_{jc}$ and $\hat{\delta}_{cy}$ were estimated from

$$\hat{\delta}_{jc} = \hat{\text{TOAC}}_{j-1} - \hat{\text{TOAC}}_j \quad (4-3)$$

and

*LPA's at the Yankee transmitter were removed from the data before performing the manipulations.

$$\delta_{cy} = (\widehat{TDC - TDY})_{t_j} - (\widehat{TDC - TDY})_{t_{j-1}} \quad (4-4)$$

where

$TOAC_j$ is derived from a fit to calibrator time of arrival

measurement at site j

TDC = calibrator time difference at site Jean

TDY = Yankee time difference at site Jean

$(\widehat{TDC - TDY})_{t_j}$ = an estimate of $TDC - TDY$ extrapolated from
TD measurements at site Jean to time t_j .

Inserting (5-3) and (5-4) into (5-1)

$$\begin{aligned} \Delta TOAY_j = & \widehat{TOAY}_j - \widehat{TOAY}_{j-1} - \widehat{TOAC}_j + \widehat{TOAC}_{j-1} \\ & + (\widehat{TDC - TDY})_{t_j} - (\widehat{TDC - TDY})_{t_{j-1}} \end{aligned} \quad (4-5)$$

which can be manipulated to give

$$\begin{aligned} \Delta TOAY_j = & (\widehat{TOAC} - \widehat{TOAY})_{j-1} - (\widehat{TOAC} - \widehat{TOAY})_j \\ & + (\widehat{TDC - TDY})_{t_j} - (\widehat{TDC - TDY})_{t_{j-1}} \end{aligned} \quad (4-6)$$

In the data manipulation, $(\widehat{TOAC} - \widehat{TOAY})_j$ was estimated at selected reference times using a straight line fit to data taken at the beginning and end of the measurement period at site j . $(\widehat{TDC - TDY})_{t_j}$ was computed at the same selected reference times, using a straight line fit to TD data taken before and after the measurements at site j . The slopes of the $\widehat{TDC - TDY}$ data at Jean and the $\widehat{TOAC} - \widehat{TOAY}$ data at the sites were not consistently constant. The slopes were nearly equal at the first three measurement sites, but were significantly different at the last three measurement sites.

Table 4-3 (second column) shows a range of values for the quantities in Equation 4-6, which is obtained by computing the values at the beginning and the end of the measurement period at each of the sites.

Table 4-3. Calibrator and time of arrival data for WCP measurement sites.

CALIBRATOR DATA				TOA DATA ONLY
Site	TDC - TDY- (TOAC - TOAY) (μ s)	Δ TOA (From previous site) (μ s)	CUM Δ TOA (From Tecopa) (μ s)	Δ TOA ₂ (From previous site) (μ s)
Tecopa	226.602 + 226.629			
Death Valley	443.305 + 443.389	216.676 + 216.787	216.676 + 216.787	216.700 + 216.766
Darwin	711.863 + 711.902	268.474 + 268.597	485.234 + 485.300	268.372 + 268.378
Delilah	No Data			
Friant	1369.160 + 1369.168	657.258 + 657.305	1142.531 + 1142.566	657.295 + 657.381
Merced	1573.904 + 1573.930	204.736 + 204.770	1347.275 + 1347.328	
Crows Landing	1813.031 + 1813.257	239.101 + 239.353	1586.402 + 1586.655	
Livermore	2022.633 + 2077.697	209.376 + 209.666	1796.004 + 1796.095	209.194 + 209.232
Ft. Cronkhite	2264.954 + 2264.971	242.257 + 242.338	2038.325 + 2038.369	

The difference results from the difference in slopes of the regression lines fit to the time difference and TOA data and represents a first order estimate of the maximum measurement error. Using the mid-range value as the estimate, the error is plus or minus one half the difference between the two estimates. The site to site change in TOA (column 3) and the cumulative change in TOA (column 4) is also shown.

An alternate procedure for estimating the site-to-site change in TOA can be used when cesium reference power is maintained over the measurement time period for two adjacent sites. The phase change, δ_{jy} (see Equation 5-1) can be estimated from

$$\delta_{jy} = S_L \cdot \Delta T \quad (4-7)$$

where S_L is the slope (μ s/s) of the linear least squares fit to the TOA data and ΔT is the time interval in seconds between measurements at adjacent sites. Again, a range of values is obtained since the slopes of the linear fits are not identical for measurements at adjacent sites. The range of values for Δ TOA computed using the TOA slopes are also shown in Table 4-3 (Δ TOA₂, column 5) for those pairs of sites where cesium power was maintained. The Δ TOA's obtained this

way are close (within ≈ 100 ns) to the value obtained using the calibrator with the exception of the Crows Landing to Livermore value, where a disparity greater than 150 ns occurs.

In general the measurements appears to be within $\approx \pm 50$ ns for sites up to Crows Landing and are $\approx \pm 150$ ns for Crows Landing and Livermore sites.

The measured values at Ft. Cronkhite, obtained by two separate measurements at Ft. Cronkhite and at Jean, again show experimental accuracy of about ± 50 ns.

The experimental data are reduced to incremental and cumulative secondary phase values and compared to predicted results in the next section.

SECTION 5

WORST CASE PATH PREDICTIONS AND COMPARISON WITH EXPERIMENTAL RESULTS

The primary prediction calculations for the worst case path were obtained using the integral equation technique program, HUFLOC (INEQ2E) (Reference 5-1). The use of this program required a significant effort to prepare both the terrain elevation profile and electrical impedance profile which comprise the basic input data. It was then found that the straightforward application of the HUFLOC program was extremely sensitive to the integration step size which was used. This sensitivity was related to the scale distance between the elevation data points primarily although there was some effect from the impedance changes. We first indicate the technique used for obtaining the elevation and impedance profiles along the path. This is followed by a description of the numerical predictions that were obtained and their sensitivity to changes in the terrain and electrical impedance profile and integration step size. The predictions are then compared to the measured data.

TERRAIN DATA

The terrain (altitude) profile along the worst case path was obtained from USGS 7.5 minute and 15 minute topographic maps covering the entire path. The geodesic points along the path from Searchlight to Fort Cronkhite were obtained using the Sodano method. These points were then corrected from WGS72 to NAD27 using overlays provided by DMA. The elevation data were obtained in feet above mean sea level as a function of distance in kilometers from Searchlight, Nevada. When the data is read into the program (through Subroutine GETELV) the elevation data are

5-1. Johler, J.R., and L.A. Berry, *Loran-D Phase Corrections Over Inhomogeneous, Irregular Terrain*, ESSA Technical Report IER59-ITSA56, 1967.

converted to meters relative to mean sea level and the distance is converted from kilometers to meters to be consistent with the distance measure used within the integration routine. The elevation is eventually adjusted to meters relative to the altitude of the transmitter. The actual raw elevation data used are given in Appendix E. Figure 5-1 shows the altitude as a function of the position along the path. This figure was obtained using all of the elevation data points along the path. The elevation is in meters relative to sea level. The original proposed data collection points are indicated and are given in Table 5-1. Also shown in the table are the primary phase delays using two values for the refractive index of air, 1.000338 and 1.000260. The former corresponds to the value used in earlier Loran-C propagation studies and provided with the HUFLOC code. It is also the value used throughout all but one of the worst case propagation path calculations. The lower value 1.00026, was obtained using the formulae in Section 3 in conjunction with the weather data and the fact that the mean altitude of the propagation path is considerably above sea level. It may be noted that there is a difference of 195 nanoseconds in the prediction of the primary portion of the phase at Fort Cronkhite from this change in the index of refraction.

Table 5-1. Worst case path data collection points.

Point No.	Name	Distance from Searchlight (km)	Primary Phase Delay (us)	
			$n=1.000338$	$n=1.000260$
1	Tecopa	136.678	456.062	456.0
2	Death Valley	201.449	672.188	672.136
3	Darwin	281.737	940.091	940.017
4	Delilah	422.010	1408.149	1408.039
5	Friant	478.270	1595.875	1595.751
6	Merced	539.778	1801.113	1800.973
7	Crows Landing	611.493	2040.410	2040.250
8	Livermore	674.053	2249.158	2248.982
9	Fort Cronkhite	746.697	2491.554	2491.359

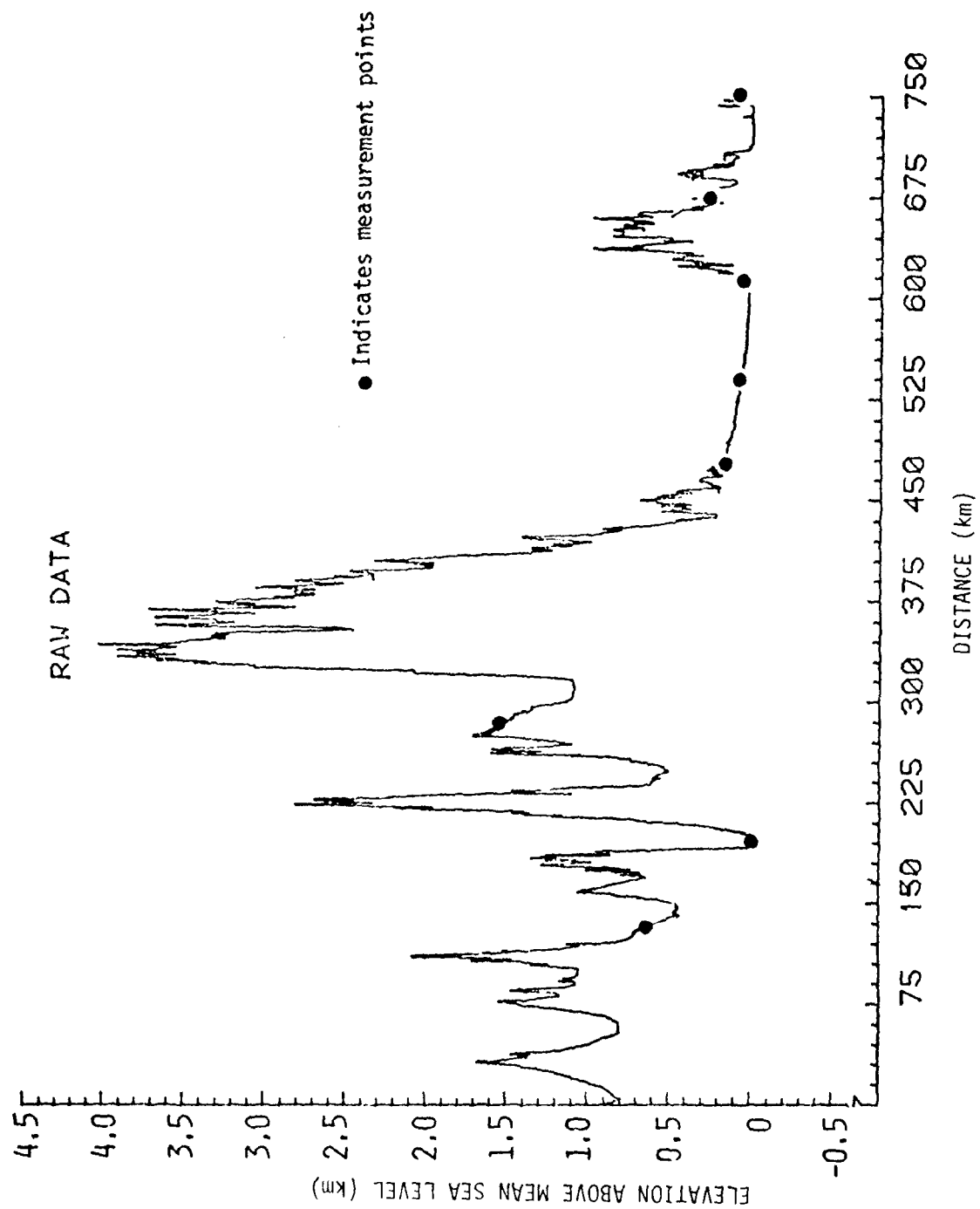


Figure 5-1. Original worst case path terrain data.

SURFACE IMPEDANCE

The surface impedance along the worst case propagation path can be computed using the techniques discussed in Appendix D if the conductivity and dielectric constant are known along the path as a function of depth. However, this information is not easily obtained. The conductivity of the earth as a function of depth depends on frequency and many geologic parameters; a partial list of the parameters include the type of soil or rock, its age, porosity, water content with associated dissolved salt, metallic mineral content, and temperature. If the indicated parameters of a rock are known, then the conductivity can be estimated by the application of various empirical relationships and mixing rules. Since many of the parameters are usually unknown, the general procedure is to measure the conductivity experimentally.

The experimental measurements can be divided into discrete and average measurements. Individual rocks can be brought into the laboratory and their conductivity measured. In the field, electric well logs can measure the conductivity as a function of depth at a particular well site. These discrete measurements are useful as general guides, but cannot be extrapolated over distances as required in our problem because of the inhomogeneity of the earth. The conductivity profiles from two wells situated only a few meters apart may be significantly different. An example of an average measurement is the earth conductivity estimated from the decay in field strength about a commercial radio transmitter. Such measurements are required by all broadcast stations. The conductivities determined from these field strength surveys represent the average values of the earth over an area of a few square miles about the broadcasting station to a depth of about a hundred feet. The estimates used for the worst case path are based on these average measurements.

Keller and Frischknecht, Reference 5-2, have summarized the radio data from some 7000 measurements. Table 5-2 shows the general range

5-2. Keller, G.V., and F.C. Frischknecht, *Electrical Methods in Geophysical Prospecting*, Pergamon Press, 1966 (Reprinted 1977).

Table 5-2. Generalized resistivity ranges for rocks of different lithology and age. (From Reference 5-2.)

Age	Marine sedimentary rocks	Terrestrial sedimentary rocks	Extrusive rocks (basalt, rhyolite)	Intrusive rocks (granite, gabbro)	Chemical precipitates (limestone, salt)
Quaternary and Tertiary age	1-10	15-50	10-200	500-2000	50-5000
Mesozoic	5-20	25-100	20-500	500-2000	100-10,000
Carboniferous Paleozoic	10-40	50-300	50-100	500-2000	200-100,000
Early Paleozoic	40-200	100-500	100-500	500-2000	10,000-100,000
Precambrian	100-2000	300-5000	200-500	500-2000	10,000-100,000

of resistivity (the inverse of the conductivity) for different categories of rocks. Figure 5-2 is a map of the United States, showing areas of high, moderate, and low near-surface resistivity. The worst case path lies generally in a region of high conductivity (low resistivity). Finally Table 5-3 shows Keller and Frischknecht's summary of resistivities for various specific rocks and formations.

Just as for the topographic profile, the worst case propagation path was plotted on geologic survey maps of California and Nevada. For the Nevada portion of the path the Geologic Map of Clark County, Nevada was used. In addition to indicating the surface soil properties, this map also indicates substructure properties. Maps for California were obtained from the California Division of Mines and Geology. These maps indicate the surface soil parameters. The bedrock structure along the path for the state of California was obtained from the Oil and Gas Investigations MAP OM-215 from the Department of the Interior, USGS.

The following procedure was used to estimate the conductivity values along our path. First, geologic maps were used to estimate the type of soil and rock as a function of distance along the path. Up to three layers were allowed to define the rock type with depth.

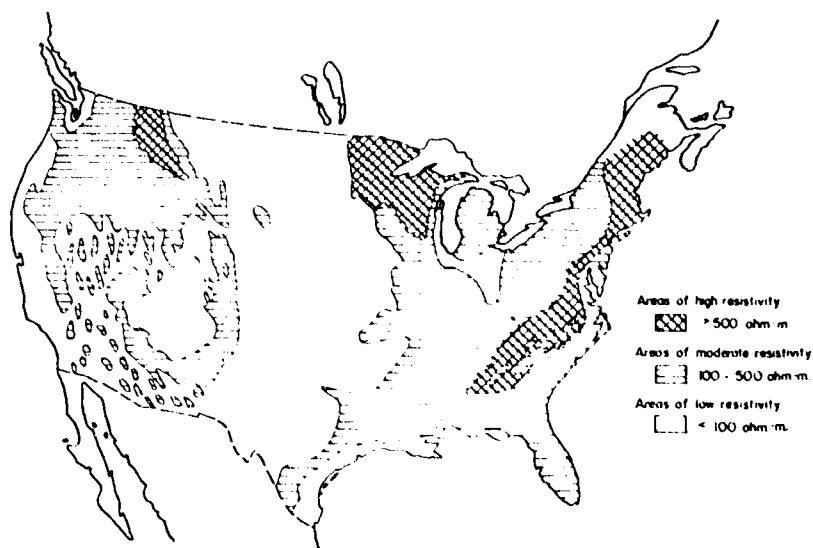


Figure 5-2. Areas of high, moderate and low near-surface resistivity in the United States, as indicated by resistivity measurements near radio stations. (From Reference 5-2).

Then for each material type, a range of conductivity values was determined from the radio resistivity summaries. Since the path lies in a region of generally high conductivity, a value on the high side of the mean conductivity was then chosen.

At radio frequencies, the dielectric constant is of secondary importance in determining the signal propagation. The dielectric constant is determined by the type and fractions of the materials in the soil or rocks. Most dry rock material has a relative dielectric constant of about 3.5; water has a value of about 81; and air has a value of 1. If the fraction of each of these three components in a rock are known, then the composite relative dielectric constant can be calculated from the appropriate mixing relations. We do not know the component fractions of the rocks, so again we rely on general summary data.

Table 5-3. Summary of resistivities measured about radio stations.
(From Reference 5-2).

Area and age of rocks	Formation names	Lithology	Average resistivity (ohm-m)	95% range in resistivity
Quaternary alluvium, Pacific coast		Alluvium, lake deposits, beach sand, glacial drift	75	43-130
Quaternary alluvium, Rocky Mountains	Gila conglomerate	Alluvium, bolson deposits, lake beds, windblown sands	99	58-170
Quaternary alluvium, Mississippi Valley		Alluvium	182	105-308
Quaternary sedimentary rocks, Gulf Coast states	Beaumont clay	Sand and gravel	78	40-155
Quaternary sedimentary rocks, Atlantic coast states	Lissie formation	Sand and gravel	340	182-645
Quaternary limestones, Atlantic and Gulf coast states	Anastasia formation	Limestone	143	106-183
	Miami colita			
	Key Largo limestone			
Tertiary sedimentary rocks, Pacific coast states (terrestrial)		Terrestrial sediments, volcanics	275	172-440
Tertiary marine sedimentary rocks, Pacific coast		Sandstone and shale	167	114-247
Tertiary volcanics, Rocky Mountains	Challis volcanics	Latite lava, basalt, andesite, rhyolite, breccias	167	114-247
	Hinsdale formation			
	San Juan tuff			
	Silverton series			
	Potosi series			
Miocene and Pliocene sedimentary rocks, Rocky Mountains	Santa Fe formation	Terrestrial sediments, lake beds	80	
Miocene and Pliocene sedimentary rocks, Great Plains	Ogallala formation	Channel deposits, sand, silt and gravel	55	38-82
Miocene sedimentary rocks, Gulf Coast states	Arikaree formation			
	Alum Bluff group	Fresh-water marls, sand, silt and gravel	480	263-830
	Choctawhatchee fm.			
	Hattiesburg clay			
	Oakville formation			
Miocene sedimentary rocks, mid-Atlantic coast	Yorktown formation	Unconsolidated sand, clay, coquina rock, shell beds	457	320-620
	Duplin marl			
Miocene sedimentary rocks, south Atlantic coast	Tampa limestone	Limestone, sandstone	209	119-357
Miocene and Pliocene volcanics, Pacific northwest	Catahoula sandstone			
	Columbia River basalt	Basalt, andesite, rhyolite flows and tuff	257	132-500
	Cascade andesite			
	Yakima basalt			
	Wenas basalt			
Oligocene sedimentary rocks, Great Plains	White River group	Terrestrial clays, silts, and sandstones	103	
Eocene and Oligocene, sedimentary rocks, Gulf and Atlantic coast	Castle Rock conglomerate			
	Vicksburg group	Marl, limestone, sand, and clay	180	104-340
	Jackson group			
	Clairborne group			
	Wilcox group			
	Midway group			
Eocene sedimentary rocks, Great Plains and Rocky Mountains	Green River formation	Shale and limestone	63	38-108
	Wasatch formation			
	Denver formation			
	Arapahoe formation			
	Fort Union formation			

Table 5-3. Continued.

Area and age of rocks	Formation names	Lithology	Average resistivity (ohm-m)	95% range in resistivity
Upper Cretaceous sedimentary rocks, Great Plains	Montana group Pierre shale Foxhills sandstone Laramie formation Niobrara formation Benton shale Dakota sandstone	Shale, sandstone, lignite, chalk, calcareous shale	40	33-71
Cretaceous sedimentary rocks, Rocky Mountains	Mesa Verde formation Colorado shale Dakota sandstone Morrison formation	Shale and sandstone	80	53-143
Cretaceous sedimentary rocks, Gulf and Atlantic coast	Ripley formation Selma chalk Eutaw formation Tuscaloosa formation	Marine sandstones, marls, clay, chalk	410	130-1300
Cretaceous sedimentary rocks, Texas and Oklahoma	Navarro formation Taylor marl Austin chalk Eagle Ford formation Woodbine formation	Marine sandstones, marls, chalk, clay	48	28-82
Lower Cretaceous sedimentary rocks, Texas and Oklahoma	Washita group Fredericksburg group Trinity group	Sandstone, anhydrite, limestone	95	48-188
Triassic rocks, New England states	Chicopee shale Granby tuff Longmeadow sandstone Mount Toby conglomerate Sugarloaf arkose	Intrusive diabase, basalt, tuff, shale, sandstone, conglomerate, arkose	613	310-1220
Permian sedimentary rocks, mid-continent	Cloud Chief formation Duncan formation Woodward group Enid formation Wichita formation Cottonwood limestone	Dolomite, limestone, gypsum, salt, shale, anhydrite, sandstone	48	29-88
Pennsylvanian sedimentary rocks, mid-continent	Pontotoc group Nelagoney formation Ochelata formation Seminole conglomerate Holdenville shale Wetumka shale Calvin sandstone	Sandstone and shale	70	46-105
Pennsylvanian sedimentary rocks, Great Lakes and northeast states	Monongahela formation Conemaugh formation Allegheny formation Pottsville group	Sandstone, shale, coal, limestone, iron ore	154	88-270
Mississippian sedimentary rocks, midwestern states	Chester age Meramec age Osage age Kinderhook age	Sandstone, shale, salt, coal, gypsum, dolomite, anhydrite, limestone	230	109-490
Mississippian sedimentary rocks, Ohio and Indiana	Meramec age Osage age	Sandstone, shale, limestone	116	83-135
Carboniferous granite, Appalachians		Granite intrusions	420	313-555

Table 5-3. Continued.

Area and age of rocks	Formation names	Lithology	Average resistivity (ohm-m)	95% range in resistivity
Carboniferous and Devonian rocks, New England states	Cambridge slate Roxbury conglomerate Mattapan volcanics Dighton conglomerate Rhode Island formation Wamsutta formation Worcester phyllite	Volcanics slate, conglomerate, phyllite	680	340-1380
Upper Devonian sedimentary rocks, midwest and northeast states	Hamilton age Marcellus age Onondaga age Helderberg age	Sandstone, shale, limestone	135	75-244
Upper Devonian sedimentary rocks, midwest and New England	Portage age	Black shale, sandstone	223	127-395
Silurian sedimentary rocks, New England states	Catskill age Cayuga age Lockport age Clinton age	Limestone, dolomite, shale	162	111-233
Silurian sedimentary rocks, midwestern states	Cayuga age Lockport age Clinton age	Limestone, dolomite, shale, calcareous shale	82	63-114
Ordovician sedimentary rocks, northeastern states	Maysville age Eden age Trenton age Chazy age Beekmantown limestone	Shale, limestone, dolomite	185	111-313
Ordovician and Cambrian sedimentary rocks, Great Lakes area	St. Peter sandstone Prairie du Chien dolo. St. Croixan rocks	Sandstone, limestone, dolomite, conglomerate	213	132-345
Ordovician and Cambrian rocks, western New England	Taconic sequences		303	147-525
Cambrian rocks, Appalachian area	Conococheague ls. Honaker limestone Potadam sandstone Waynesboro shale	limestone, shale, quartzite, sandstone	385	340-1380
Algonkian and Archean rocks, New England states		Phyllite, schist, gneiss	1200	250-590
Keewenawan and Huronian rocks, Great Lakes area	Portage Lake series	Sandstone, conglomerate, basalt, rhyolite, slate, iron formation	185	890-1670
Algonkian and Archean rocks, Appalachian area	Wissahicken schist Cockeysville marble Setters formation	Schist, phyllonite, marble volcanics, limestone, granite	500	119-389
Algonkian and Archean rocks, southern Appalachians		Granite, gabbro, gneiss, metabasalt, aporhyolite	530	312-813
Algonkian rocks, Montana	Wallace formation Helena limestone	Limestone, shale, quartzitic limestone	320	323-870

The relative dielectric constant normally ranges from values as low as 4 for dry quartzitic rocks to as much as 20 for rocks with a high water content. For our path we assume a range of values from 5 to 20, correlated with the (assumed) water content of the materials. Dry rocks such as volcanics and other high resistivity (low conductivity) rocks will be assumed to have low relative dielectric constants. High water content materials such as basin and stream channel deposits will be assumed to have high relative dielectric constants. The intermediate materials will be assumed to have intermediate values.

The actual data used to calculate the impedance along the worst case path is described in appendix F. The impedance amplitude is shown in Figure 5-3 as a function of distance along the path. In general, the phase of the impedance varies between $.246\pi$ and $.250\pi$, the lower phase going with the higher impedance. From this small range in the phase of the impedance it can be seen that the relative dielectric constant is essentially unimportant for these calculations since the impedance can be represented very closely by a constant multiplied by \sqrt{r} .

PREDICTIONS

The initial test calculations for the worst case path were made using the topographic data, exactly as it had been derived. An integration step is determined from the requirement that an integral number of steps be taken between the transmitter and receiver. It was then noted that when calculations were made at increasing distances from the transmitter the integration step changed by a few percent (or less) and the computed phase for a given intermediate point (interpolated from the calculated phase) could vary over a range of many hundred nanoseconds. This problem was traced to the fine grain description of the topographic profile. The computed profile picked out from the data base for use in the predictions might change drastically in some regions because of the rapidly varying surface. Large altitude fluctuations can occur over a distance of a few tenths of a kilometer. As the integration step size was varied slightly,

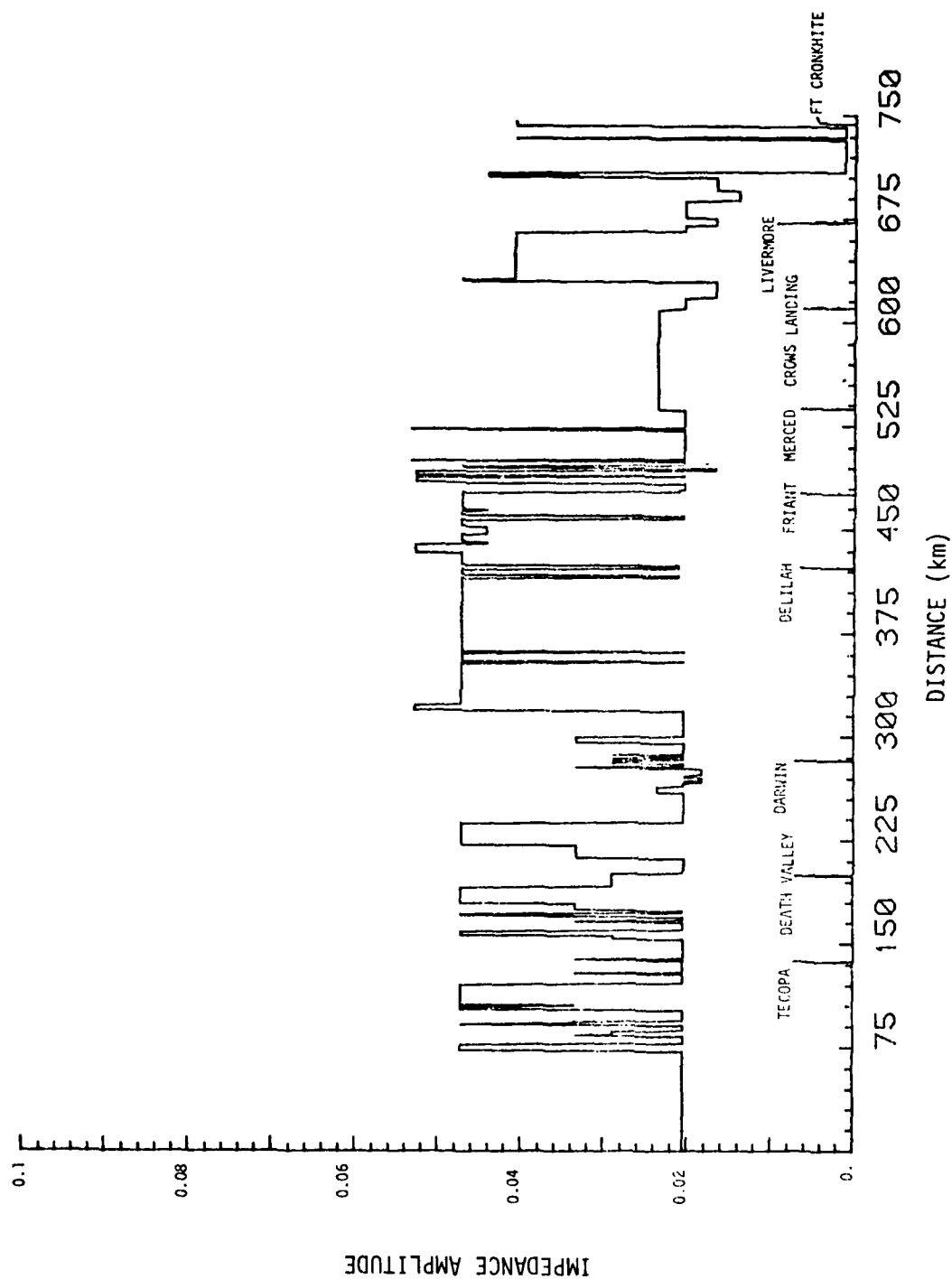


Figure 5-3. Amplitude of the surface impedance as a function of distance along the worst case path.

entirely different profiles were obtained for the height and its first and second derivative. Some unusual values were also obtained because of the use of a quadratic interpolation routine on an arbitrary distribution of data points.

Reducing the step size to solve this problem is impractical and the decision was made to smooth or filter the topographic data. Since the wavelength of the Loran-C wave is 3 kilometers, we expect that surface fluctuations of a scale size smaller than a wavelength should not be important in the far field for the propagating surface wave. Also, the method of solution assumes that the surface impedance and topographic variations will be relatively smooth from one integration step to the next.

The original topographic data were shown in Figure 5-1. The result of smoothing the topography over a distance of 2.2 and 6 kilometers is shown in Figure 5-4. The upper curve has been offset upward by 1000 meters. Note that in this figure the terrain data has been referenced to the transmitter altitude, thus the significant offset from the original data referenced to sea level. The effect of smoothing over 2.2 kilometers is shown for the individual sites in Figure 5-5a through 5-5h. For Livermore an obvious error in the original data can be seen. In the first test calculation over the worst case path the incorrect point was not picked up because of the particular grid size. Had it been picked up, there would have been a divide check and overflow in the computation because of the interpolation routine. This error in the data was corrected.

Initially no smoothing was done for the surface impedance or conductivity. Eventually two test cases were run for which the surface impedance was smoothed but the smoothing of the impedance had little effect on the computed phase at the data collecting sites, except near Delilah.*

For the discussion of the prediction capability, ten separate calculations have been chosen. Table 5-4 indicates the important parameters used for each calculation. For all but two runs, the integration step was nominally 0.9 kilometers. The initial calculation

*The site unfortunately was bypassed as a data collection site.

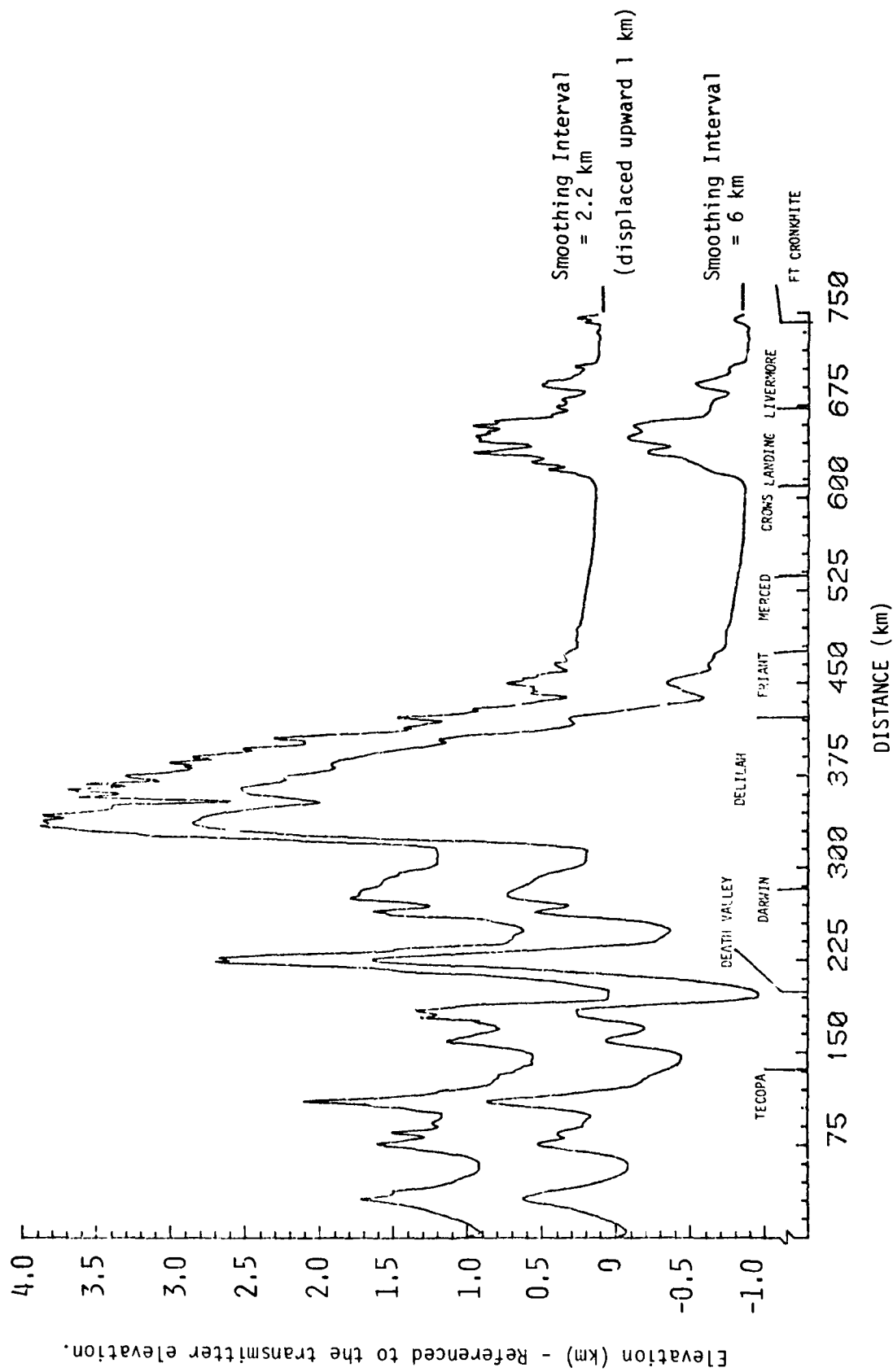


Figure 5-4. Smooth terrain data for the worst case path.

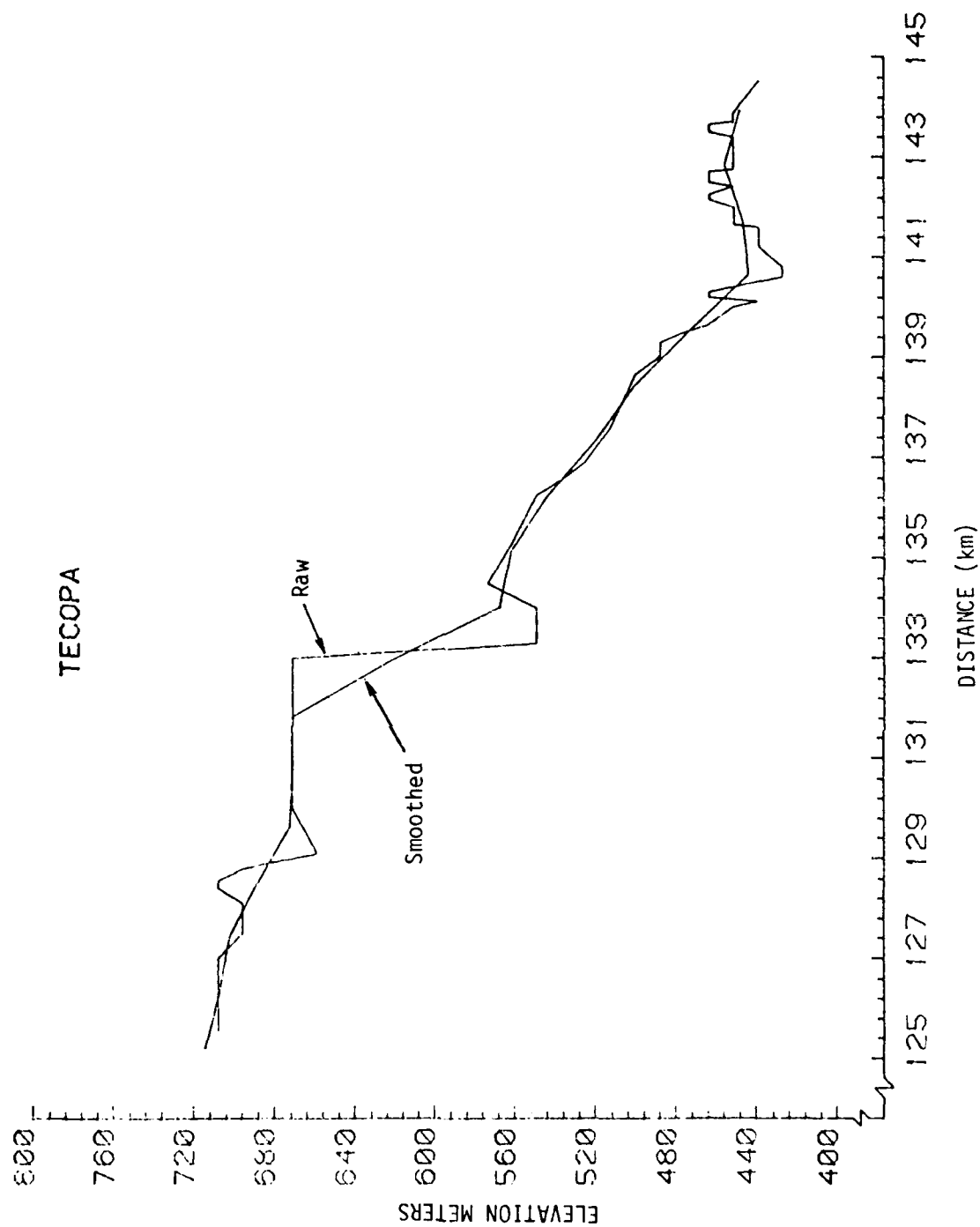


Figure 5-5a. Comparison between smoothed and raw data in the vicinity of site Tecopa.

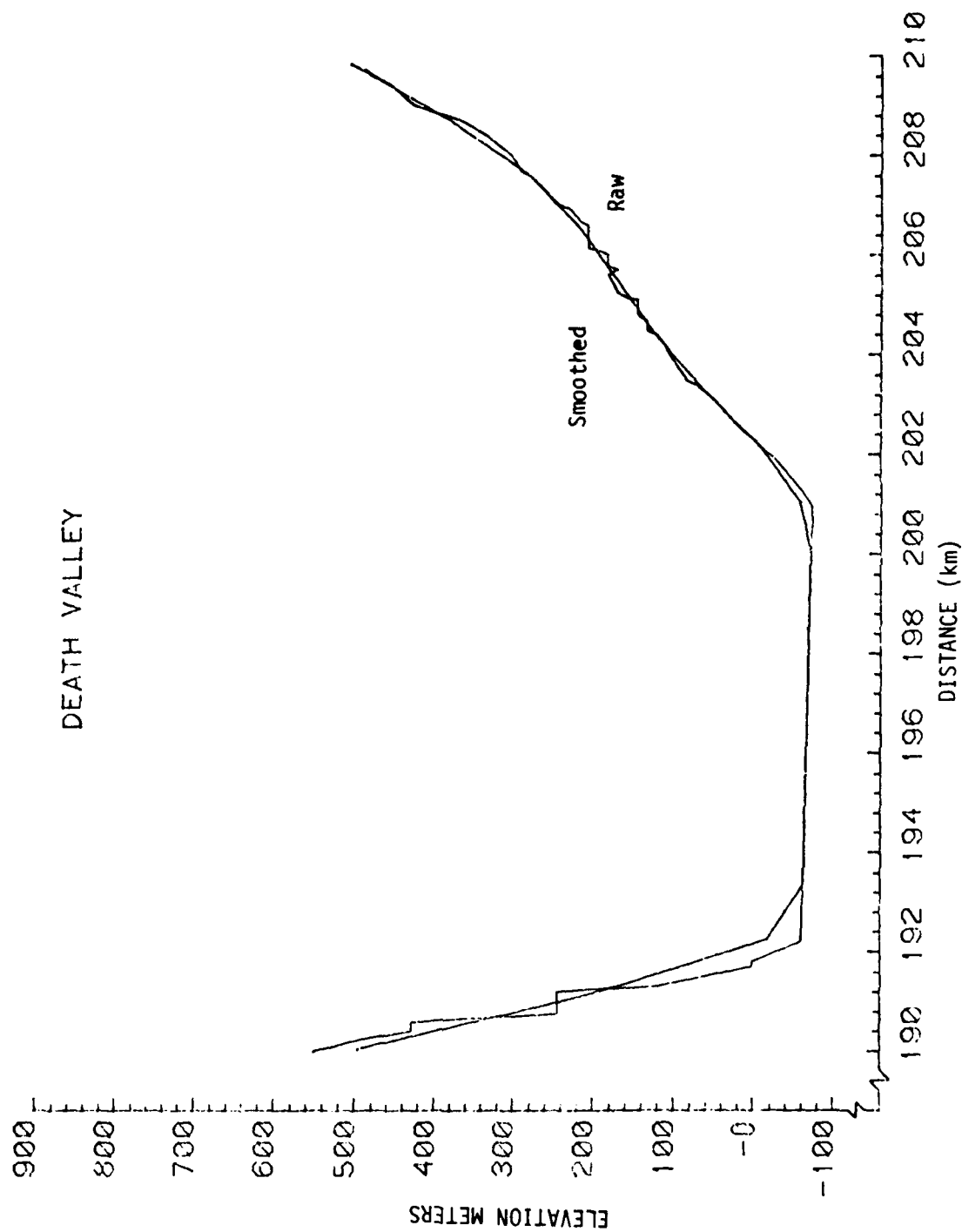


Figure 5-5b. Comparison between smoothed and raw data in the vicinity of site Death Valley.

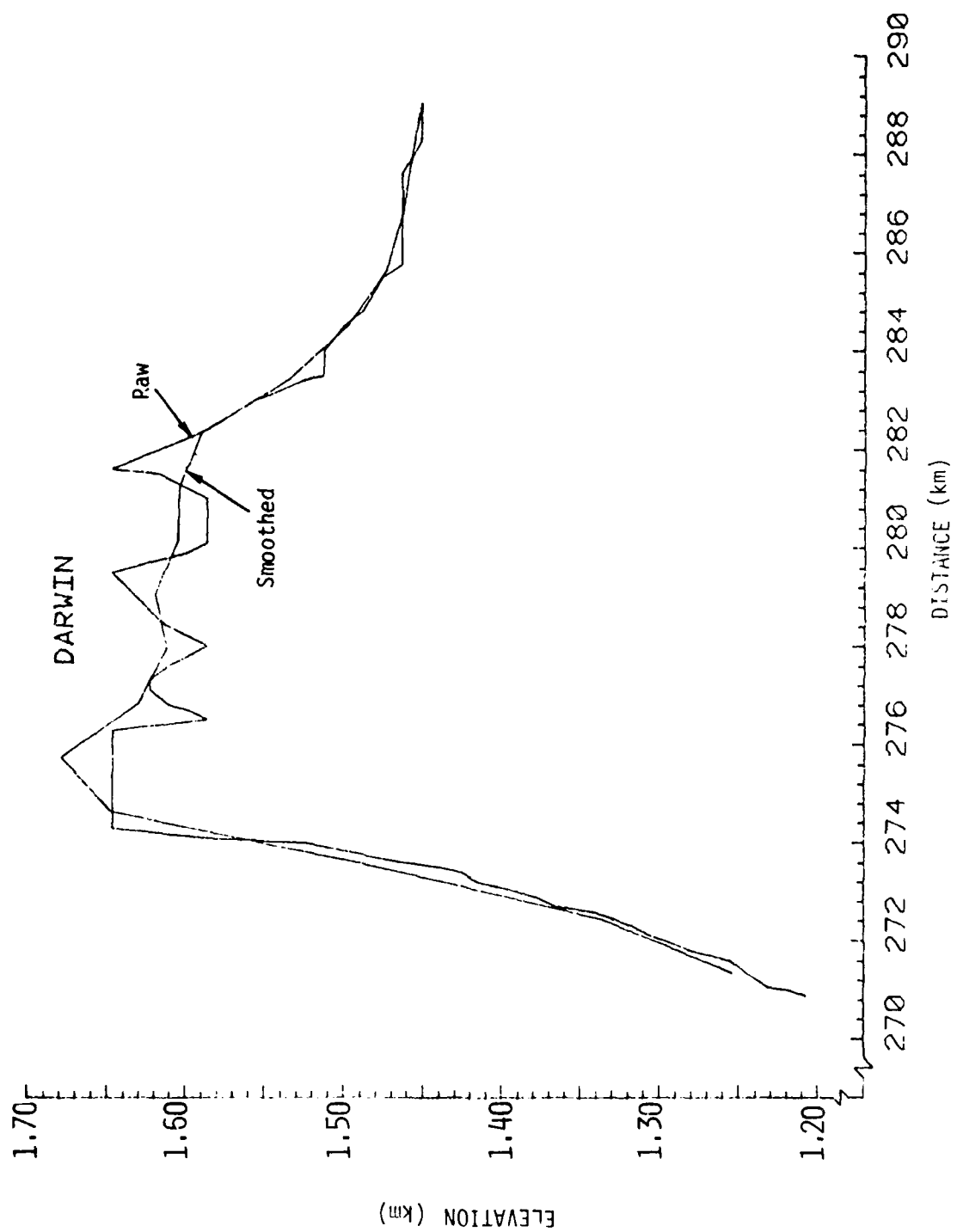


Figure 5-5c. Comparison between smoothed and raw data in the vicinity of site Darwin.

AD-A084 338

GENERAL ELECTRIC CO SANTA BARBARA CA TEMPO
LORAN-C SIGNAL ANALYSIS PROPAGATION MODEL EVALUATION.(U)
JUL 79 B GAMBILL, K SCHWARTZ
6E78TMP-51

F/6 20/14

DOT-C6-64810-A

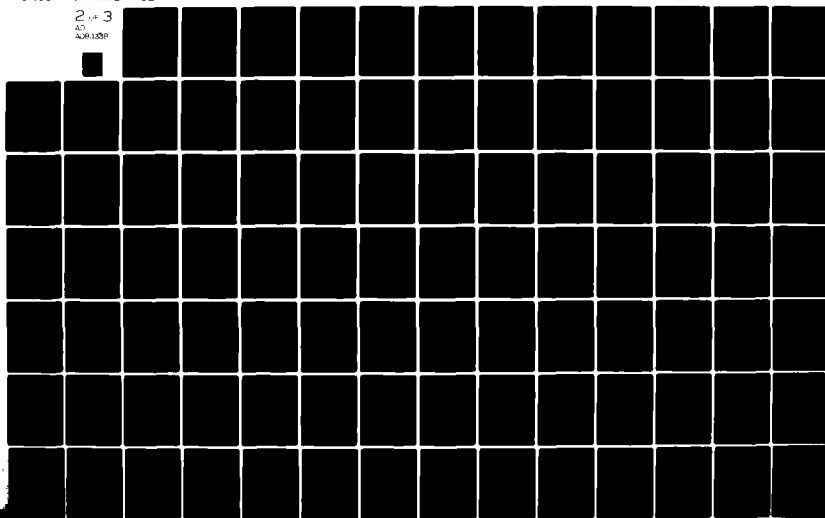
UNCLASSIFIED

USCG -D-20-80

NL

2 of 3

AD
A084338



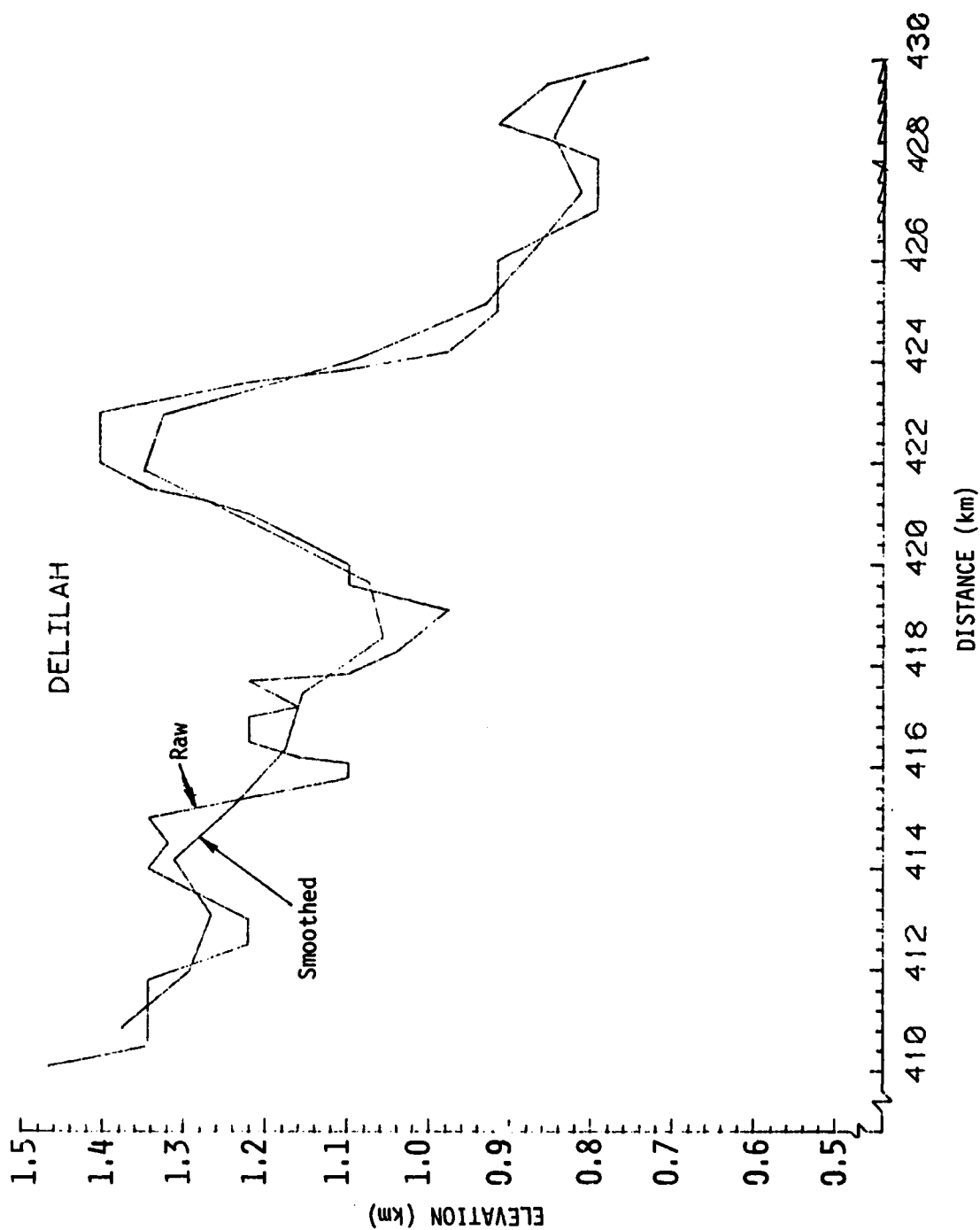


Figure 5-5d. Comparison between smoothed and raw data in the vicinity of site Delilah.

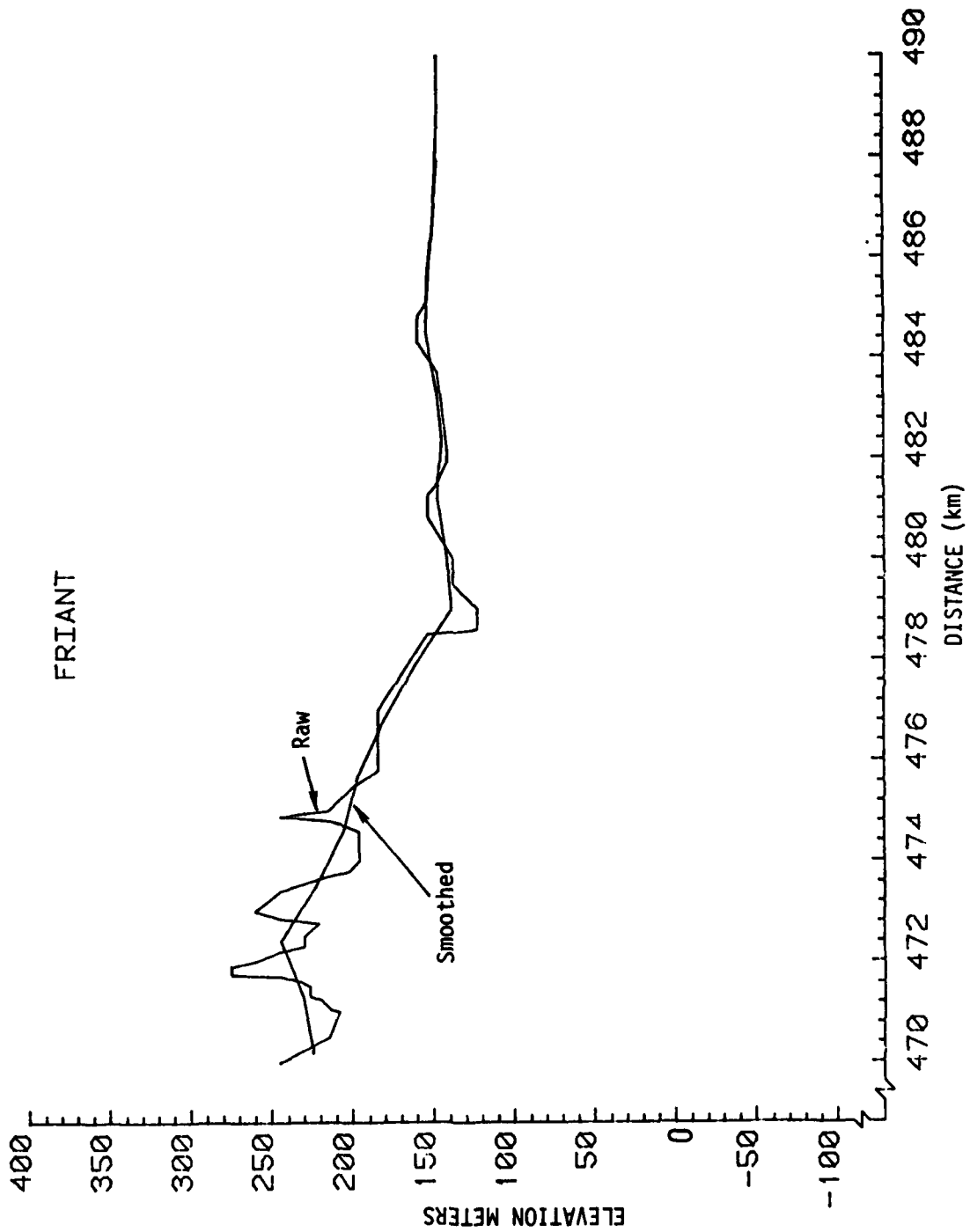


Figure 5-5e. Comparison between smoothed and raw data in the vicinity of site Friant.

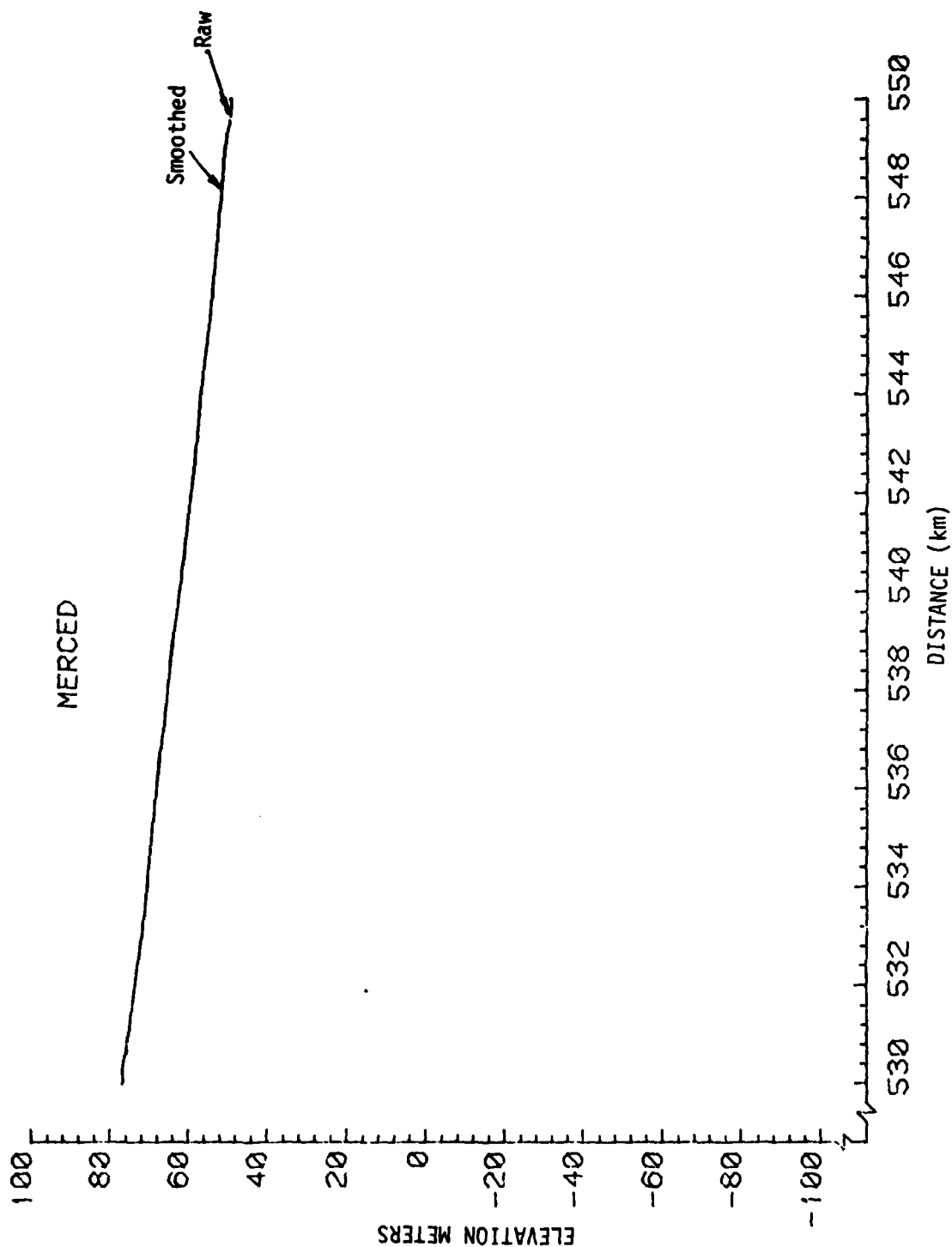


Figure 5-5f. Comparison between smoothed and raw data in the vicinity of site Merced.

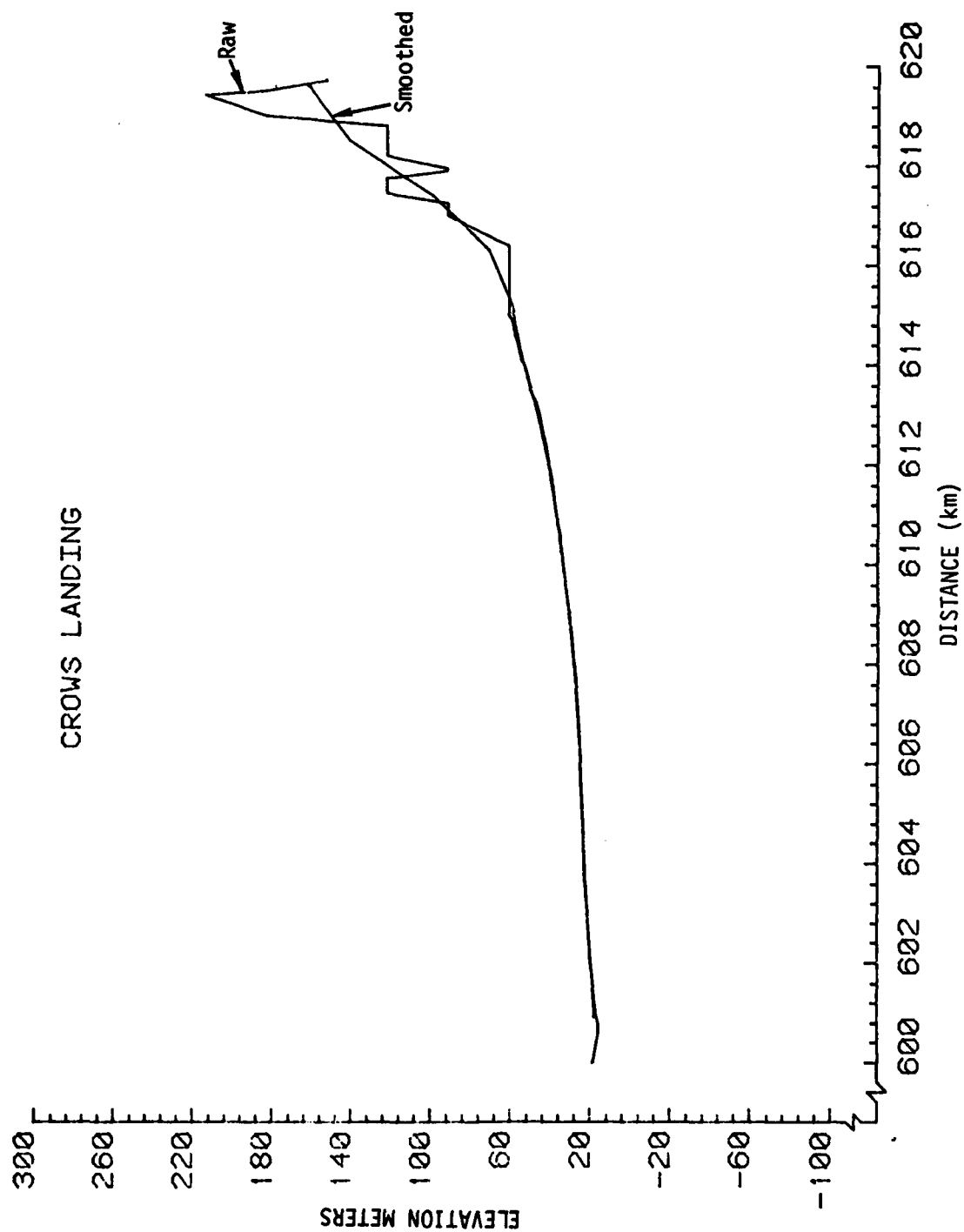


Figure 5-5g. Comparison between smoothed and raw data in the vicinity of site Crows Landing.

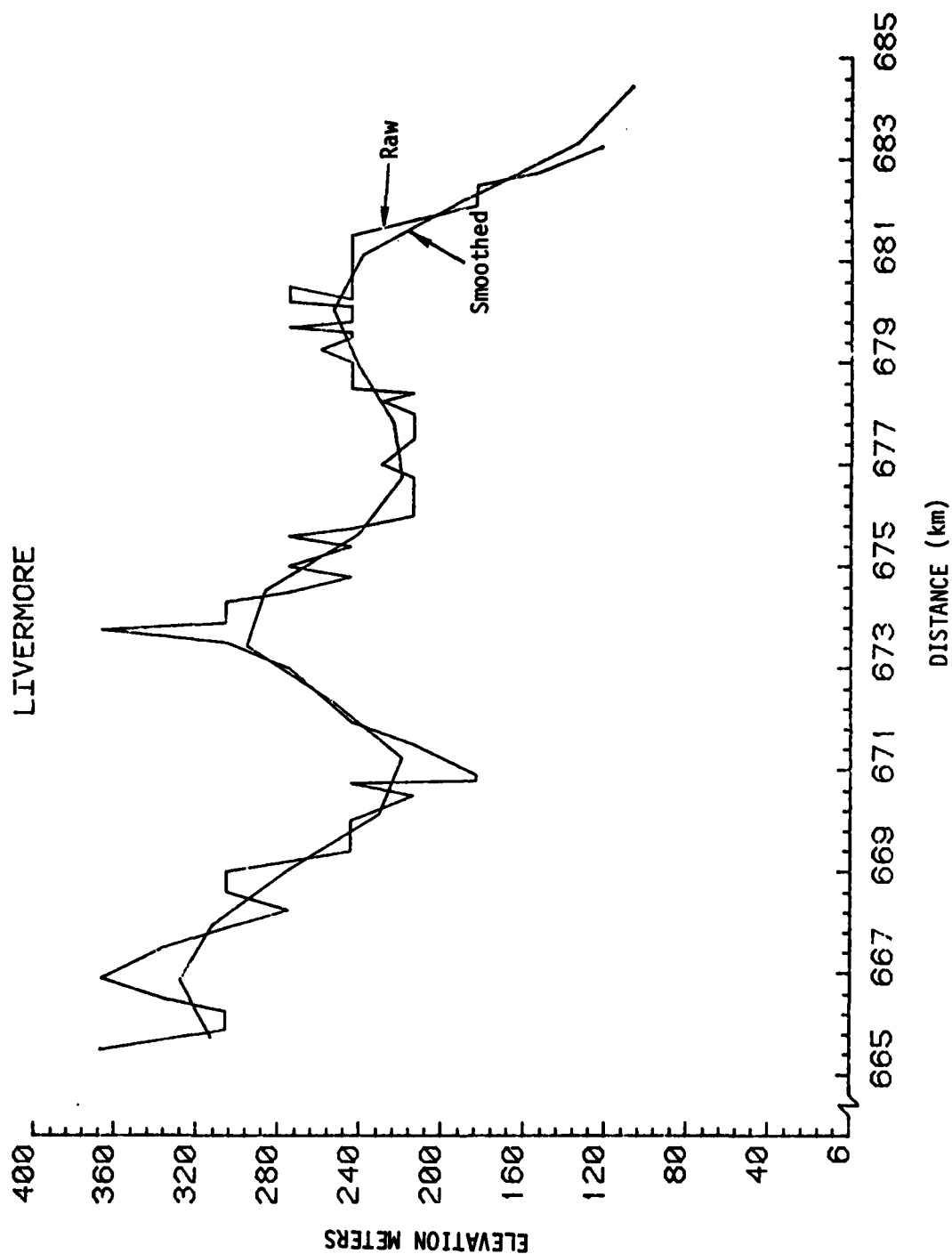


Figure 5-5h. Comparison between smoothed and raw data in the vicinity of Livermore.

Table 5-4. Parameters for different HUFLOC (INEQ2E) computer runs for worst case path.

Case No.	Δx Integration Step (km)	S_z , Smoothing Interval for Terrain (km)	S_Δ , Smoothing Interval for Impedance (km)	η	a/a_e	a_e
1	1.0	2.2	0.	1.000338	0.85	7491 km
2	0.9	2.2	0.	↓	↓	↓
3	0.9	6.0	0.			
4	0.45	6.0	0.			
5 ^a	0.9	6.0	0.			
6	0.9	6.0	6.0			
7	0.9	30.0	30.0			
8 ^b	0.9	6.0	0.			
9	0.9	∞^c	0.	↓	↓	↓
10	0.9	6.0	0.			
				1.000260	0.79	8060 km

^aA run for which the term $\sqrt{1+z'^2}$ was removed from the integral equation formulation. See discussion in Section 2.

^bA case for which all values of the conductivity along the path were halved.

^c(∞) for S_z indicates a case for smooth earth calculation, ie, $z=z'=z''=0$.

used 1.0 kilometers and a short test calculation was run with $\Delta x = 0.45$ kilometers. For all but the last calculation the index of refraction of air was taken as 1.000338 and the ratio of earth's radius to effective radius was taken as 0.85. These essentially empirical values have been extensively employed in previous applications of the integral equation program (Reference 5-3). From the section on weather data, it can be seen (Figure 3-1) that these two values are not consistent with the theory based on the linear gradient of the refractive index, since $\eta = 1.000200$ would correspond to $a/a_e = 0.85$, and $\eta = 1.000338$ would require $a/a_e = 0.67$. As discussed in Section 3 and in the recommendations, a methodology for incorporating nonlinear gradients of the atmospheric refractive index would be required to permit proper treatment of the refractive index and its variations.

5-3. Horowitz, S., *User's Guide for ESD Loran Grid Prediction Program*, RADC-TR-77-407, December 1977.

The predicted secondary phase at the original nine observational sites are shown in Table 5-5 for the ten different cases in Table 5-4. For column 1, case 1, $\Delta x \sim 1.0$ km and only the elevation profile was smoothed with an averaging distance of 2.2 kilometers. The conditions for the calculations in the second column were identical to those of the first column except that Δx was decreased from ~ 1.0 km to ~ 0.9 km. The changes ranged from one nanosecond for Friant to 23 ns at Livermore (the 56 ns change at Delilah will be ignored since no data was collected at these). It should be noted that the differences are both positive and negative.

For the calculations in column 3, the smoothing distance was increased to 6 km. This further smoothing of the topography tends to decrease the secondary phase. The computed secondary phase as a function of distance for this case is shown in Figure 5-6. The experimental data points are also shown on the figure. The sensitivity to integration step size is still inherent in the computer program. This can be seen from the three computed points in column 4 where the step size was halved. We have chosen to use case 3 as the base case in subsequent comparisons with measured data. Similar conclusions would result from choosing case 1, 2, 4, or 6.

Table 5-5. Computed secondary phase in nanoseconds at the original Worst Case Path data sites for the different calculational conditions given in Table 5-4.

Site \ Case	1	2	3	4	5	6	7	8	9	10
Tecopa	1313	1292	1224	1240	1222	1222	1208	1572	950	1215
Death Valley	1788	1797	1679	1679	1677	1667	1460	2139	1307	1663
Darwin	1964	1953	1851	1870	1844	1854	1646	2335	1580	1822
Delilah	3624	3680	3442		3427	3505	3290	4196	2518	3384
Friant	3743	3742	3616		3602	3614	3394	4379	2811	3554
Merced	3608	3620	3510		3496	3506	3309	4213	2883	3441
Crows Landing	3706	3713	3613		3600	3615	3396	4326	3101	3536
Livermore	4038	4061	3949		3936	3951	3774	4711	3384	3865
Fort Cronkhite	4198	4187	4048		4035	4049	3726	4840	3563	3957

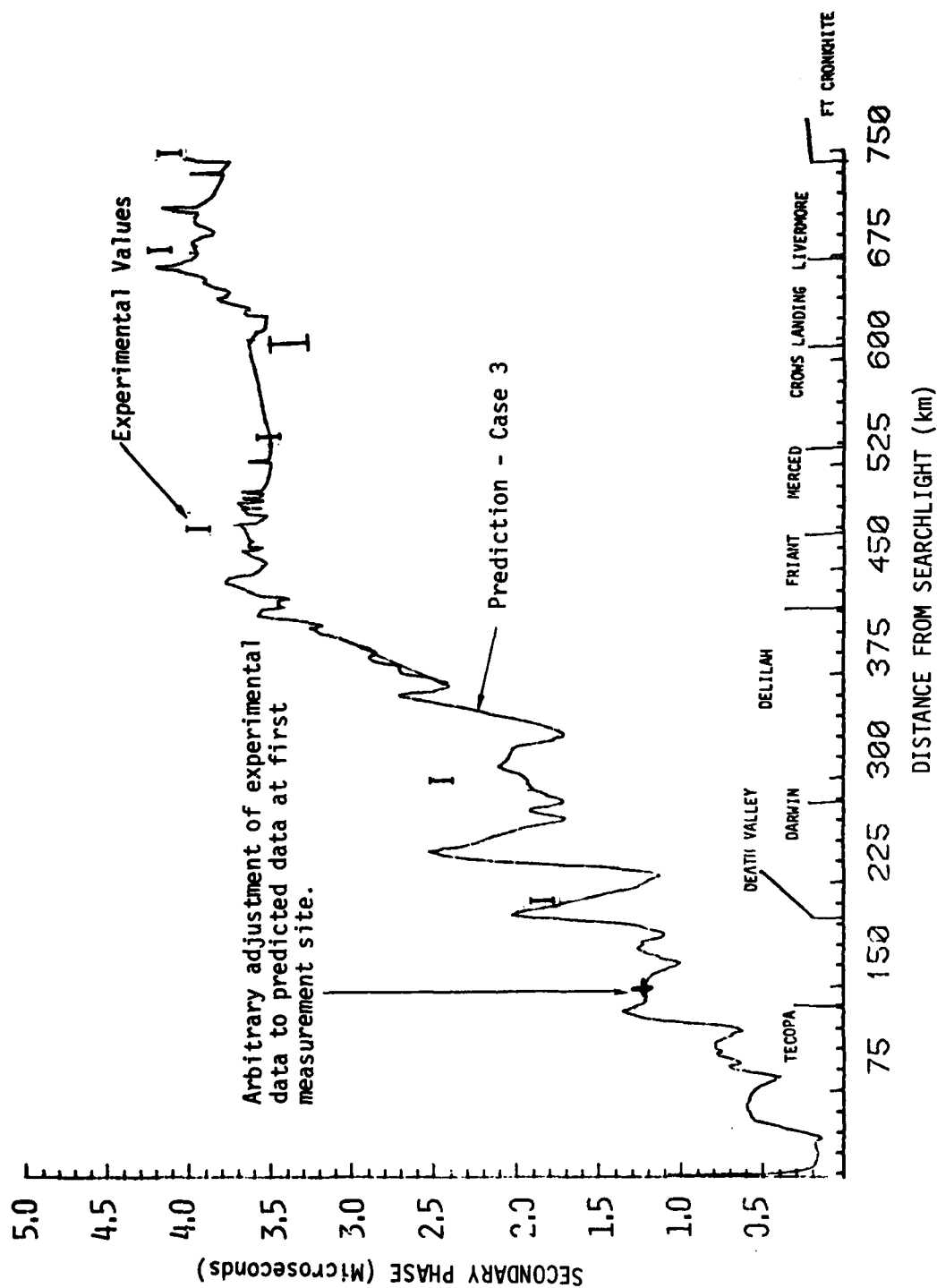


Figure 5-6. Secondary phase along the worst case path
 $S = 3$, $\Delta X = 0.9$ km.

Case 5 is a special one for which the integration routine was modified to eliminate the factor $\sqrt{1 + (z')^{-2}}$ in the integrand (see Equation 2-9). As pointed out in our discussion, this factor would not appear if more rigor had been used in the derivation of the integral equation techniques. However, for the degree of smoothing, this term has been rendered negligible as can be seen by comparing columns 3 and 5. The effect is a net decrease of ~ 13 to 15 ns from Darwin out to Fort Cronkhite.

For case 6, the smoothing was applied to the surface impedance as well as the height profile. Comparing these results to those in column 3 shows that for most of the points, the smoothing of the impedance introduces a negligible change in the computed phase. The one exception is Delilah where there is a very rapid fluctuation in the impedance. This fluctuation is almost eliminated by the smoothing technique applied.

The calculations for column 7 indicate the effect of smoothing both the height profile and the surface impedance over a larger distance, in this case 30 km. The first three data points are almost unchanged, but the smoothing of the high mountain region decreases the phase by 300 ns by the time Fort Cronkhite is reached. Part of the decrease apparently resulted because the smoothing significantly reduced the altitude of the highest peaks.

The purpose of case 7 was to test the conjecture that a crude model of the terrain, while not reproducing the detailed phase variations, would provide an estimate of terrain effects in regions well beyond (ie, on the receiver side) large terrain features. It can be seen by comparing with case 9, where terrain effects were suppressed, and with experimental results that this crude representation of the terrain is a significant improvement over ignoring terrain effects altogether.

Case 8 indicates the strong dependence of the additive phase on the estimate of the surface and subsurface conductivity. For this case, all values of the conductivity were decreased by a factor of

two. This has a negligible effect for those regions where the conductivity is very high (like sea water) but has a large integrated effect in the low and intermediate conductivity regions. There is an immediate ~ 350 ns increase in the computed phase at Tecopa and an 800 ns increase at Livermore and Fort Cronkhite. The computed secondary phase for this case is also shown in Figure 5-7 (upper curve). The curve for case 3 and experimental data are also shown for reference. Obviously small adjustments in the choice of material conductivity could be used to make the theory and experiment match.

Case 9 was a special case with $z = z' = z'' = 0$, ie, a smooth earth calculation with worst case path impedance. It can be seen, by comparing with column 3, that the net effect of including the height profile is to increase the additive phase. The largest change occurs at Delilah and then tends to decrease with increasing distance.

The final example, column 10, was calculated using an index of refraction $n = 1.000260$ and $a/a_e = 0.79$. The value for the index of refraction was obtained by taking into account the weather conditions along the path and the fact that the path is well above sea level. An air pressure of 870 mb was used instead of 1000 mb. The increased effective earth radius produces a progressive decrease in the additive phase as a function of distance. The net change at Fort Cronkhite is 91 ns. To this decrease must be added the decrease in the primary phase obtained from using the lower value of the index of refraction. This was listed earlier in Table 5-1. For Fort Cronkhite there is a phase reduction of 195 ns for a net decrease of 286 ns. Obviously, the total calculated phase is strongly dependent on the value of the index of refraction and the effective earth radius values as well as on the conductivity and elevation profile along the propagation path.

COMPARISON BETWEEN PREDICTED AND MEASURED VALUES

The measured results have been shown graphically for comparison with various predictions. Table 5-6 is a compilation of measured and predicted results, using case 3 (Table 5-5) as the base case prediction.

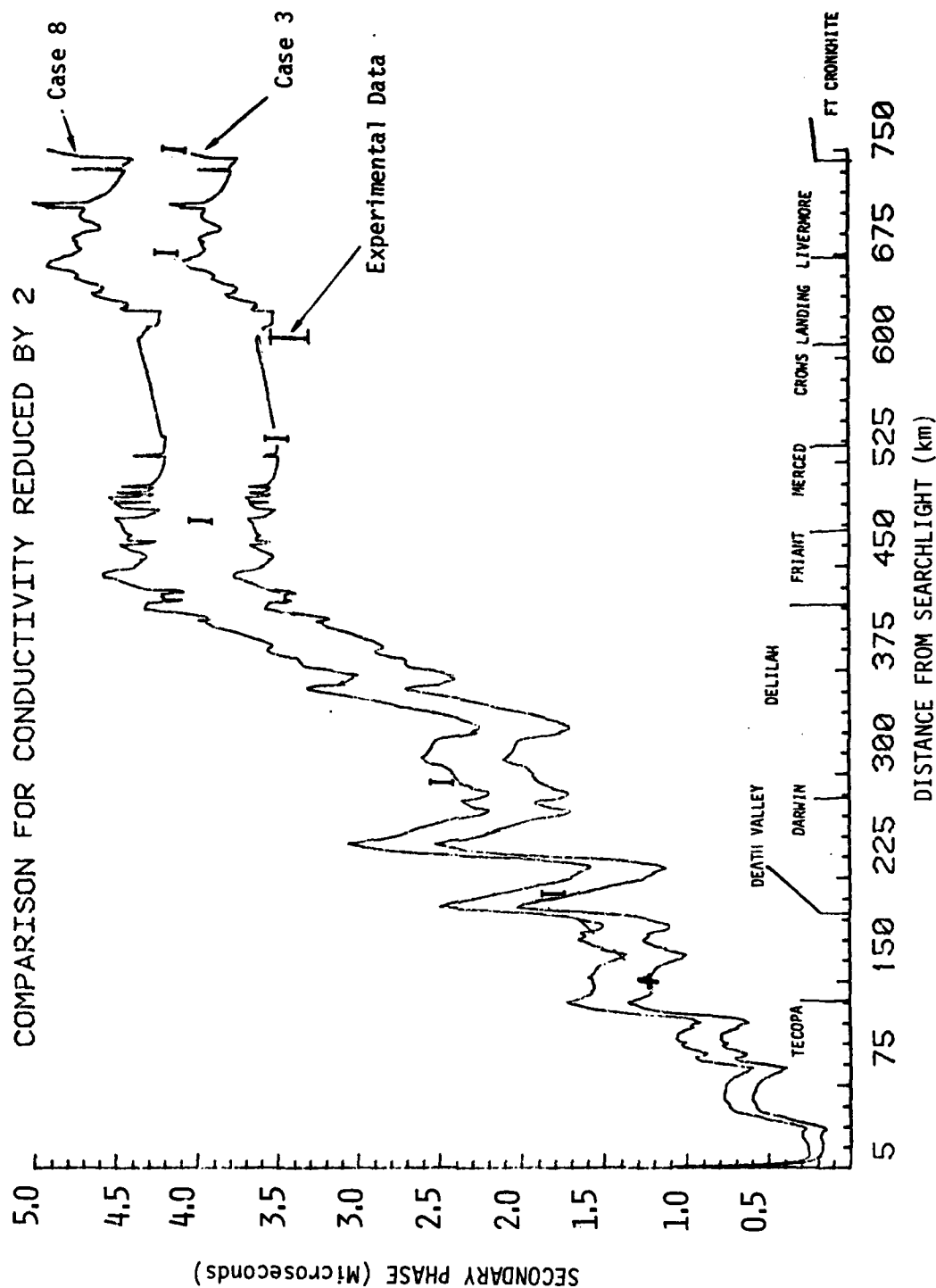


Figure 5-7. Computed secondary phase on worst case path, $S = 6$ km, $\Delta X = 0.9$ km comparing effect of original impedance to that for which each conductivity value was reduced by a factor of 2.

Shown in the table are time of arrival, incremental (site-to-site) changes in the time of arrival, secondary phase and incremental (site-to-site) changes in secondary phase. Since there is no absolute reference for measured TOA's, we were forced to choose one. Both time of arrival and secondary phase values have been arbitrarily adjusted to match predictions at Tecopa. Other choices, such as minimizing the square difference between measured and predicted values could also be used. Any other choice would not change our basic conclusions. The meaningful comparisons are between measured and predicted incremental TOA's.

After the first two or three sites the differences between measured and predicted incremental values are as large or larger than the differences between measured and predicted cumulative values, ie, there is no error buildup. This is attributed to the highly variable terrain and impedance and the sensitivity of both measured and predicted values to local variations. The effects of local variations, while strongly affecting the local measurement or prediction tend to average out for observations or predictions further down the path.

The good agreement between measured and predicted values at Ft. Cronkhite is of course dependent on the choice of the origin for the cumulative predictions and thus may be considered fortuitous. However, we do expect predictions to be better in a region beyond a significant terrain feature than at locations where terrain and impedance features are varying rapidly.

In general, the combination of measurement error and the difference between measurements and predictions were in the vicinity of a half microsecond. The probable measurement error was significantly smaller than a half microsecond, with the possible exception of the Livermore/Crows Landing measurement.

Finally, it should be noted that the difference between measurements and predictions can be made very small by small adjustments of impedance value. Figure 5-7 clearly illustrates this possibility. The predicted phase value for the original impedance values and for an increase of about $\sqrt{2}$ in impedance magnitude bracket the measured results.

Table 5-6. Comparison of predicted (case 3) and measured results from the worst case path.

Site	Time of Arrival (us)			Incremental Time of Arrival (us)			Secondary Phase (ns)			Incremental Secondary Phase (ns)		
	Measured	Predicted	Measured-Predicted (Mean Value)	Measured	Predicted	Measured-Predicted (Mean Value)	Measured	Predicted	Measured-Predicted (Mean Value)	Measured	Predicted	Measured-Predicted (Mean Value)
Tecopa	451.286*	457.286		-	-	-	1224	1224*		-	-	-
Death Valley	673.962+	673.867	0.151	216.676+	216.581	0.151	1774+	1679	151	550+	455	151
Darwin	674.073			216.787			1885			661		
	942.521+	941.942	0.612	268.448+	268.075	0.462	2430+	1851	612	545+	172	462
	942.587			268.625			2496			722		
Friant	1599.817+	1599.491	0.344	657.230+	657.549	-0.269	3942+	3616	344	1446+	1765	-269
	1599.852			657.331			3977			1547		
Merced	1804.561+	1804.623	-0.036	204.709+	205.132	-0.379	3448+	3510	-36	-529+	-106	-379
	1804.614			204.797			3501			-441		
Crows Landing	2043.689+	2044.023	-0.208	239.075+	239.400	-0.172	3279+	3613	-208	-222+	103	-172
	2043.942			239.381			3532			84		
Livermore	2253.290+	2253.107	0.299	209.348+	209.084	0.436	4132+	3949	229	601+	331	442
	2253.381			209.692			4223			945		
Fort Cronkhite	2495.611+	2495.602	0.033	242.232+	242.495	-0.197	4060+	4048	33	-164+	99	-197
	2495.655			242.364			4101			-32		

*Arbitrarily adjusted to predicted value for Tecopa.

COMPARISON BETWEEN MILLINGTON'S TECHNIQUE AND THE INTEGRAL EQUATION METHOD

A set of comparison test calculations were made using Millington's technique and HUFLOC for the Worst Case Path. The Millington method was used to calculate both the phase and amplitude of the attenuation function using a twelve segment approximation for the worst case path impedance. The amplitude of the approximate surface impedance is shown in Figure 5-8 as the heavy line against the surface impedance used by HUFLOC for the worst case path. The computed secondary phase is shown in Figure 5-9 where it is compared to the reference case integral equation results. As in the previous figures the experimental data are referenced to the predicted value of Tecopa, using case 3 (Table 5-5). If the experimental data was referenced to the Millington calculation for Tecopa, all the experimental points would be lowered by ~ 400 ns. The integral equation calculation would still appear as the better prediction however. The log of the amplitude of W, calculated using Millington's technique is compared to the reference case in Figure 5-10. From this comparison it appears that the average long range attenuation is primarily a function of the surface impedance for the integral calculation although the topography does cause rapid local fluctuations.

As an additional test, the terrain profile was suppressed in the HUFLOC calculation, ie, $z = z' = z'' = 0$. The results of this run and the Millington calculation are shown in Figure 5-11. It can be seen that the rapid changes in the original worst case path impedance produce, on the average, only local fluctuations in the secondary phase.

Optimization With Millington's Technique

A procedure similar to the U.S. Coast Guard procedure for optimizing impedance maps was used to adjust the impedance to minimize the standard deviation between predicted and measured value at the first seven measurement sites. In this procedure, the surface impedance of the segments is allowed to vary in an iterative calculation and impedance values are determined that minimize the rms error between measured and predicted results. The impedance results are shown in Figure 5-12.

SURFACE IMPEDANCE
(12 SEGMENT MILLINGTON APPROXIMATION
INDICATED BY HEAVY LINES)

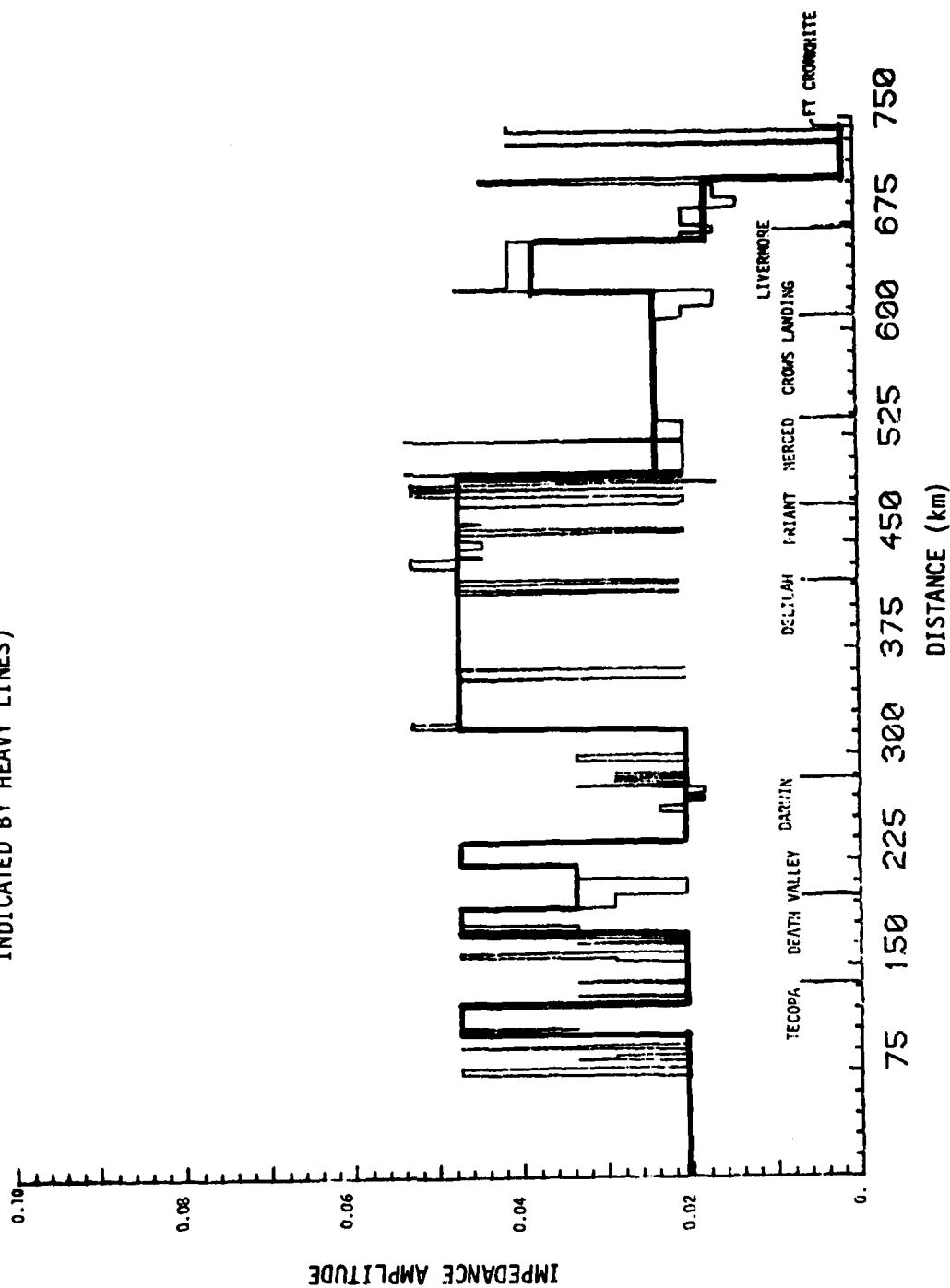


Figure 5-8. Approximation to the surface impedance for a Millington calculation.

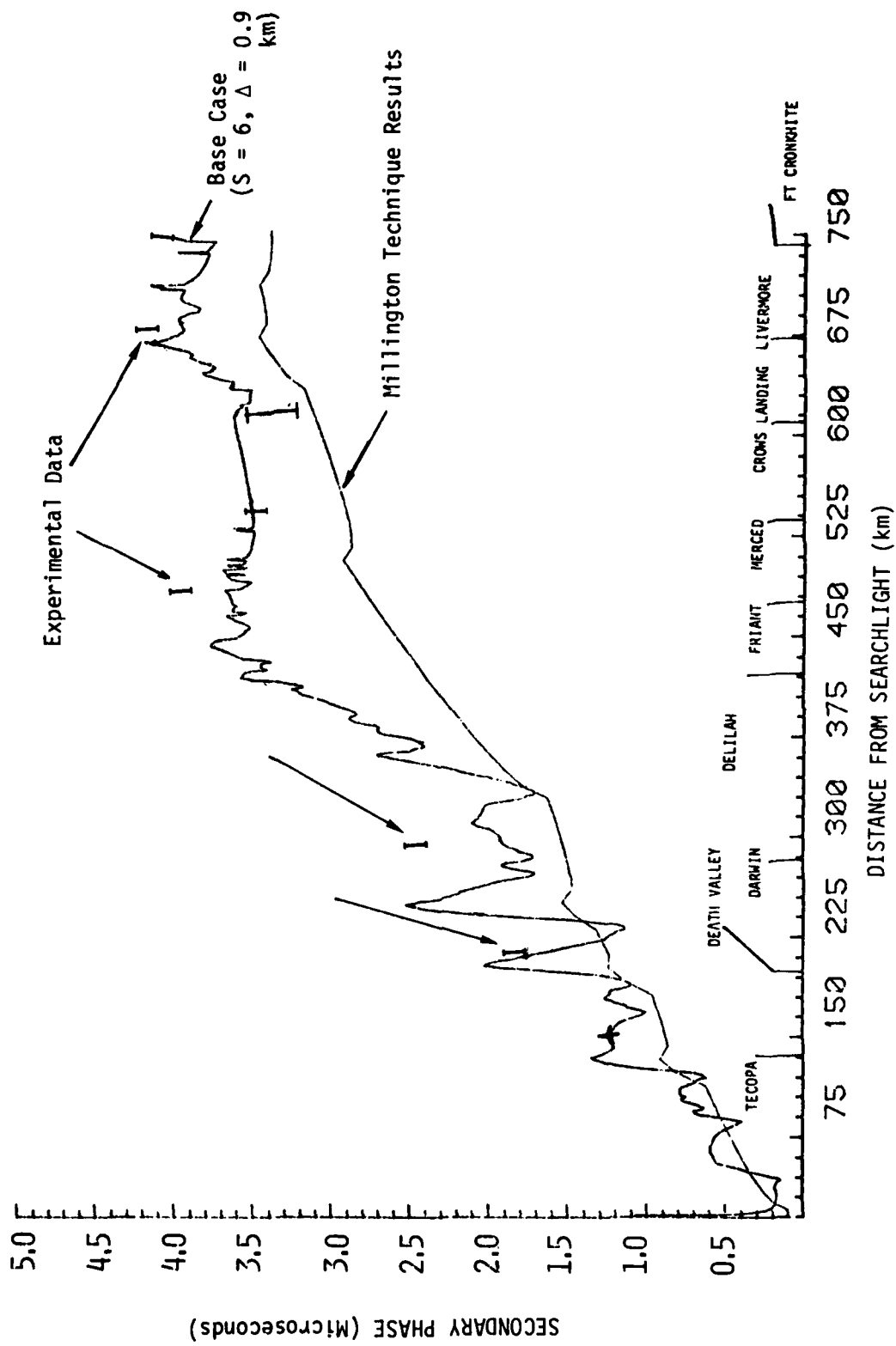


Figure 5-9. Comparison between the integral equation and Millington's Technique results.

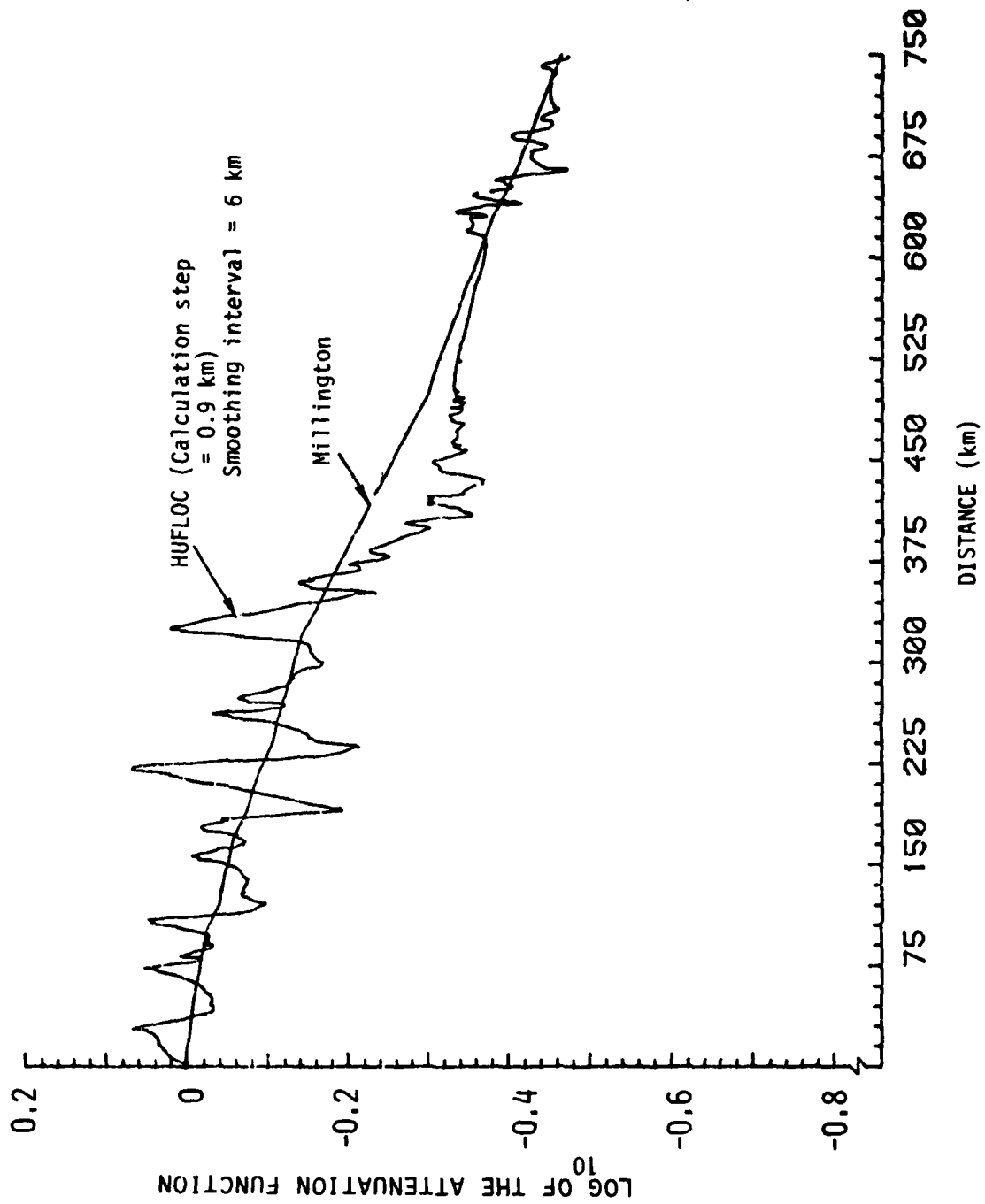


Figure 5-10. Comparison of HUFLOC and Millington amplitude calculation results for worst case path.

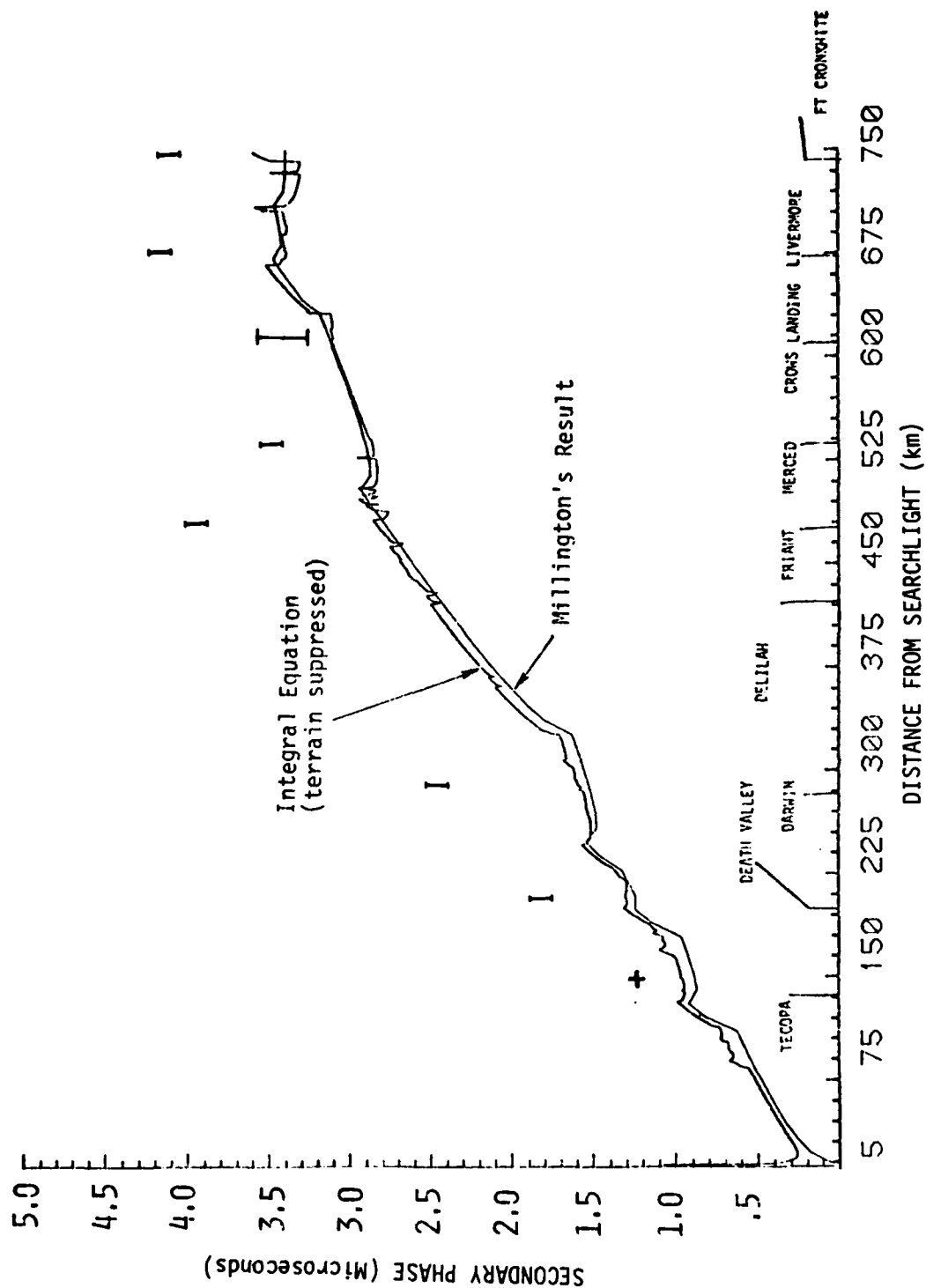


Figure 5-11. Comparison of Millington's technique with the integral equation technique (with terrain variations suppressed).

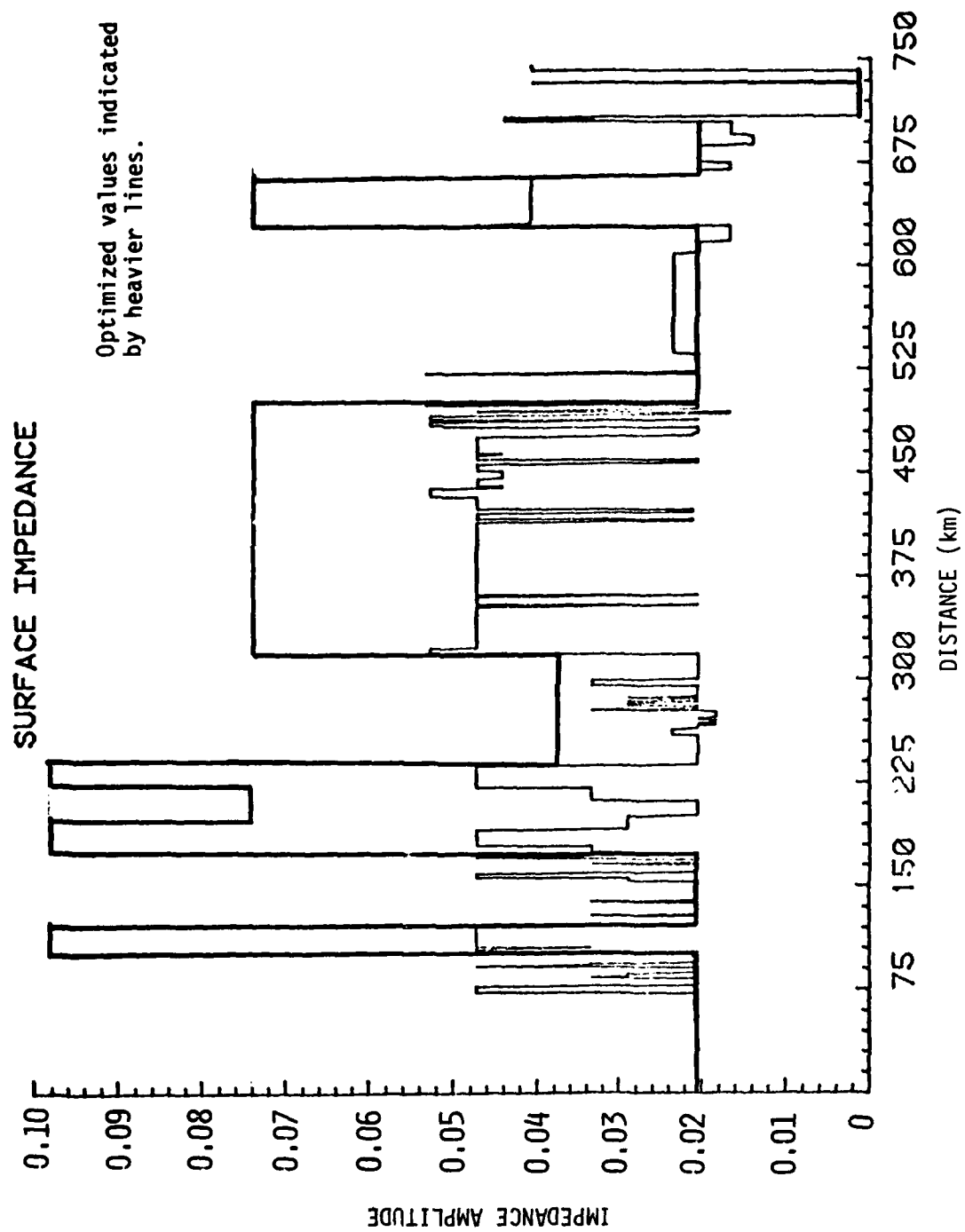


Figure 5-12. Results of Millington's impedance optimization.

The secondary phase predictions are shown as filled circles on Figure 5-13. The results indicate that impedance adjustment can be utilized to compensate for terrain induced variations.

COMPARISON WITH USCG CONDUCTIVITY MAP

The impedance profile along the WCP was approximated using the USCG conductivity map for the West Coast Chain and the secondary phase calculated using Millington technique. The original secondary phase prediction calculated by Millington's technique using the USCG conductivity values was about 1 microsecond higher than the more detailed predictions along the WCP. The large difference occurred because we used a lapse rate of 0.85 while the USCG conductivity fit is derived from secondary phase data calculated for a lapse rate of 0.75. Performing the calculation with a lapse rate of 0.75 produced much better agreement between the integral equation results and Millington results, although the Millington results are still high. Table 5-7 shows the HUFLOC base case predictions, measured values, total secondary phase values using Millington's technique for lapse rates of 0.75 and 0.85, and additional secondary phase values for a lapse rate of 0.75. USCG predicted values for the ASF are also shown (Reference 5-3). Our predicted ASF values are still higher than the USCG values. This could be explained by a difference in segment length for conductivity area obtained from the conductivity map.

This comparison exercise indicates that using the best estimate of the actual lapse rate during the calibration period would improve the accuracy of conductivity estimates.

5-3. Private communication. Comment on Report GE78TMP-51, transmitted via Mr. L.D. Dowdy, contracting officer, October 1978.

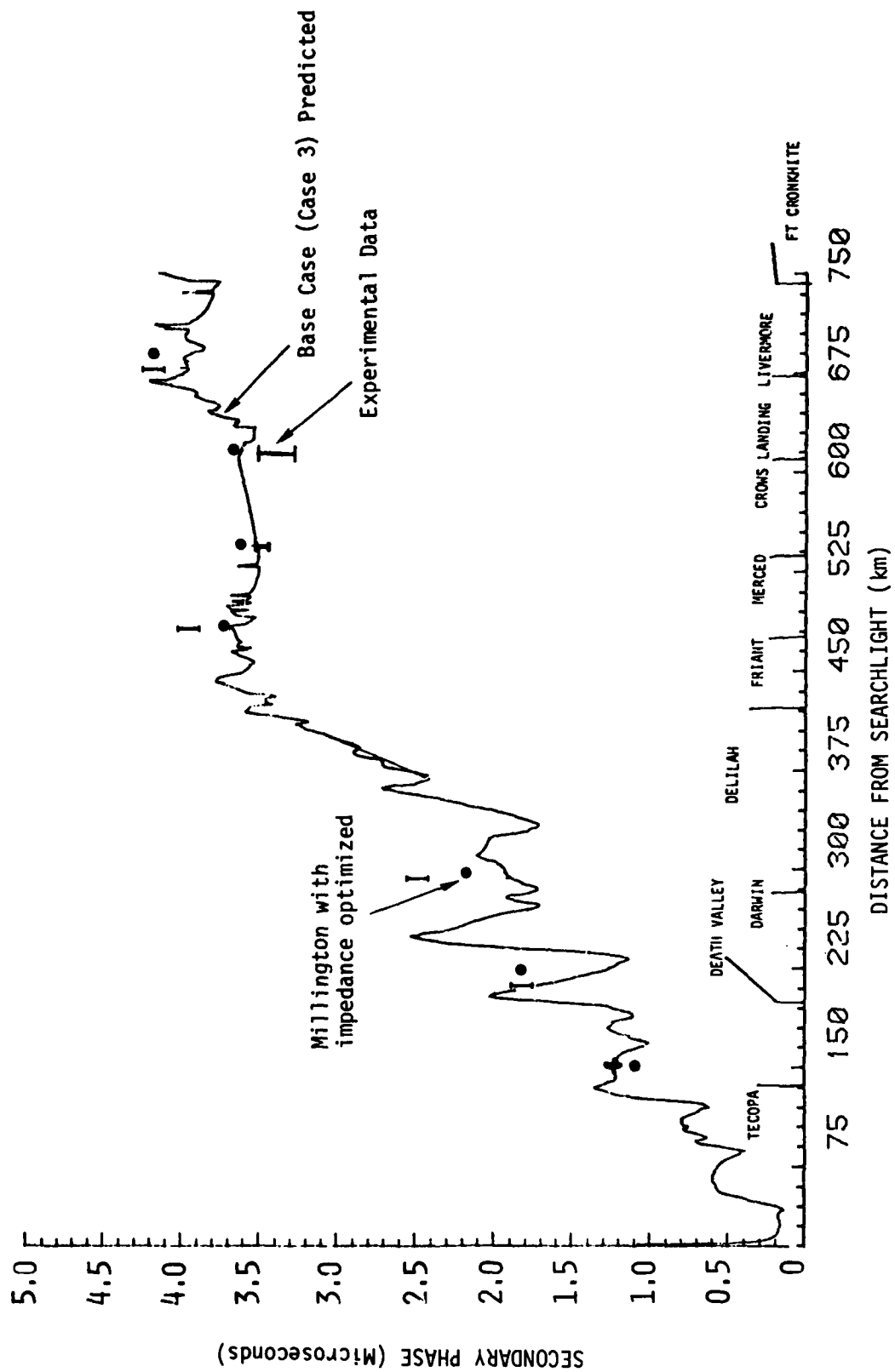


Figure 5-13. Comparison of Millington with impedance optimized and experimental results.

Table 5-7. Secondary phase (ns) relative to Tecopa.
Derived from USCG conductivity map.

Site	Base Case Prediction (Case-HUFLOC)	Measured (Mean Value)	Secondary Phase Values		Additional Secondary Phase Values	
			Millington's Phase Using USCG Conductivity Map $\alpha=0.85$	Millington's Phase Using USCG Conductivity Map $\alpha=0.75$	Millington's Values ($\alpha=0.75$) Less Seawater Values	USCG Value
Death Valley	455	605	430	411	320	292
Darwin	627	1254	1550	1478	1260	1086
Friant	2392	2735	2270	2092	1507	1422
Merced	2286	2250	2310	2122	1411	1136
Crows Landing	2389	2181	2470	2350	1493	1231
Livermore	2725	2953	3000	2798	1803	1675
Ft. Cronkhite	2824	2856	3300	3041	1895	1686

SECTION 6

PREPARATION OF HARBOR GRID

One of the experiments using the U.S. West Coast chain was designed to acquire data to calibrate San Francisco Harbor. This section describes some of the initial predictions that were made to assist in planning the San Francisco Harbor Calibration Experiment. A summary of results for the Harbor Experiment is also included.

INITIAL PROCEDURES - SIMPLIFIED PREDICTIONS USING LOCAL DISTURBANCES

There are two primary effects that may distort the TDX-TDY grid lines in the region of San Francisco Harbor. The more widespread of these two effects is the result of propagation path properties changing abruptly when the path makes the transition from land into San Francisco Bay. At the land-sea transition the secondary phase undergoes a rapid decrease as is illustrated by a simple example in Figure 6-1. For a homogeneous path, the secondary phase increases almost linearly with distance. In the figure, the distance measure is in kilometers from the land-sea transition. At the transition the phase suddenly drops by over 100 ns and is just beginning to increase with distance again 45 kilometers from the coastal transition. This behavior is typical of all transitions from a higher to lower surface impedance. For the land to sea ($\sigma = 5$ mho/m) transition the difference between the all land path and the land to sea path is primarily a function of the land conductivity and only weakly dependent on the distance from the transmitter to the transition as long as this distance is greater than ~ 100 km. Figure 6-2 shows the calculated difference as a function of distance from the transition for $\sigma_g = .002$ and $.005$ mho/m. This transition effect was employed to calculate the first order spatial anomalies relative to an idealized TDX-TDY grid for the San Francisco Bay area.

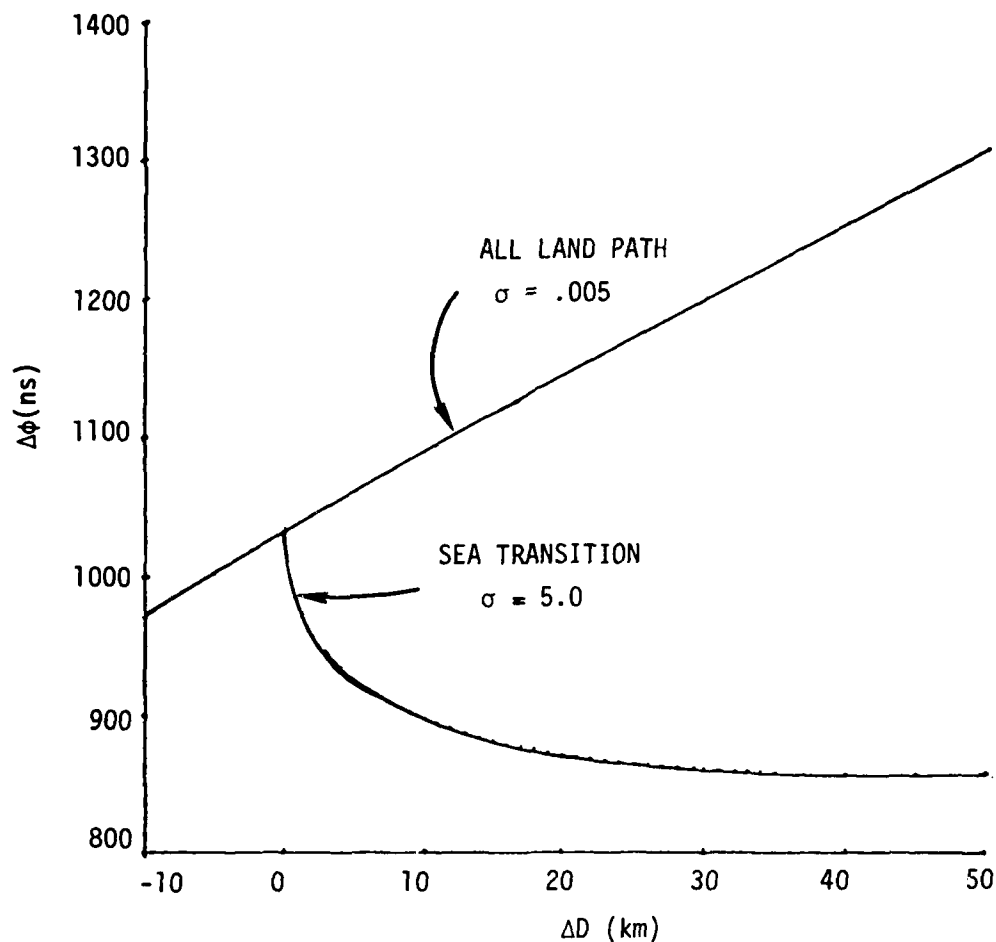


Figure 6-1. Effect of a land sea interface on the secondary phase.

The second major perturbation to the LORAN-C signals is the system of major bridges which cross San Francisco Bay. Reflections from the bridges should produce a distortion in the phase in the neighborhood of the bridge. This effect has been investigated theoretically in an approximate way to estimate the magnitude and spatial extent of the phase perturbation.

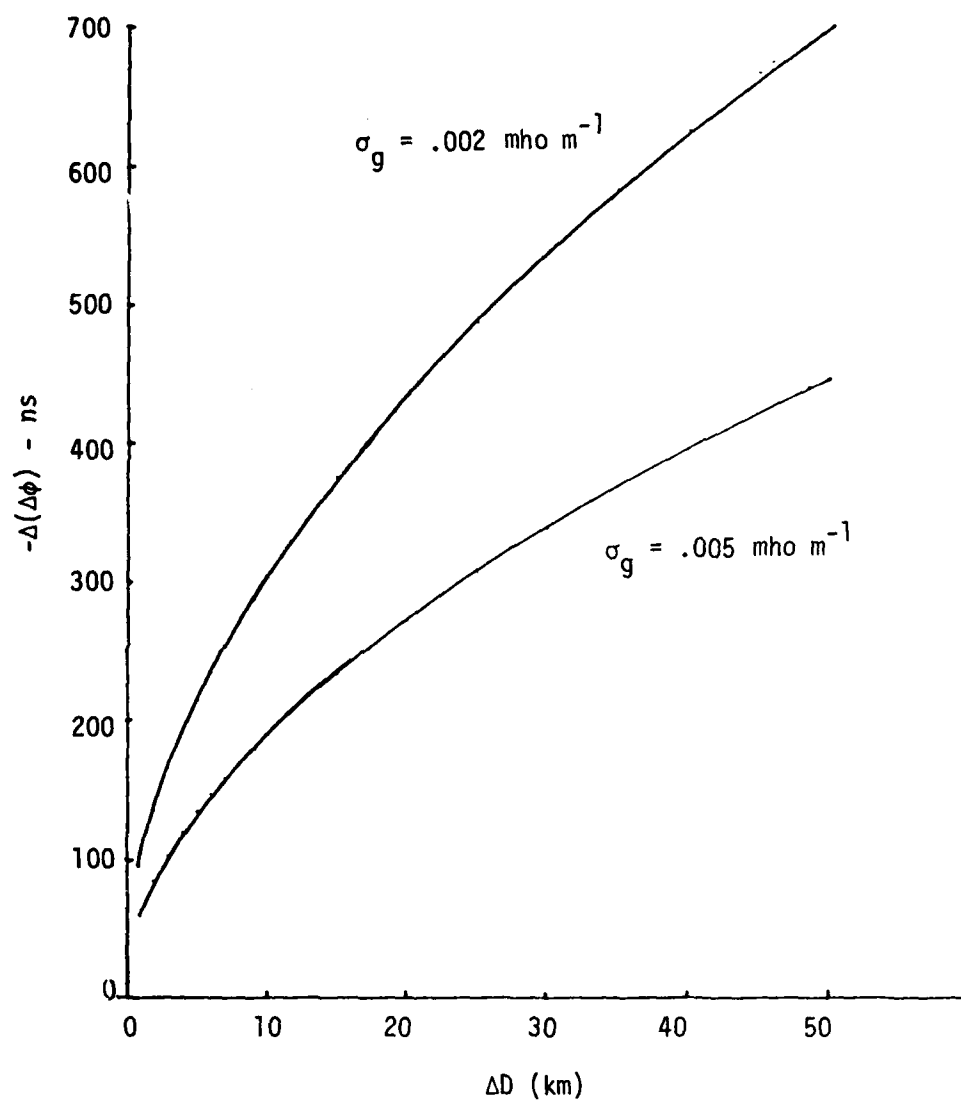


Figure 6-2. Phase change vs distance from the land sea transition.

Idealized Grid and Land-Sea Interface Distortions

To provide a visual aid for experiment planning, TEMPO prepared an idealized grid for the harbor. An idealized grid for the 2 LOPs is parameterized by 6 quantities; 4 average phase velocities and 2 emission delays. The time differences for any user position with latitude L and longitude λ are given by

$$\text{TDX}(L,\lambda) = E_X + d_X(L,\lambda)/\bar{V}_X - d_M(L,\lambda)/\bar{V}_{MX} \quad (6-1a)$$

$$\text{TDY}(L,\lambda) = E_Y + d_Y(L,\lambda)/\bar{V}_Y - d_M(L,\lambda)/\bar{V}_{MY} \quad (6-1b)$$

where

L = Latitude of user position

λ = Longitude of user position

E_X = Emission delay for X-ray (μs)

E_Y = Emission delay for Yankee (μs)

\bar{V}_{MX} = Average phase velocity from Master for TDX ($\text{km}/\mu\text{s}$)

\bar{V}_{MY}^* = Average phase velocity from Master for TDY ($\text{km}/\mu\text{s}$)

\bar{V}_X = Average phase velocity from X-ray ($\text{km}/\mu\text{s}$)

\bar{V}_Y = Average phase velocity from Yankee ($\text{km}/\mu\text{s}$)

$d_M(L,\lambda)$ = The geodetic distance to Master (km)

$d_X(L,\lambda)$ = The geodetic distance to X-ray (km)

$d_Y(L,\lambda)$ = The geodetic distance to Yankee (km)

Note that TD measurements at three positions (3 TDX, 3 TDY) are sufficient to determine all the parameters in the idealized model. When less than three measurements are available, parameters must be estimated by predictions or obtained from other sources. To obtain sufficient accuracy, in Equation 6.1, distances are computed using geodetic formulae for an ellipsoidal earth and as a result there is no closed form inverse (latitude, longitude, given TD's) of Equation 6-1.

*Obviously, in the real world, \bar{V}_{MX} and \bar{V}_{MY} must be equal, and they are treated so in this subsection. However, 6.1 can be used as a numerical fit to data, as it is in later sections and a better fit can be obtained by allowing $\bar{V}_{MX} \neq \bar{V}_{MY}$.

It must be solved by an iterative procedure which is started by calculating L_0 and λ_0 for a spherical earth for which a closed form solution exists. A Newton-Raphson iteration is then performed to solve for L and λ . This procedure is very powerful and usually converges in 2 or 3 iterations.

To obtain the necessary parameters for the initial idealized grid from available data, Ft. Cronkhite data and USCG chain calibration data were used. From the chain calibration data the values of the emission delays were determined by averaging TD data taken on the baseline extensions. The values obtained were

$$\begin{aligned} E_X &= 28094.467 \quad \mu s \\ E_Y &= 41967.620 \quad \mu s \end{aligned}$$

The phase velocity \bar{V}_Y was estimated using the phase predicted from the integral equation program for the Yankee path to Ft. Cronkhite. Then values were assigned to \bar{V}_X , \bar{V}_{MX} and \bar{V}_{MY} which, when adjusted for the land to sea interface effects, matched the Ft. Cronkhite data for TDX and TDY reasonably well. The phase velocities determined were

$$\begin{aligned} \bar{V}_{MX} &= \bar{V}_{MY} = \bar{V}_M = 0.299061 \quad \text{km}/\mu s \\ \bar{V}_X &= 0.298304 \quad \text{km}/\mu s \\ \bar{V}_Y &= 0.299150 \quad \text{km}/\mu s \end{aligned}$$

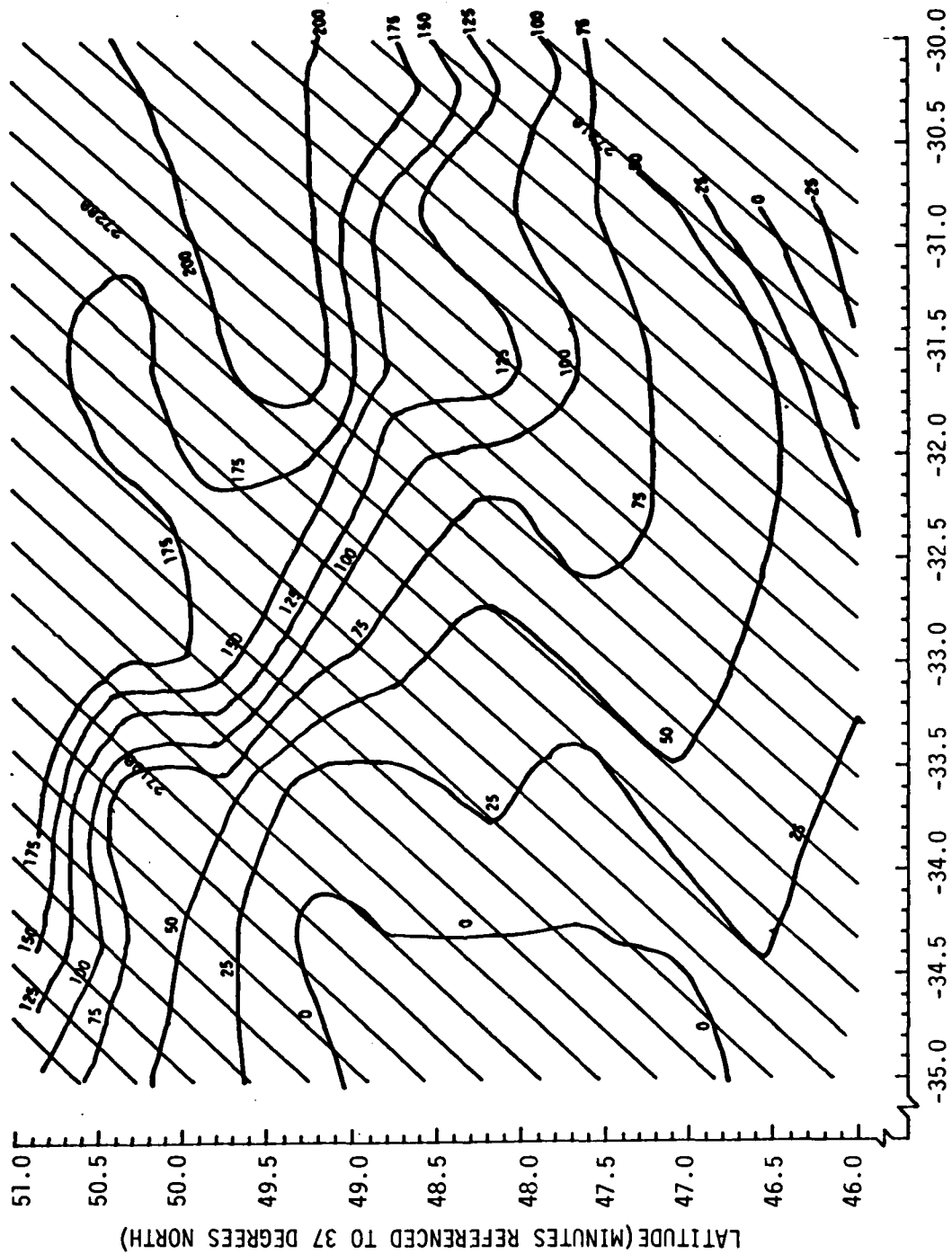
The above parameters were used with Equation 6-1 to prepare linear grids for the harbor. An example of this grid is shown in Figure 6-3.

To estimate the magnitude of spatial distortion relative to the idealized grid due to the land-sea interface, a Cartesian grid was drawn up over San Francisco harbor. The over water distance between each grid point and the shoreline was estimated for the propagation paths to the Master and X- and Y- transmitter of the Loran-C chain. These distances were converted to changes in TDX and TDY from the initial grid values using the data shown in Figure 6-2. For the Master and Y transmitter paths the curve calculated with $\sigma = 0.005$ mho/m ($\epsilon/\epsilon_0 = 12$) was used while the curve for $\sigma = 0.002$ mho/m ($\epsilon/\epsilon_0 = 12$)

was used for the X paths. Equal phase change contours were then computed by interpolating between the data obtained at the grid points. It is assumed, to a first approximation, that all transitions after the first would occur in pairs (at least for sea water points) and would approximately cancel. With these assumptions the first order corrections were easily obtained. It was found that the land-sea boundaries around San Francisco bay can produce large spatial anomalies in TDX and TDY that vary strongly with position.

Time difference error contours derived as described above are superimposed on the linear grids. Outside the Golden Gate bridge the TDX variation produced by the land-sea transition ranges from +200 ns to -25 ns while the TDY variation ranges between +50 ns to -75 ns (see Figures 6-4 and 6-5). It must be remembered that these variation contours have been calculated using only estimated distances and ignoring localized effects other than surface impedance variations. The predicted TDX distortion is negative throughout the inner harbor ranging from ~ -200 ns to ~ -400 ns. Again, the predicted TDY distortion is less than for TDX, ranging from ~ -75 ns to ~ +50 ns.

Although the assumption of a constant average phase velocity appears reasonable for the propagation paths to the master transmitter (Fallon) and to the Yankee transmitter (Searchlight), we anticipated that this assumption would very likely be poor for the X-ray path (Middletown). Investigation of conductivity maps suggest that even over the small variation in azimuth for a path from Middletown to positions in San Francisco Harbor, there is at least one major change in the path impedance. Due to the marshy nature of the northern end of San Pablo Bay it is also difficult to determine where the change from low to high conductivity occurs. This could lead to significant errors in estimation. The actual errors as determined by the fixed site data, and an explanation of the errors are discussed later in this section.



LONGITUDE (MINUTES REFERENCED TO 122 DEGREES WEST)

Figure 6-4. First order TDx variations (ns) produced by land sea boundary effect.

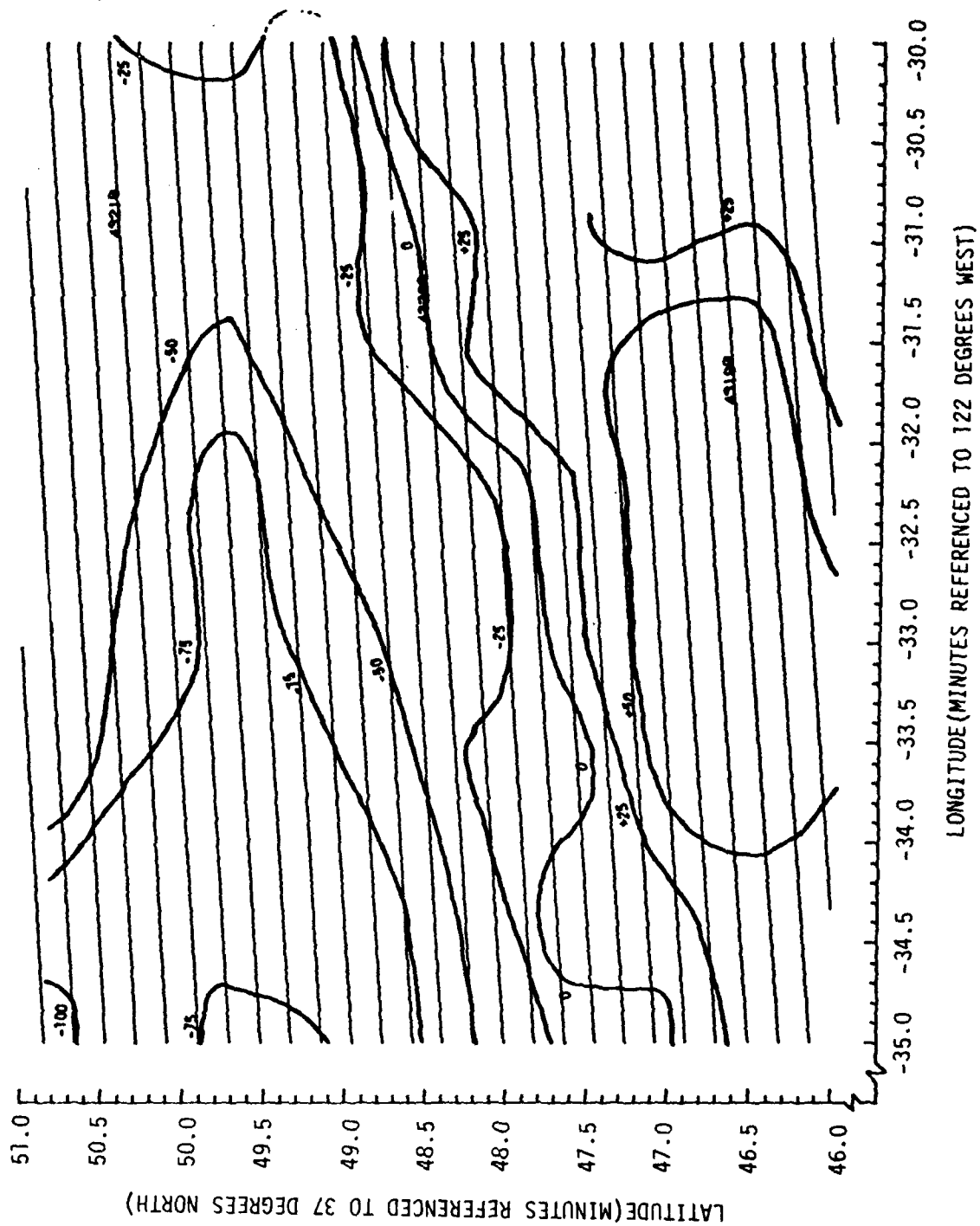


Figure 6-5. First order TDY variation (ns) produced by land sea boundary effect.

Phase Perturbations From Large Bridges

Several bridges cross San Francisco Bay shipping channels. These bridges are long enough and high enough so that their overall dimensions are an appreciable fraction of a wavelength at Loran-C frequencies ($\lambda = 3$ kilometers). Thus it might be expected that reflections from the bridges could produce phase distortions and hence errors in the received Loran-C signals, producing errors in the TOA's.

The following approximate calculations was carried out to investigate the magnitude and areal extent of the possible distortion. The Golden Gate bridge was used as a model. The bridge is 1380 meters long and the two main support towers are 230 meters high. These dimensions correspond to $\sim \lambda/2$ and $\lambda/12$ respectively. Steel cables extend across the tops of the support towers with the road bed suspended by closely spaced vertical steel wires.

As a first approximation for the scattering efficiency, the bridge is replaced by a perfectly conducting rectangular plate. The water surface is also assumed to be perfectly conducting. The scattering cross-section, σ , for a flat plate of length b and width h at normal incidence is given by

$$\sigma \approx 4\pi(bh/\lambda)^2 \quad \text{m}^2 \quad (6-2)$$

Because of the reflection in the water surface the dimension h is twice the height of the bridge, ie, $\lambda/6$; thus, one obtains

$$\sigma \approx \pi\lambda^2/36 \quad (6-3)$$

For $R \gg \lambda$ we would expect that the ratio of the scattered power P_s to the incident power, P_i would vary as

$$\frac{P_s}{P_i} \sim \frac{\sigma}{4\pi R^2} = \frac{\pi}{144} \left(\frac{\lambda}{R}\right)^2 \quad (6-4)$$

where R is the distance from the bridge in the same units as the wave length λ .

Near the bridge ($R \ll \lambda$), we would not expect the bridge to look like a perfectly conducting plate. The maximum value that P_s/P_i could attain would be unity. For this analysis we assume that the maximum value which can be attained is less than unity and given by

$$\left\langle \frac{P_s}{P_i} \right\rangle_{\max} \approx 4\pi(bh/\lambda^2)^2 \approx \frac{\pi}{36} \quad (6-5)$$

Then

$$\frac{P_s}{P_i} \approx \frac{\sigma}{\lambda^2 + 4\pi R^2} = \frac{\pi^2/36}{\pi + (kR)^2}, \quad k = \frac{2\pi}{\lambda} \quad (6-6)$$

rather than equation 6-1. With this approximation the ratio of the amplitudes of the scattered to incident electric field is given by

$$\left| \frac{E_s}{E_i} \right| = \left(\frac{P_s}{P_i} \right)^{1/2} \approx \frac{\pi/6}{\sqrt{\pi + (kR)^2}} \quad (6-7)$$

The phase fluctuation can be examined by summing two complex terms representing the incident and reflected waves. The incident E_i and scattered E_s waves can be represented by

$$E_i = E_o \exp(-ikR) \quad (6-8)$$

$$E_s = E_{so}(R) \exp(ikR + i\delta) \quad (6-9)$$

where

$$E_{so}(x) = \frac{E_o \pi/6}{\sqrt{\pi + (kR)^2}}$$

where δ is the phase change produced when the incident wave is scattered by the bridge and the time dependence $e^{i\omega_0 t}$ has been suppressed. Then the totals field at any distance R from the bridge is given by

$$E_T = E_i + E_s = E_o \exp(-ikR) \left\{ 1 + \frac{E_{so}}{E_o} \exp(2ikR + i\delta) \right\} \quad (6-10)$$

For a perfectly reflecting scatterer δ would equal to π radians and for this rough approximation we will use $\delta = \pi$. Then the phase fluctuation of a CW signal scattered backward by the bridge is given by

$$\Delta\phi = \text{Phase} \left\{ 1 + \frac{E_{so}}{E_o} \exp (2ikR + i\delta) \right\} \quad (6-11)$$

This phase fluctuation in nanoseconds has been calculated as a function of x and is shown as the dotted line in Figure 6-6. The two horizontal lines in the figure indicate the ± 50 ns region. If the wave were incident at an oblique angle, then the spatial period of the fluctuations might be expected to decrease.

The results so far derived have not taken into account the fact that Loran-C operates in a pulsed mode rather than in a CW-mode. Further, the measurements are made at a zero crossing approximately $30 \mu s$ from the beginning of the pulse. Therefore, if the round trip time between the observation point and the reflection point is greater than $30 \mu s$, there will be no interference. To see how this affects the results obtained above, assume that the envelop of the Loran-C pulse is given by

$$f(t) = t^2 \exp (-2t/65) \quad (6-12)$$

where t is the time in μs . Then E_{so} must now be represented by

$$E_{so}(x) = \frac{E_o \pi/6}{\sqrt{\pi + (kx)^2}} \begin{cases} f(\tau)/f(30) & \tau = 30 - \frac{2x\eta}{c} > 0 \\ 0 & \tau \leq 0 \end{cases} \quad (6-13)$$

Using this functional dependence rather than that given by Equation 6-8 the solid curve in Figure 6-6 was computed. The pulse processing at approximately the third zero crossing decreases the magnitude and extent of the phase perturbation.

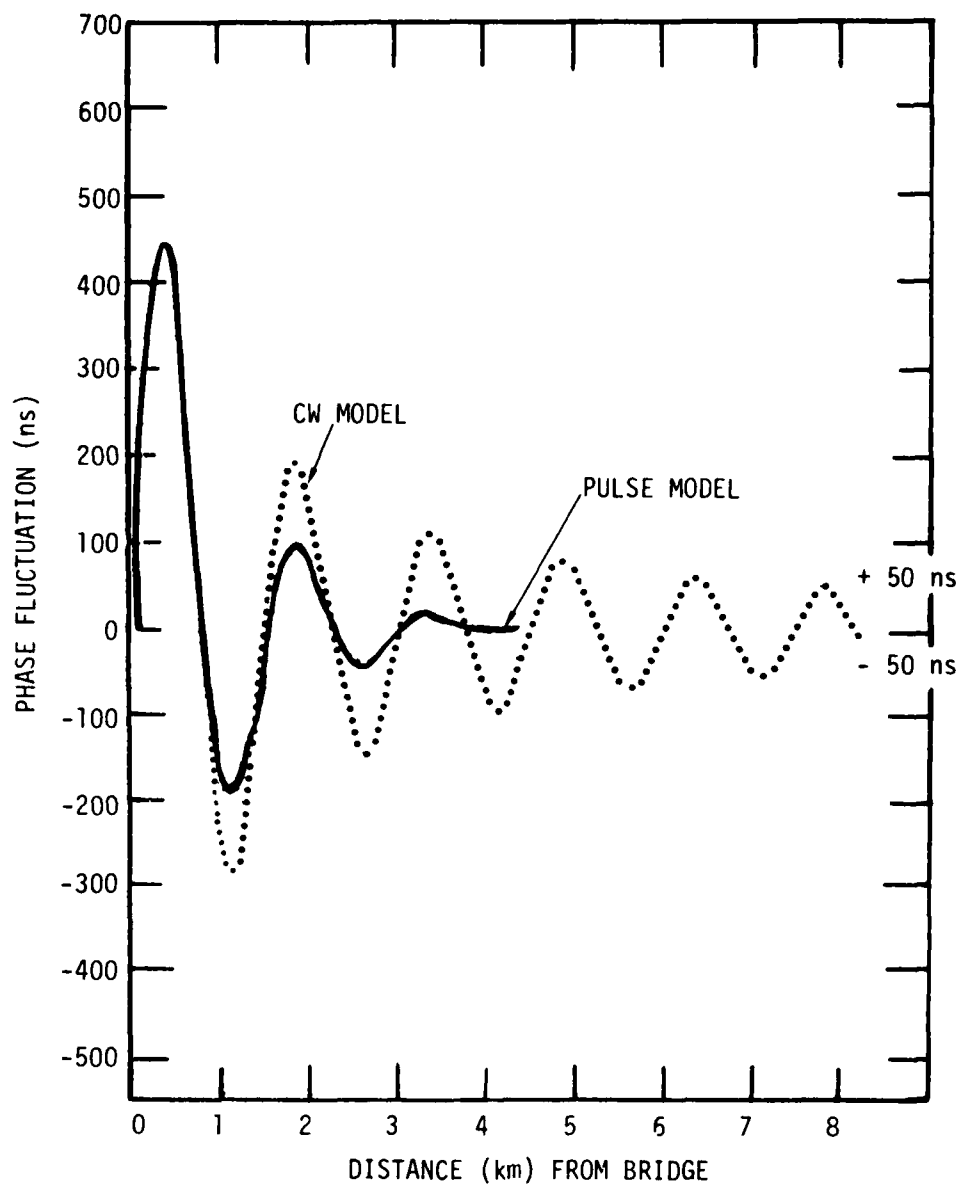


Figure 6-6. Phase error produced by reflection from Golden Gate Bridge.

HARBOR EXPERIMENT

The San Francisco Harbor Experiment was designed to provide data for an evaluation of the potential use of Loran-C for high accuracy, all-weather navigation in a harbor and harbor entrance environment. Specifically, data were obtained to evaluate three modes of Loran-C navigation; normal, repeatable and differential. Procedures used in the evaluation were to prepare a Loran-C grid using fixed site data, to compare vessel position as measured by the Trisponder positioning system and Loran-C, and to display TD errors versus position.

The harbor experiment was divided into three parts: a planning phase, described previously, a land-based data collection at various sites around the periphery of the harbor, and a vessel data collection made on board the U.S. Geological Survey Research Vessel Polaris throughout the harbor.

Fixed Site Data

The land harbor measurements were made using five receivers in three deployments of approximately one week each. Since two sites were visited twice, data were collected at a total of thirteen sites. TOA and TD measurements were made on board the Polaris while steaming the major shipping lanes in San Francisco harbor. Figure 6-7 shows the land sites and an outline of the areas covered by the Polaris. The crosses represent deployment 1 sites, the circles represent deployment 2 sites, the triangles represent deployment 3 sites, and the squares represent sites which were common to deployments 2 and 3. The vessel position was accurately* obtained using a short baseline, microwave positioning system, the Trisponder system.

The analysis method used was to use some of the fixed set data to prepare an idealized grid and to compare data taken at other sites with values predicted using the grid. A thorough discussion of the

*Accuracy requirements were determined by examining data collected at Ft. Cronkhite between August 3, 1977 and November 1, 1977.

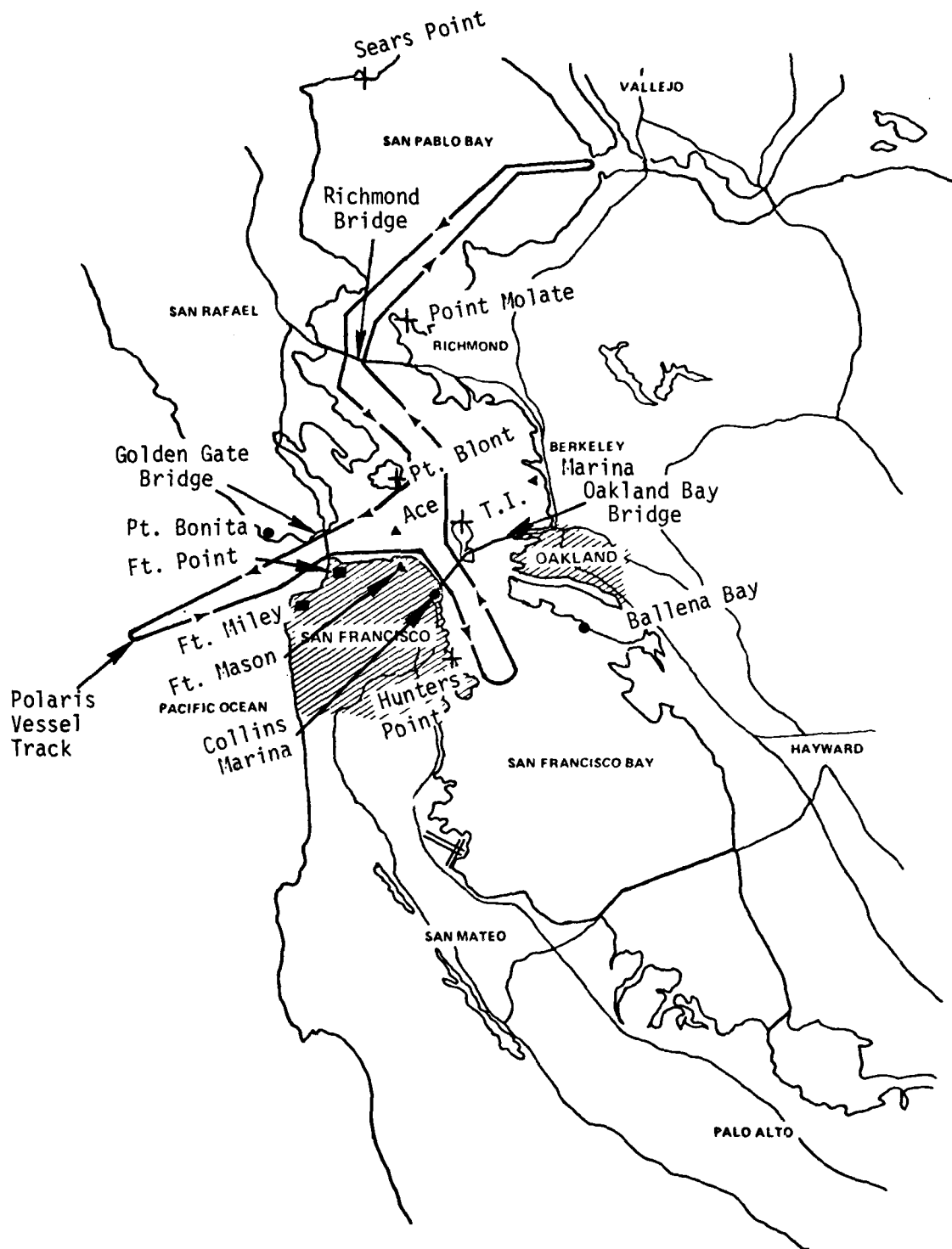


Figure 6-7. San Francisco Harbor test area.

various methods used to derive the parameters for the idealized grid and the explanation of the observed variations between grid position and actual position is provided in Reference 6-1. A summary of the results is provided here.

The measured time differences at the fixed sites were compared to idealized grids derived using the following data:

- a. The original parameter estimates determined during the planning phase.
- b. Fixed site data taken at Fort Cronkhite, Sears Point, Ballena Bay and Berkeley Marina. (See Figure 6-7). The data chosen for determining the parameters resulted in using all overland paths.
- c. Fixed site data from both on-shore and mid-harbor data (Sears Point, Alcatraz Island and Fort Miley)
- d. Data from all thirteen fixed sites, with parameters chosen to minimize the mean square difference between measured and grid-predicted values at the measurement sites.

The idealized grids progressively improved from (a) through (d). The results are summarized in Table 6-1 which shows the site name, the distance from the site to the three transmitters, the mean measured time difference, the predicted time difference from the idealized grid, and the differences between grid and measured values.

Note that for the least squares fit, the standard deviations of TDX and TDY error (grid value - measured value) are 111 and 81 nanoseconds, respectively and the maximum TDX and TDY errors are 211 and 141 nanoseconds, respectively.

Vessel Data

A time difference data collection unit was installed aboard the research vessel Polaris to collect Loran-C data. In addition, a short baseline, microwave-frequency positioning system, the Trisponder System,

6-1. Nelson, L.W., "Loran-C Signal Analysis: Final System Analysis Report, GE78TMP-108, General Electric-TEMPO, Draft.

Table 6-1. Summary of harbor fixed site data reduction and grid preparation.

Site	Distances to Master X-ray and Yankee			Predicted Using Measured		Estimated Parameters Used in Experiment Plan		Overland Path Data		On Shore and Mid Harbor Data		Least Square Fit to 13 Sites	
	D _M (km)	D _X (km)	D _Y (km)	TDX (μs)	TDY (μs)	TDX (μs)	TDY (μs)	TDX (μs)	TDY (μs)	TDX (μs)	TDY (μs)	TDX (μs)	TDY (μs)
Fort Cronkhite	374.588	104.539	746.697	192.402*	210.969*	192.363	211.134	192.402	210.796	191.975	211.100	192.191	211.027
Fort Miley	375.085	110.973	741.214	211.731	191.125	212.271	191.143	212.307	190.780	211.731	191.125	211.908	191.052
Point Bonita	374.455	106.654	744.558	199.492	204.203	199.899	204.427	199.937	204.082	199.456	204.392	199.653	204.321
Fort Point	370.808	108.400	738.861	217.586	197.579	217.947	197.581	217.984	197.242	217.398	197.482	217.511	197.438
Point Blunt	364.550	103.375	736.769	221.664	211.281	222.026	211.511	222.065	211.213	221.496	211.293	221.526	211.290
Alcatraz Island	366.363	106.368	735.957	225.426	202.555	226.000	202.736	226.037	202.420	225.426	202.554	225.468	202.540
Fort Mason	368.020	108.381	735.873	226.586	196.801	227.207	196.916	227.243	196.587	226.611	196.767	226.670	196.742
Hunter's Point	368.596	117.796	727.833	256.082	167.859	256.842	168.113	256.873	167.749	256.019	167.983	256.020	167.960
Ballena Bay	360.146	114.395	722.439	272.699	178.016	273.694	178.335	273.726	178.016	272.812	178.049	272.674	178.082
Collins Marina	366.266	111.073	731.574	241.496	188.164	242.097	188.410	242.131	188.078	241.403	188.231	241.408	188.220
Treasure Island	362.770	106.559	732.047	238.051	201.469	238.754	201.678	238.790	201.375	238.112	201.431	238.084	201.441
Berkeley Marina	356.070	103.164	728.493	248.770	211.938	249.675	212.202	249.713	211.938	249.005	211.830	248.873	211.884
Point Molate	359.703	92.988	741.023	203.070	241.758	203.415	241.942	203.459	241.698	203.063	241.626	203.077	241.650
Sears Point	350.111	70.240	750.937	159.285	306.640	159.229	307.152	159.285	307.021	159.285	306.639	159.283	306.716
Measured Minus Predictions													
	Site		(ns)	TDY (ns)	TDY (ns)	TDY (ns)	TDY (ns)	TDY (ns)	TDY (ns)	TDY (ns)	TDY (ns)	TDY (ns)	TDY (ns)
	Fort Cronkhite		+39	-165	-0.1	+172.6	+426.7	-130.6	+210.8	-57.9			
	Fort Miley		-540	-18	-575.6	+344.7	+0.3	+0.5	-176.7	+73.2			
	Point Bonita		-407	-224	-444.5	+121.5	+36.2	-189.1	-161.1	-118.3			
	Fort Point		-353	+13	-397.6	+336.8	+188.1	+97.1	+74.5	+141.5			
	Point Blunt		-362	-230	-400.7	+68.1	+167.9	-12.5	+137.9	-8.6			
	Alcatraz Island		-574	-181	-600.1	+134.6	+0.5	+0.8	-42.3	+15.4			
	Fort Mason		-617	-111	-657.2	+213.6	-24.6	+34.4	-84.2	+59.3			
	Hunter's Point		-760	-254	-791.3	+110.5	+63.0	-124.4	+62.5	-101.0			
	Ballena Bay		-995	-319	-1027.1	+0.4	-112.8	-32.8	+24.9	-65.5			
	Collins Marina		-601	-246	-635.1	+86.4	+93.4	-67.0	+87.8	-55.7			
	Treasure Island		-703	-209	-739.3	+94.0	-61.3	+37.8	-32.7	+27.6			
	Berkeley Marina		-905	-264	-942.9	+0.0	-235.1	+107.9	-102.6	+53.7			
	Point Molate		-345	-184	389.0	+59.8	+7.0	+131.5	-7.1	+108.1			
	Sears Point		+56	-512	+0.1	-380.5	+0.3	+0.8	+1.6	-76.3			

Original Estimated Parameters	On Shore + Harbor	Least Squares
For TDX)	505	0.5
	307	111
For TDY)	207	0.3
	127	81
For TDX)	995	211
For TDY)	512	141

	Original Estimated Parameters	Overland Paths	On Shore + Harbor	Least Squares
Mean TDX Error	505	544	-39	0.5
Std Dev. (TDX)	307	302	154.5	111
Mean TDY Error	207	-97	10.4	0.3
Std Dev. (TDY)	127	173	93.4	81
Max Error (TDX)	995	1027	426	211
Max Error (TDY)	512	380.5	124	141

*Add 27000 to TDX
Add 43000 to TDY

was used to accurately locate the vessel. A discussion of the processing of the vessel data (to remove effects of vessel motion during 100 second or 10 second sampling intervals) and of the Kalman filter processing of the Trisponder data is given in Reference 6-1. In addition Reference 6-1 provides graphical presentations showing the error between Loran-C position (inferred using the linear grid obtained from a least square fit to the fixed site data) and the Trisponder measured position.

The results of the vessel data analysis indicated the following

- In the inner harbor, excluding the neighborhood of the bridges, the mean TDX and TDY errors difference between Loran-C idealized grid positions and radar-measured positions were 34 and -1 ns, respectively and the standard deviations in TDX and TDY were both about 65 ns.
- In the outer harbor beyond the Golden Gate Bridge (out to about 15 km from the bridge) TDX and TDY errors magnitude were 300-400 nanoseconds for TDX and 100 to 200 nanoseconds for TDY. This increased error is expected since this vessel track is outside the area bounded by the measurement site and the effect of additional land-sea phase recovery is expected to distort the idealized grid. The track is approximately along a radial from the master transmitter and approximately at right angles to the X-ray transmitter, resulting in a greater increase in the over water path for Master than for X-ray. This is expected to increase the measured TDX, relative to the linearized grid value, which was observed.
- The behavior of TDY, where the path to Yankee has both an increasing sea water portion near the vessel, but also intersects a larger land segment across San Francisco City as the vessel moves out, is much more complicated and would require some detailed calculation for explanation.

- In the neighborhood of the Golden Gate and Oakland Bay bridges, the Loran-C position data became unusable (TD errors of several microseconds). There were no significant errors noted near the Richmond bridge.

The 100-second data samples were too coarse to accurately define the onset and recovery of the Loran-C as the vessel approached and passed under the bridge. However, one set of data was taken at 10-second intervals while the vessel passed under the Golden Gate Bridge. Here, as the vessel approached the bridge from the harbor site, a position error buildup started at about 1000-1200 meters from the bridge and the signal became useless (Loran-C vessel track turned around) at about 400-600 meters from the bridge. Note that this agrees reasonably well with the simpler predictions described earlier (see Figure 6-6). After passing under the bridge, the position data recovered at a distance of 400-500 meters beyond the bridge.

HARBOR EXPERIMENT CONCLUSIONS

- A linearized grid based on overland path measurements corrected by simple adjustments for phase recovery for over water portions of propagation paths is not adequate to define spatial anomalies in time differences relative to the idealized grid. However, the effect of phase recovery is clearly evident in the data, and taking it into account is necessary for the proper selection of measurement sites.
- In all attempts to fit an idealized grid to the harbor, TDX errors were larger than TDY errors. This results because the path length from X-ray transmitter to the harbor is shorter which in turn produced greater variation in propagation azimuth (and surface impedance variations) as the measurement point was moved around the harbor. The impedance variations are magnified by the greater sensitivity of short path secondary phase to surface impedance variations.

In general, providing an accurate grid in a limited area is more difficult, in terms of spatial anomalies, for a short baseline system than for a long baseline system. For a situation where the propagation paths are not primarily over sea water, the short baseline calibration will require a very dense set of carefully selected measurement points, and a segmented or warped grid. Grid fitting methods for short baseline systems that ignore the physical effects of impedance variations as path positions change will not work well.

- The idealized grid prepared by a least squares fit to data at the 13 fixed sites provided an accuracy of about 100 ns for the harbor in the area bounded by the fixed sites. This accuracy could be improved by dividing the harbor area into smaller areas and fitting a grid to data in those areas. We believe 50 ns accuracy could be achieved by dividing the harbor into 3 or 4 sub-areas. This is significantly less than the number of linear grids (fit to a single data point using local gradients) that would be required for the harbor area.
- Loran-C data taken on a vessel inside San Francisco harbor, (exclusive of data taken in the vicinity of the bridges) when converted to position using the idealized grid and compared with accurate radar data, showed a standard deviation in TD error of about 70 ns, which is in agreement with the fit to the land site data. The comments made above relative to improved accuracy from using multiple grids apply here.
- Data taken outside the harbor entrance and well beyond (seaward) any of the measurement sites showed larger differences between Loran-C and radar positions than observed in the harbor, using the same constants for the idealized grid that were used in the harbor. This is an expected result because of the increasing effect of land-sea phase recovery. The measurement track was essentially along a radial from master, with increasing length of sea water path. On the other hand, it

was nearly at right angles to the path from X-ray, resulting in only a small increase in sea water portion of the X-ray path. The data suggests that data taken in and around the harbor could be corrected theoretically to improve charts in the harbor approaches.

- The Loran-C signal becomes useless in the immediate neighborhood of large bridges such as the Golden Gate and Bay Bridges. As anticipated from simplified theory, signal reflection from a large bridge when the user and transmitters are on the same side of the bridge is more of a problem than shadowing effects beyond the bridge. Data taken at 10-second intervals in the vicinity of the Golden Gate Bridge indicated the following:

For a vessel approaching the bridge from the land side (vessel and Loran transmitter on the same side of the bridge) the position error buildup starts at about 1000-1200 meters from the bridge and the position information becomes unusable at about 400 to 600 meters from the bridge.

On the seaward (shadowed) side of the bridge, the position accuracy recovery is essentially complete at about 400-500 meters from the bridge. Thus, dead reckoning or other systems are required for a distance of about 1 to 1.5 kilometers when passing under the Golden Gate Bridge from the harbor to the open sea.

SECTION 7

CONCLUSIONS AND RECOMMENDATIONS

CONCLUSIONS

The results and conclusions obtained during the preparation of this report are summarized below.

1. For a smooth, inhomogeneous earth Millington's technique and Wait's multiple segment technique produce nearly identical results. Therefore, Millington's technique should be used in preference to Wait's because of its greater simplicity and shorter running time.
2. Millington's technique and the integral equation technique give nearly identical results for a highly inhomogeneous impedance path when the terrain variations are suppressed for the integral equation calculations. Those variations that are observed are most probably due to the finer detail of the surface impedance data for the integral equation test calculation. Thus, Millington's technique is adequate where terrain variations are not important.
3. The predicted value of weather induced phase fluctuations based on changes in the index of refraction and equivalent earth radius along the propagation path are very small for path lengths typical of those for which measurements were taken in the West Coast experiment. The predicted values were of the order of ± 10 ns based on the simplified theory of Section 3 and weather data obtained from Reno, Nevada.
4. Based on integral equation calculations both terrain and surface impedance variations are important in predicting

secondary phase for the WCP. Our numerical computations indicated that the terrain can be defined with sufficient accuracy with data points spaced at approximately one kilometer. Our experimental observations and predictions indicate that to obtain prediction accuracy on the order of 0.5 microseconds or better requires that the surface impedance uncertainty be less than a factor of two for overland paths. The computed results are much less sensitive to the impedance specification when the conductivity is high. The surface impedance values cannot be specified with sufficient accuracy at the present time without a significant effort in path calibration.

5. The effect of terrain variations (in this case elevations greater than one wavelength above the mean geoid) was to increase the secondary phase. Thus, matching calibration data with impedance variations alone requires higher than actual impedance values to compensate for the terrain effect. This requirement is illustrated by the USCG conductivity map for the west coast chain, which shows conductivity values lower (higher impedance) than those required to match experimental data when terrain effects are included.
6. Data preparation for the integral equation method is a formidable task. The hand preparation of the data for the worst case path required an effort of about one man-month. Digital terrain data tapes for the WCP were not available. Similar preparation of data for a coverage area would not be practical.
7. Computation time for the integral equation method is very long. For computational accuracy, an integration step size of approximately 1 kilometer is required. It should be noted that computational errors observed in idealized test cases discussed in Section 2 tend to average out for

a realistic path where the terrain profile and impedance profile have large fine grain excursions. Thus, although the calculation at any particular point may have an error associated with it, the errors tend to cancel rather than build up. This is well illustrated by the comparison between predicted and measured results for incremental (site-to-site) and cumulative secondary phase values for the WCP. Differences in the incremental results were significant, but the cumulative results showed no error accumulation.

8. Results from the worst case path experiment show that good experimental data can be acquired using the techniques described in Section 4 and that the uncertainty associated with the experimental data are of the order of ± 50 ns.
9. Differences between the theoretically predicted and measured incremental phase changes, using the actual terrain data and surface impedance derived from geological data along the path, ranged from tens of nanoseconds to half a microsecond. By adjusting the surface impedance values, the predicted values can be made to match the experimental data. Results shown in Section 5 show that the original predictions and predictions made by decreasing the conductivity by a factor of 2 along the entire worst case path bracket the experimental results. Selective adjustment of conductivity values by a factor of 2 or less could produce agreement between predicted and measured results.
10. The highly variable terrain and surface impedance along the worst case path and the differences between predicted and measured values indicate the need for more closely spaced measurements points to adequately calibrate phase change along the overland portion of the path. On the other hand, measurements made beyond the region of major terrain variations can be used to compensate for the cumulative effect of terrain induced fluctuations.

11. An idealized harbor grid based on overland path measurements corrected by simple adjustments for phase recovery for over water portions of propagation paths is not adequate to define spatial anomalies in time differences relative to the idealized grid. However, the effect of phase recovery is clearly evident in the data, and taking it into account is necessary for the proper selection of measurement sites.
12. TDX errors relative to an idealized grid of the harbor, were larger than TDY errors because the path length from X-ray transmitter to the harbor is shorter which in turn produced greater variation in propagation azimuth (and surface impedance variations) as the measurement point was moved around the harbor. The impedance variations are magnified by the greater sensitivity of short path secondary phase to surface impedance variations. In general, providing an accurate grid in a limited area is more difficult, in terms of spatial anomalies, for a short baseline system than for a long baseline system.
13. The idealized grid prepared by a least squares fit to data at the 13 fixed sites provided an accuracy of about 100 ns for the harbor in the area bounded by the fixed sites. This accuracy could be improved by dividing the harbor area into smaller areas and fitting a grid to data in those areas. We believe 50 ns accuracy could be achieved by dividing the harbor into 3 or 4 sub-areas. This is significantly less than the number of linear grids (fit to a single data point using local gradients) that would be required for the harbor area.
14. Loran-C data taken on a vessel inside San Francisco harbor, (exclusive of data taken in the vicinity of the bridges) when converted to position using the least squares idealized grid and compared with accurate radar data, showed a standard deviation in TD error of about 70 ns, which is in agreement

with the fit to the land site data. The comments made above relative to improved accuracy from using multiple grids apply here.

15. Data taken outside the harbor entrance and well beyond (seaward) any of the measurement sites showed larger differences between Loran-C and radar positions than observed in the harbor, using the same constants for the idealized grid that were used in the harbor. This is an expected result because of the increasing effect of land-sea phase recovery.
16. The Loran-C signal becomes useless in the immediate neighborhood of large bridges such as the Golden Gate and Bay Bridges. As anticipated from simplified theory, signal reflection from a large bridge when the user and transmitters are on the same side of the bridge is more of a problem than shadowing effects beyond the bridge. Data taken at 10-second intervals in the vicinity of the Golden Gate Bridge indicated the following:

For a vessel approaching the bridge from the land side (vessel and Loran transmitter on the same side of the bridge) the position error buildup starts at about 1000-1200 meters from the bridge and the position information becomes unusable at about 400 to 600 meters from the bridge.

On the seaward (shadowed) side of the bridge, the position accuracy recovery is essentially complete at about 400-500 meters from the bridge. Thus, dead reckoning or other systems are required for a distance of about 1 to 1.5 kilometers when passing under the Golden Gate Bridge from the harbor to the open sea.

RECOMMENDATIONS

Based on the work described in this report, the following recommendations are made for additional effort on propagation prediction.

1. Procedures more efficient than scaling and reading quantities from maps by hand must be developed for generating the terrain and surface impedance data bases that are required for the proper employment of numerical predictive techniques. The surface impedance data base is a requirement not only for the integral equation technique but also for the Millington technique or Wait-Multisegment theory.
2. A more complete propagation theory incorporating arbitrary weather variations should be developed. This theory should be based on an arbitrary variation of the index of refraction with altitude and if possible, with distance. The theory could be used to test the validity of the currently employed constant slope refractive index model, and a resulting model could be used to determine the altitude range over which the index of refraction needs to be specified.
3. The test calculations on the integral equation technique which are described in Sections 2 and 5 indicate that a systematic sensitivity study is required. This study should begin with the numerical analysis techniques used to obtain the solution and should include variation of the computation step size and the terrain and surface impedance specification. The study should be aimed at determining the sensitivity of computed results to computation step size and variations in the detail of the terrain and impedance profiles along the propagation (integration) path. It should also develop the criteria for determining when terrain variations can be ignored (so that simpler techniques can be employed) and determine the detail of data input for both the terrain and impedance profiles consistent with the accuracy of the available data.

4. Until a better understanding of the limitations of and data requirements for the integral equation technique are established, the current combination of calibration and the utilization of Millington's technique should be continued. The method of modifying the impedance data to make the prediction of the Millington's technique match the experimental data is also common to the proposed use of the integral equation technique. The impedance description which results from such an "optimization" is not necessarily unique. The main criterion is that the "optimized" impedance data generate the correct position results in areas like San Francisco Harbor or other regions beyond the west coast for example. Since the ocean can be considered a smooth homogeneous path, the major criterion for a prediction code is that it predict the correct phase and the correct land surface impedance at the land-sea boundary. The results over the water path should then follow. With a sufficient number of calibration points and impedance parameters a code based on Millington's technique should be able to accomplish this task much more efficiently than a code based on integral methods. A potential improvement could result from using the integral equation technique to develop empirical techniques for evaluating the effects of significant terrain features. A combined impedance/terrain model would have a better physical basis than an impedance-only model and should allow better extrapolation to areas between calibration points.
5. Future experiments to obtain data for comparison with prediction techniques should use control procedures similar to those described in Section 4 but with the emphasis on more frequent closures with calibration equipment. Data should be acquired at more sites (less data collection per site). The choice of measurement sites should be based on prior

detailed predictions. Measurements should be made at sites slightly offset from originally established sites (both along and transverse to the geodesic) when in-field data analysis and comparison with predictions indicates large differences between experimental and predicted results.

6. The idealized grid used in this report is a useful way to derive parameters for an accurate calibrated grid and should be considered, in conjunction with prediction procedures, to select measurement points for harbor or restricted waterway calibration.

APPENDIX A

DETAILS OF THE SMOOTH HOMOGENEOUS EARTH THEORY

There are three forms of the attenuation function W used in the smooth homogeneous spherical earth theory. These are commonly used as building blocks for more complicated theories. The general problem is solved in the form of a series expansion. This expansion is very accurate but requires more and more terms as the distance between the transmitter and receiver decreases. This led to the development of two short distance approximations to the solution. In the following discussion, a brief description is given for the two short distance approximations and for the series expansion. The descriptions are followed by a discussion of the number of terms necessary in the series expansion for a given accuracy and the rationale for choosing switch points, i.e. determining when to use the short distance approximations rather than the series solution.

SHORT DISTANCE APPROXIMATIONS

Wait (Reference A-1) and Bremmer (Reference A-2) have developed two procedures for calculating the attenuation function W at locations close to the transmitter. One is a power series in the numerical distance given by

$$W = \sum_{m=0}^{10} A_m \left[e^{i\pi/4} qX^{1/2} \right]^m \quad (A-1)$$

where q is the normalized surface impedance, X is the numerical (i.e., normalized) distance and the A_m 's are functions of q :

A-1. Wait, J.R., and K. Spies, "On the Calculation of Antenna Patterns for an Inhomogeneous Spherical Earth," Radio Science Vol. 2 (New Series), No. 11, Nov. 1967, pp. 1361-1378.

$$q = -i \left(\frac{k_1 a_e}{2} \right)^{1/3} \Delta, \quad (A-2)$$

$$\chi = \left(\frac{k_1 a_e}{2} \right)^{1/3} \frac{d}{a_e} \quad (A-3)$$

where

a_e = equivalent earth radius (km)*

k_1 = wave number in air (km^{-1})

d = distance between transmitter and calculation point

Δ = effective electromagnetic surface impedance relative to air

and the A_m 's are defined by

$$\begin{aligned} A_0(q) &= 1, & A_1(q) &= -i\pi^{1/2}, \\ A_2(q) &= -2, & A_3(q) &= i\pi^{1/2} \left(1 + \frac{1}{4q^4} \right), \\ A_4(q) &= \frac{4}{3} \left(1 + \frac{1}{2q^4} \right), & A_5(q) &= -\frac{i\pi^{1/2}}{2} \left(1 + \frac{3}{4q^4} \right), \\ A_6(q) &= -\frac{8}{15} \left(1 + \frac{1}{q^4} + \frac{7}{32q^8} \right), \\ A_7(q) &= \frac{i\pi^{1/2}}{6} \left(1 + \frac{5}{4q^4} + \frac{1}{2q^8} \right), \\ A_8(q) &= \frac{16}{105} \left(1 + \frac{3}{2q^4} + \frac{27}{32q^8} \right), \\ A_9(q) &= -\frac{i\pi^{1/2}}{24} \left(1 + \frac{7}{4q^4} + \frac{5}{4q^8} + \frac{21}{64q^{12}} \right), \\ A_{10}(q) &= -\frac{32}{945} \left(1 + \frac{2}{q^4} + \frac{55}{32q^8} + \frac{19}{64q^{12}} \right). \end{aligned}$$

For a uniform earth the effective impedance Δ is given by

A-2. Bremmer, H., "Applications of Operational Calculus to Ground Wave Propagation, Particularly for Long Waves," IRE Trans. on Antennas and Propagation, AP-6, No. 3, July, 1958, pp. 267-272.

* The determination of the equivalent earth's radius is discussed in Section 3.

$$\Delta = \left[\frac{i\epsilon_o \omega \eta^2}{\sigma_g + i\epsilon_g \epsilon_o \omega} \right]^{1/2} \left[1 - \frac{i\epsilon_o \omega \eta^2}{\sigma_g + i\epsilon_g \epsilon_o \omega} \right]^{1/2} \quad (\text{A-4})$$

where

$$\begin{aligned} \epsilon_o &= \text{permittivity of free space} \\ &= 8.8541853367 \times 10^{-12} \quad \text{farads/m} \\ \sigma_g &= \text{earth conductivity} \quad (\text{mhos/m}) \\ \epsilon_g &= \text{relative dielectric constant of the earth} \\ \eta &= \text{refractive index of air} \\ \omega &= 2\pi f, \quad f = \text{wave frequency.} \end{aligned}$$

The series in A-1 converges rapidly if X is small and $|q| < 1$.

The second short distance approximation is an expansion in inverse powers of q , when $|q| > 1$ and is given by

$$W = F(P) - F_1 + F_2 - F_3 \quad (\text{A-5})$$

where

$$\begin{aligned} P &= iXq^2 \\ F(P) &= 1 - i(\pi P)^{1/2} e^{-P} \operatorname{erfc}(iP^{1/2}) \\ F_1 &= [(1 + 2P) F(P) + i(\pi P)^{1/2} - 1]/4q^3 \\ F_2 &= [(P^2/2 - 1) F(P) - i(\pi P)^{1/2} (1 - P) \\ &\quad + 1 - 2P + 5/6P^2]/4q^6 \\ F_3 &= \left[\left(\frac{35}{8} - \frac{P^2}{4} + \frac{P^2}{6} \right) F(P) + i(\pi P)^{1/2} \left(\frac{35}{8} - \frac{35P}{8} \right. \right. \\ &\quad \left. \left. + \frac{31P^2}{16} - \frac{5P^3}{16} \right) - \frac{35}{4} + \frac{35P}{4} - \frac{67P^2}{12} + \frac{5P^3}{3} \right] / 8q^9 \end{aligned}$$

The expansion (A-5) converges if $|q| > 1$ and the distance is short, i.e., $p < 1$ and $F(P) \approx 1$. The quantity $\operatorname{erfc}(x)$ is the complementary

error function defined in Reference A-3 as

$$\operatorname{erfc}(x) = \frac{2}{\sqrt{\pi}} \int_x^{\infty} e^{-t^2} dt = 1 - \frac{2}{\sqrt{\pi}} \int_0^x e^{-t^2} dt = 1 - \operatorname{erf}(x) \quad (\text{A-6})$$

SERIES SOLUTION

The series solution for W is given by (Reference A-1)

$$W = \left(\frac{\pi X}{i} \right)^{1/2} \sum_{s=1}^{\infty} \frac{e^{-iXt_s}}{t_s - q^2} \quad (\text{A-7})$$

When $|q| < 1$, the values of t_s are solution to

$$\frac{dt}{dq} = \frac{1}{t - q^2} \quad (\text{A-8})$$

or equivalently, are roots of

$$w_1'(t_s) = qw_1(t_s) \quad (\text{A-9})$$

where w_1 is an Airy function defined by Wait (Reference A-4, page 112, 113, and 213), and w_1' is the derivative of w_1 with respect to the argument.

When $|q| > 1$, \hat{q} is defined as

$$\hat{q} = 1/q \quad (\text{A-10})$$

and the values of t_s are solutions of

$$\frac{dt}{d\hat{q}} = \frac{1}{1 - \hat{q}^2 t} \quad (\text{A-11})$$

or, equivalently, are roots of

$$\hat{q} w_1'(t_s) = w_1(t) \quad (\text{A-12})$$

A-3. "Handbook of Mathematical Functions," Edited by M. Abramowitz and I.A. Stegun, NBS Applied Mathematics Series, 55, National Bureau of Standards, Washington, D.C., 1964.

A-4. Wait, J.R., "Electromagnetic Waves in Stratified Media," Pergamon Press, the MacMillan Co., New York, Second Edition, 1970.

When $|q| < 1$, the roots can be found by integrating Equation (A-8), using starting values $t_s(o)$, defined by

$$t_s(o) = \gamma'_s e^{-i\pi/3} \quad (A-13)$$

where γ'_s is a zero of $A'_1(-\gamma)$, and A'_1 is the derivative of the Airy function defined in Reference A-3, Page 446. The zeros are tabulated on page 478 of Reference A-3. A_1 is simply related to the Airy function defined by Wait, w_2 .

When $|q| > 1$, the roots can be found by integrating (A-11) using starting values, $t_s(o)$ defined by

$$t_s(o) = \gamma_s e^{-i\pi/3} \quad (A-14)$$

γ_s is a zero of the Airy Function, $A_1(-\gamma)$.

In the TEMPO computer program a fourth order Runge-Kutta formula is used to integrate Equation A-8 or A-11. After the integration, a test is made to see if

$$w'_1(t_s^I) - qw_1(t_s^I) < \epsilon, \quad |q| < 1 \quad (A-15)$$

or

$$\hat{q}w'_1(t_s^I) - w_1(t_s^I) < \epsilon, \quad |q| > 1 \quad (A-16)$$

where ϵ is a small number and t_s^I is the result of the integration process.

When Equation A-15 or A-16 is not satisfied the integration step size is decreased and the integration repeated. An alternate procedure is to use a Newton-Raphson iteration technique to improve the solution.

For Equation A-9, this procedure produces a correction to t_s^I given by

$$\Delta t_s = - \frac{w'_1(t_s^I) - qw_1(t_s^I)}{t_s^I w_1(t_s^I) - q w'_1(t_s^I)} \quad (A-17)$$

and for Equation A-12, the correction to t_s^I is

$$\Delta t_s = - \frac{\hat{q} w_1'(t_s^I) - w_1(t_s^I)}{\hat{q} t_s^I w_1(t_s^I) - w_1'(t_s^I)} \quad (\text{A-18})$$

This correction procedure works well for small t , where the Airy function can easily be defined accurately. Wait (Reference A-1) and Bremmer (Reference A-5) also define series expansion in terms of q or $1/q$.

The series defined by Equation A-7 requires many terms for convergence when the distance is small. The number of terms required can be estimated by rewriting Equation A-7, in the form

$$W = \left(\frac{\pi X}{i}\right)^{1/2} \frac{e^{-iXt_1}}{t_1 - q^2} \left| 1 + \sum_2^S \frac{e^{+iX(t_1-t_s)}}{t_s - q^2} (t_1 - q^2) \right| \quad (\text{A-19})$$

For N digit accuracy

$$\left| e^{+iX(t_1 - t_s)} \frac{t_1 - q^2}{t_s - q^2} \right| \leq 10^{-N} \quad (\text{A-20})$$

Equation A-20 can be solved to give

$$\text{Im}X(t_1 - t_s) \geq \ln \left| \frac{(t_1 - q^2) 10^N}{t_s - q^2} \right| \quad (\text{A-21})$$

where Im means the imaginary part.

Using Equation A-3 to relate X and the distance d , we obtain

$$d \geq \ln \left| \frac{10^N (t_1 - q^2)}{t_s - q^2} \right| \frac{a_e}{\text{Im}(t_1 - t_s)} \left(\frac{ka_e}{2} \right)^{-1/3} \quad (\text{A-22})$$

A-5. Bremmer, H., "Terrestrial Radio Waves," Elsevier Publishing Company, 1949.

For large s , the values of t_s are approximately independent of q and are given by

$$t_s \approx \frac{3\pi(4s-n)}{8}^{2/3} e^{-i\pi/3} \quad (A-23)$$

where $n = 3$ for $|q| < 1$ and $n = 1$ for $|q| > 1$.

Using A-22 and A-23, the values in Table A-1 were computed for various values of conductivity. Based on the entries in Table A-1, 100 terms are adequate for distance greater than 100 km. At distances less than 100 km, it is convenient, and will conserve computer time, to use either Equation A-1 for $|q| < 1$ or Equation A-5 for $|q| > 1$. Table A-2 shows a comparison of the values produced by Equations A-1, A-5, and A-7, using 100 terms in Equation A-7. The overlapping region for using Equations A-1 and A-7 or A-5 and A-7 is boxed in the table. Comparing the table entries indicates that a distance of about 80 km is a satisfactory transition point between the short distance formulas and the series.

$S \backslash n$	2	4	6	8	
10	210	420	630	840	$\left. \begin{array}{l} \sigma = 10^{-4} \\ \epsilon/\epsilon_0 = 10 \end{array} \right\}$
20	120	240	360	480	
50	55	115	175	235	
100	30	65	105	140	
10	125	320	520	720	$\left. \begin{array}{l} \sigma = 10^{-3} \\ \epsilon/\epsilon_0 = 15 \end{array} \right\}$
20	58	175	290	400	
50	22	60	140	200	
100	10	45	85	120	
10	90	280	440	660	$\left. \begin{array}{l} \sigma = 10^{-2} \\ \epsilon/\epsilon_0 = 15 \end{array} \right\}$
20	40	155	270	380	
50	15	75	130	190	
100	5	40	80	115	
10	90	280	470	660	$\left. \begin{array}{l} \sigma = 5 \\ \epsilon/\epsilon_0 = 80 \end{array} \right\}$
20	40	150	270	380	
50	15	75	130	190	
100	-	40	80	115	

Table A-1. Minimum distance in kilometers to obtain N digit accuracy with S terms in the series expansion for the ground wave attenuation functions (Equation A-7).

Table A-2. Comparison of procedures for computing the attenuation function for $\sigma = 10^{-4}$ mhos/m, $\epsilon/\epsilon_0 = 10$

Distance (km)	Equation A-7 100 term		Equation A-5		Equation A-1	
	Real (W)	Imag. (W)	Real (W)	Imag. (W)	Real (W)	Imag. (W)
10.00	0.228779	-0.436276	0.278891	-0.547183	0.278923	-0.546832
20.00	0.057093	-0.436332	0.047345	-0.461005	0.048756	-0.446553
30.00	-0.046080	-0.359489	-0.051860	-0.362088	-0.033264	-0.235202
40.00	-0.092458	-0.282267	-0.093958	-0.281761	0.016614	0.305399
50.00	-0.109283	-0.221039	-0.109492	-0.220678	0.320278	1.693371
60.00	-0.112357	-0.175040	-0.112347	-0.174922	1.170057	4.828102
70.00	-0.109267	-0.140606	-0.109272	-0.140594	3.088284	11.093026
80.00	-0.103561	-0.114557	-0.103584	-0.114559	6.898494	22.461503
90.00	-0.096938	-0.094573	-0.096969	-0.094575	13.803263	41.602485
100.00	-0.090222	-0.079017	-0.090268	-0.079015	25.466436	71.985245
110.00	-0.083802	-0.066728	-0.083853	-0.066723	44.098518	117.982946
120.00	-0.077845	-0.056878	-0.077900	-0.056871	72.544544	184.975229
130.00	-0.072400	-0.048873	-0.072459	-0.048859	114.373751	279.449722
140.00	-0.067461	-0.042278	-0.067522	-0.042261	173.971153	409.102871
150.00	-0.062993	-0.036777	-0.063058	-0.036758	256.629993	582.939674
160.00	-0.058953	-0.032135	-0.059019	-0.032113	368.645798	811.373100
170.00	-0.055295	-0.028176	-0.055364	-0.028153	517.411316	106.322403
180.00	-0.051973	-0.024766	-0.051958	-0.024557	711.511841	1311340
190.00	-0.048948	-0.021803	-0.048984	-0.021615	960.822357	1565567
200.00	-0.046184	-0.019209	-0.046234	-0.019095	1276.604431	19534.109528

$$\sigma = 10^{-4}$$

$$\epsilon/\epsilon_0 = 10$$

Table A-2 (continued). $\sigma = 10^{-3}$, $\epsilon/\epsilon_0 = 15$

Distance (km)	Equation A-7 100 term		Equation A-5		Equation A-1	
	Real (W)	Imag. (W)	Real (W)	Imag. (W)	Real (W)	Imag. (W)
10.00	0.806821	-0.306796	0.872221	-0.394673	0.872231	-0.394644
20.00	0.766754	-0.498962	0.763830	-0.522636	0.763879	-0.522531
30.00	0.669464	-0.596497	0.665035	-0.600346	0.665184	-0.600139
40.00	0.576023	-0.650296	0.574370	-0.650572	0.574652	-0.650236
50.00	0.491662	-0.682537	0.490964	-0.682751	0.491408	-0.682261
60.00	0.414863	-0.701530	0.414148	-0.702015	0.414794	-0.701357
70.00	0.344428	-0.710951	0.343435	-0.711614	0.344255	-0.710740
80.00	0.279697	-0.712984	0.278356	-0.713752	0.279297	-0.712595
90.00	0.220728	-0.709196	0.218510	-0.710029	0.219462	-0.708491
100.00	0.165653	-0.700784	0.163532	-0.701654	0.164319	-0.699590
110.00	0.115635	-0.688685	0.113041	-0.689534	0.113449	-0.686772
120.00	0.069864	-0.673647	0.066805	-0.674461	0.066443	-0.670715
130.00	0.028052	-0.656273	0.024512	-0.657018	0.022891	-0.651936
140.00	-0.010070	-0.637056	-0.014103	-0.637700	-0.017616	-0.630833
150.00	-0.044749	-0.616405	-0.049281	-0.616914	-0.055498	-0.607702
160.00	-0.076217	-0.594660	-0.081250	-0.595003	-0.091186	-0.582754
170.00	-0.104692	-0.572105	-0.110290	-0.572204	-0.125125	-0.556131
180.00	-0.130376	-0.548482	-0.136489	-0.548639	-0.157781	-0.527911
190.00	-0.153458	-0.525493	-0.160080	-0.525078	-0.189643	-0.498115
200.00	-0.174115	-0.501810	-0.181238	-0.501097	-0.221225	-0.466717

$$\sigma = 10^{-3}$$

$$\epsilon/\epsilon_0 = 15$$

Table A-2 (continued). $\sigma = 10^2$, $\epsilon/\epsilon_0 = 15$

Distance (km)	Equation A-7 100 term		Equation A-5		Equation A-1	
	Real (W)	Imag. (W)	Real (W)	Imag. (W)	Real (W)	Imag. (W)
10.00	0.921473	-0.050433	0.9A6465	-0.135A0A	0.9A6511	-0.135492
20.00	0.974700	-0.16A719	0.971933	-0.193029	0.972230	-0.19173A
30.00	0.961386	-0.231217	0.956623	-0.237546	0.957246	-0.234832
40.00	0.943036	-0.271041	0.940392	-0.2757A3	0.941674	-0.271009
50.00	0.925841	-0.30290A	0.923355	-0.310043	0.925591	-0.302669
60.00	0.909061	-0.331124	0.905535	-0.341537	0.909056	-0.331034
70.00	0.892099	-0.356A44	0.8A6955	-0.370955	0.892116	-0.356824
80.00	0.874801	-0.38050A	0.867621	-0.398758	0.874A13	-0.380504
90.00	0.857170	-0.402398	0.847557	-0.425240	0.857181	-0.402394
100.00	0.839237	-0.422732	0.826771	-0.450620	0.839254	-0.422724
110.00	0.821033	-0.441681	0.805269	-0.475052	0.821060	-0.441668
120.00	0.802587	-0.459377	0.783058	-0.498655	0.802629	-0.459357
130.00	0.783923	-0.475926	0.760151	-0.521519	0.783986	-0.475895
140.00	0.765065	-0.491410	0.736555	-0.543717	0.765157	-0.491367
150.00	0.746036	-0.505901	0.7122A3	-0.565294	0.746167	-0.505840
160.00	0.72685A	-0.519454	0.6A733A	-0.586298	0.727039	-0.519371
170.00	0.707551	-0.532119	0.661720	-0.606775	0.707797	-0.532009
180.00	0.688135	-0.543937	0.635448	-0.626740	0.688465	-0.543792
190.00	0.668631	-0.554944	0.608536	-0.646227	0.669065	-0.554757
200.00	0.649056	-0.565172	0.580981	-0.665252	0.649620	-0.564933

$$\sigma = 10^{-2}$$

$$\epsilon/\epsilon_0 = 15$$

Table A-2 (continued). $\sigma = 5$, $\epsilon/\epsilon_0 = 80$

Distance (km)	Equation A-7 100 term		Equation A-1	
	Real (W)	Imag. (W)	Real (W)	Imag. (W)
10.00	0.933794	0.077511	0.998775	-0.007240
20.00	0.998970	0.011053	0.996548	-0.011902
30.00	0.997783	-0.012980	0.993664	-0.016593
40.00	0.991605	-0.021488	0.990247	-0.021460
50.00	0.986619	-0.026770	0.986369	-0.026532
60.00	0.982085	-0.031895	0.982078	-0.031806
70.00	0.977397	-0.037289	0.977412	-0.037271
80.00	0.972390	-0.042912	0.972396	-0.042910
90.00	0.967054	-0.048708	0.967056	-0.048709
100.00	0.961409	-0.054650	0.961410	-0.054650
110.00	0.955473	-0.060717	0.955476	-0.060716
120.00	0.949262	-0.066895	0.949267	-0.066893
130.00	0.942790	-0.073168	0.942797	-0.073165
140.00	0.936069	-0.079521	0.936080	-0.079518
150.00	0.929109	-0.085941	0.929125	-0.085937
160.00	0.921921	-0.092415	0.921943	-0.092408
170.00	0.914514	-0.098929	0.914545	-0.098920
180.00	0.906897	-0.105471	0.906941	-0.105460
190.00	0.899080	-0.112030	0.899139	-0.112015
200.00	0.891069	-0.118594	0.891149	-0.118575

$\sigma = 5$
 $\epsilon/\epsilon_0 = 80$

APPENDIX B NUMERICAL EVALUATION AND ADDITIONAL INVESTIGATIONS OF WAIT'S MULTIPLE SEGMENT TECHNIQUE

COMPUTER SOLUTION

The general formulae for evaluating the attenuation function $W'(d, \Delta_1, \Delta_2, \dots, \Delta_n)$ were given in Section 2, Equations 2-4 through 2-6. A special computer code (MULSEG) was developed at TEMPO to evaluate W' . The path is divided into equal increments, δ . For simplicity, each segment contains an integral number of δ 's. For small δ 's and imprecisely defined boundaries, this simplification should be acceptable.

In all but the two segment path, one or more of the attenuation functions must be defined numerically from a prior integration. Using an integral number of δ 's per segment allows the use of a simple integration scheme, with the attenuation functions defined at the end of each increment. A modified Simpson's rule integration has been used in preparing the program. This integration method has proven adequate, except that small step size, δ , is required for paths with transitions from high impedance to low impedance.

Assuming the W' functions are to be evaluated at equal increments, the computer formulation is developed by considering a general integral of the form

$$I_{sn} = - \left(\frac{ikd}{2} \right)^{1/2} (\Delta_s - \Delta_n) \int_a^b \frac{W[(d-\gamma), \Delta_n] W'(\gamma, \Delta_1, \Delta_2, \dots, \Delta_{n-1})}{[\gamma(d-\gamma)]^{1/2}} d\gamma$$

(B-1)

or for notational ease

$$I_n = A_{sn} \int_a^b \frac{F_n(\gamma)}{[\gamma(d-\gamma)]^{1/2}} d\gamma. \quad (B-2)$$

Since the attenuation functions vary slowly with distance, I_n can be approximated numerically by

$$I_n = A_{sn} \left[F_n(a) \int_a^{a+\frac{\delta}{2}} \frac{d\gamma}{[\gamma(d-\gamma)]^{1/2}} + F_n(a+\delta) \int_{a+\frac{\delta}{2}}^{a+\frac{3\delta}{2}} \frac{d\gamma}{[\gamma(d-\gamma)]^{1/2}} \right. \\ \left. \dots \dots \dots + F_n(b) \int_{b-\frac{\delta}{2}}^b \frac{d\gamma}{[\gamma(d-\gamma)]^{1/2}} \right] \quad (B-3)$$

This form avoids the problem of singularities at the end point ($a=0$ or $b=d$) since the integrals are finite at those points. Performing the integration in B-2 gives

$$I_n = A_{sn} \left[F_n(a) \left\{ \sin^{-1} \left(\frac{2a+\delta-d}{d} \right) - \sin^{-1} \left(\frac{2a-d}{d} \right) \right\} + \right. \\ F_n(a+\delta) \left\{ \sin^{-1} \left(\frac{2a+3\delta-d}{d} \right) - \sin^{-1} \left(\frac{2a+\delta-d}{d} \right) \right\} + \dots \\ \left. F_n(b) \left\{ \sin^{-1} \left(\frac{2b-d}{d} \right) - \sin^{-1} \left(\frac{2b-\delta-d}{d} \right) \right\} \right] \quad (B-4)$$

Using this approach, the general equation for computer solution can be written

$$W'(d, \Delta_1, \Delta_2, \dots, \Delta_n) = W(d, \Delta_n) - \\ \sum_{i=1}^{n_p} W((n_T-i)\delta, \Delta_n) \cdot W'((i-1)\delta, \Delta_1, \Delta_2, \dots, \Delta_{n-1}) A_{sn} \cdot G_i \quad (B-5)$$

where

$W'((i-1)\delta, \Delta_1, \Delta_2, \dots, \Delta_{n-1})$ is the appropriate value of the composite attenuation function developed by a prior integration (evaluated at intervals of δ)

n_T = one plus number of intervals in d

n_p = one plus number of intervals in first $n-1$ segments

A_{sn} is the impedance weighting function

$$A_{sn} = \Delta_s - \Delta_n \quad (B-6)$$

where s is defined implicitly by

$$\sum_{j=1}^s d_j < i\delta < \sum_{j=1}^{s+1} d_j \quad (B-7)$$

The G_i are the result of integrating $\frac{d\gamma}{(\gamma(d-\gamma))^{1/2}}$ and are

$$G_1 = \sin^{-1} \left(\frac{\delta-d}{d} \right) + \frac{\pi}{2} \quad (B-8)$$

$$G_i = \sin^{-1} \left(\frac{(2i-1)\delta-d}{d} \right) - \sin^{-1} \left(\frac{(2i-3)\delta-d}{d} \right), \quad 1 < i < n_p \quad (B-9)$$

$$G_{n_p} = \sin^{-1} \left(\frac{2(n_p-1)\delta-d}{d} \right) - \sin^{-1} \left(\frac{(2n_p-3)\delta-d}{d} \right) \quad (B-10)$$

Equations B-5 through B-10 have been programmed and combined with the procedures for computing attenuation functions for a homogeneous earth to provide a complete package for computing the attenuation functions for inhomogeneous earth. Test cases have been executed and results are in close agreement with results presented in Reference 2-4 for a two-segment path.

Additional tests of the program are described in Section 2 in the comparison with other techniques.

INVESTIGATION OF APPROXIMATIONS

Since initial comparisons between the results using Wait's technique and the GFE integral equation program (described in Section 2 and Appendix C) were not good, we decided to investigate some of the approximations made by Wait in going from his original theoretical developments to the form defined by Equations 2-4 through 2-5.

We follow the basic derivation developed by Wait (Reference 2-4). The object of this exercise is to include several basic propagation factors which were dropped during Wait's development and to attempt an initial assessment of their possible effects on the accuracy of the predictions of computer codes based on the final equations. The notation used here, is modified from Wait's original notation to remain consistent within this report.

Wait's development begins with the application of the Lorentz reciprocity theorem in a form presented by Monteath (Reference B-1).

$$Z'_{ab} - Z_{ab} = \frac{1}{I_a I_b} \iint_S (\vec{E}_b \times \vec{H}'_a - \vec{E}'_a \times \vec{H}_b) \cdot \vec{i}_r dS \quad (B-11)$$

where S is the surface of the sphere, dS is an element of area and \vec{i}_r is the unit vector normal to the sphere.

$$Z_{ab} = \frac{I_a I_b i \mu_0 \omega}{2\pi d} e^{-ikd} \left(1 + \frac{1}{ikd} - \frac{1}{k^2 d^2} \right) W(d, \Delta) \quad (B-12)$$

is the mutual impedance between two vertical electric dipoles of length I_a and I_b situated a distance d apart on a homogeneous curved earth with normalized surface impedance Δ at frequency f ($\omega = 2\pi f$, $k = \omega/c$). $W(d, \Delta)$

B-1. Monteath, G.D., "Applications of the compensation theorem to certain radiation and propagation problems," Proc. Instr. Elect. Engrs. 98, Pt.4, pp 23-30, 1951.

is normalized so that it would become unity for a perfectly conducting flat earth ($a_e \rightarrow \infty$ where a_e is the effective earth radius). The geometry is shown in Figure B-1.

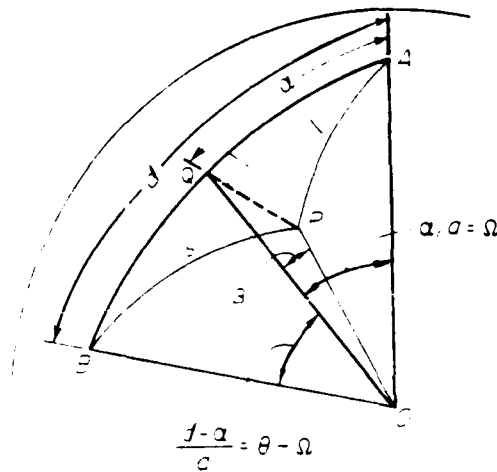


Figure B-1. Coordinates for describing wave propagation on a spherical surface.

The quantity Z'_{ab} given by

$$Z'_{ab} = \frac{I_a I_b i \mu_0 \omega}{2\pi d} e^{-ikd} \left(1 + \frac{1}{ikd} - \frac{1}{k^2 d^2} \right) W'(d, \Delta, \Delta') \quad (B-13)$$

is the mutual impedance between the two dipoles for the inhomogeneous curved earth. The attenuation function $W(d, \Delta)$ can be obtained from

$$W(d, \Delta) \cong \left(\frac{\pi x}{i} \right)^{1/2} \left(\sum_{s=1,2,3} \frac{e^{-ixt_s}}{t_s - q^2} \right) \left(\frac{(d/a)}{\sin(d/a)} \right)^{1/2} \quad (B-14)$$

where

$$x = (ka/2)^{1/3} (d/a), \text{ and}$$

$$q = -i(ka/2)^{1/3} \Delta$$

The complex factors t_s are found from the roots of

$$w_1'(t) - qw_1(t) = 0 \quad (B-15)$$

The representation of the attenuation function given above is valid everywhere on the globe except near the antipode. The electric and magnetic field \vec{H}_{bt} and \vec{E}_{bt} correspond to the fields produced at point P by a transmitter at point B for the homogeneous earth with normalized surface impedance Δ . The field components H'_{at} and E'_{at} are the fields produced at point P by a transmitter at A for an inhomogeneous smooth earth with normalized surface impedance Δ' which is a function of position. Over the surface of the sphere it is assumed that the tangential field vectors satisfy the approximate Leontovich boundary condition

$$\vec{i}_r \times \vec{H}_{bt} = \eta \Delta \vec{E}_{bt} \quad (B-16)$$

$$\vec{i}_r \times \vec{H}'_{at} = \eta \Delta' \vec{E}'_{at} \quad (B-17)$$

where $\eta = \sqrt{\mu_0/\epsilon_A}$, ϵ_A being the electric permittivity of air.

Making use of Equations B-16 and B-17, Equation B-11 becomes

$$I_a I_b (Z'_{ab} - Z_{ab}) = \left(1 + \frac{1}{ikd} - \frac{1}{k^2 d^2}\right)^{-1} Z \iint_S (\vec{H}'_{at} \cdot \vec{H}_{bt}) (\Delta' - \Delta) dS \quad (B-18)$$

This is the result Wait obtained except for the factor in front of the integral. Over almost the entire range this factor is very close to unity in amplitude but does have a phase factor different from zero for distances up to 100 wave lengths ($k = 2\pi/\lambda$). The amplitude and phase as a function of kd are shown in Table B-1 as a function of kd . Since one degree of phase is equivalent to ~ 28 ns at $f \approx 100$ kHz, it would appear that this term should not be neglected for the present Loran-C calculations.

The next step in Wait's development is to express the tangential magnetic field vectors at the point P in terms of the attenuation functions $W(s, \Delta)$ and $W'(\ell, \Delta, \Delta')$;

Table B-1. Amplitude and phase as a function of kd .

kd	$(1 + \frac{1}{ikd} - \frac{1}{k_d^2})^{-1}$		$(1 + \frac{1}{ikd})$	
	Amp	Phase ($^\circ$)	Amp	Phase ($^\circ$)
.1	.01005	174	10.04988	-84.3
.3	.09393	162	3.48010	-73.3
.5	.27735	146	2.23607	-63.4
1.0	1.00000	90	1.41421	-45.0
2.0	1.10940	33.7	1.11803	-26.6
4.0	1.03065	14.9	1.03078	-14.0
7.0	1.01015	8.3	1.01015	- 8.13
10	1.00409	5.8	1.00499	- 5.7
15	1.00222	3.83	1.00222	- 3.81
20	1.00125	2.87	1.00125	- 2.86
30	1.00056	1.91	1.00056	- 1.91
40	1.00031	1.43	1.00031	- 1.43
50	1.00020	1.15	1.00020	- 1.15
70	1.00010	.82	1.00010	- .82
100	1.00005	.57	1.00005	- .57
150	1.00002	.38	1.00002	- .38
200	1.00001	.29	1.00001	- .29
300	1.00001	.19	1.00001	- .19

$$\vec{H}_{bt} = \frac{ikI_b h_b}{2\pi s} e^{-iks} \left(1 + \frac{1}{iks}\right) W(s, \Delta) (\vec{i}_r \times \vec{i}_s) \quad (B-19)$$

and

$$\vec{H}_{at} = \frac{ikI_a h_a}{2\pi \ell} e^{-ik\ell} \left(1 + \frac{1}{ik\ell}\right) W(\ell, \Delta, \Delta') (\vec{i}_r \times \vec{i}_\ell) \quad (B-20)$$

where \vec{i}_s and \vec{i}_ℓ are unit vectors in the directions of increasing s and ℓ , respectively. Inserting equations B-19 and B-20 into B-18 leads to the result

$$W'(d, \Delta, \Delta') = W(d, \Delta) + \left(1 + \frac{1}{ikd} - \frac{1}{k^2 d^2}\right)^{-1} \frac{ikd}{2\pi} \iint_s \frac{e^{-ik(s+\ell-d)}}{s\ell} \\ \cdot (\Delta' - \Delta) \left(1 + \frac{1}{iks}\right) \left(1 + \frac{1}{ik\ell}\right) W(s, \Delta) W'(\ell, \Delta, \Delta') \cos \delta \, dS \quad (B-21)$$

where

δ is the angle between \vec{i}_s and \vec{i}_ℓ .

This is an integral equation that could possibly be solved iteratively on a modern high-speed computer. However, the standard procedure is to simplify the integral by employing a stationary phase approximation.

Wait's argument is as follows (Reference 4-1):

The function $\exp\{-ik(s + \ell - d)\}$ is rapidly varying compared with other factors in the integrand. Therefore, one may expect that the principal contribution to the integrand will occur when $(s + \ell) \cong d$, provided that the surface impedance contrast $(\Delta' - \Delta)$ does not change rapidly in a direction transverse to the path. Therefore, in the other factors in the integrand ℓ may be replaced by α and s by $d - \alpha$, where α is the great circle distance from A to the point \underline{Q} on the great circle between A and B. (The arc \underline{OQ} is perpendicular to AB.) Furthermore, over most of the region of integration, $(1/ks)$ and $(1/k\ell)$ can be neglected compared with unity and, finally, $\cos \delta$ is replaced by -1 .

We follow Wait for the moment, except that we will not ignore $1/ks$, $1/k\ell$, or $1/kd$ with respect to unity. The reduced form of the integral equation is

$$W'(d, \Delta, \Delta') = W(d, \Delta) - \left(1 + \frac{1}{ikd} - \frac{1}{k^2 d^2}\right)^{-1} \frac{ikd}{2\pi} \iint_S \frac{e^{-ik(s+\ell-d)}}{\alpha(d-\alpha)} \cdot (\Delta'(\alpha) - \Delta) W(d-\alpha, Z) W'(\alpha, \Delta, \Delta') \left(1 + \frac{1}{ik(d-\alpha)}\right) \left(1 + \frac{1}{ik\alpha}\right) dS \quad (B-22)$$

where all quantities except the exponential factor are now functions only of α , the measure of distance from point A to B along the great circle path (see Figure B-2).

Wait then proceeds to integrate over the transverse coordinate y to obtain a final integral of the form

$$W'(d, \Delta, \Delta') = W(d, \Delta) - \left(1 + \frac{1}{ikd} - \frac{1}{k^2 d^2}\right) \left(\frac{ikd}{2\pi}\right)^{1/2} \int_{\alpha_1}^{\alpha_2} (\Delta'(\alpha) - \Delta) \cdot W(d-\alpha, \Delta) W'(\alpha, \Delta, \Delta') \left(1 + \frac{1}{ik\alpha}\right) \left(1 + \frac{1}{ik(d-\alpha)}\right) \frac{d\alpha}{\sqrt{\alpha(d-\alpha)}} \quad (B-23)$$

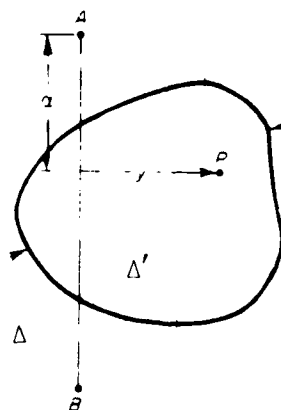


Figure B-2. Plane view of the inhomogeneous surface showing the coordinates α and y and the boundary for the inhomogeneous region.

As long as the limits of integration do not include $\alpha=0$ or $\alpha=d$, the integral equation appears perfectly well behaved. In fact, when $(k\alpha)^{-1}$ and $(k(d-\alpha))^{-1}$ are ignored with respect to unity as was done by Wait, the singularity of $\alpha=d$ is still integrable.

When the function $\Delta'(\alpha)$ is approximated by a series of constant Δ segments, the integral Equation B-23 can be rewritten in terms of a set of multiple integrals which then include the singularity. The question then is, "Where did the nonintegrable singularity come from?" In fact, it does not exist and is only a result of the stationary phase approximation being applied in a region where more caution is necessary. To see this, go back to Equation B-21. We will examine the integral in the vicinity of either $\alpha=0$ or $\alpha=d$ (ie, either is the neighborhood of Point A or B) with the assumption that Δ', Δ is not zero but does not vary rapidly over a small distance e/k . Figure B-3 shows the approximate geometry (assuming flat earth) for the vectors $\bar{\ell}$ or \bar{s} in the vicinity of A.

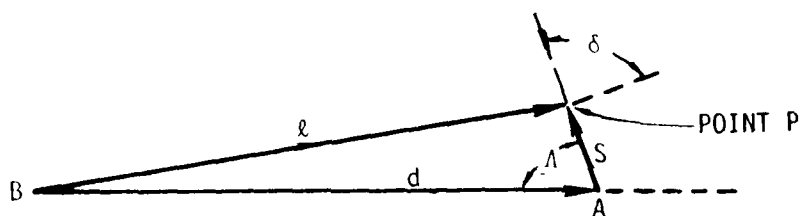


Figure B-3. Geometry near singular point.

In terms of the angle A we can express ℓ and $\cos \delta$ as

$$\ell \approx d - s \cos A \quad (B-24)$$

using the law of cosines and the fact that $\frac{s}{d}$ and $\frac{s}{\ell}$ are much less than unity and

$$\cos \delta \approx -\cos A \quad (B-25)$$

The portion of the surface integral in the vicinity of Point A can then be written in the form

$$I_A = K \int_0^{\epsilon/k} ds \int_0^{2\pi} d\Lambda e^{-iks(1-\cos\Lambda)} \cos\Lambda \left(1 + \frac{1}{iks}\right) \quad (B-26)$$

where

$$K = \left(1 + \frac{1}{ikd} - \frac{1}{k^2 d^2}\right)^{-1} \frac{ik}{2\pi} \left(\Delta'(A) - \Delta\right) \left(1 + \frac{1}{ikd}\right) \cdot$$

$$\bullet W(d, \Delta) W'(0, \Delta, \Delta') \quad (B-27)$$

The integral over Λ can be done first:

$$\int_0^{2\pi} e^{iks \cos\Lambda} \cos\Lambda d\Lambda = J_1(ks) \quad (B-28)$$

where $J_1(x)$ is the Bessel function of order 1. Then I_A becomes

$$I_A = K \int_0^{\epsilon/k} e^{-iks} J_1(ks) \left(1 + \frac{1}{iks}\right) ds$$

The term $e^{-iks} J_1(ks)$ can be expanded in a power series and then integrated term by term with the result

$$I_A = \frac{K}{k} \left\{ -\frac{i\epsilon}{2} - \frac{3i\epsilon^3}{48} - \frac{\epsilon^4}{24} + \frac{7i\epsilon^5}{384} + \dots \right\} \quad (B-29)$$

where $\epsilon = k\Delta r$. For $\epsilon \ll 1$ this can be truncated after two terms to give

$$I_A \approx -\frac{iK\epsilon}{2k} \left(1 + \frac{3\epsilon^2}{24} + \dots\right) \quad (B-30)$$

It is instructive to contrast this result with the value which would be obtained from Wait's original development if it were expanded around one of the singular points. Ignoring $\frac{1}{ikd}$, $\frac{1}{ik\alpha}$, $\frac{1}{ik(d-\alpha)}$ with respect to unity in Equation B-23 as Wait did we obtain

$$I'_A \approx K' \int_0^{\Delta R} \frac{d\alpha}{\sqrt{\alpha(d-\alpha)}} \quad (B-31)$$

* $W(0, \Delta) = W'(0, \Delta', \Delta) = 1$.

where

$$K' = \left(\frac{ikd}{2\pi} \right)^{1/2} W(d, \Delta) W'(\alpha, \Delta, \Delta') (\Delta' (A) - \Delta) . \quad (B-32)$$

The integral in Equation B-31 can be easily evaluated with the result:

$$I'_A \approx K' \left\{ \sin^{-1} \left(\frac{2\Delta R}{d} - 1 \right) + \frac{\pi}{2} \right\} . \quad (B-33)$$

For values of $|\frac{\Delta R}{d}| \ll 1$ this can be expanded to become

$$I'_A = 2K' \sqrt{\Delta R/d} \quad (B-34)$$

We then find that the ratio I_A/I'_A becomes

$$I_A/I'_A \sim \left(1 + \frac{1}{ikd} - \frac{1}{k^2 d^2} \right)^{-1} \left(1 + \frac{1}{ikd} \right) \frac{1}{4} \sqrt{\frac{k\Delta R}{2\pi i}} . \quad (B-35)$$

From Table B-1 for $kd > 4$ the first two terms effectively cancel and

$$I_A/I'_A \sim \frac{1}{4} \sqrt{\frac{\Delta R}{\lambda i}} \quad (B-36)$$

The ratio of the two terms has a phase of -45 degrees and depending on the wavelength λ and ΔR used can be quite small in magnitude, although the actual importance of the contribution to the integral must be tested by further numerical analysis. It is possible that the contributions to the integral in the vicinity of $\alpha = 0$ and $\alpha = d$ may make an important modification to the resulting solutions, along with the inclusion of the extra propagation terms within the integrand.

APPENDIX C

DETAILS OF INTEGRAL EQUATION FORMULATION

Integral Derivation

The only readily available documentation for the HUFLOC code is found in Reference C-1 although Johler (Ref. C-2) has written a report attempting to clarify some of the more difficult inputs. Unfortunately, there are several typographical and/or algebraic errors in Ref. C-1. Examination of the INEQ2E coding in the HUFLOC program indicates that most of the errors were detected and the corrections incorporated into the computer code. This appendix traces the important steps in the derivation of the integral equation for $W(0)$, the attenuation function for the inhomogeneous and irregular surface as defined by Johler and Berry. All terms will initially be retained in order to indicate the differences from the original text in Reference C-1.

The starting point is Equation 2.21 of Reference C-1, which is rewritten in the form

$$W(0)-1 = - \frac{ik_1}{2\pi} \int_{S_0} W(Q) \exp \left[-ik_1(r_1+r_2-r_0) \right] \\ \cdot \left[\Delta + \left(1 + \frac{1}{ik_1 r_2} \right) \frac{\partial r_2}{\partial n} \right] \frac{r_0 dA}{r_1 r_2} \quad (C-1)$$

- C-1. J. R. Johler and L. A. Berry, "LORAN-D Phase Corrections over Inhomogeneous, Irregular Terrain," ESSA Tech. Report IER59-ITSA56, 1967.
C-2. J. R. Johler, CPRL, 77-9, December 1, 1977.

where Δ is the normalized surface impedance.

In obtaining the equation Johler and Berry made use of an approximate boundary condition of the form

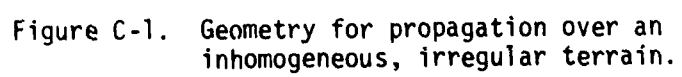
$$\frac{\partial E}{\partial n} \doteq ik_1 \Delta E \left\{ 1 + \left(\frac{\partial z}{\partial s} \right)^2 \right\}^{-1/2} \approx ik_1 \Delta E \quad (C-2)$$

where k_1 is the wave number in air, s is the distance along the propagation path, and z is the terrain elevation above the reference spherical surface. The assumption that the square root term is essentially unity requires that the slope at any point must be quite small. For 1% error this means that $\left| \frac{\partial z}{\partial s} \right| \leq 0.15$. This condition may not be met by the terrain along an arbitrary path. Moreover, the inclusion of this term would have simplified the integral somewhat at a later point. The distances r_0 , r_1 , and r_2 are defined in Figure C-1. The transmitter (source) is at point S, the receiver (observer) is at point O and the integration point is Q. In the figure the barred quantities (i.e., \bar{O} vs. O) denote points or distance for which the observation point is on the surface. For this appendix we shall be interested only in the observer on the surface and we will drop the bar notation. Equation C-1 is an integral equation for W but the integral is over a surface rather than along a single path.

The accepted (i.e., normal mathematical and numerical) technique followed to obtain a solution for W is based on the assumption that variations in the surface physical parameters are negligible in the direction transverse to the great circle path connecting S to O. Following Johler and Berry we first project the integration surface S_0 to the surface of the terrestrial sphere of radius a_e and define distance r'_0 , r'_1 , and r'_2 as great circle arcs between the projections of S and O, S and Q, and Q and O. First note that

$$\hat{n} \cdot \hat{e}_r dA = \left(1 + \frac{z}{a} \right)^2 dA' \quad (C-3)$$

where \hat{n} is the unit vector normal to the surface dA , \hat{e}_r is the unit vector in the radial direction and z is the height of dA above the reference sphere. The term $\hat{n} \cdot \hat{e}_r$ takes into account any tilting of the original



surface and $(1 + \frac{z}{a})^2$ accounts for the stretching (shrinking) of the spherical surface. In general $[(1 + \frac{z}{a})^2 - 1]$ is very small ($\sim 10^{-3}$ or less) and can be ignored. The other term $(\hat{n} \cdot \hat{e}_r)$ is always less than or equal to unity and will appear in the denominator of the integral over S'_0 . Continuing to follow Johler and Berry we make the following change of variables.

$$\left. \begin{aligned} r'_2 + r'_1 &= r'_0 \cosh u \\ r'_2 - r'_1 &= r'_0 \cos v \end{aligned} \right\} \quad (C-4)$$

For a plane surface the element of area dA' can be written as

$$dA' = r'_1 r'_2 du dv. \quad (C-5)$$

This form is used in the present case since most of the contribution to the surface integral is expected to occur on or in the vicinity of the great circle path connecting 0 to S. With these changes Equation C-1 becomes

$$\begin{aligned} W(0)-1 &= -\frac{ik_1 r_0}{2\pi} \int_{S'_0} \frac{r'_1 r'_2}{r_1 r_2} W(Q) \exp \left\{ -ik_1 r'_0 (\cosh u - 1) \right\} \\ &\times \exp \left\{ ik_1 \left[(r_0 - r'_0) - (r_1 - r'_1) - (r_2 - r'_2) \right] \right\} \frac{(1 + \frac{z}{a})^2}{\hat{n} \cdot \hat{e}_r} \\ &\times \left\{ \Delta + \left(1 + \frac{1}{ik_1 r_2} \right) \frac{\partial r_2}{\partial n} \right\} du dv. \end{aligned} \quad (C-6)$$

The integration limit for v and u are taken as $0 \leq v \leq \pi$ and $-\infty \leq u \leq \infty$, the latter clearly showing the use of a flat plane approximation. It is assumed that any error arising from the use of the plane vs. sphere will be washed out by the rapid oscillation caused by the term $\exp -ik_1 r'_0 (\cosh u - 1)$ as u becomes large, corresponding to contributions to the integral being negligible for points far off the great circle path.

It is now assumed that the major contribution to the integral will occur only along the great circle path. The portion of the integrand given by

$$I_1 = \frac{-ik_1 r_0}{2\pi} \left(\frac{r'_1 r'_2}{r_1 r_2} \right) W(Q) \frac{(1 + \frac{h}{a})^2}{\hat{n} \cdot \hat{e}_r} \exp \left\{ ik_1 [(r_0 - r'_0) - (r_1 - r'_1) - (r_2 - r'_2)] \right\} \\ \times \left\{ \Delta + \left(1 + \frac{1}{ik_1 r_2} \right) \frac{\partial r_2}{\partial n} \right\} \quad (C-7)$$

is written only in terms of the variable v on the great circle path between 0 and S where, since $u = 0$ in the saddle point approximation,

$$r'_0 - r'_1 - r'_2 = 0. \quad (C-8)$$

Then the double integral breaks into the product of two single integrals

$$W(0) - 1 = \int_0^\pi I_1 dv \times \int_{-\infty}^{+\infty} \exp \left\{ -ik_1 r'_0 (\cosh u - 1) \right\} du. \quad (C-9)$$

Within the exponential, $\cosh u$ is expanded with only the first 2 terms being kept so that

$$\begin{aligned} & \int_{-\infty}^{+\infty} \exp \left\{ -ik_1 r'_0 (\cosh u - 1) \right\} du \\ & \approx \int_{-\infty}^{+\infty} \exp \left\{ -ik_1 r'_0 u^2/2 \right\} du = \left(\frac{2\pi}{ik_1 r'_0} \right)^{1/2} \end{aligned} \quad (C-10)$$

Then Equation C-9 becomes

$$\begin{aligned} W(0) - 1 &= -\frac{r_0}{r'_0} \sqrt{\frac{ik_1 r'_0}{2\pi}} \int_0^\pi \frac{r'_1 r'_2}{r_1 r_2} W(Q) \exp \left\{ -ik_1 (r_1 + r_2 - r_0) \right\} \\ &\times \left\{ \Delta + \left(1 + \frac{1}{ik_1 r_2} \right) \frac{\partial r_2}{\partial n} \right\} \frac{(1 + \frac{z}{a})^2}{\hat{e}_r \cdot \hat{n}} d\Omega. \end{aligned} \quad (C-11)$$

To obtain the form given by Johler and Berry the additional change of variables and definitions is made.

$$\left. \begin{aligned} x &= r'_0 \\ s &= r'_1 \\ x-s &= r'_2 \end{aligned} \right\} \quad (C-12)$$

from which it can be shown that

$$d\Omega = \frac{2ds}{\sin \nu} = \frac{ds}{\sqrt{s(x-s)}}$$

using

$$\cos v = \frac{r_2' - r_1'}{r_0'} = \frac{x - 2s}{x}.$$

With this change we obtain

$$\begin{aligned} W(0) - 1 = & \frac{-r_0}{x} \sqrt{\frac{ik}{2\pi}} \int_0^x W(s) \exp \left\{ -ik_1(r_1 + r_2 - r_0) \right\} \\ & \times \left\{ \Delta + \left(1 + \frac{1}{ik_1 r_2} \right) \frac{\partial r_2}{\partial n} \right\} \frac{\sqrt{x} ds}{\sqrt{s(x-s)}} \times \left(\frac{r_1' r_2'}{r_1 r_2} \right) \frac{(1 + \frac{z}{a})^2}{\hat{e}_r \cdot \hat{n}} \end{aligned} \quad (C-13)$$

This is identical to equation 2.28 in Johler and Berry except for the misprint in the integration limit (Π should be x) and the omission of the two terms

$$\left(\frac{r_1' r_2'}{r_1 r_2} \right) \frac{(1 + \frac{z}{a})^2}{\hat{e}_r \cdot \hat{n}}.$$

(C-14)

In examining the INEQ2E coding we have found that these terms are included except for $(1 + \frac{z}{a})^2$. Considering the magnitude of this term, the omission appears justified. The largest possible value for h in the surface integral would be less than 10 kilometers so that

$$\left(1 + \frac{z_{\max}}{a} \right)^2 - 1 \approx .003 \quad (C-15)$$

In general this factor would be much smaller.

It can be shown that the term $(\hat{e}_r \cdot \hat{n})^{-1}$ can be evaluated as

$$(\hat{e}_r \cdot \hat{n})^{-1} = \left\{ 1 + \left(\frac{\partial z}{\partial s} \right)^2 \right\}^{1/2} \quad (C-16)$$

Further, in the numerical evaluation of $\frac{\partial r_2}{\partial n}$ there is a factor of the form

$$\left\{ 1 + \left(\frac{a_e \frac{\partial z}{\partial s}}{a_e + z} \right)^2 \right\}^{-1/2} \approx \left\{ 1 + \left(\frac{\partial z}{\partial s} \right)^2 \right\}^{-1/2} \quad (C-17)$$

The inclusion of the term given by C-17 and the omitted term in the surface boundary condition would have canceled the term arising from $(e_r \cdot n)^{-1}$. In Reference C-2 Johler attempts to justify the omission of two of the three terms by arguing that the cancellation would have occurred had he included them. Unfortunately, one is retained in the coding, $(\hat{e} \cdot \hat{n})^{-1}$ which places an inordinate weight in the region where the terrain is changing rapidly.

Calculation Procedures in the GFE Program

The important formulae and numerical procedures in the GFE computer program (HUFLOC) are now defined. The effort was performed originally to compare the program model with the theoretical formulation.

The geometric quantities are defined using standard trigonometric formulas, i.e.

$$r_0 = \sqrt{2a_e(r_e + z_i) \left(1 - \cos \left(\frac{x_i}{a_e} \right) \right) + z_i^2} \quad (C-18)$$

$$r_1 = \sqrt{2a_e(a_e + z_k) \left(1 - \cos \left(\frac{x_k}{a_e} \right) \right) + z_k^2} \quad (C-19)$$

$$r_2 = \sqrt{2(a_e + z_i + h_r) \left(1 - \cos \left(\frac{x_i - x_k}{a_e} \right) \right) + (z_i + h_r - z_k)^2} \quad (C-20)$$

$$r = r_1 + r_2 - c_0 \quad (C-21)$$

where

a_e = equivalent earth's radius

z_i = elevation above the reference sphere at x_i

z_k = elevation above the reference sphere at x_k

h_r = receiver altitude (0 in our case)

A special routine is used to evaluate $(1 - \cos \theta)$ when θ is very small.

To obtain a numerical solution for C-13 we first rewrite it in the form

$$W(x) = 1 - B \int_0^x W(s) K(x,s) ds \quad (C-22)$$

where

$$B = e^{i\pi/4} \frac{r_0}{x} \sqrt{\frac{k_1}{2\pi}} \quad (C-23)$$

$$K(x,s) = \sqrt{\frac{x}{s(x-s)}} \left\{ \Delta + \left(1 + \frac{1}{ik_1 r_2} \right) \frac{\partial r_2}{\partial n} \right\} P \exp(-ik_1 r) \quad (C-24)$$

$$P = \frac{s(x-s)}{r_1 r_2} \frac{r_0}{x} \sqrt{1 + \left(\frac{\partial z}{\partial s} \right)^2} \quad (C-25)$$

$$r = r_1 + r_2 - r_0 \quad (C-26)$$

The solution will be obtained algebraically from the equation

$$W(x_1) = \left\{ 1 - B \sum_{\ell=0}^{i-1} W(x_\ell) A(x_i, s_\ell) \right\} \cdot \left\{ 1 + B A(x_i, x_i) \right\}^{-1} \quad (C-27)$$

Following Reference C-2 the $A(x_i, x_\ell)$ are determined by

$$W(x) A(x_i, x_\ell) = \int_{x_{\ell-1}}^{x_\ell} W(s) K(x_i, s) \alpha S \quad (C-28)$$

Defining the quantity $p = 2 - i \bmod 2$ such that $p = 1$ if i is odd and $p = 2$ if i is even we rewrite C-22 in the form

$$\begin{aligned} W(x_i) = & 1 - B \int_0^{x_2} W(s) F(x_i, s) \left\{ s(x_i - s) \right\}^{-1/2} ds \\ & - B \int_{x_2}^{x_{i-p}} W(s) F(x_i, s) \left\{ s(x_i - s) \right\}^{-1/2} ds \\ & - B \int_{x_{i-p}}^{x_{i-1}} W(s) F(x_i, s) \left\{ s(x_i - s) \right\}^{-1/2} ds \\ & - B \int_{x_{i-1}}^{x_i} W(s) F(x_i, s) \left\{ s(x_i - s) \right\}^{-1/2} ds, \end{aligned} \quad (C-28)$$

where

$$x_i = (i-1) \Delta x.$$

and

$$F(x_i, s) = P \exp(-ik_1 r) \left\{ \Delta + \left(1 + \frac{1}{ik_1 r_2} \right) \frac{\partial r_2}{\partial n} \right\} \quad (C-29)$$

The first integral has the form

$$\int_0^{x_2} s^{-1/2} f(s) ds$$

and can be integrated using the modified Gaussian integration formula in Reference C-3, formula 25.4.37 with $b=0$, $a=x_2$.

$$\int_0^{x_2} s^{-1/2} f(s) ds = \sqrt{x_2} \sum_{k=1}^N p_k f(x_k) + R \quad (C-30)$$

where $p_k = 2\omega_k$, ω_k are the gaussian weights of order $2N$ and

$$x_k = \xi_k^2 \Delta x$$

where ξ_k is the k^{th} positive zero of the Legendre polynomial of order $2N$. In INEQLE, $N = 5$ and the first integral becomes

$$\int_0^{x_2} W(s) f(x_i, s) [s(x_i - s)]^{-1/2} ds = x_2^{1/2} \sum_{k=1}^5 p_k W(x_k) F(x_i, x_k) (x_i - x_k)^{-1/2} \quad (C-31)$$

The second integral in equation (C-28) can be evaluated by the extended Simpson's rule [Reference C-3; p. 886, equation (25.4.6)]:

$$\int_{x_2}^{x_{i-p}} f(s) ds = \frac{x}{3} [f(x_2) + 4 [f(x_3) + f(x_5) + \dots]]$$

C-3. "Handbook of Mathematical Functions," Ed. M. Abramowitz and I.A. Stegun, NBS App. Math Series, 55, NBS, Washington, D.C. 1964.

$$\begin{aligned}
& + 2 \left[f(x_4) + f(x_6) + \dots \right] \\
& + f(x_{i-p}) \Big] . \qquad \qquad \qquad (C-32)
\end{aligned}$$

Note that $i-p$ is always an even integer. Then,

$$\begin{aligned}
& \int_{x_2}^{x_{i-p}} W(s) F(x_i, s) [s(x_i - s)]^{-1/2} ds = \\
& \frac{\Delta x}{3} \left[W(x_2) F(x_i, x_2) [x_2(x_i - x_2)]^{-1/2} \right. \\
& + \sum_{\ell=3}^{i-p-1} \frac{4}{p} W(x_\ell) F(x_i, x_\ell) [x_\ell(x_i - x_\ell)]^{-1/2} \\
& \left. + W(x_{i-p}) F(x_i, x_{i-p}) [x_{i-p}(x_i - x_{i-p})]^{-1/2} \right] \qquad (C-35)
\end{aligned}$$

Johler (References C-2) evaluates the third integral by a combination of Simpson's rule and the trapezoidal rule. To obtain sufficient points for the Simpson's rule integration the lower limit of integral 3 is changed to $t-p-1$, a correction term using the trapezoidal rule is added and the total is divided by 2. The result is

$$\begin{aligned}
& \int_x^{x_{i-1}} W(s) F(x_i, s) [s(x_i - s)]^{-1/2} ds = \\
& 1/2(p-1) \frac{\Delta x}{3} \left[W(x_i - x_2) F(x_i, x_i - x_2) [x_2(x_i - x_2)]^{-1/2} \right. \\
& + 4 W(x_i - x_3) F(x_i, x_i - x_3) [\Delta x(x_i - x_3)]^{-1/2} \\
& \left. + W(x_i - x_4) F(x_i, x_i - x_4) [x_4(x_i - x_4)]^{-1/2} \right]
\end{aligned}$$

$$+ \frac{3}{2} W(x_i - x_2) F(x_i, x_i - x_2) [x_2(x_i - x_2)]^{-1/2} \\ - \frac{3}{2} W(x_i - x_4) F(x_i, x_i - x_4) [x_4(x_i - x_4)]^{-1/2} \Bigg] .$$

It is not obvious that this technique is really more accurate than a trapezoidal integration over the original range of integration. In the form shown in equation C-34 note that $x_{i-j} = x_i - (i-j)\Delta x = x_i - x_{i-j+1}$ and $x_i - x_{i-j} = (i-j)\Delta x = x_{i-j+1}$. This integral is identically zero for $p = 1$ (i, odd).

The derivation of the formula representing the evaluation of the final integral in equation C-28 is still obscure even after studying Reference C-2. As Johler points out this integral requires special treatment because of the singularity at $x = x_i$. The formula given by Johler after much algebra is

$$\int_{x_{i-1}}^{x_i} W(s) F(x_i, s) [s(x_i - s)]^{-1/2} ds = \\ - \frac{2\sqrt{2}\Delta x}{15} W(x_i - x_3) F(x_i, x_i - x_3) [x_3(x_i - x_3)]^{-1/2} \\ + \frac{14\Delta x}{15} W(x_i - x_2) F(x_i, x_i - x_2) [x_2(x_i - x_2)]^{-1/2} \\ + 0.6 W(x_i) \int_{x_{i-1}}^{x_i} F(x_i, s) [s(x_i - s)]^{-1/2} ds \quad (C-35)$$

with

$$\int_{x_{i-1}}^{x_i} F(x_i, s) [s(x_i - s)]^{-1/2} ds =$$

$$2\sqrt{\frac{x_2}{x_i}} \left\{ \Delta(x_i) + \frac{\partial^2 z_i}{\partial x_i^2} \left[jk_1 \left(1 + \left[\frac{\partial z_i}{\partial x_i} \right]^2 \right) \right]^{-1} \right\} \quad (C-36)$$

Sensitivity to Surface Impedance and Terrain Models

A thorough sensitivity analysis of the integral equation program sensitivity to errors in defining input quantities (surface impedance and terrain) requires extensive parametric computer calculations. However, an initial insight can be gained by examining Equation C-11. The terrain and surface impedance definitions have their most important effect through the term, T , where

$$T = \left[\Delta + \left(1 + \frac{1}{jk_1 r_2} \right) \frac{\partial r_2}{\partial \hat{n}} \right]$$

Errors in defining T will result in errors in the integrand. The effect of errors will depend on where they occur in the integration interval. Fluctuating errors may tend to compensate one another. Bias or constant errors will produce a similar constant error in the result.

Impedance variations for a multilayer earth are discussed in Appendix D. Data there show variations in effective impedance amplitude and phase for various electrical properties and depths of surface and subsurface layers. The data show clearly that uncertainties in total soil depths and depth of saturated and unsaturated layers can produce phase uncertainties in the impedance values of 10ths of radians. This error, translated to an equivalent phase error in the definition of W would result in prediction phase errors of 100's of nanoseconds.

Effects of the term $\left[1 + \frac{1}{ik_1 r_2}\right] \frac{\partial r_2}{\partial n}$

can be estimated by comparing variations in it with the impedance, Δ .
Typical value of Δ are

σ (mhos/m)	ϵ/ϵ_0	Δ
10^{-4}	10	$0.19 + i .11$
10^{-3}	15	$0.054 + i 0.050$
10^{-2}	15	$0.016 + i 0.016$

Calculation of $\frac{\partial r_2}{\partial n}$ (for a receiver on the ground) is performed using

$$\frac{\partial r_2}{\partial n} = \left[a_e (1 - \cos \Delta\theta) + z_k - z_i \cos \Delta\theta + \frac{az'_k}{a + z_k} \right] \cdot \frac{1}{r_2} \quad (C-38)$$

where the geometric quantities are defined in Figure C-2. z'_k is the derivative of z_k with respect to s ,

$$r_2^2 = (a_e + z_k)^2 + (a_e + z_i)^2 - 2(a_e + z_k)(a_e + z_i) \cos \Delta\theta, \quad (C-39)$$

and

$$\Delta\theta = (x-s)/a_e. \quad (C-40)$$

Using Equations C-38 through C-40, the values in Table C-1 were computed for $\frac{\partial r_2}{\partial n}$ at various points along the path and various values of z_k , r_2 , and z'_k .

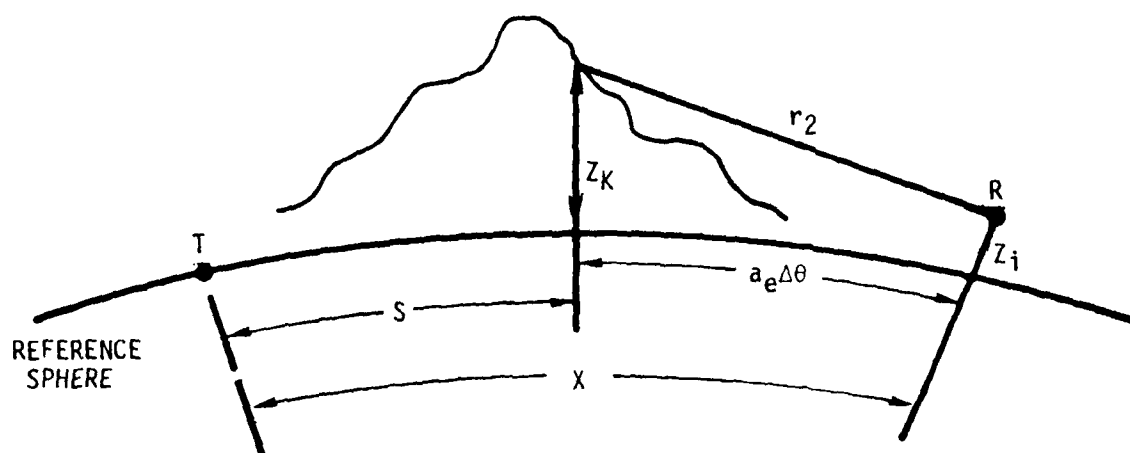


Figure C-2. Geometry used for defining variations in $\frac{\partial r_2}{\partial n}$.

$$\frac{\partial r_2}{\partial n}, z_k = 0$$

$\frac{z_k}{r_2(km)}$						
	0	0.01	0.1	0.2	0.3	0.4
20	0.002	0.012	0.096	0.184	0.264	0.339
100	0.008	0.017	0.103	0.190	0.270	0.345
200	0.016	0.025	0.110	0.197	0.277	0.351
300	0.024	0.033	0.118	0.204	0.284	0.358
500	0.039	0.049	0.133	0.218	0.297	0.371
700	0.055	0.064	0.148	0.233	0.311	0.384

$$\frac{\partial r_2}{\partial n}, z_k = 2.5 \text{ km}$$

$\frac{z_k}{r_2(km)}$						
	0	0.01	0.1	0.2	0.3	0.4
20	0.127	0.135	0.215	0.237	0.372	0.442
100	0.033	0.043	0.127	0.212	0.292	0.366
200	0.028	0.038	0.122	0.208	0.288	0.362
300	0.032	0.041	0.126	0.212	0.291	0.365
500	0.044	0.053	0.137	0.223	0.302	0.375
700	0.059	0.068	0.151	0.236	0.314	0.387

$$\frac{\partial r_2}{\partial n}, z_k = 5 \text{ km}$$

$\frac{z_k}{r_2(km)}$						
	0	0.01	0.1	0.2	0.3	0.4
20	0.251	0.260	0.332	0.406	0.475	0.540
100	0.058	0.067	0.150	0.235	0.313	0.386
200	0.041	0.050	0.134	0.219	0.298	0.372
300	0.040	0.050	0.134	0.219	0.298	0.372
500	0.049	0.059	0.142	0.227	0.306	0.379
700	0.062	0.072	0.154	0.239	0.317	0.390

Table C-1. Variation of $\frac{\partial r_2}{\partial n}$ due to variation in local terrain slope at various distances from the receiver.

Examination of the tabular values indicates that the variation of $\frac{\partial r_2}{\partial n}$ is about 0.8 to 0.9 times the variation in z'_k . To obtain an estimate of the sensitivity of the term T (Equation C-36) to errors in elevation values, we can use

$$z'_k = \frac{z_{k+1} - z_k}{d_k}, \quad (C-41)$$

where z_k and z_{k+1} are elevations at two adjacent points along the path and d_k is the spacing between them. Using C-40, the amplitude and phase variations in the term T as a function of the error in the difference ($z_{k+1} - z_k$) was computed for two typical situations. The results are shown in Figure C-3 and C-4. For a surface slope near zero, the phase and amplitude errors can be large for elevation errors as small as a few meters. For a nominal surface slope of 0.1, the phase errors are significantly reduced (due to the large nominal value of $\frac{\partial r_2}{\partial n}$) but Figure C-4 shows that even in this case, elevation errors measured in 10's of meters are significant.

One further point can be noted from Table C-1. When the slope is large the value of $\frac{\partial r_2}{\partial n}$ significantly exceeds Δ . This indicates that for a large portion of the path from Searchlight, Nevada to Ft. Cronkhite, California, the elevation values should dominate conductivity variations.

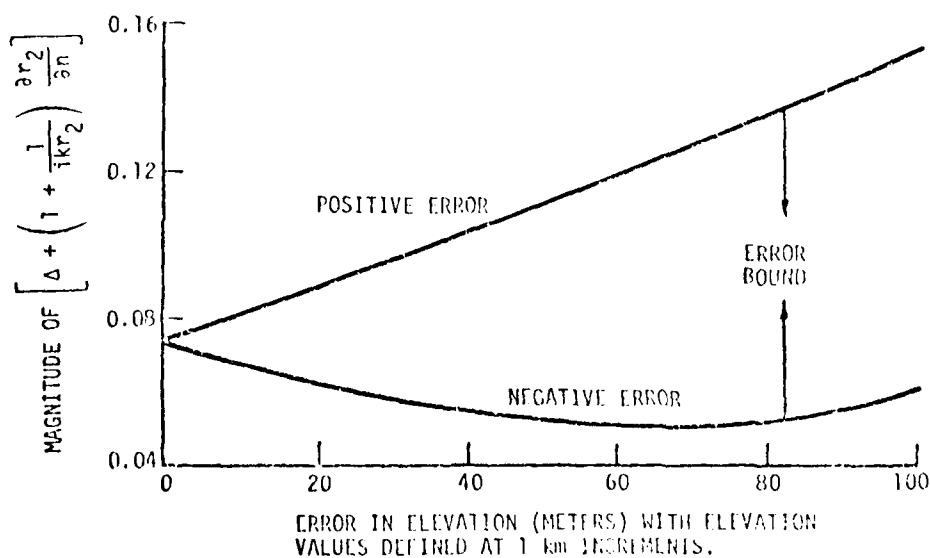
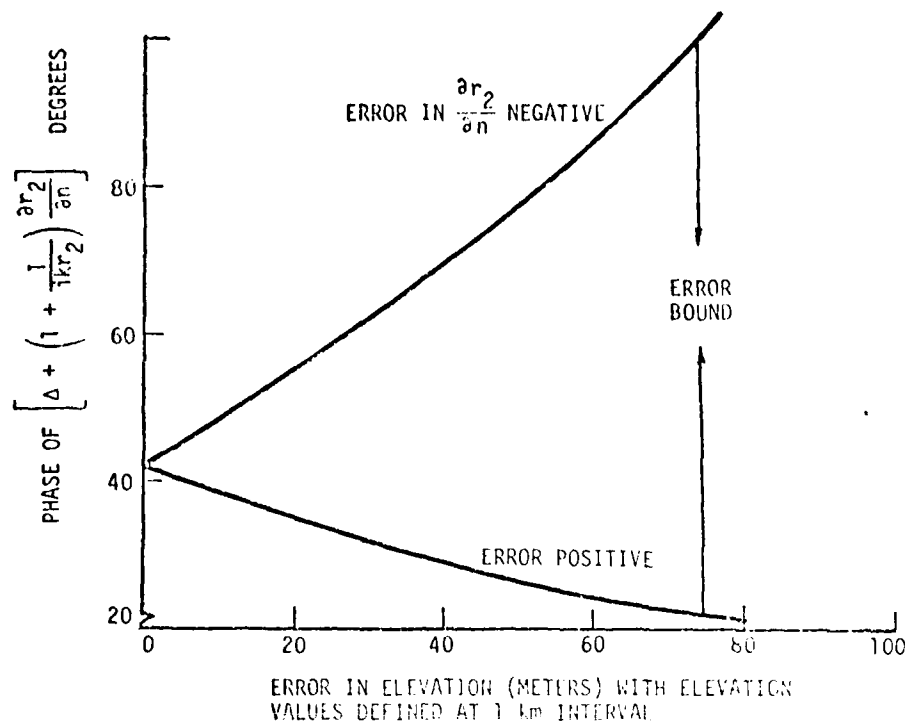


Figure C-3. Amplitude and phase errors of term T as a function of elevation error for $(\sigma = 10^{-3}, \epsilon/\epsilon_0 = 15, r_2 = 300 \text{ km}, \text{ and nominal slope } (z'_k = 0))$.

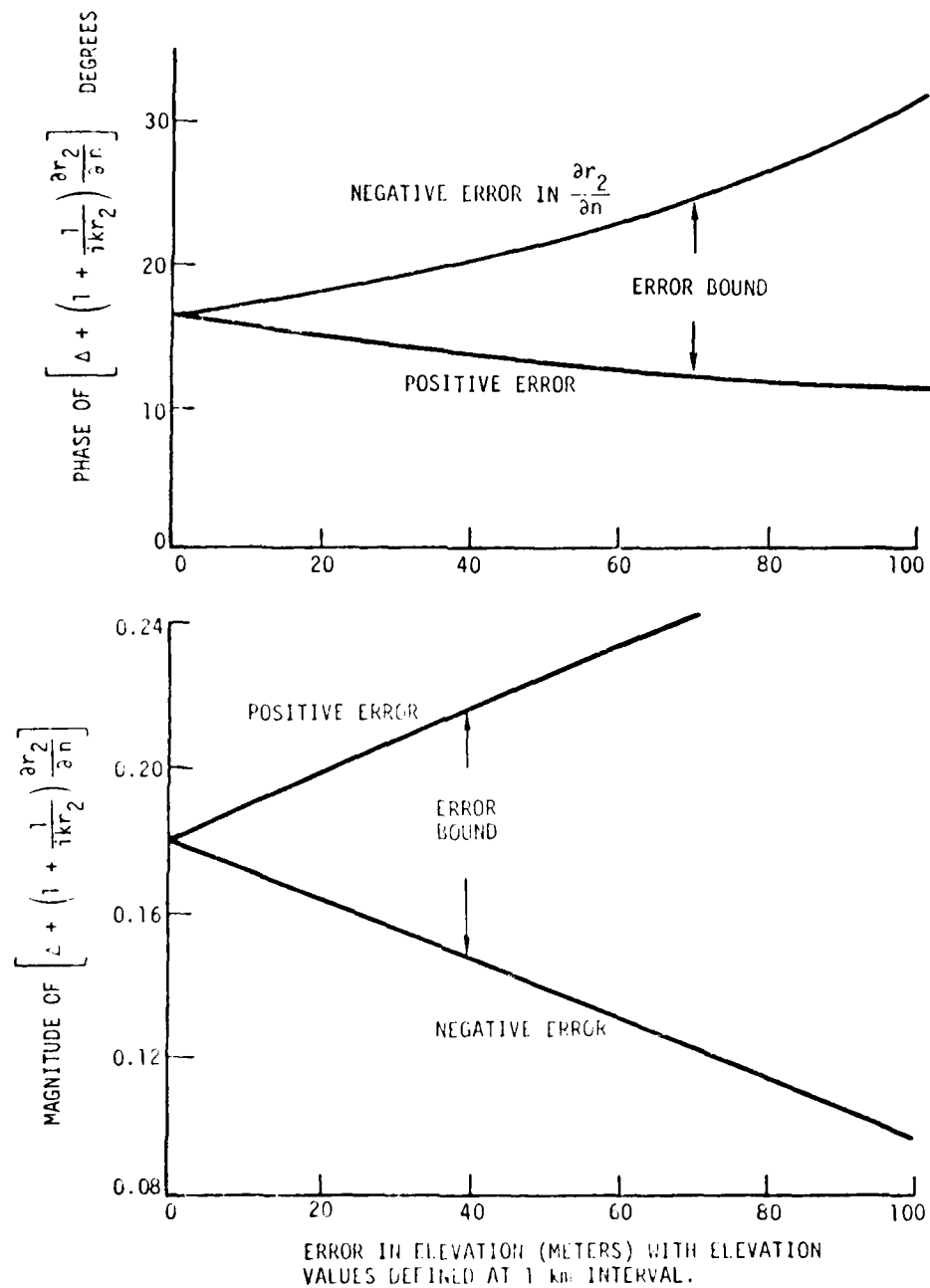


Figure C-4. Amplitude and phase errors of term T as a function of elevation error for ($\sigma = 10^{-3}$, $\epsilon/\epsilon_0 = 15$, $r_2 = 300$ km and nominal slope $z'_k = 0.1$).

APPENDIX D MULTILAYER IMPEDANCE

The electrical properties of the earth are inhomogeneous in the vertical direction, and the skin depth at 100 kHz is large enough to require consideration of the subsurface layers. Wait (Ref. D-1) has developed formulae for the effective surface impedance. The calculation requires an iterative solution for the effective impedance, Z_e , defined by

$$\begin{aligned} Z_e = Z_1 &= K_1 \frac{Z_2 + K_1 \tanh u_1 h_1}{K_1 + Z_2 \tanh u_1 h_1} \\ Z_2 &= K_2 \frac{Z_3 + K_2 \tanh u_2 h_2}{K_2 + Z_3 \tanh u_2 h_2} \\ Z_m &= K_m \frac{Z_{m+1} + K_m \tanh u_m h_m}{K_m + Z_{m+1} \tanh u_m h_m} \\ Z_{M-1} &= K_{M-1} \frac{K_M + K_{M-1} \tanh u_{M-1} h_{M-1}}{K_{M-1} + K_M \tanh u_{M-1} h_{M-1}} \end{aligned} \quad (D-1)$$

where layer 1 is the top layer, 2 the next layer and the M^{th} layer is the bottom layer, assumed to be semi-infinite.

The quantities are defined by

$$K_m = \frac{u_m}{\sigma_m + i \omega \epsilon_n} \quad (D-2)$$

$$u_m = (\lambda^2 + \gamma_m^2)^{1/2} \quad (D-3)$$

$$\gamma_m = (i \sigma \mu_m \omega - \epsilon_m \mu_m \omega^2)^{1/2} \quad (D-4)$$

$$\lambda = -i \gamma_0 \sin \theta \quad (D-5)$$

γ_0 is defined for the air above the surface

μ_m = permeability of the layer

ϵ_m = permittivity of the layer (farads/m)

D-1. Wait, J.R., *Electromagnetic Waves in Stratified Media*, 1962, Pergamon Press, New York, NY.

ω = wave frequency, radian

h_m = layer thickness (meters)

σ_m = layer conductivity (mhos/meter)

θ = angle of incidence of the plane wave on the earth's surface.

In the calculation for vertically polarized ground waves, it is assumed that $\sin \theta \approx 1$.

The solution is obtained by computing K_M , K_{M-1} , then Z_{M-1} , and continuing for the required number of layers.

The procedure has been used to calculate the effective normalized surface impedance for an assumed 3 layer model of the earth. The layers considered are unsaturated soil, saturated soil and bedrock. Figures D-1 through D-12 show the amplitude and phase of the surface impedance for a range of values of the electrical properties of each of the layers. σ_1 is the conductivity of the top layer, σ_2 the conductivity of the second layer, etc. The relative dielectric constant was assumed to be 15 in all cases. The graphical data indicate a significant sensitivity to the definition of layer thickness and electrical properties.

In the formulae on the various propagation models, the relative impedance Δ is used rather than Z_e . Δ is related to Z_e by

$$\Delta = Z_e / Z_{\text{air}} \quad (\text{D-6})$$

where

$$Z_{\text{air}} = \eta^{-1} \mu_0 / \epsilon_0 \quad (\text{D-7})$$

where η is the refractive index of air. For $u_1 h_1 \rightarrow \infty$, the formula for Δ approaches that of a single layer.

$$\Delta_1 = \sqrt{\frac{i\omega\eta^2\epsilon_0}{\sigma_g + i\epsilon_g\epsilon_0\omega}} \sqrt{1 - \frac{i\epsilon_0\eta^2\omega}{\sigma_g + i\epsilon_g\epsilon_0\omega}} \quad (\text{D-8})$$

AD-A084 338

GENERAL ELECTRIC CO. SANTA BARBARA CA TEMPO
LORAN-C SIGNAL ANALYSIS PROPAGATION MODEL EVALUATION.(U)
JUL 79 B GAMBILL, K SCHWARTZ
GE78TMP-51

F/6 20/14

UNCLASSIFIED

USCG -D-20-80

DOT-C6-64810-A

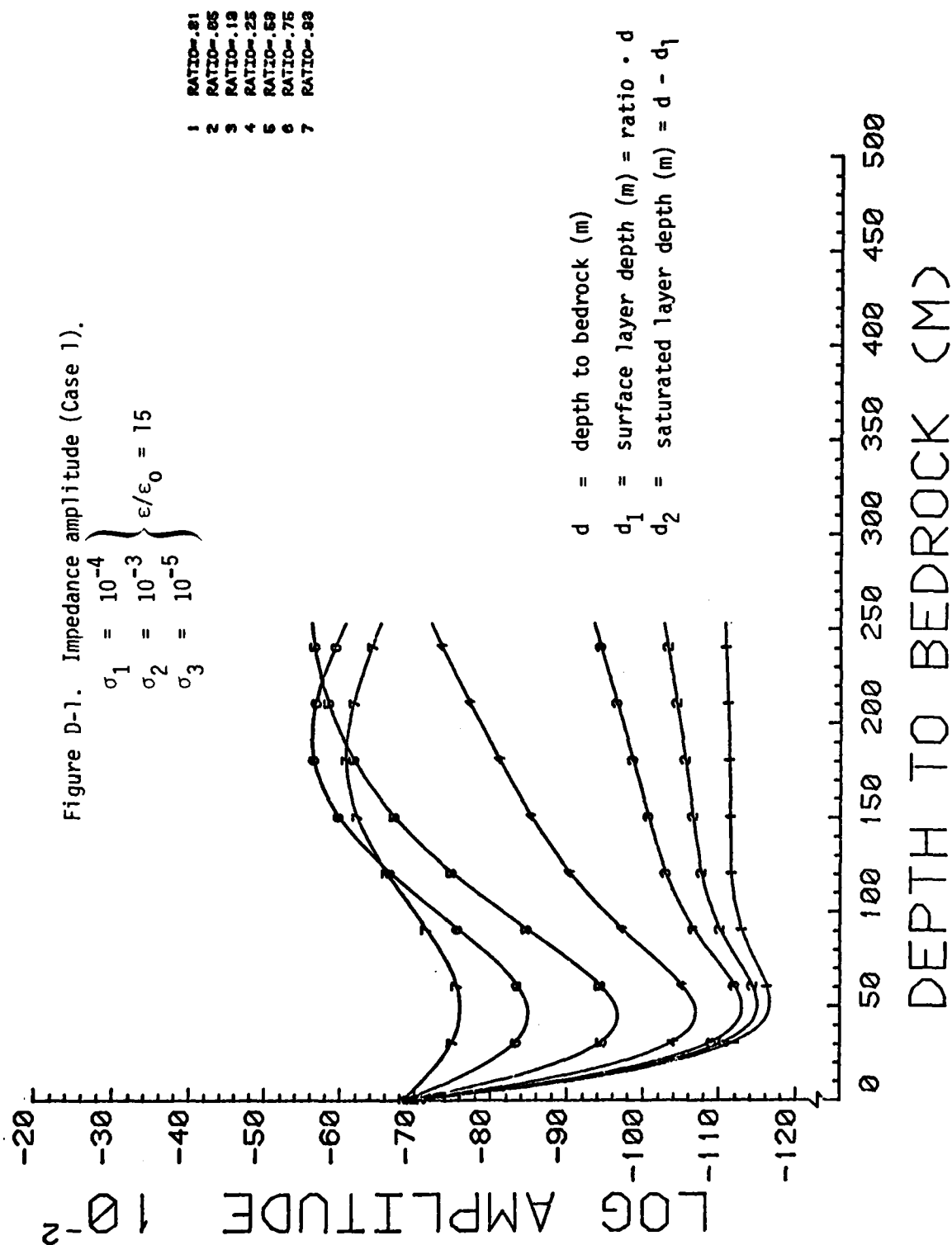
NL

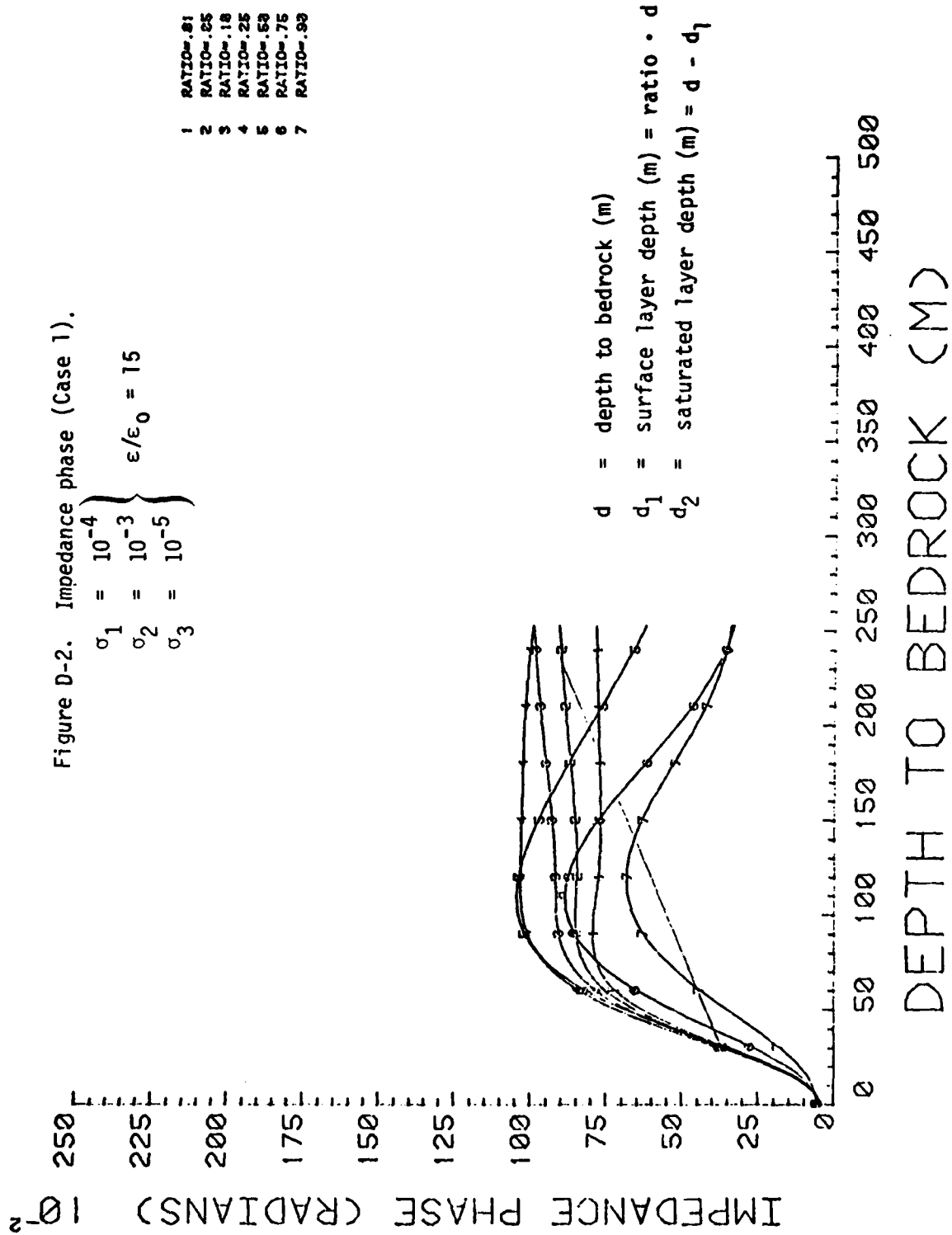
3 of 3

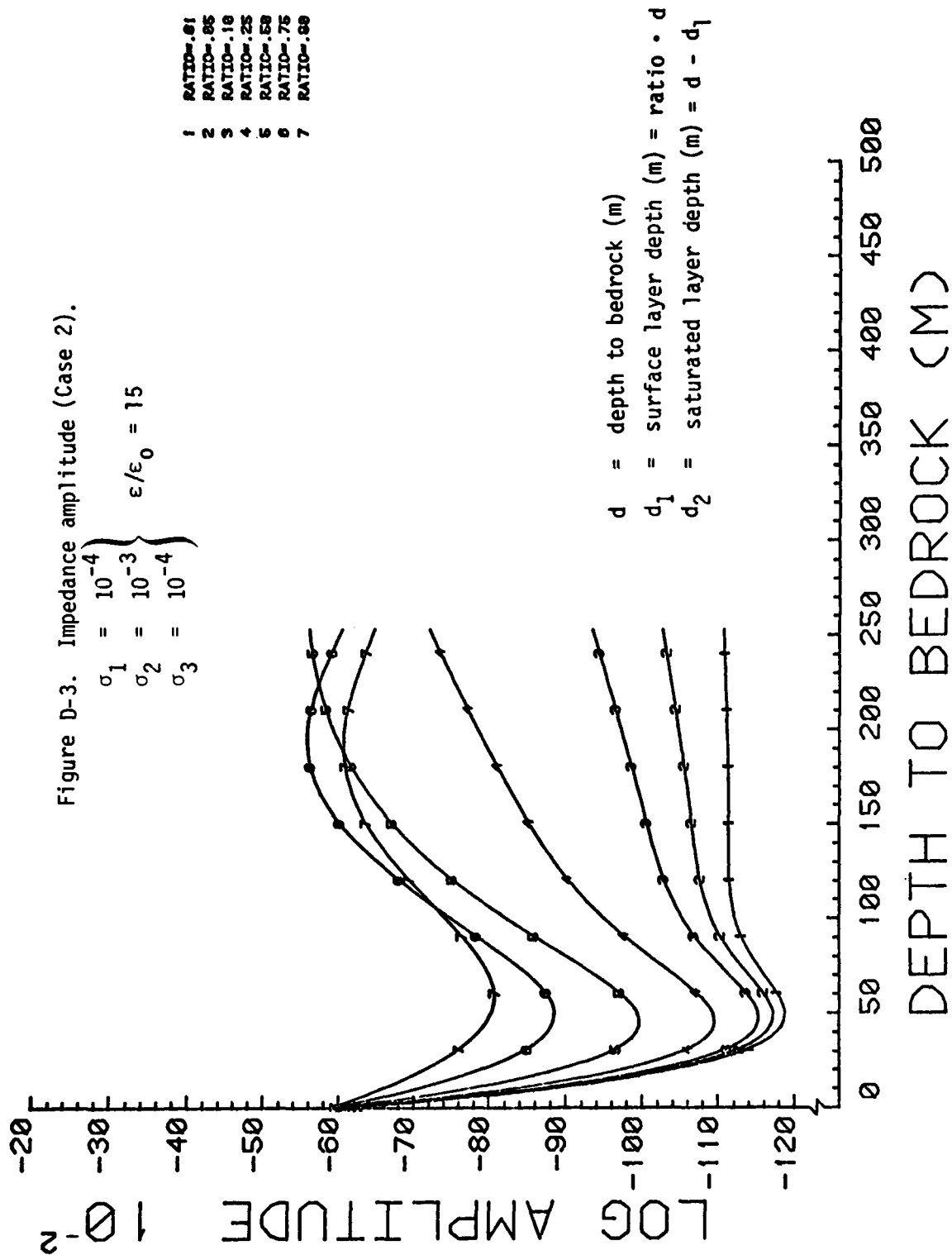
ALL INFORMATION CONTAINED HEREIN IS UNCLASSIFIED

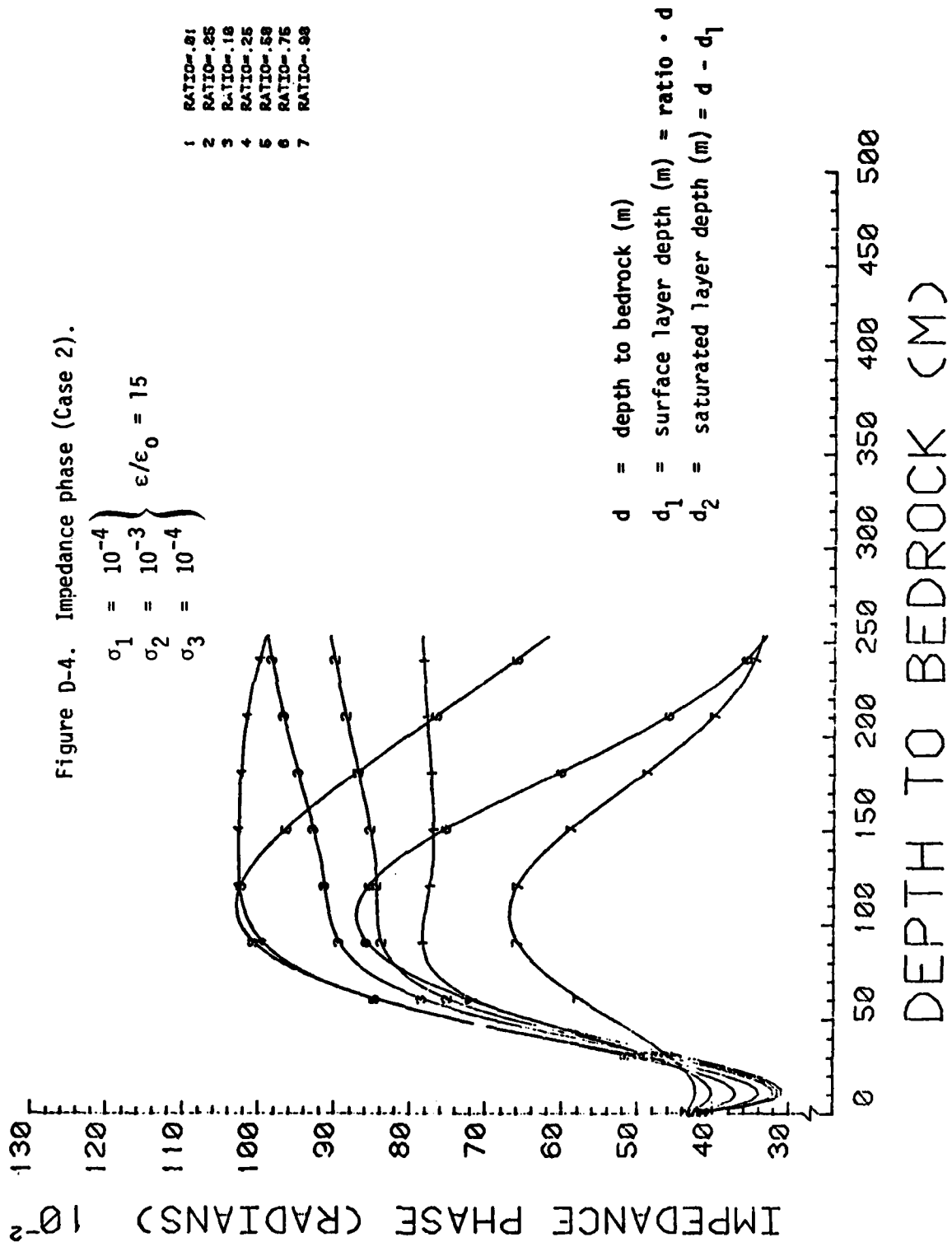


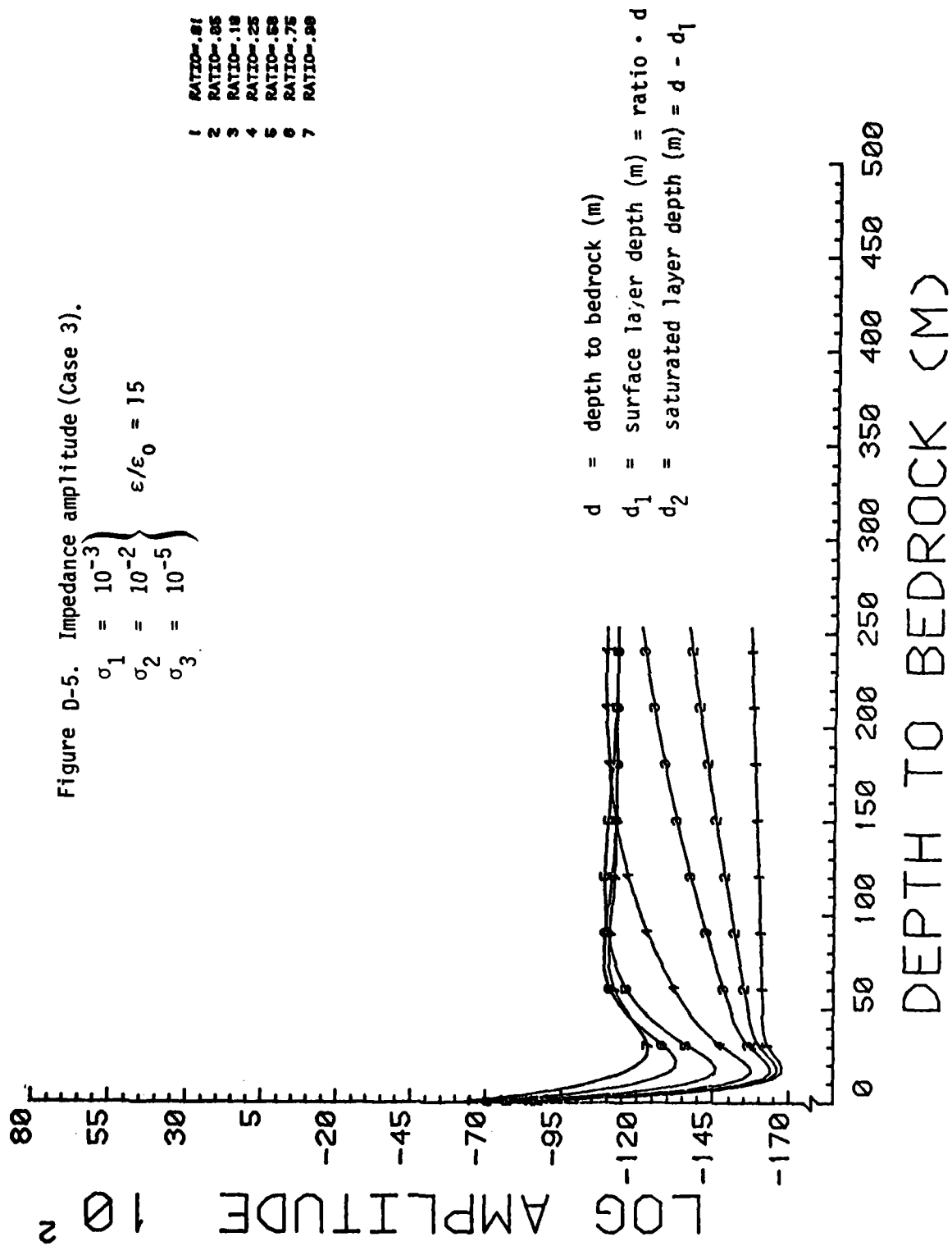
END
DATE
FILMED
6 80
DTIC

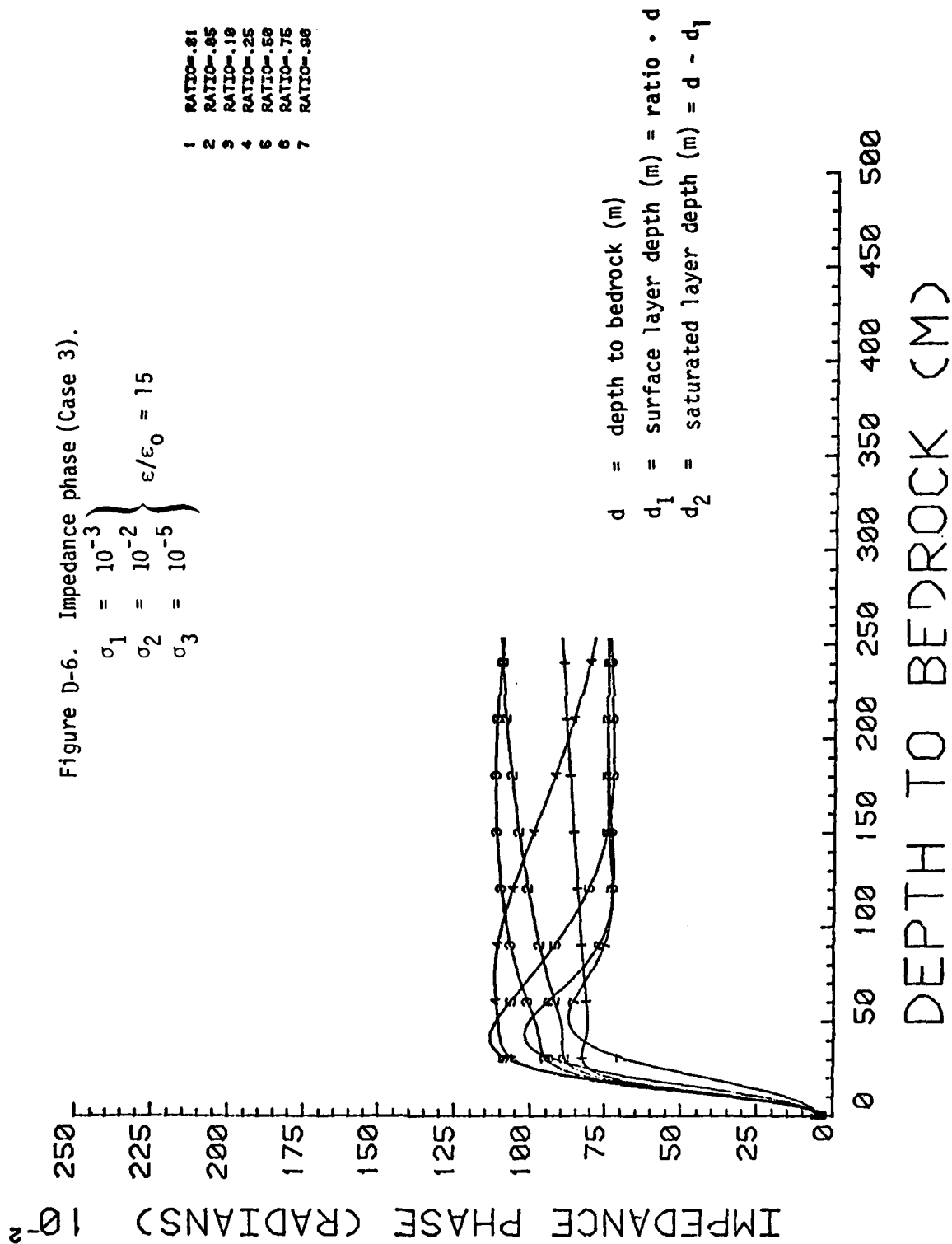


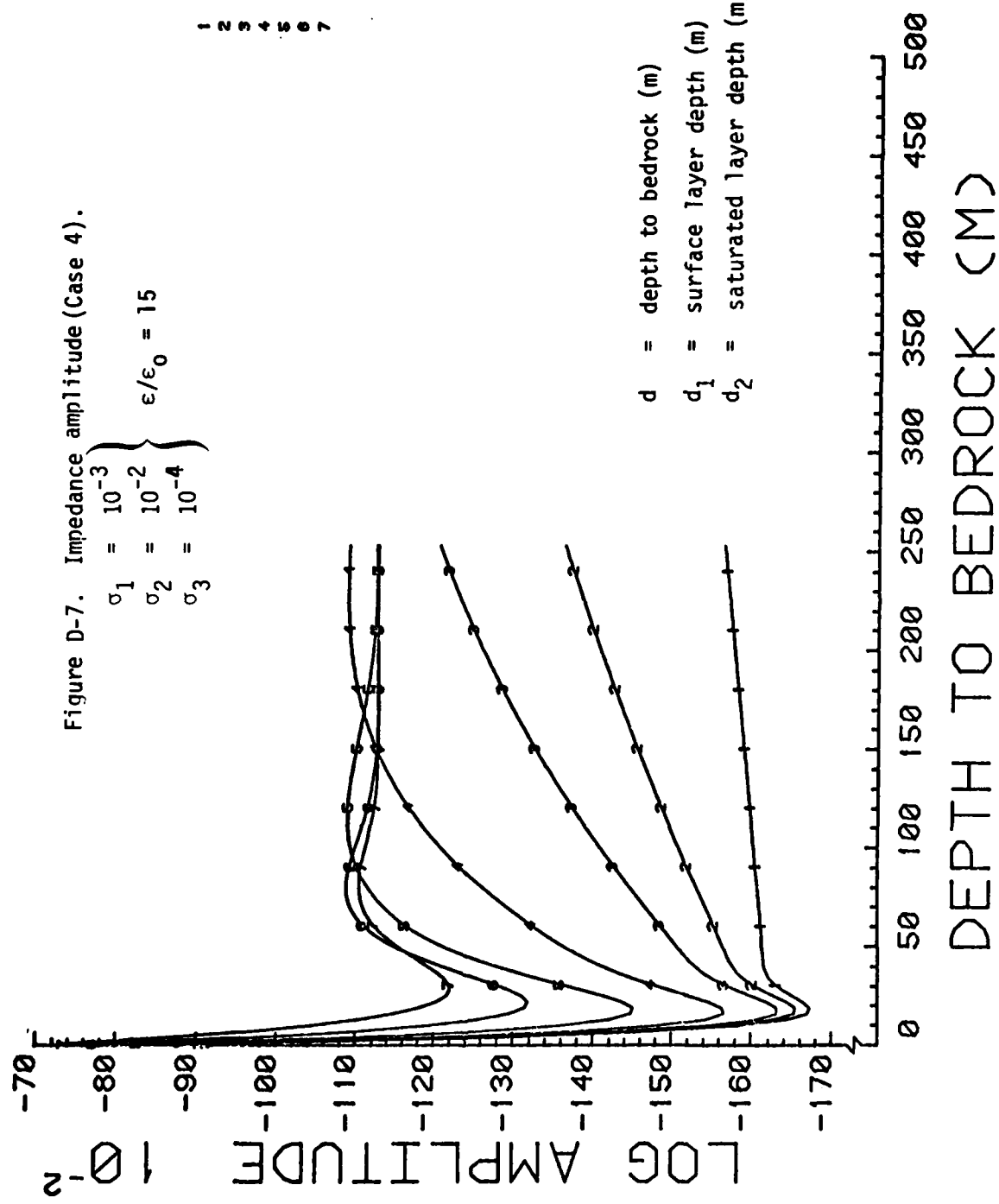


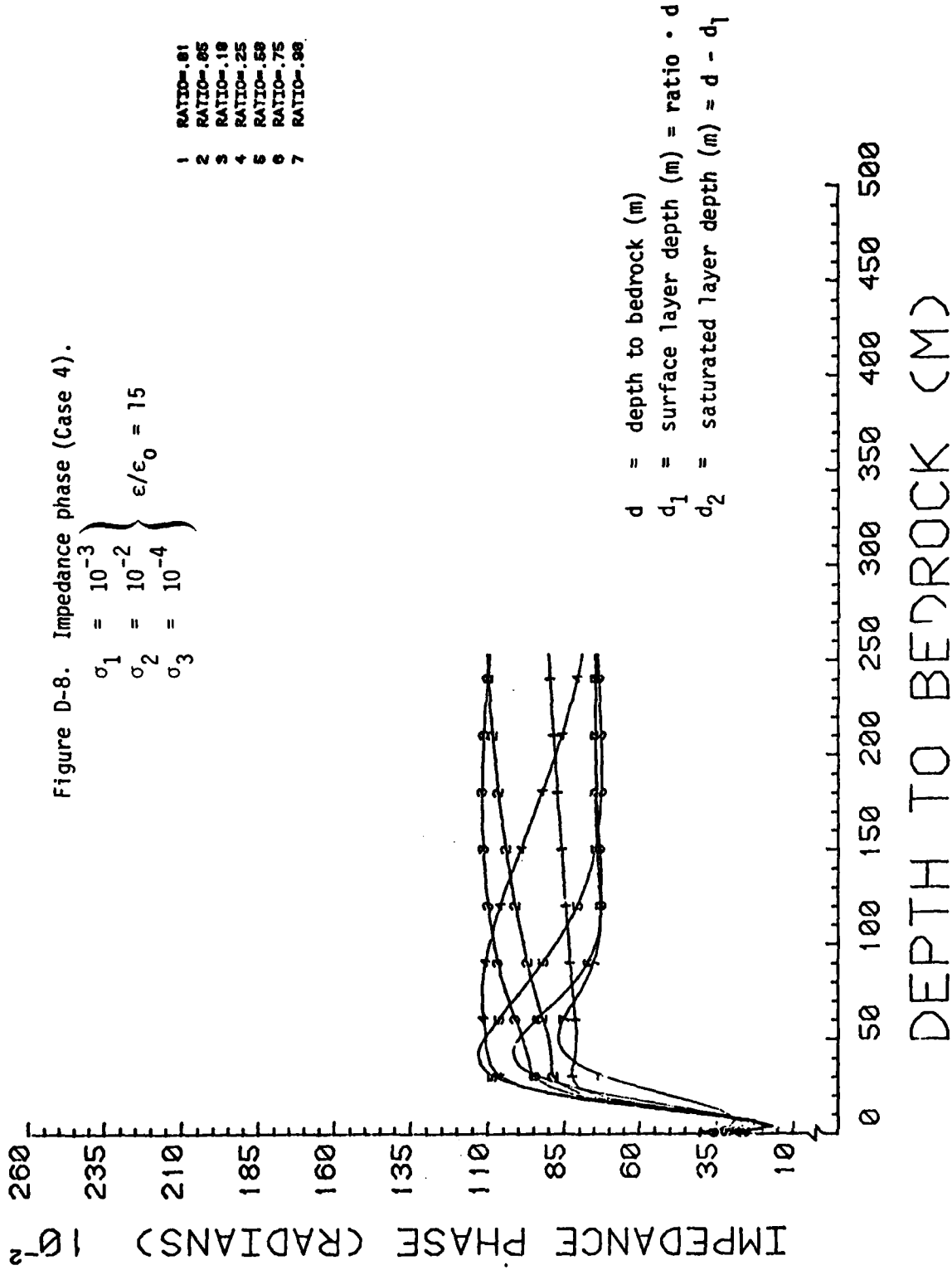


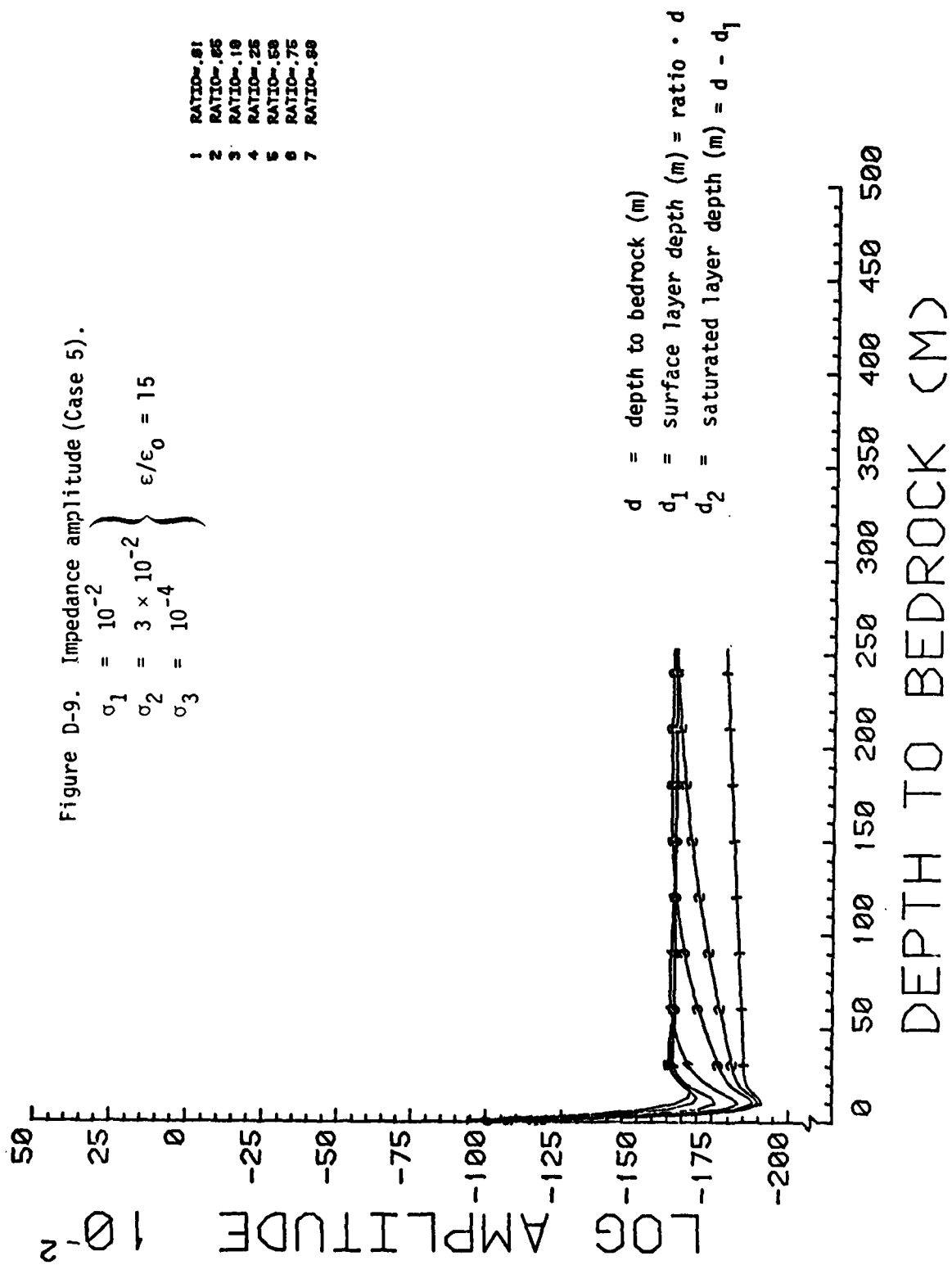


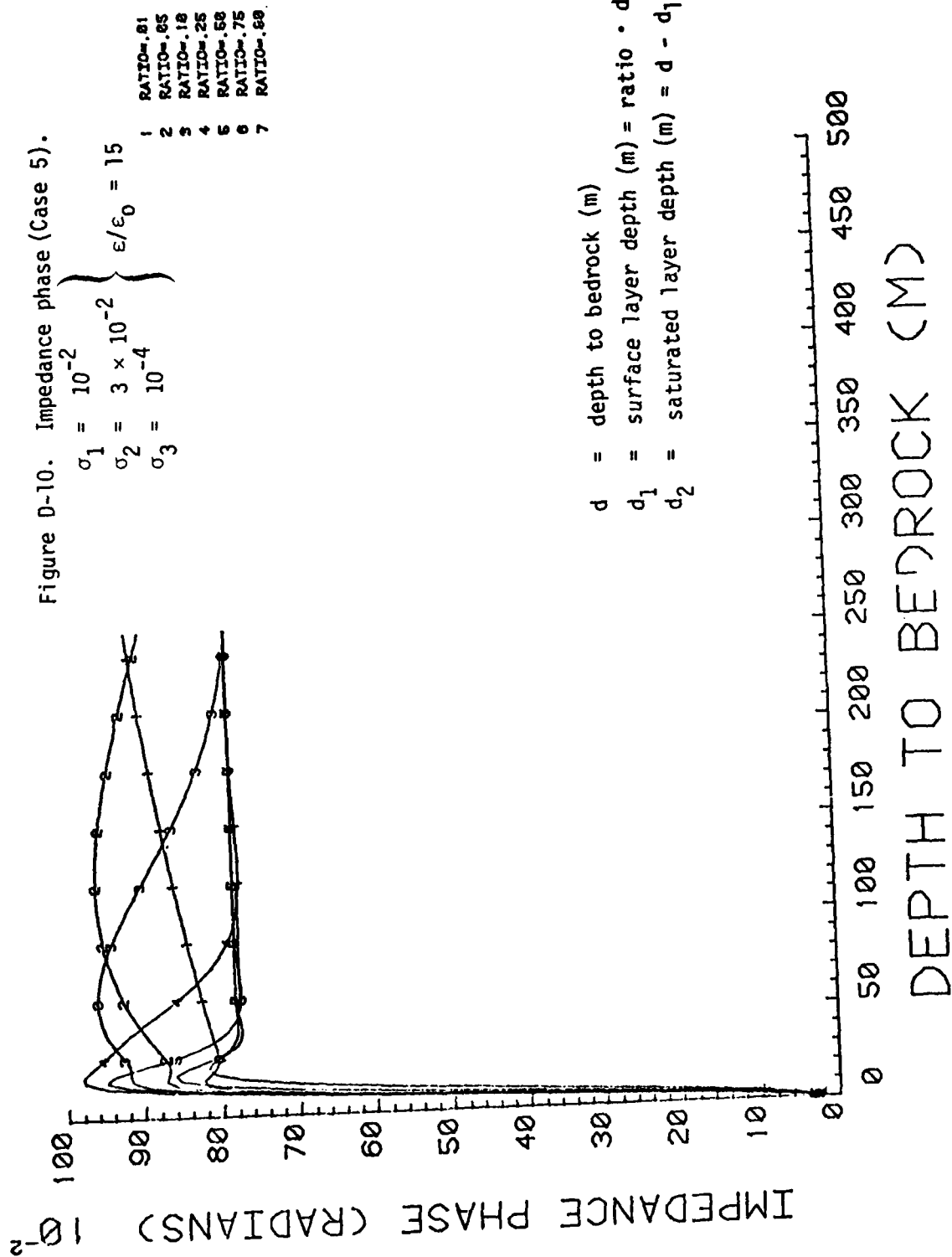


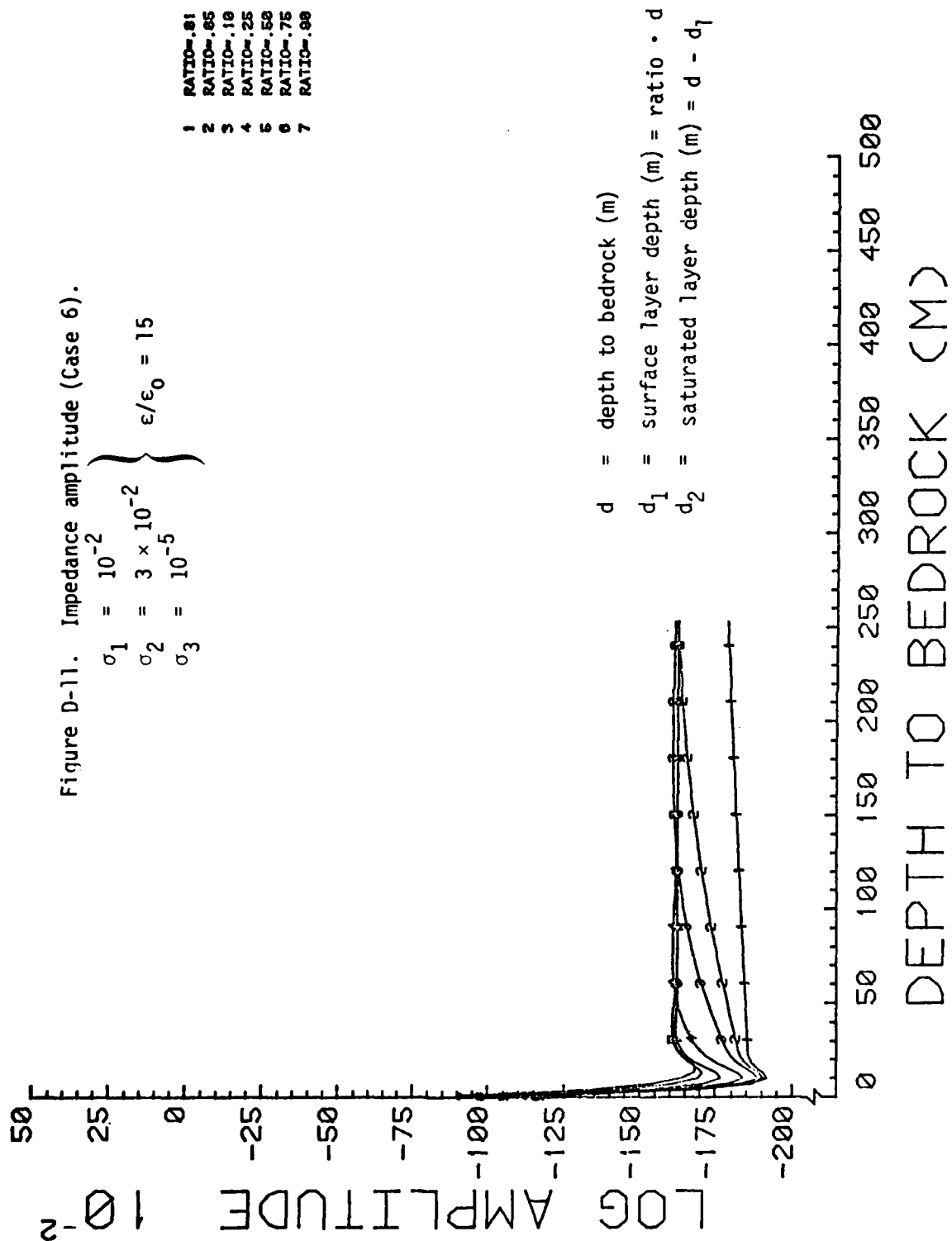


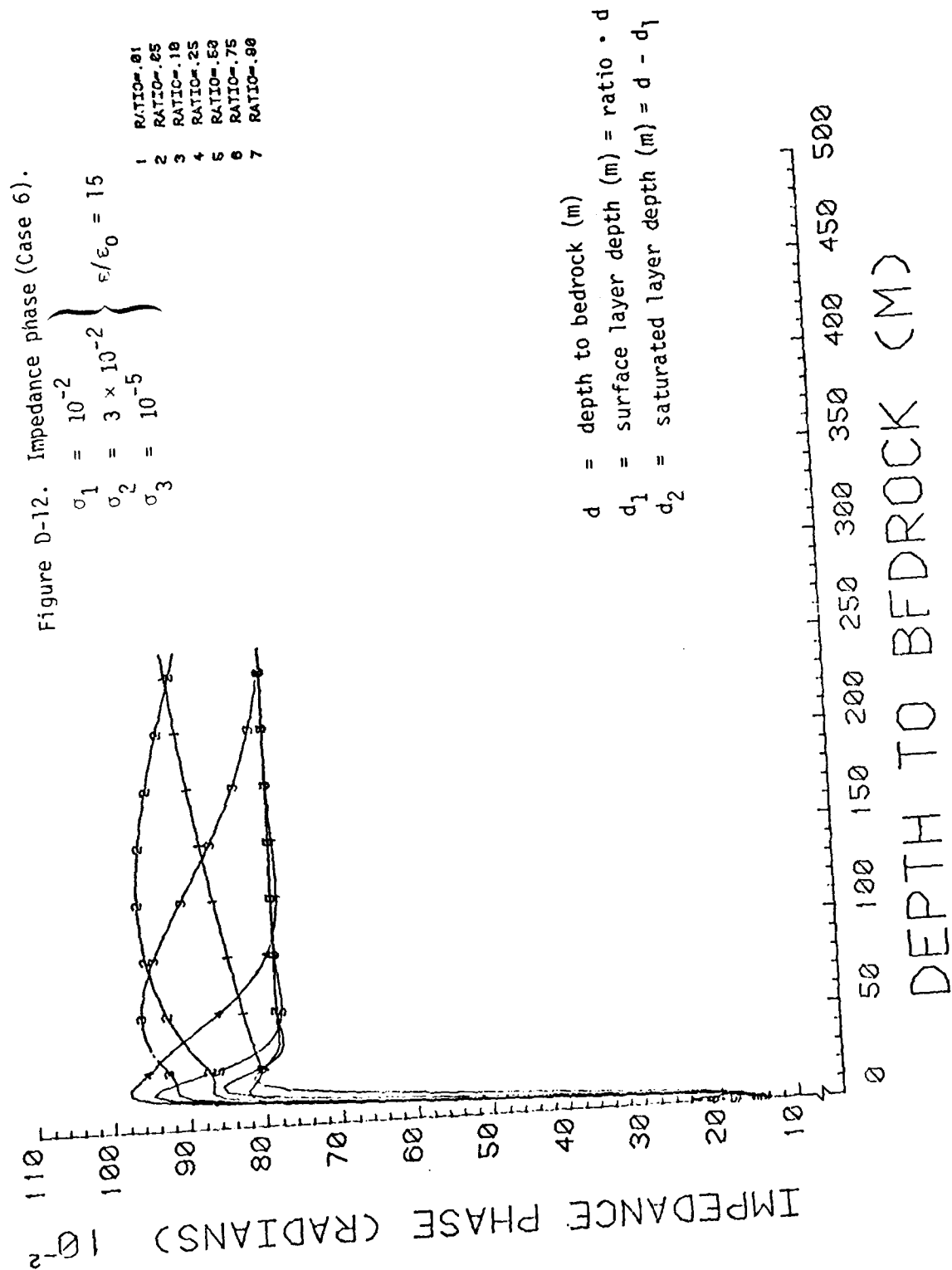












APPENDIX E
TERRAIN DATA FOR WORST CASE PATH

The terrain data for the worst case path were originally obtained as surface altitude in feet above mean sea level as a function of distance in kilometers from Searchlight, Nevada. The worst case path is the Geodesic connecting Searchlight to Fort Cronkhite, California. As the original data is read into the program, it is converted to altitude in meters above mean sea level.

The approximately 2400 entries making up this data base were printed out and are reproduced on the following pages. The distance, $D(\text{km})$, is in kilometers from Searchlight and the altitude, $H(\text{M})$, is in meters above mean sea level.

D(KM)	H(M)	D(KM)	H(M)	D(KM)	H(M)	D(KM)	H(M)
0.	890.0	0.25	883.9	0.50	877.8	0.75	871.7
1.00	865.6	1.40	853.4	1.85	841.2	2.35	829.1
3.05	816.9	4.10	780.3	4.53	780.3	5.58	816.9
6.65	829.1	7.75	841.2	8.85	853.4	9.93	865.6
10.93	877.8	11.88	890.0	12.70	902.2	13.33	914.4
13.90	926.6	14.40	938.8	14.88	951.0	15.53	963.2
15.83	975.4	16.30	987.6	16.80	999.7	17.20	1011.9
17.75	1024.1	18.10	1036.3	18.58	1048.5	18.95	1060.7
19.45	1072.9	19.90	1085.1	20.38	1097.3	20.95	1109.5
21.45	1121.7	21.95	1133.9	22.45	1146.0	23.25	1170.4
23.70	1182.6	24.05	1194.8	24.30	1207.0	24.60	1219.2
25.00	1231.4	25.28	1243.6	25.60	1255.8	25.83	1268.0
26.10	1280.2	26.25	1292.4	26.75	1304.5	26.93	1316.7
27.05	1328.9	27.30	1341.1	27.65	1353.3	27.90	1365.5
28.03	1377.7	28.35	1389.9	28.50	1402.1	28.65	1414.3
28.93	1426.5	29.20	1438.7	29.25	1450.8	29.35	1463.0
29.45	1475.2	29.55	1487.4	29.70	1499.6	29.90	1511.8
30.00	1524.0	30.45	1524.0	30.50	1536.2	30.55	1548.1
30.60	1560.6	30.65	1572.8	30.73	1585.0	30.80	1597.2
30.85	1609.3	30.90	1609.3	30.95	1597.2	31.05	1585.0
31.10	1597.2	31.13	1609.3	31.15	1621.5	31.25	1633.7
31.30	1645.9	31.35	1658.1	31.60	1670.3	31.70	1645.9
31.80	1633.7	31.85	1621.5	31.90	1609.3	31.95	1597.2
32.00	1585.0	32.05	1572.8	32.20	1560.6	32.30	1548.4
32.50	1536.2	32.65	1524.0	32.80	1511.8	33.05	1499.6
33.20	1487.4	33.55	1463.0	33.75	1450.8	33.95	1438.7
34.25	1426.5	34.50	1414.3	34.70	1402.1	35.00	1389.9
35.25	1377.7	35.70	1365.5	36.20	1377.7	36.35	1369.9
36.40	1402.1	36.45	1414.3	36.55	1402.1	36.60	1389.9
36.75	1377.7	36.85	1365.5	36.95	1353.3	37.00	1341.1
37.05	1353.3	37.10	1341.1	37.20	1353.3	37.30	1463.0
37.40	1341.1	37.45	1353.3	37.55	1365.5	37.60	1353.3
37.70	1341.1	37.75	1341.1	37.80	1353.3	37.85	1365.5
37.90	1377.7	37.95	1389.9	38.00	1402.1	38.10	1414.3
38.20	1426.5	38.30	1414.3	38.40	1402.1	38.50	1389.9
38.60	1377.7	38.70	1365.5	38.80	1353.3	39.00	1341.1
39.02	1328.9	39.04	1316.7	39.06	1304.5	39.08	1292.4
39.10	1280.2	39.25	1268.0	39.35	1255.8	39.45	1243.6
39.55	1231.4	39.75	1219.2	39.80	1207.0	39.85	1194.8
40.00	1182.6	40.10	1170.4	40.35	1158.2	40.60	1146.0
40.90	1133.9	41.15	1121.7	41.55	1109.5	41.80	1097.3
42.10	1085.1	42.40	1072.9	42.70	1060.7	43.00	1048.5
43.25	1036.3	43.55	1024.1	44.05	1011.9	44.50	999.7
44.75	987.6	45.25	975.4	45.90	963.2	46.90	951.0
47.55	938.8	48.05	926.6	48.53	914.4	49.10	902.2
48.80	877.8	50.65	853.4	51.75	829.1	53.25	804.7
61.50	804.7	62.85	829.1	64.10	853.4	65.25	877.8
66.05	902.2	66.70	926.6	67.20	951.0	67.75	975.4
68.25	999.7	68.75	1024.1	69.15	1048.5	69.50	1072.9
69.90	1097.3	70.25	1121.7	70.65	1146.0	71.20	1170.4

D(KM)	H(M)	D(KM)	H(M)	D(KM)	H(M)	D(KM)	H(M)
71.60	1194.8	71.80	1219.2	72.00	1243.6	72.10	1243.6
72.40	1268.0	72.70	1292.4	72.80	1292.4	73.15	1316.7
73.40	1341.1	73.60	1365.5	73.80	1389.9	74.00	1389.9
74.10	1414.3	75.30	1438.7	75.40	1463.0	75.60	1487.4
75.75	1487.4	76.40	1511.8	76.90	1536.2	77.30	1463.0
77.40	1438.7	77.45	1414.3	77.60	1389.9	78.00	1365.5
78.40	1341.1	78.50	1316.7	78.90	1292.4	79.40	1268.0
79.70	1243.6	80.25	1219.2	80.35	1194.8	81.00	1194.8
81.20	1170.4	81.60	1170.4	82.30	1170.4	83.00	1194.8
83.30	1194.8	83.40	1194.8	83.50	1219.2	83.70	1243.6
83.85	1268.0	83.90	1292.4	84.00	1292.4	84.10	1292.4
84.20	1316.7	84.25	1341.1	84.33	1365.5	84.38	1389.9
84.45	1414.3	84.50	1438.7	84.75	1463.0	84.80	1463.0
84.85	1438.7	85.00	1414.3	85.08	1389.9	85.18	1365.5
85.20	1341.1	85.35	1341.1	85.40	1365.5	85.65	1389.9
85.70	1414.3	85.95	1414.3	86.25	1389.9	86.33	1365.5
86.37	1341.1	86.45	1316.7	86.50	1292.4	86.55	1268.0
86.65	1243.6	87.00	1219.2	87.08	1194.8	87.20	1170.4
87.53	1146.0	87.75	1121.7	88.60	1097.3	89.45	1072.9
91.35	1072.9	91.60	1097.3	91.70	1121.7	91.75	1146.0
91.80	1146.0	91.90	1121.7	92.00	1121.7	92.20	1146.0
92.25	1170.4	92.30	1170.4	92.35	1146.0	92.80	1121.7
92.45	1097.3	93.60	1097.3	94.08	1146.0	94.18	1121.7
94.30	1097.3	95.00	1072.9	96.90	1048.5	97.60	1060.7
97.70	1048.5	97.85	1048.5	97.90	1048.5	98.30	1048.5
98.60	1048.5	101.00	1048.5	101.75	1072.9	101.95	1097.3
102.00	1121.7	102.10	1146.0	102.20	1170.4	102.95	1194.8
103.00	1219.2	103.40	1243.6	103.55	1268.0	103.60	1292.4
103.70	1316.7	103.75	1341.1	104.00	1316.7	104.08	1292.4
104.40	1268.0	104.80	1243.6	105.00	1268.0	105.10	1292.4
105.20	1316.7	105.60	1341.1	105.85	1365.5	106.10	1389.9
106.30	1414.3	106.35	1438.7	106.43	1463.0	106.45	1487.4
106.50	1511.8	106.55	1536.2	106.60	1560.6	106.70	1585.0
106.80	1609.3	106.63	1633.7	106.65	1658.1	106.68	1682.5
106.90	1706.9	106.95	1706.9	106.97	1682.5	106.98	1658.1
107.00	1633.7	107.05	1609.3	107.10	1585.0	107.15	1560.6
107.30	1536.2	107.40	1536.2	107.45	1560.6	107.48	1585.0
107.55	1560.6	107.58	1536.2	107.65	1511.8	107.70	1487.4
107.75	1463.0	107.80	1463.0	107.85	1487.4	107.88	1511.8
107.90	1536.2	107.95	1560.6	108.00	1585.0	108.05	1560.6
108.25	1536.2	108.30	1560.6	108.55	1585.0	108.60	1609.3
108.65	1633.7	108.70	1658.1	109.10	1682.5	109.20	1706.9
109.28	1731.3	109.30	1755.6	109.35	1780.0	109.55	1804.4
109.75	1828.8	109.80	1853.2	109.85	1877.6	109.88	1902.0
109.92	1926.3	109.95	1950.7	109.98	1975.1	110.00	1999.5
110.05	2023.9	110.08	2048.3	110.10	2072.6	110.15	2048.3
110.45	2072.6	111.25	2048.3	111.30	2023.9	111.35	1999.5
111.40	1950.7	111.45	1926.3	111.50	1902.0	111.55	1877.6
111.60	1853.2	111.70	1828.8	111.75	1804.4	111.78	1780.0
111.80	1755.6	111.85	1731.3	111.90	1706.9	111.95	1682.5

D(KM)	H(M)	D(KM)	H(M)	D(KM)	H(M)	D(KM)	H(M)
111.98	1658.1	112.05	1633.7	112.10	1609.3	112.15	1585.0
112.20	1609.3	112.25	1609.3	112.30	1585.0	112.40	1560.6
112.53	1560.6	112.55	1585.0	112.60	1609.3	112.65	1633.7
112.75	1633.7	112.80	1609.3	112.85	1585.0	112.88	1560.6
112.90	1536.2	112.95	1511.8	113.00	1487.4	113.20	1487.4
113.30	1487.4	113.40	1487.4	113.55	1463.0	113.60	1487.4
113.75	1487.4	113.80	1463.0	113.83	1487.4	113.85	1511.8
114.00	1511.8	114.15	1487.4	114.20	1463.0	114.25	1438.7
114.30	1414.3	114.35	1389.9	114.40	1365.5	114.55	1341.1
114.58	1316.7	114.65	1316.7	114.75	1341.1	115.00	1341.1
115.10	1316.7	115.20	1292.4	115.30	1268.0	115.40	1243.6
115.55	1219.2	115.80	1194.8	116.00	1170.4	116.40	1146.0
117.10	1121.7	117.30	1097.3	117.80	1072.9	117.90	1048.5
118.10	1048.5	118.20	1072.9	118.40	1048.5	118.60	1036.3
118.70	1048.5	118.75	1060.7	118.80	1072.9	118.90	1085.1
119.00	1097.3	119.20	1097.3	119.25	1085.1	119.30	1072.9
119.35	1060.7	119.38	1048.5	119.40	1036.3	119.43	1048.5
119.45	1060.7	119.50	1072.9	119.55	1085.1	119.60	1097.3
119.65	1109.5	119.67	1121.7	119.69	1121.7	119.70	1109.5
119.75	1097.3	119.78	1085.1	119.80	1072.9	119.85	1060.7
119.90	1048.5	119.95	1036.3	120.00	1024.1	120.05	1011.9
120.08	999.7	120.09	987.6	120.10	975.4	120.13	963.2
120.15	951.0	120.18	938.8	120.19	926.6	120.20	914.4
120.25	902.2	120.30	890.0	120.40	877.8	120.45	865.6
120.55	853.4	120.90	841.2	121.10	829.1	121.40	816.9
121.75	804.7	122.10	792.5	122.50	780.3	122.85	768.1
123.25	755.9	123.65	743.7	124.00	731.5	124.60	719.3
125.60	707.1	126.00	707.1	126.20	707.1	127.00	707.1
127.50	694.9	127.80	694.9	128.10	694.9	128.40	707.1
128.55	707.1	128.80	694.9	128.90	682.8	129.00	670.6
129.10	658.4	130.00	670.6	131.00	670.6	132.00	670.6
132.40	670.6	133.00	670.6	133.30	548.6	133.70	548.6
134.00	548.6	134.50	573.0	135.30	560.8	136.25	548.6
136.55	536.4	136.90	524.3	137.60	512.1	138.65	499.9
139.00	487.7	139.10	487.7	139.30	487.7	139.50	475.5
139.65	463.3	140.00	451.1	140.10	438.9	140.20	463.3
140.30	463.3	140.60	426.7	140.80	426.7	141.20	438.9
141.30	438.9	141.80	438.9	141.65	451.1	141.80	451.1
142.00	451.1	142.15	463.3	142.25	463.3	142.40	451.1
142.50	463.3	142.70	463.3	142.75	451.1	142.80	451.1
143.00	451.1						
143.40	451.1	143.50	463.3	143.60	463.3	143.65	463.3
143.70	451.1	143.85	451.1	144.50	438.9	145.10	438.9
145.25	438.9	145.60	438.9	146.10	438.9	146.65	451.1
146.70	451.1	146.95	451.1	147.10	451.1	147.15	451.1
147.40	438.9	147.60	438.9	147.75	438.9	147.85	438.9
148.00	438.9	148.25	451.1	148.35	451.1	148.50	451.1
148.80	451.1	149.00	451.1	149.75	463.3	150.10	475.5
150.40	487.7	150.70	499.9	151.10	512.1	151.40	524.3
151.80	536.4	152.00	548.6	152.40	560.8	152.80	573.0

D(KM)	H(M)	D(KM)	H(M)	D(KM)	H(M)	D(KM)	H(M)
152.90	573.0	153.10	585.2	153.20	597.4	153.35	609.6
153.45	621.8	153.50	634.0	153.55	646.2	153.60	658.4
153.70	670.6	153.75	682.8	153.90	670.6	154.00	670.6
154.20	670.6	154.35	682.8	154.50	682.8	154.60	694.9
154.70	694.9	154.80	707.1	155.00	719.3	155.20	731.5
155.25	743.7	155.30	755.9	155.35	768.1	155.40	780.3
155.45	792.5	155.50	804.7	155.55	816.9	155.60	816.9
155.65	804.7	155.70	792.5	155.75	804.7	155.80	816.9
155.95	816.9	156.00	804.7	156.20	816.9	156.30	829.1
156.40	829.1	156.50	841.2	156.70	853.4	157.00	853.4
157.13	865.6	157.25	877.8	157.40	890.0	157.55	902.2
157.60	914.4	157.70	926.6	157.75	938.8	157.80	951.0
157.90	963.2	158.00	975.4	158.05	987.6	158.13	999.7
158.15	1011.9	158.17	1024.1	158.20	1036.3	158.23	1048.5
158.25	1060.7	158.28	1060.7	158.29	1048.5	158.30	1036.3
158.35	1024.1	158.40	1011.9	158.50	999.7	158.80	1011.9
158.90	1024.1	159.00	1036.3	159.20	1036.3	159.30	1036.3
159.40	1036.3	159.50	1036.3	159.80	1024.1	160.00	1011.9
160.15	999.7	160.40	987.6	160.60	975.4	160.70	963.2
161.00	951.0	161.30	938.8	161.60	926.6	161.80	914.4
162.00	902.2	162.30	890.0	162.60	877.8	163.00	865.6
163.40	853.4	164.00	841.2	164.30	829.1	164.40	829.1
164.50	829.1	165.00	816.9	165.10	804.7	165.40	792.5
165.60	755.9	165.80	768.1	166.00	755.9	166.40	743.7
166.90	731.5	167.00	731.5	167.40	731.5	167.45	719.3
167.50	707.1	167.50	694.9	167.80	682.8	168.00	670.6
168.30	670.6	168.40	670.6	168.50	670.6	168.70	640.1
168.80	658.4	169.20	658.4	169.40	646.2	169.60	634.0
169.75	634.0	169.80	646.2	169.85	658.4	169.90	670.6
170.10	731.5	170.15	731.5	170.20	719.3	170.25	707.1
170.30	694.9	170.35	692.8	170.40	670.6	170.60	664.5
170.70	664.5	170.80	670.6	170.85	682.8	170.87	694.9
170.90	707.1	170.95	719.3	171.10	731.5	171.13	743.7
171.17	755.9	171.20	768.1	171.23	780.3	171.26	742.5
171.30	780.3	171.33	768.1	171.36	755.9	171.38	743.7
171.40	731.5	171.43	719.3	171.45	707.1	171.50	694.9
171.55	682.8	171.60	670.6	171.63	682.8	171.65	694.9
171.70	682.8	171.75	670.6	172.00	670.6	172.10	682.8
172.15	694.9	172.20	707.1	172.25	719.3	172.35	731.5
172.40	719.3	172.45	707.1	172.50	694.9	172.55	682.8
172.60	670.6	172.70	692.8	172.95	694.9	173.00	707.1
173.05	719.3	173.10	731.5	173.15	743.7	173.18	755.9
173.20	768.1	173.50	780.3	173.70	792.5	173.75	804.7
173.78	816.9	173.80	829.1	173.90	841.2	174.00	853.4
174.25	853.4	174.30	883.9	174.40	914.4	174.45	944.9
174.50	975.4	174.55	1005.8	174.60	975.4	174.65	944.9
174.70	914.4	174.75	883.9	174.80	853.4	174.90	823.0
175.00	792.5	175.20	762.0	175.40	731.5	175.60	731.5
175.80	762.0	175.90	792.5	176.10	823.0	176.30	853.4
176.40	883.9	176.50	914.4	176.75	944.9	177.00	975.4

D(KM)	H(M)	D(KM)	H(M)	D(KM)	H(M)	D(KM)	H(M)
177.10	1005.8	177.20	1036.3	177.30	1066.8	177.40	1097.3
177.50	1158.2	177.70	1182.6	177.80	1158.2	178.00	1158.2
178.05	1188.7	178.10	1219.2	178.30	1249.7	178.40	1280.2
178.65	1280.2	178.90	1249.7	179.20	1219.2	179.30	1188.7
179.35	1158.2	179.60	1127.8	179.90	1097.3	179.95	1066.8
180.00	1036.3	180.20	1097.3	180.40	1036.3	180.50	1005.8
180.60	975.4	180.80	975.4	180.85	1005.8	180.90	1036.3
181.01	1036.3	181.30	1066.8	181.40	1097.3	181.50	1127.8
181.52	1158.2	181.55	1188.7	181.65	1219.2	181.70	1249.7
181.80	1219.2	182.05	1219.2	182.10	1219.2	182.20	1188.7
182.30	1158.2	182.40	1127.8	182.50	1097.3	182.70	1066.8
182.85	1097.3	182.90	1127.8	183.00	1158.2	183.10	1127.8
183.20	1158.2	183.30	1188.7	183.40	1219.2	183.45	1188.7
183.50	1219.2	183.55	1249.7	183.60	1280.2	183.70	1310.6
183.80	1341.1	183.90	1341.1	184.00	1310.6	184.10	1280.2
184.15	1249.7	184.20	1219.2	184.60	1280.2	184.80	1280.2
185.00	1219.2	185.10	1188.7	185.20	1158.2	185.25	1127.8
185.30	1097.3	185.35	1066.8	185.40	1036.3	185.45	1005.8
185.50	975.4	185.53	944.9	185.55	914.4	185.65	853.4
185.67	853.4	185.70	853.4	185.75	883.9	185.80	914.4
185.85	944.9	185.90	975.4	185.93	1005.8	185.95	1036.3
186.00	1066.8	186.05	1097.3	186.07	1127.8	186.10	1158.2
186.20	1188.7	186.30	1249.7	186.35	1188.7	186.40	1158.2
186.45	1127.8	186.50	1097.3	186.55	1066.8	186.60	1036.3
186.63	1005.8	186.65	975.4	186.70	944.9	186.75	914.4
186.70	853.4	187.00	914.4	187.50	914.4	187.90	914.4
186.95	944.9	188.00	975.4	188.10	975.4	188.15	944.9
188.20	914.4	188.25	883.9	188.30	853.4	188.35	722.5
188.45	731.5	188.50	670.6	188.60	670.6	188.70	731.5
188.90	731.5	189.00	670.6	189.25	731.5	189.30	731.5
189.35	670.6	189.40	609.6	189.80	548.6	190.00	548.6
190.25	487.7	190.40	426.7	190.60	426.7	190.65	355.8
190.70	304.8	190.75	243.8	191.00	243.8	191.20	243.8
191.25	182.9	191.30	121.9	191.50	61.0	191.70	0.
191.80	0.	192.20	-61.0	200.95	-73.2	201.25	-61.0
201.50	-48.8	201.70	-36.6	201.95	-24.4	202.10	-12.2
202.30	0.	202.45	12.2	202.65	24.4	202.85	36.6
203.05	48.8	203.25	61.0	203.40	73.2	203.50	85.3
203.80	97.5	204.10	109.7	204.40	121.9	204.50	134.1
204.70	134.1	204.80	146.3	205.00	146.3	205.10	146.3
205.15	158.5	205.25	170.7	205.60	182.9	205.70	170.7
205.80	182.9	206.00	182.9	206.10	195.1	206.15	207.3
206.30	207.3	206.60	207.3	206.70	219.5	206.95	231.6
207.00	243.8	207.20	256.0	207.40	268.2	207.60	280.4
207.70	282.6	208.00	304.8	208.40	335.3	208.70	365.8
209.00	426.7	209.40	457.2	209.70	487.7	210.40	548.6
210.60	609.6	211.20	670.6	212.40	731.5	213.00	792.5
213.40	853.4	213.50	914.4	213.60	975.4	214.10	1036.3
214.30	1097.3	214.40	1158.2	214.50	1219.2	214.80	1219.2
215.00	1219.2	215.20	1158.2	215.40	1158.2	215.50	1219.2

D(KM)	H(M)	D(KM)	H(M)	D(KM)	H(M)	D(KM)	H(M)
215.90	1280.2	216.10	1341.1	216.20	1402.1	216.40	1341.1
216.60	1402.1	217.00	1463.0	217.30	1438.7	217.50	1463.0
217.55	1438.7	217.60	1414.3	217.65	1389.9	217.80	1365.5
218.00	1365.5	218.20	1389.9	218.25	1414.3	218.40	1438.7
218.60	1463.0	218.80	1524.0	219.00	1585.0	219.50	1706.9
219.60	1828.8	219.80	1950.7	219.85	1975.1	219.90	1999.5
220.00	2023.9	220.05	1999.5	220.35	1975.1	220.40	1950.7
220.60	1950.7	221.10	2072.6	221.40	2194.6	221.60	2072.6
222.01	1950.7	222.20	2194.6	222.40	2316.5	222.70	2438.4
223.00	2560.3	223.15	2682.2	223.40	2804.2	223.60	2682.2
223.80	2804.2	224.00	2682.2	224.20	2560.3	224.50	2438.4
225.00	2316.5	225.30	2621.3	225.60	2560.3	226.00	2438.4
226.50	2438.4	226.90	2560.3	227.10	2682.2	227.20	2682.2
227.40	2560.3	227.60	2682.2	227.80	2560.3	228.00	2438.4
228.40	2438.4	228.50	2316.5	228.80	2194.6	229.00	2194.6
229.20	2225.0	229.40	2194.6	230.00	2072.6	230.40	2072.6
230.60	1950.7	231.00	1950.7	231.10	1828.8	231.30	1706.9
231.60	1585.0	231.65	1560.6	231.70	1231.4	231.80	1097.3
232.00	1097.3	232.05	1219.2	232.10	1341.1	232.50	1341.1
232.80	1463.0	233.10	1463.0	233.30	1341.1	233.90	1463.0
234.20	1341.1	235.40	1219.2	236.70	1097.3	235.00	975.4
235.30	975.4	235.50	951.0	236.00	597.4	236.40	634.0
236.70	975.4	237.20	853.4	237.40	731.5	237.45	707.1
237.50	682.8	237.60	658.4	238.00	634.0	238.50	634.0
239.00	609.6	240.00	597.4	241.00	609.6	241.50	579.1
242.00	579.1	242.50	579.1	243.00	548.6	243.40	597.4
244.00	573.0	244.50	573.0	245.00	573.0	245.50	573.0
246.00	548.6	246.50	536.4	247.20	524.3	247.60	512.1
248.00	499.9	249.20	499.9	249.30	512.1	249.50	524.3
250.00	524.3	251.00	524.3	251.60	536.4	252.10	548.6
252.70	560.8	253.20	573.0	253.60	585.2	253.90	597.4
254.00	609.6	254.30	621.8	254.20	634.0	254.60	646.2
254.70	658.4	255.00	670.6	255.30	670.6	255.40	670.6
255.70	701.0	256.00	731.5	257.00	731.5	257.60	731.5
257.80	743.7	257.90	755.9	258.10	768.1	258.20	792.5
258.40	804.7	258.60	816.9	258.70	829.1	258.80	841.2
258.90	853.4	259.20	865.6	259.60	914.4	259.70	975.4
259.80	1036.3	259.90	1097.3	260.20	1036.3	260.60	1036.3
261.00	1280.2	261.20	1402.1	261.40	1463.0	261.70	1524.0
262.00	1585.0	262.10	1524.0	262.20	1463.0	262.70	1463.0
262.80	1402.1	263.00	1341.1	263.30	1280.2	263.50	1341.1
263.70	1402.1	263.80	1463.0	264.00	1524.0	265.00	1585.0
265.10	1524.0	265.30	1463.0	265.50	1524.0	265.70	1463.0
265.90	1402.1	266.00	1389.9	266.05	1377.7	266.10	1365.5
266.20	1353.3	266.30	1341.1	266.70	1310.6	266.90	1280.2
267.20	1249.7	267.50	1219.2	267.60	1207.0	267.70	1194.8
268.00	1182.6	268.20	1170.4	268.30	1158.2	269.00	1097.3
269.50	1127.8	270.00	1158.2	270.30	1170.4	270.40	1182.6
270.45	1144.8	270.90	1207.0	271.00	1219.2	271.05	1231.4
271.30	1243.6	271.60	1255.6	271.70	1268.0	271.80	1280.2

D(KM)	H(M)	D(KM)	H(M)	D(KM)	H(M)	D(KM)	H(M)
271.95	1292.4	272.10	1304.5	272.30	1316.7	272.45	1328.9
272.60	1341.1	272.65	1353.3	272.70	1365.5	272.90	1377.7
273.00	1389.9	273.10	1402.1	273.20	1414.3	273.40	1426.5
273.50	1438.7	273.55	1450.8	273.60	1463.0	274.00	1524.0
274.10	1585.0	274.30	1645.9	274.50	1706.9	275.00	1706.9
276.00	1706.9	276.30	1645.9	276.50	1585.0	276.70	1597.2
276.80	1609.3	277.10	1621.5	277.30	1621.5	277.60	1609.3
277.80	1597.2	278.00	1585.0	278.50	1615.4	279.50	1645.9
279.60	1633.7	279.70	1621.5	279.80	1609.3	279.90	1597.2
280.10	1585.0	281.00	1585.0	281.50	1615.4	281.60	1645.9
282.40	1585.0	283.00	1554.5	283.40	1524.0	283.50	1511.8
284.00	1511.8	284.30	1499.6	284.80	1487.4	285.50	1475.2
285.75	1463.0	285.90	1463.0	287.00	1463.0	287.60	1463.0
288.25	1450.8	289.00	1450.8	290.40	1450.8	290.50	1438.7
290.70	1438.7	290.90	1426.5	291.70	1432.6	292.00	1402.1
292.40	1402.1	292.60	1402.1	292.70	1371.6	293.00	1402.1
293.20	1377.7	293.30	1365.5	293.50	1353.3	294.00	1341.1
294.50	1341.1	295.00	1341.1	296.00	1341.1	296.40	1341.1
297.70	1280.2	298.20	1219.2	298.40	1219.2	298.60	1219.2
298.70	1207.0	299.00	1194.8	299.20	1194.8	299.30	1182.6
299.40	1170.4	299.60	1158.2	300.10	1146.0	300.30	1133.9
300.70	1121.7	301.80	1109.5	302.30	1097.3	302.60	1091.5
303.20	1088.1	304.80	1085.1	310.30	1082.0	316.60	1097.3
317.00	1097.3	317.20	1121.7	317.30	1133.9	317.40	1146.0
317.65	1170.4	317.80	1194.8	318.35	1219.2	318.60	1243.6
318.80	1268.0	318.90	1292.4	319.00	1316.7	319.05	1341.1
319.10	1365.5	319.15	1389.9	319.20	1414.3	319.30	1438.7
319.40	1463.0	319.75	1524.0	320.05	1585.0	320.20	1645.9
320.45	1706.9	320.60	1767.8	320.75	1828.8	320.90	1889.8
321.10	1950.7	321.20	2011.7	321.50	2072.6	322.00	2072.6
323.00	2072.6	323.40	2072.6	323.50	2133.6	323.60	2194.6
323.60	2255.5	324.00	2316.5	324.10	2377.4	324.20	2438.4
324.40	2560.3	324.70	2682.2	325.00	2804.2	325.30	2926.1
325.40	3048.0	325.70	3048.0	326.10	3048.0	326.70	3048.0
327.00	3048.0	327.60	3048.0	328.00	3145.5	328.30	3291.8
328.40	3316.2	328.60	3340.6	328.85	3426.0	329.00	3426.0
329.05	3426.0	329.80	3340.6	330.10	3340.6	330.20	3365.0
330.30	3349.4	330.80	3657.6	331.20	3511.3	331.50	3535.7
332.00	3560.1	332.10	3584.4	332.30	3608.8	332.40	3633.2
332.70	3657.6	333.00	3730.8	333.50	3779.5	334.00	3901.4
334.50	3730.8	334.75	3657.6	335.00	3535.7	335.50	3657.6
336.00	3779.5	336.80	3657.6	337.00	3779.5	337.60	3779.5
338.00	3657.6	338.50	3901.4	338.65	3779.5	338.80	3657.6
339.00	3657.6	340.00	3657.6	340.30	3535.7	340.90	3535.7
341.60	3657.6	342.25	3779.5	342.30	3901.4	342.60	4023.4
342.90	3901.4	342.95	3779.5	343.10	3657.6	343.50	3535.7
344.80	3535.7	344.00	3511.3	345.00	3511.3	345.50	3462.5
346.00	3462.5	346.25	3413.8	346.40	3389.4	346.75	3365.0
346.80	3340.6	347.00	3316.2	347.20	3291.8	347.50	3230.9
348.00	3230.9	348.40	3291.8	348.80	3291.8	348.90	3316.2

D(KM)	H(M)	D(KM)	H(M)	D(KM)	H(M)	D(KM)	H(M)
349.40	3316.2	349.50	3291.8	349.60	3267.5	349.70	3243.1
350.00	3218.7	350.60	3218.7	350.70	3243.1	350.80	3267.5
351.00	3291.8	351.30	3291.8	351.50	3267.5	351.60	3243.1
351.70	3214.7	351.80	3194.3	352.00	3169.9	352.20	3048.0
352.35	2926.1	352.80	2804.2	353.00	2682.2	352.30	2560.3
354.00	2434.4	355.30	2560.3	355.60	2682.2	355.80	2804.2
355.85	2926.1	355.90	3048.0	356.00	3169.9	356.15	3291.8
356.40	3413.8	356.60	3535.7	357.00	3657.6	357.20	3657.6
357.60	3535.7	358.00	3413.8	358.70	3291.8	359.40	3169.9
360.00	3169.9	360.50	3291.8	361.00	3291.8	362.00	3352.8
362.45	3413.8	362.60	3535.7	362.80	3657.6	363.05	3657.6
363.30	3633.2	363.50	3657.6	363.70	3657.6	364.00	3535.7
364.40	3413.8	364.60	3352.8	364.90	3291.8	365.10	3365.0
365.40	3291.8	365.70	3291.8	365.90	3169.9	366.20	3048.0
366.50	3048.0	366.90	3169.9	367.10	3291.8	367.70	3413.8
368.30	3535.7	368.50	3707.9	368.70	3535.7	369.10	3413.8
369.50	3291.8	369.80	3169.9	370.05	3048.0	370.30	2926.1
370.50	2804.2	371.10	2804.2	371.40	2926.1	371.80	3048.0
372.05	3169.9	372.60	3200.4	372.70	3218.7	372.80	3169.9
373.00	3048.0	373.20	3169.9	373.50	3169.9	373.80	3048.0
374.10	3169.9	374.40	3291.8	374.60	3291.8	374.90	3169.9
375.20	3169.9	375.90	3169.9	376.10	3169.9	376.40	3048.0
376.70	2926.1	377.30	2926.1	378.00	2804.2	378.50	2926.1
379.00	2804.2	379.60	2682.2	379.70	2804.2	380.50	2682.2
381.00	2755.4	382.00	2779.8	382.30	2604.2	383.20	2804.2
383.40	2682.2	384.20	2642.2	384.60	2804.2	385.05	2926.1
385.30	3048.0	385.90	2926.1	386.10	2901.7	386.20	2677.3
386.30	2852.9	386.40	2628.5	386.50	2804.2	387.10	2682.2
387.60	2560.3	388.00	2494.9	388.40	2560.3	388.80	2682.2
389.60	2731.0	389.70	2755.4	389.80	2779.8	390.00	2804.2
390.50	2804.2	390.95	2682.2	391.20	2657.9	391.50	2633.5
391.70	2609.1	391.40	2584.7	392.00	2560.3	392.60	2535.9
392.65	2511.0	392.70	2487.2	392.80	2462.8	392.90	2439.4
393.30	2560.3	393.70	2438.4	394.50	2316.5	394.90	2316.5
395.20	2316.5	396.00	2340.9	396.60	2365.2	396.80	2389.6
396.90	2414.0	397.20	2438.4	397.50	2462.8	397.75	2462.8
397.90	2438.4	398.00	2377.4	398.10	2316.5	398.50	2194.6
398.55	2170.2	398.60	2145.8	398.70	2121.4	399.20	2097.0
399.30	2072.6	399.40	2042.2	399.70	2023.9	399.75	1999.5
399.80	1975.1	400.00	1950.7	400.70	1950.7	400.80	1975.1
401.00	1999.5	401.50	1999.5	402.00	1950.7	402.50	2072.6
402.80	1950.7	403.80	1950.7	404.10	2072.6	404.70	2194.6
405.50	2316.5	406.10	2194.6	406.40	2072.6	407.10	1950.7
407.15	1926.3	407.50	1902.0	408.00	1877.6	408.30	1853.2
408.50	1828.8	409.00	1706.9	409.40	1585.0	409.70	1585.0
410.10	1463.0	410.50	1341.1	410.90	1341.1	411.80	1341.1
412.50	1219.2	413.00	1219.2	413.50	1280.2	414.00	1341.1
414.50	1316.7	415.00	1341.1	415.40	1219.2	415.80	1097.3
416.10	1097.3	416.20	1158.2	416.50	1219.2	417.00	1219.2
417.20	1158.2	417.70	1219.2	417.85	1097.3	418.30	1036.3

D(KM)	H(M)	D(KM)	H(M)	D(KM)	H(M)	D(KM)	H(M)
419.10	975.4	419.60	1097.3	420.00	1097.3	420.50	1158.2
421.00	1219.2	421.30	1280.2	421.50	1341.1	422.00	1402.1
422.50	1402.1	423.00	1402.1	423.60	1219.2	423.85	1097.3
424.20	975.4	425.00	914.4	426.00	914.4	426.50	853.4
427.00	792.5	428.00	792.5	428.40	853.4	428.70	914.4
429.50	853.4	430.00	731.5	430.50	670.6	431.00	609.6
431.50	609.6	432.00	548.6	433.00	487.7	433.40	487.7
433.60	457.2	433.80	463.3	434.40	451.1	434.50	426.7
434.70	396.2	435.00	365.8	435.13	396.2	435.25	426.7
435.30	457.2	435.40	426.7	435.50	396.2	435.80	381.0
436.00	365.8	436.13	335.3	436.37	304.8	436.50	304.8
436.70	335.3	436.85	335.3	436.95	304.8	437.00	274.3
437.15	243.8	437.25	213.4	437.55	213.4	438.25	213.4
439.40	213.4	439.90	243.8	440.00	274.3	440.40	304.8
440.50	335.3	440.60	365.8	440.80	396.2	440.90	426.7
441.00	457.2	441.25	487.7	441.40	518.2	441.45	548.6
441.55	548.6	441.60	518.2	441.65	487.7	441.75	457.2
441.90	457.2	442.00	457.2	442.13	457.2	442.30	487.7
442.50	426.7	442.75	426.7	442.90	487.7	443.00	426.7
443.30	365.8	443.50	396.2	444.00	426.7	444.50	402.3
445.00	426.7	445.20	457.2	445.40	487.7	445.65	548.6
445.70	548.6	445.85	487.7	446.20	426.7	446.50	365.8
446.95	396.2	447.00	426.7	447.10	426.7	447.40	426.7
447.60	457.2	447.65	487.7	447.75	518.2	447.80	548.6
447.95	548.6	448.00	548.6	448.10	579.1	448.30	548.6
448.80	548.6	448.90	579.1	449.00	579.1	449.25	594.4
449.50	609.6	449.75	640.1	450.00	670.6	450.25	682.8
450.50	670.6	450.70	609.6	450.75	579.1	450.90	548.6
451.10	518.2	451.40	487.7	451.70	457.2	451.80	457.2
452.00	426.7	452.25	457.2	452.30	487.7	452.35	518.2
452.40	548.6	452.50	579.1	452.75	579.1	452.85	548.6
453.00	518.2	453.50	518.2	453.80	548.6	454.00	518.2
454.10	487.7	454.40	457.2	454.60	426.7	455.00	396.2
455.30	365.8	455.55	365.8	455.70	365.8	455.90	396.2
456.00	426.7	456.20	457.2	456.45	457.2	456.50	426.7
456.60	396.2	456.70	396.2	456.80	426.7	457.00	457.2
457.25	426.7	457.30	396.2	457.45	396.2	457.70	396.2
457.75	365.8	457.90	335.3	457.95	329.2	458.00	310.9
458.75	304.8	458.80	274.3	458.90	243.8	459.00	213.4
459.05	207.3	459.15	201.2	459.30	195.1	459.40	195.1
459.50	189.0	459.85	195.1	460.25	195.1	460.40	195.1
460.50	201.2	460.60	207.3	460.65	213.4	460.80	219.5
460.90	225.6	461.10	231.6	461.20	237.7	461.30	243.8
461.40	249.9	461.55	249.9	461.60	249.9	461.75	249.9
461.90	249.9	461.95	249.9	462.25	249.9	462.30	249.9
462.50	249.9	462.75	243.8	462.80	249.9	462.90	256.0
462.95	262.1	463.25	262.1	463.40	268.2	463.45	274.3
463.75	280.4	463.80	286.5	463.90	292.6	464.00	298.7
464.05	304.8	464.10	317.0	464.25	304.8	464.45	292.6
464.70	298.7	464.80	304.8	465.00	304.8	465.25	304.8

D(KM)	H(M)	D(KM)	H(M)	D(KM)	H(M)	D(KM)	H(M)
465.30	317.0	465.50	304.8	465.25	274.3	465.90	304.8
466.00	304.8	466.25	274.3	466.50	274.3	467.10	274.3
467.30	243.8	467.50	213.4	467.75	198.1	468.05	182.9
468.50	198.1	468.70	182.9	468.80	213.4	469.00	243.8
469.25	213.4	469.80	243.8	470.00	243.8	1.00	0.
470.50	213.4	471.00	207.3	471.05	213.4	471.25	219.5
471.30	225.6	471.45	225.6	471.50	225.6	471.60	231.6
471.65	237.7	471.70	243.8	471.75	274.3	471.90	274.3
472.00	259.1	472.20	243.8	472.30	228.6	472.50	228.6
472.75	219.5	472.85	243.8	473.00	259.1	473.40	243.8
473.70	213.4	473.75	207.3	473.80	201.2	474.00	195.1
474.60	195.1	474.75	207.3	474.80	213.4	474.90	243.8
475.00	213.4	475.50	198.1	475.80	182.9	476.75	182.9
477.00	182.9	478.50	152.4	478.60	121.9	479.00	121.9
479.50	137.2	480.00	137.2	480.80	152.4	481.25	152.4
481.50	146.3	481.90	140.2	482.00	140.2	482.05	140.2
483.70	146.3	484.00	152.4	484.30	158.5	484.80	158.5
485.10	152.4	487.90	146.3	490.10	146.3	490.60	146.3
490.75	146.3	491.40	140.2	491.75	140.2	492.00	146.3
492.10	146.3	492.25	152.4	493.60	152.4	494.20	134.1
494.50	134.1	495.00	137.2	495.60	128.0	496.00	128.0
496.50	121.9	496.90	121.9	497.75	121.9	497.45	121.9
504.25	106.7	504.40	106.7	505.60	106.7	505.95	106.7
506.80	109.7	507.80	112.8	508.00	114.3	508.30	114.3
508.80	106.7	509.50	106.7	510.00	100.6	511.00	100.6
512.20	99.1	513.00	99.1	514.00	99.1	515.00	99.1
516.00	97.5	516.20	96.0	516.80	96.0	517.40	96.0
517.75	96.0	518.00	96.0	518.70	94.5	518.80	94.5
519.75	93.0	520.30	91.4	521.00	91.4	521.30	89.9
521.50	84.4	521.75	84.4	522.45	91.4	522.75	91.4
522.40	83.8	523.00	84.4	523.40	85.3	523.60	83.8
523.95	83.8	524.50	83.8	525.70	83.8	526.50	82.3
527.70	80.4	528.00	79.2	529.00	76.2	530.00	76.2
530.25	76.2	531.05	74.7	532.00	73.2	532.75	71.6
533.95	70.1	535.30	68.6	536.55	67.1	537.30	65.5
538.40	64.0	539.55	62.5	540.50	61.0	541.55	59.4
542.50	57.9	543.95	56.4	544.90	54.9	546.00	53.3
547.60	51.8	549.00	50.3	549.75	48.8	550.00	48.8
551.55	47.2	552.50	45.7	553.50	45.7	554.90	44.2
556.05	42.7	557.50	44.2	557.60	42.7	558.40	41.1
560.30	39.6	562.50	36.1	563.25	38.1	564.60	36.6
564.95	36.6	565.20	36.6	566.75	35.1	567.75	33.5
568.50	33.5	569.25	32.0	570.40	32.0	571.00	33.5
572.80	32.0	573.50	32.0	575.00	32.0	577.25	30.5
574.00	30.5	581.40	29.0	581.95	29.0	582.70	29.0
584.10	29.0	585.75	27.4	587.90	25.9	590.75	24.4
591.30	22.9	591.50	22.9	591.75	22.9	593.50	22.9
595.50	21.3	596.85	19.8	600.00	18.3	600.60	15.2
600.70	15.2	601.00	16.8	602.05	19.8	603.00	21.3
605.65	22.9	604.05	22.9	605.50	24.4	607.00	25.9

D(KM)	H(M)	D(KM)	H(M)	D(KM)	H(M)	D(KM)	H(M)
607.75	27.4	608.50	29.0	609.00	30.5	609.40	32.0
610.00	33.5	610.60	35.1	610.80	36.6	611.30	38.1
611.80	39.6	612.05	41.1	612.45	42.7	612.70	44.2
613.00	45.7	613.25	47.2	613.50	50.3	613.75	51.8
614.00	53.3	614.10	54.9	614.40	56.4	614.60	57.9
614.90	59.4	615.00	61.0	615.45	61.0	616.40	61.0
616.50	67.1	617.00	91.4	617.25	91.4	617.45	121.9
617.75	121.9	617.90	91.4	617.95	91.4	618.20	121.9
618.30	121.9	618.80	121.9	618.90	152.4	619.00	182.9
619.40	213.4	619.50	182.9	619.70	152.4	620.50	152.4
620.75	182.9	620.90	213.4	621.10	213.4	621.50	213.4
621.60	243.8	621.90	274.3	622.00	304.8	622.10	335.3
622.40	335.3	622.50	304.8	622.75	274.3	622.80	304.8
622.95	335.3	623.00	365.8	623.25	396.2	623.60	426.7
623.75	457.2	623.90	396.2	623.95	365.8	624.05	335.3
624.25	304.8	624.40	274.3	624.50	243.8	624.55	213.4
624.60	182.9	624.70	152.4	624.90	121.9	625.00	152.4
625.20	182.9	625.50	182.9	625.80	243.8	625.95	304.8
626.00	365.8	626.40	365.8	626.55	304.8	627.00	304.8
627.25	304.8	627.50	365.8	627.60	426.7	627.70	426.7
628.00	426.7	628.20	365.8	628.25	426.7	628.60	487.7
629.00	487.7	629.40	487.7	629.50	426.7	629.75	426.7
630.90	426.7	631.00	426.7	631.20	365.8	631.50	304.8
631.75	365.8	632.00	365.8	632.25	365.8	633.00	426.7
633.25	426.7	633.50	365.8	633.75	426.7	634.00	487.7
634.25	487.7	634.45	487.7	634.75	548.6	634.90	609.6
635.50	670.6	635.75	731.5	635.90	792.5	636.10	853.4
636.20	883.9	636.25	914.4	636.45	944.9	636.60	975.4
636.90	975.4	637.00	914.4	637.20	853.4	637.30	792.5
637.50	731.5	637.75	670.6	638.25	731.5	638.50	670.6
638.75	670.6	639.60	609.6	639.80	548.6	640.95	487.7
640.10	426.7	640.30	365.8	640.50	365.8	640.75	426.7
641.00	487.7	641.25	426.7	641.45	365.8	641.55	365.8
641.75	426.7	641.90	487.7	642.25	548.6	642.50	487.7
643.00	487.7	644.25	487.7	644.55	548.6	644.75	609.6
644.00	670.6	644.50	670.6	644.75	731.5	645.00	731.5
645.20	792.5	645.40	853.4	645.60	853.4	646.25	792.5
646.50	792.5	647.50	792.5	648.10	792.5	648.50	792.5
649.25	792.5	649.45	792.5	649.75	853.4	650.00	853.4
650.50	853.4	651.10	792.5	651.50	731.5	652.00	670.6
652.10	670.6	652.40	731.5	652.75	731.5	652.90	731.5
653.20	792.5	653.50	792.5	654.00	792.5	654.20	731.5
654.40	670.6	654.75	670.6	654.90	609.6	655.10	670.6
655.50	701.0	656.00	731.5	656.10	731.5	656.25	609.6
657.25	670.6	657.00	731.5	657.75	792.5	658.25	853.4
658.75	914.4	658.90	975.4	659.00	975.4	659.10	914.4
659.30	853.4	659.50	792.5	659.75	731.5	659.95	670.6
660.10	609.6	661.00	670.6	661.50	670.6	662.00	701.0
663.00	701.0	663.40	670.6	663.60	609.6	663.95	548.6
664.40	487.7	664.90	426.7	665.50	365.8	645.70	304.8

D(KM)	H(M)	D(KM)	H(M)	D(KM)	H(M)	D(KM)	H(M)
665.90	304.8	666.00	304.8	666.25	304.8	666.50	335.3
666.90	365.8	67.25	365.8	667.50	335.3	667.90	304.8
668.25	274.3	668.60	304.8	669.00	304.8	669.40	243.8
669.50	243.8	670.00	243.8	670.50	213.4	670.75	243.8
670.80	182.9	670.90	182.9	671.50	213.4	671.95	243.8
673.00	274.3	673.50	304.8	673.75	365.3	673.90	304.8
674.30	304.8	674.50	274.3	674.80	243.8	675.00	274.3
675.40	243.8	675.60	274.3	675.75	243.8	676.00	213.4
676.50	213.4	676.75	213.4	677.00	228.6	677.50	213.4
678.00	213.4	678.25	228.6	678.40	213.4	678.50	243.8
679.00	243.8	679.25	259.1	679.50	243.8	679.60	243.8
679.70	274.3	679.80	243.8	680.00	243.8	680.10	243.8
680.20	274.3	680.50	274.3	680.75	243.8	681.00	243.8
681.50	243.8	681.80	213.4	682.10	182.9	682.50	182.9
682.75	152.4	683.25	121.9	685.10	97.5	685.40	97.5
686.90	97.5	687.00	97.5	687.60	121.9	688.00	182.9
688.50	243.8	688.70	304.8	689.00	365.8	689.50	365.8
689.75	304.8	689.95	304.8	690.25	304.8	690.40	365.8
690.50	304.8	690.60	365.8	691.00	365.8	691.10	426.7
691.50	457.2	692.00	426.7	692.25	365.8	692.50	304.8
692.80	304.8	693.10	304.8	693.25	365.8	693.75	365.8
694.00	346.2	694.50	365.8	694.75	365.8	695.10	304.8
696.50	243.8	696.60	213.4	697.00	182.9	697.25	182.9
696.60	243.8	696.90	243.8	696.00	274.3	696.25	274.3
696.50	243.8	696.60	213.4	697.00	182.9	697.25	182.9
697.50	152.4	697.20	121.9	698.25	152.4	698.30	182.9
698.40	213.4	698.50	243.8	698.75	243.8	699.10	213.4
699.20	182.9	699.30	152.4	699.40	121.9	700.20	152.4
701.00	121.9	702.00	121.9	703.00	121.9	704.05	91.4
705.00	91.4	705.80	121.9	706.00	152.4	706.10	182.9
706.50	182.9	707.00	182.9	707.25	182.9	707.75	152.4
707.80	121.9	708.00	91.4	708.50	61.0	708.80	24.4
709.75	18.3	710.50	18.3	711.30	15.2	711.50	12.2
712.90	6.1	714.00	3.0	715.00	1.5	716.00	0.
717.00	0.	717.50	1.5	717.60	1.8	718.00	2.1
719.00	3.0	719.50	3.0	720.50	3.0	721.20	3.0
721.37	0.	721.40	0.	722.25	0.	722.27	0.
722.30	3.0	722.75	3.0	722.80	0.	722.81	0.
732.90	0.	732.91	0.	733.00	3.0	733.60	30.5
733.64	51.0	733.80	61.0	734.10	30.5	734.12	22.9
734.20	21.3	734.80	7.6	735.20	7.6	735.30	4.6
735.45	0.	735.46	0.	741.43	0.	741.64	0.
741.72	7.6	741.76	30.5	741.80	61.0	741.85	91.4
741.95	121.9	742.00	152.4	742.15	182.9	742.25	213.4
742.35	213.4	742.40	182.9	742.84	121.9	743.00	73.2
743.12	61.0	743.28	48.8	743.36	36.6	743.44	24.4
744.40	36.6	744.64	48.8	744.70	61.0	744.80	61.0
745.05	121.9	745.12	121.9	745.36	121.9	745.40	134.1
745.44	146.3	745.50	158.5	745.74	146.3	745.92	158.5
746.00	158.5	746.16	158.5	746.36	170.7	746.44	182.9

D(KM)	H(M)	D(KM)	H(M)	D(KM)	H(M)	D(KM)	H(M)
746.86	182.9	747.00	121.9	747.16	61.0	747.30	109.7
747.40	109.7	747.44	61.0	747.64	121.9	747.68	61.0
747.75	12.2	748.00	61.0	748.10	12.2	748.14	0.
748.16	0.	748.98	0.	749.00	0.		
801.00	0.						

APPENDIX F
MATERIALS AND CONDUCTIVITIES ALONG THE WORST CASE PATH

Table F-1 shows the age data, symbol and computer symbol for the different types of materials used in the geological description of the worst case path. The actual data were obtained in terms of the distance from a given measurement site, with Searchlight having the index 0 and $r = 0$ and Fort Cronkhite having index 9 with $r_9 = 746.70$ km. The values of r_i used are given in Table F-2. The conductivities ($\mu\text{hos/m}$) and relative dielectric constant (ϵ/ϵ_0) are given in Table F-3 for each of the 44 materials used to describe the path. Finally, the actual input data as a function of distance is given in Table F-4. The actual distance for a given entry is given by

$$\text{Distance} = r_i + \text{DELR}$$

where r_i is the value of RINDEX corresponding to the value of the INDEX. The column labeled DEPTH (m) is actually the layer thickness in meters. In general most of the path is described by two layers with a few single or three layer segments.

Table F-1. Age and geologic material symbols.

<u>Age</u>	<u>Material Symbol</u>	<u>Fortran Symbol</u>
Cenozoic	Qs	QS
	Qa1	QAL
	Qsc	QSC
	Qf	QF
	Qb	QB
	Qst	QST
	Q1	QL
	Qt	QT
	Qm	QM
	Qpv ^b	QPVb
	Qc	QC
	QP	QP
	Pc	PC
	Pv	PV
Mesozoic	Mu	MU
	Ep	EP
	K	K
	Ku	KU
	Kjfv	KJFV
	gr	GR
	grt	GRT
	gr ^g	GRG
	kjf	KJF
	Jk	JK
	bi	BI
	Ju	JU
	ub	UB
	JRv	JTRV

Table F-1 (Continued).

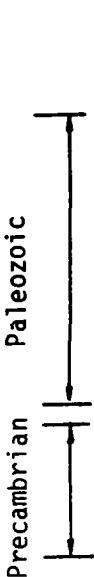
<u>Age</u>	<u>Material Symbol</u>	<u>Fortran Symbol</u>
	mv	MV
	Undivided	ms
	gr-m	GRM
	Permian	Pm
	PM	Carboniferous
	CP	CP
	CM	CM
	Devonian	D
	D	Ordovician
	O	O
	6	C
	6	CPC
	p	PC
	lp6	LPC
	ep6	EPC
Fresh Water	H2O	
Salt Water	SEA	
Salt Water Saturated		
Aluvian	QALS	

Table F-2. R-index vs index.

INDEX= 0	RINDEX=	0.
INDEX= 1	RINDEX=	136.634
INDEX= 2	RINDEX=	201.450
INDEX= 3	RINDEX=	281.737
INDEX= 4	RINDEX=	422.011
INDEX= 5	RINDEX=	478.298
INDEX= 6	RINDEX=	539.822
INDEX= 7	RINDEX=	611.471
INDEX= 8	RINDEX=	674.052
INDEX= 9	RINDEX=	746.698

Table F-3. Conductivity and dielectric constant values
for materials used on worst case path.

XNAME	SIGNAM	EPSNAM
QS	2.0000E-02	5.0
QAL	1.3300E-02	12.0
QSC	1.3300E-02	15.0
QF	1.3300E-02	15.0
QB	1.0000E-02	20.0
QST	6.6700E-03	5.0
QL	1.3300E-02	20.0
QT	1.6700E-02	15.0
QM	2.8600E-02	15.0
QPVH	5.0000E-03	5.0
QC	1.3300E-02	20.0
QP	1.3300E-02	12.0
PC	1.3300E-02	12.0
PV	5.0000E-03	5.0
MU	2.0000E-02	15.0
EP	2.0000E-02	15.0
K	2.8600E-02	12.0
KU	2.0000E-02	12.0
KJFV	2.5000E-03	5.0
GR	2.5000E-03	10.0
GRT	2.5000E-03	10.0
GRG	2.5000E-03	10.0
KJF	3.3300E-03	10.0
JK	1.0000E-02	10.0
BI	2.8600E-03	10.0
JU	2.0000E-02	10.0
UR	2.8600E-03	10.0
JTRV	2.5000E-03	5.0
MV	2.5000E-03	5.0
MS	1.2500E-02	10.0
GRM	2.0000E-03	5.0
PM	1.6700E-02	10.0
CP	1.3300E-02	10.0
CM	1.0000E-02	10.0
D	6.6700E-03	10.0
O	6.6700E-03	10.0
C	6.6700E-03	10.0
CPC	5.0000E-03	10.0
PC	3.3300E-03	5.0
LPC	2.5000E-03	5.0
EPC	2.5000E-03	5.0
H2O	2.0000E-03	81.0
SEA	4.0000E 00	81.0
QALS	4.0000E 00	81.0

Table F-4. Assumed geologic structure along the worst case path.

INDEX	DELR(KM)	MAT	DEPTH(M)	MAT	DEPTH(M)	MAT	DEPTH(M)
0	27.487	QAL	300.	PC	100000.		0.
0	28.487	QAL	100.	PC	100000.		0.
0	39.066	PC	100000.		0.		0.
0	40.066	QAL	100.	PC	100000.		0.
0	56.081	QAL	300.	PC	100000.		0.
0	60.351	QL	300.	PC	100000.		0.
0	71.714	QAL	300.	EPC	100000.		0.
0	72.714	QAL	100.	EPC	100000.		0.
0	78.195	EPC	100000.		0.		0.
0	79.195	QC	100.	EPC	100000.		0.
0	81.700	QC	200.	EPC	100000.		0.
0	82.847	QAL	100.	CPC	100000.		0.
0	83.739	CPC	100000.		0.		0.
0	86.480	C	100000.		0.		0.
0	86.926	CPC	100000.		0.		0.
0	89.000	QAL	200.	CPC	100000.		0.
0	89.941	QAL	200.	EPC	100000.		0.
0	90.941	QAL	100.	EPC	100000.		0.
0	91.833	EPC	100000.		0.		0.
0	94.255	CPC	100000.		0.		0.
0	95.255	QAL	100.	CPC	100000.		0.
0	100.774	QAL	200.	CPC	100000.		0.
0	101.774	QAL	100.	LPC	100000.		0.
0	104.833	LPC	100000.		0.		0.
0	105.407	CPC	100000.		0.		0.
0	106.108	LPC	100000.		0.		0.
0	120.893	GR	100000.		0.		0.
0	121.893	QAL	100.	GR	100000.		0.
0	126.839	QAL	200.	GR	100000.		0.
0	127.839	QAL	100.	CPC	100000.		0.
0	129.241	CPC	100000.		0.		0.
0	130.241	QC	100.	CPC	100000.		0.
0	136.634	QC	300.	CPC	100000.		0.
1	0.333	QC	300.	CPC	100000.		0.
1	1.333	QC	100.	CPC	100000.		0.
1	2.349	CPC	100000.		0.		0.
1	3.809	QC	100.	CPC	100000.		0.
1	4.317	CPC	100000.		0.		0.
1	5.317	QC	100.	CPC	100000.		0.
1	8.316	QC	500.	CPC	100000.		0.
1	15.823	QAL	300.	QC	500.	CPC	100000.
1	16.823	QAL	100.	C	100000.		0.
1	18.156	C	100000.		0.		0.
1	18.410	QAL	100.	C	100000.		0.
1	19.610	C	100000.		0.		0.
1	22.854	EPC	100000.		0.		0.
1	23.854	QAL	100.	EPC	100000.		0.
1	28.646	QAL	200.	EPC	100000.		0.
1	29.646	QAL	100.	CPC	100000.		0.
1	30.662	CPC	100000.		0.		0.

INDEX	DELR(KM)	MAT	DEPTH(M)	MAT	DEPTH(M)	MAT	DEPTH(M)
1	31.805	QAL	100.	QP	200.	CPC	100000.
1	32.186	QP	200.	CPC	100000.		0.
1	33.329	QAL	100.	QP	200.	CPC	100000.
1	33.773	CPC	100000.		0.		0.
1	35.233	EPC	100000.		0.		0.
1	37.455	QP	200.	CPC	100000.		0.
1	38.217	PV	200.	CPC	100000.		0.
1	38.471	C	200.	CPC	100000.		0.
1	42.914	CPC	100000.		0.		0.
1	43.422	EPC	100000.		0.		0.
1	50.088	GR	100000.		0.		0.
1	54.976	EPC	100000.		0.		0.
1	55.976	QST	50.	QAL	100.	EPC	100000.
1	64.308	QST	50.	QAL	400.	EPC	100000.
1	64.816	QAL	400.	EPC	100000.		0.
2	9.815	QAL	400.	EPC	100000.		0.
2	10.815	QAL	100.	CPC	100000.		0.
2	20.231	CPC	100000.		0.		0.
2	23.539	GR	100000.		0.		0.
2	36.263	EPC	100000.		0.		0.
2	37.263	QAL	100.	EPC	100000.		0.
2	46.841	QAL	200.	QP	400.	EPC	100000.
2	47.841	QAL	100.	QP	400.	EPC	100000.
2	48.923	QP	400.	EPC	100000.		0.
2	52.740	QAL	100.	QP	400.	EPC	100000.
2	55.794	QP	400.	EPC	100000.		0.
2	57.893	QAL	100.	CM	100000.		0.
2	62.219	CM	100000.		0.		0.
2	64.446	CP	100000.		0.		0.
2	64.955	QP	100.	PM	100000.		0.
2	65.909	PM	100000.		0.		0.
2	67.182	QP	100.	PM	100000.		0.
2	68.454	PM	100000.		0.		0.
2	68.889	QAL	100.	PM	100000.		0.
2	69.281	PM	100000.		0.		0.
2	70.744	QAL	100.	PM	100000.		0.
2	74.752	PM	100000.		0.		0.
2	76.215	QAL	100.	CP	100000.		0.
2	76.915	QPVH	100.	CP	100000.		0.
2	78.251	CP	100000.		0.		0.
2	79.651	QAL	100.	D	100000.		0.
2	80.287	D	100000.		0.		0.
3	0.826	D	100000.		0.		0.
3	1.335	Q	100000.		0.		0.
3	2.225	QAL	200.	D	100000.		0.
3	2.733	Q	100000.		0.		0.
3	4.703	QAL	300.	Q	100000.		0.
3	5.466	Q	100000.		0.		0.
3	7.881	QAL	200.	QC	500.	GR	100000.
3	13.474	QC	500.	GR	100000.		0.

INDEX	DELTA(KM)	MAT	DEPTH(M)	MAT	DEPTH(M)	MAT	DEPTH(M)
3	17.987	QPVR	200.	QC	500.	GR	100000.
3	19.957	QAL	200.	QC	700.	GR	100000.
3	35.148	QL	300.	QC	700.	GR	100000.
3	37.055	QAL	200.	QC	700.	GR	100000.
3	41.250	GRM	100000.		0.		0.
3	71.821	GK	100000.		0.		0.
3	72.838	QAL	50.	GR	100000.		0.
3	79.639	GR	100000.		0.		0.
3	80.084	QAL	50.	GR	100000.		0.
3	133.791	GR	100000.		0.		0.
3	135.571	MS	100000.		0.		0.
3	139.575	GR	100000.		0.		0.
3	140.274	MS	100000.		0.		0.
4	2.096	MS	100000.		0.		0.
4	11.562	GR	100000.		0.		0.
4	15.056	GRM	100000.		0.		0.
4	17.344	H2O	50.	UB	100000.		0.
4	19.059	UB	100000.		0.		0.
4	25.031	MV	200.	UB	100000.		0.
4	29.859	UB	100000.		0.		0.
4	33.035	MV	200.	GRG	100000.		0.
4	33.607	GRG	100000.		0.		0.
4	35.767	MV	200.	GRG	100000.		0.
4	38.118	QAL	50.	GRT	100000.		0.
4	41.358	GRT	100000.		0.		0.
4	42.565	BI	100000.		0.		0.
4	45.741	MV	200.	GRG	100000.		0.
4	54.826	GRG	100000.		0.		0.
4	56.287	MS	100000.		0.		0.
5	0.445	MS	100000.		0.		0.
5	5.085	QC	150.	GR	100000.		0.
5	6.165	GR	100000.		0.		0.
5	9.915	GRM	100000.		0.		0.
5	10.551	QC	100.	GRM	100000.		0.
5	14.364	GRM	100000.		0.		0.
5	16.017	JU	100000.		0.		0.
5	17.415	JTRV	300.	JU	100000.		0.
5	19.639	QC	150.	JU	100000.		0.
5	21.101	QF	150.	JU	100000.		0.
5	22.627	H2O	25.	QC	150.	JU	100000.
5	24.000	QC	150.	JU	100000.		0.
5	27.000	QC	250.	JU	100000.		0.
5	30.000	QC	350.	JU	100000.		0.
5	33.000	QC	450.	JU	100000.		0.
5	34.194	QC	550.	JU	100000.		0.
5	34.703	QF	25.	QC	550.	JU	100000.
5	36.000	QC	550.	JU	100000.		0.
5	39.000	QC	650.	JU	100000.		0.
5	42.000	QC	750.	JU	100000.		0.
5	43.728	QC	850.	JU	100000.		0.

INDEX	DELR(KM)	MAT	DEPTH(M)	MAT	DEPTH(M)	MAT	DEPTH(M)
5	44.109	QS	25.	QC	850.	JU	100000.
5	44.490	H2U	25.	QC	850.	JU	100000.
5	44.872	QC	850.	JU	100000.		0.
5	45.000	QF	25.	QC	850.	JU	100000.
5	45.889	QF	25.	QC	950.	JU	100000.
5	48.000	QC	950.	JU	100000.		0.
5	50.211	QC	1050.	JU	100000.		0.
5	51.000	QF	200.	QC	1050.	JU	100000.
5	54.000	QF	200.	QC	1150.	JU	100000.
5	57.000	QF	200.	QC	1250.	JU	100000.
5	58.473	QF	200.	QC	1350.	JU	100000.
5	60.000	QH	200.	QC	1350.	JU	100000.
5	61.524	QB	200.	QC	1450.	JU	100000.
6	2.000	QB	200.	QC	1450.	JU	100000.
6	5.000	QB	300.	QC	1650.	JU	100000.
6	8.000	QB	400.	QC	1850.	JU	100000.
6	11.000	QB	500.	QC	2050.	JU	100000.
6	14.000	QB	600.	QC	2250.	JU	100000.
6	17.000	QB	700.	QC	2450.	JU	100000.
6	20.000	QB	800.	QC	2650.	JU	100000.
6	23.000	QB	900.	QC	2850.	JU	100000.
6	26.000	QB	1000.	QC	3050.	JU	100000.
6	29.000	QB	1000.	QC	3300.	JU	100000.
6	32.000	QB	1000.	QC	3550.	JU	100000.
6	35.000	QB	1000.	QC	3800.	JU	100000.
6	39.000	QB	1000.	QC	4000.	JU	100000.
6	42.000	QB	1000.	QC	3800.	KJF	100000.
6	45.000	QB	1000.	QC	3550.	KJF	100000.
6	48.000	QB	900.	QC	3300.	KJF	100000.
6	51.000	QB	800.	QC	3050.	KJF	100000.
6	54.000	QB	700.	QC	2850.	KJF	100000.
6	57.000	QB	600.	QC	2650.	KJF	100000.
6	60.000	QB	500.	QC	2450.	KJF	100000.
6	63.000	QB	400.	QC	2250.	KJF	100000.
6	66.000	QB	300.	QC	2050.	KJF	100000.
6	69.362	QB	200.	QC	1850.	KJF	100000.
6	71.649	QC	1650.	KJF	100000.		0.
7	0.509	QC	1650.	KJF	100000.		0.
7	3.000	QF	100.	QC	1300.	KJF	100000.
7	5.220	QF	100.	QC	950.	KJF	100000.
7	5.730	PC	200.	QC	950.	KJF	100000.
7	6.239	QT	100.	QC	950.	KJF	100000.
7	7.067	EP	500.	KJF	100000.		0.
7	8.085	KU	500.	KJF	100000.		0.
7	8.849	EP	500.	KJF	100000.		0.
7	18.144	KU	500.	KJF	100000.		0.
7	19.608	KJFV	150.	KJF	100000.		0.
7	19.990	UB	150.	KJF	100000.		0.
7	53.477	KJF	100000.		0.		0.
7	58.570	QP	200.	KJF	100000.		0.

INDEX	DELR(KM)	MAT	DEPTH(M)	MAT	DEPTH(M)	MAT	DEPTH(M)
7	61.626	KU	500	KJF	1.E5		
7	62.581	MU	500	KJF	1.E5		
8	.952	MU	500	KJF	1.E5		
8	9.961	QP	300	KJF	1.E5		
8	13.641	QAL	100	QP	300	KJF	1.E5
8	20.493	K	500	KJF	1.E5		
8	31.089	KU	700	KJF	1.E5		
8	31.850	UB	700	KJF	1.E5		
8	32.104	JK	700	KJF	1.E5		
8	32.611	PV	700	KJF	1.E5		
8	34.578	UB	500	KJF	1.E5		
8	40.986	QALS	150	QMS	400	KJF	1.E5
8	43.461	SEA	25	QMS	400	KJF	1.E5
8	45.110	QMS	400	KJF	1.E5		
8	53.000	SEA	25	QMS	400	KJF	1.E5
8	58.688	SEA	50	QMS	400	KJF	1.E5
8	59.132	QALS	100	QMS	400	KJF	1.E5
8	60.020	KJF	1.E5				
8	61.733	QALS	100	QMS	400	KJF	1.E5
8	63.000	SEA	50	QMS	400	KJF	1.E5
8	66.634	SEA	150	QMS	400	KJF	1.E5
8	67.634	SEA	50	QMS	400	KJF	1.E5
8	72.646	KJF	1.E5				

*U.S. GOVERNMENT PRINTING OFFICE : 1980 O-624-045/1571